

PLASTICITY THEORY FOR GRANULAR MEDIA

By

DEVO SEEREERAM

A DISSERTATION PRESENTED TO THE GRADUATE SCHOOL
OF THE UNIVERSITY OF FLORIDA IN
PARTIAL FULFILLMENT OF THE REQUIREMENTS
FOR THE DEGREE OF DOCTOR OF PHILOSOPHY

UNIVERSITY OF FLORIDA

1986

ACKNOWLEDGEMENTS

I would first like to acknowledge Dr. Frank C. Townsend, the chairman of my supervisory committee, for his tremendous support and encouragement during this study. Dr. Townsend was instrumental in acquiring the hollow cylinder test data and in locating key references.

Professor Daniel C. Drucker made fundamental and frequent contributions to the basic ideas and their connections and to the overall intellectual structure of this work. I am deeply grateful for his vigorous critical readings of early drafts of my dissertation, his constructive and creative suggestions for revision, and his major contributions which in many ways influenced the content of this study. The delight I found in our many discussions is one of my chief rewards from this project.

I am deeply indebted to the other members of my doctoral committee: Professors John L. Davidson, Martin A. Eisenberg, William Goldhurst, Lawrence E. Malvern, and Michael C. McVay for their helpful discussions and criticism of my work. I would also like to thank Paul Linton for carefully carrying out the series of in-house triaxial tests.

This acknowledgement would not be complete without mention of the love and support I received from my family and friends. Particularly, I would like to thank Charmaine, my fiancée, for her understanding and

patience during the long hours spent at work, and my mother, who put my education above everything else, and my father, who gave me the financial freedom and the motivation to seek knowledge.

Finally, I would like to acknowledge the financial support of the United States Air Force Office of Scientific Research, under Grant No. AFOSR-84-0108 (M.C. McVay, Principal Investigator), which made this study possible.

TABLE OF CONTENTS

	PAGE
ACKNOWLEDGEMENTS.....	ii
LIST OF TABLES.....	vii
LIST OF FIGURES.....	viii
KEY TO SYMBOLS.....	xvi
ABSTRACT.....	xx
CHAPTER	
1 INTRODUCTION	
1.1 The Role and Nature of Theory.....	1
1.2 Statement of the Problem.....	2
1.3 Approach.....	4
1.4 Scope.....	6
2 PRELIMINARY AND FUNDAMENTAL CONCEPTS	
2.1 Introduction.....	10
2.2 Tensors.....	11
2.2.1 Background.....	11
2.2.2 The Stress Tensor.....	16
2.2.3 The Strain Tensor.....	28
2.3 Stress-Strain Equations and Constitutive Theory.....	33
2.4 A Note on Stress and Strain in Granular Media.....	38
2.5 Anisotropic Fabric in Granular Material.....	46
2.5.1 Introduction.....	46
2.5.2 Common Symmetry Patterns.....	47
2.5.3 Fabric Measures.....	49
2.6 Elasticity.....	52
2.6.1 Cauchy Type Elasticity.....	53
2.6.2 Hyperelasticity or Green Type Elasticity.....	57
2.6.3 Hypoelasticity or Incremental Type Elasticity.....	58
2.7 Plasticity.....	61
2.7.1 Yield Surface.....	62
2.7.2 Failure Criteria.....	69
2.7.3 Incremental Plastic Stress-Strain Relation, and Prager's Theory.....	76

2.7.4	Drucker's Stability Postulate.....	84
2.7.5	Applicability of the Normality Rule to Soil Mechanics.....	87
2.7.6	Isotropic Hardening.....	91
2.7.7	Anisotropic Hardening.....	99
2.7.8	Incremental Elasto-Plastic Stress-Strain Relation.....	102
3	PROPOSED PLASTICITY THEORY FOR GRANULAR MEDIA	
3.1	Introduction.....	106
3.2	Material Behavior Perceived as Most Essential and Relevant.....	113
3.3	Details of the Yield Function And Its Evolution.....	122
3.3.1	Isotropy.....	124
3.3.2	Zero Dilation Line.....	126
3.3.3	Consolidation Portion of Yield Surface.....	130
3.3.4	Dilation Portion of Yield Surface.....	136
3.3.5	Evolutionary Rule for the Yield Surface.....	138
3.4	Choice of the Field of Plastic Moduli.....	139
3.5	Elastic Characterization.....	142
3.6	Parameter Evaluation Scheme.....	143
3.6.1	Elastic Constants.....	145
3.6.2	Field of Plastic Moduli Parameters.....	145
3.6.3	Yield Surface or Plastic Flow Parameters.....	147
3.6.4	Interpretation of Model Parameters.....	148
3.7	Comparison of Measured and Calculated Results Using the Simple Model.....	148
3.7.1	Simulation of Saada's Hollow Cylinder Tests.....	151
3.7.2	Simulation of Hettler's Triaxial Tests.....	168
3.7.3	Simulation of Tatsuoka and Ishihara's Stress Paths.....	173
3.8	Modifications to the Simple Theory to Include Hardening.....	191
3.8.1	Conventional Bounding Surface Adaptation.....	191
3.8.2	Prediction of Cavity Expansion Tests.....	196
3.8.3	Proposed Hardening Modification.....	210
3.9	Limitations and Advantages.....	225
4	A STUDY OF THE PREVOST EFFECTIVE STRESS MODEL	
4.1	Introduction.....	230
4.2	Field of Work Hardening Moduli Concept.....	231
4.3	Model Characteristics.....	237
4.4	Yield Function.....	237
4.5	Flow Rule.....	238
4.6	Hardening Rule.....	240
4.7	Initialization of Model Parameters.....	247
4.8	Verification.....	253
5	CONCLUSIONS AND RECOMMENDATIONS.....	267

APPENDICES

PAGE

A DERIVATION OF ANALYTICAL REPRESENTATION OF DILATION PORTION
OF YIELD SURFACE.....275

B COMPUTATION OF THE GRADIENT TENSOR TO THE YIELD SURFACE.....280

C EQUATIONS FOR UPDATING THE SIZE OF THE YIELD SURFACE.....283

D PREDICTIONS OF HOLLOW CYLINDER TESTS USING THE PROPOSED MODEL.....286

E PREDICTIONS OF HETTLER'S DATA USING THE PROPOSED MODEL.....297

F COMPUTATION OF THE BOUNDING SURFACE SCALAR MAPPING
PARAMETER β301

G PREDICTIONS OF HOLLOW CYLINDER TESTS USING PREVOST'S MODEL.....303

LIST OF REFERENCES.....312

BIOGRAPHICAL SKETCH.....325

LIST OF TABLES

TABLE	PAGE
3.1	Comparison of the Characteristic State and Critical State Concepts.....131
3.2	Simple Interpretation of Model Constants.....149
3.3	Expected Trends in the Magnitude of Key Parameters With Relative Density.....150
3.4	Model Constants for Reid-Bedford Sand at 75% Relative Density.....154
3.5	Computed Isotropic Strength Constants for Saada's Series of Hollow Cylinder Tests.....167
3.6	Model Parameters for Karlsruhe Sand and Dutch Dune Sand.....172
3.7	Model Parameters for Loose Fuji River Sand.....186
3.8	Summary of Pressuremeter Tests in Dense Reid-Bedford Sand...198
3.9	Model Constants Used to Simulate Pressuremeter Tests.....199
4.1	Prevost Model Parameters for Reid-Bedford Sand.....254
5.1	Typical Variation of the Magnitude of $n:dg$ Along Axial Extension and Compression Paths.....272
A.1	Formulas for Use in Inspecting the Nature of the Quadratic Function Describing the Dilation Portion of the Yield Surface.....278

LIST OF FIGURES

FIGURE	PAGE
2.1	Representation of plane stress state at a "point".....20
2.2	Typical stress-strain response of soil for a conventional 'triaxial' compression test (left) and a hydrostatic compression test (right).....40
2.3	Typical stress paths used to investigate the stress-strain behavior of soil specimens in the triaxial environment.....42
2.4	Components of strain: elastic, irreversible plastic, and reversible plastic.....44
2.5	Common fabric symmetry types.....48
2.6	Rate-independent idealizations of stress-strain response.....63
2.7	Two dimensional picture of Mohr-Coulomb failure criterion....66
2.8	Commonly adopted techniques for locating the yield stress....68
2.9	Yield surface representation in Haigh-Westergaard stress space.....71
2.10	Diagrams illustrating the modifying effects of the coefficients A_1 and A_2 : (a) $A_1 = A_2 = 1$; (b) $A_1 \neq A_2$; (c) $A_1 = A_2 = A$90
2.11	Schematic illustration of isotropic and kinematic hardening.....92
2.12	Two dimensional view of an isotropically hardening yield sphere for hydrostatic loading.....97
3.1	In conventional plasticity (a) path CAC' is purely elastic; in the proposed formulation (b) path CB'A is elastic but AB"C' is elastic-plastic.....107

FIGURE	PAGE
3.2	The current yield surface passes through the current stress point and locally separates the domain of purely elastic response from the domain of elastic-plastic response.....108
3.3	Pictorial representation for sand of the nested set of yield surfaces, the limit line, and the field of plastic moduli, shown by the $d\epsilon_p^D$ associated with a constant value of $n_{pq} d\sigma_{pq}$110
3.4	Path independent limit surface as seen in q-p stress space.....115
3.5	Axial compression stress-strain data for Karlsruhe sand over a range of porosities and at a constant confinement pressure of 50 kN/m ²116
3.6	Stress-strain response for a cyclic axial compression test on loose Fuji River sand.....117
3.7	Medium amplitude axial compression-extension test on loose Fuji River sand.....119
3.8	Plastic strain path obtained from an anisotropic consolidation test.....120
3.9	Plastic strain direction at common stress point.....121
3.10	Successive stress-strain curves for uniaxial stress or shear are the initial curve translated along the strain axis in simplest model.....123
3.11	Constant q/p ratio (as given by constant σ_1/σ_3 ratio) at zero dilation as observed from axial compression stress-strain curves on dense Fountainbleau sand. Note that the peak stress ratio decreases with increasing pressure.....128
3.12	Characteristic state friction angles in compression and extension are different, suggesting that the Mohr-Coulomb criterion is an inappropriate choice to model the zero dilation locus.....129
3.13	Establishment of the yield surfaces from the inclination of the plastic strain increment observed along axial compression paths on Ottawa sand at relative densities of (a) 39% (e=0.665), (b) 70% (e=0.555), and (c) 94% (e=0.465).....132
3.14	Typical meridional (q -p) and octahedral sections (inset) of the yield surface.....134

FIGURE	PAGE
3.15	Trace of the yield surface on the triaxial q-p plane.....135
3.16	Stress state in "thin" hollow cylinder.....152
3.17	Saada's hollow cylinder stress paths in Mohr's stress space•155
3.18	Measured vs. fitted response for hydrostatic compression (HC) test using proposed model ($p_0 = 10$ psi).....156
3.19	Measured vs. fitted response for axial compression test (DC 0 or CTC of Figure 2.3) @30 psi using proposed model....157
3.20	Measured vs. predicted response for axial compression test (DC 0 or CTC of Figure 2.3) @35 psi using proposed model....158
3.21	Measured vs. predicted response for axial compression test (DC 0 or CTC of Figure 2.3) @45 psi using proposed model....159
3.22	Measured vs. predicted response for constant mean pressure compression shear test (GC 0 or TC of Figure 2.3) using proposed model.....161
3.23	Measured vs. predicted response for reduced triaxial compression test (RTC of Figure 2.3) using proposed model...162
3.24	Measured vs. predicted response for axial extension test (DT 90 or RTE of Figure 2.3) using proposed model.....163
3.25	Volume change comparison for axial extension test.....165
3.26	Results of axial compression tests on Karlsruhe sand at various confining pressures and at a relative density of 99%.....169
3.27	Results of axial compression tests on Dutch dune sand at various confining pressures and at a relative density of 60.9%.....171
3.28	Measured and predicted response for hydrostatic compression test on Karlsruhe sand at 99% relative density•174
3.29	Measured and predicted response for axial compression test ($\sigma_3 = 50$ kN/m ²) on Karlsruhe sand at 62.5% relative density•175
3.30	Measured and predicted response for axial compression test ($\sigma_3 = 50$ kN/m ²) on Karlsruhe sand at 92.3% relative density•176
3.31	Measured and predicted response for axial compression test ($\sigma_3 = 50$ kN/m ²) on Karlsruhe sand at 99.0% relative density•177

FIGURE	PAGE
3.32	Measured and predicted response for axial compression test ($\sigma_3 = 50 \text{ kN/m}^2$) on Karlsruhe sand at 106.6% relative density.....178
3.33	Measured and predicted response for axial compression test ($\sigma_3 = 50 \text{ kN/m}^2$) on Dutch dune sand at 60.9% relative density.....179
3.34	Measured and predicted response for axial compression test ($\sigma_3 = 200 \text{ kN/m}^2$) on Dutch dune sand at 60.9% relative density.....180
3.35	Measured and predicted response for axial compression test ($\sigma_3 = 400 \text{ kN/m}^2$) on Dutch dune sand at 60.9% relative density.....181
3.36	Type "A" (top) and type "B" (bottom) stress paths of Tatsuoka and Ishihara (1974b).....182
3.37	Observed stress-strain response for type "A" loading path on loose Fuji River sand.....183
3.38	Observed stress-strain response for type "B" loading path on loose Fuji River sand.....184
3.39	Simulation of type "A" loading path on loose Fuji River sand using the simple representation.....187
3.40	Simulation of type "B" loading path on loose Fuji River sand using the simple representation.....189
3.41	Simulation of compression-extension cycle on loose Fuji river sand using the simple representation.....190
3.42	Conventional bounding surface adaptation with radial mapping rule.....193
3.43	Finite element mesh used in pressuremeter analysis.....201
3.44	Measured vs. predicted response for pressuremeter test #1.....202
3.45	Measured vs. predicted response for pressuremeter test #2.....203
3.46	Measured vs. predicted response for pressuremeter test #3.....204

FIGURE	PAGE
3.47	Measured vs. predicted response for pressuremeter test #4.....205
3.48	Measured vs. predicted response for pressuremeter test #5.....206
3.49	Variation of principal stresses and Lode angle with cavity pressure for element #1 and pressuremeter test #2.....208
3.50	Variation of plastic modulus with cavity pressure for pressuremeter test #2.....209
3.51	Meridional projection of stress path for element #1, pressuremeter test #2.....211
3.52	Principal stresses as a function of radial distance from axis of cavity at end of pressuremeter test #2.....212
3.53	Experimental stress probes of Tatsuoka and Ishihara (1974b).....214
3.54	Shapes of the hardening control surfaces as evidenced by the study of Tatsuoka and Ishihara (1974b) on Fuji River sand.....215
3.55	Illustration of proposed hardening control surface and interpolation rule for reload modulus.....217
3.56	Illustration of the role of the largest yield surface (established by the prior loading) in determining the reload plastic modulus on the hydrostatic axis.....218
3.57	Influence of isotropic preloading on an axial compression test ($\sigma_3 = 200 \text{ kN/m}^2$) on Karlsruhe sand at 99% relative density.....220
3.58	Predicted vs. measured results for hydrostatic preconsolidation followed by axial shear.....222
3.59	Shear stress vs. axial strain data for a cyclic axial compression test on Reid-Bedford sand at 75% relative density. Nominal stress amplitude $q = 70 \text{ psi}$, and confining pressure $\sigma_3 = 30 \text{ psi}$223
3.60	Prediction of the buildup of the axial strain data of Figure 3.59 using proposed cyclic hardening representation..226

FIGURE	PAGE
3.61	Any loading starting in the region A and moving to region B can go beyond the limit line as an elastic unloading or a neutral loading path.....227
4.1	Initial (a) and subsequent (b) configurations of the deviatoric sections of the field of yield surfaces.....234
4.2	Field of nesting surfaces in p-q (top) and Cp-q subspaces (bottom).....242
4.3	Measured vs. fitted stress-strain response for axial compression path using Prevost's model.....257
4.4	Initial and final configurations of yield surfaces for CTC path (see Fig. 2.3) simulation.....258
4.5	Measured vs. fitted stress-strain response for axial extension path using Prevost's model.....259
4.6	Initial and final configurations of yield surfaces for axial extension simulation.....260
4.7	Measured vs. predicted stress-strain response for constant mean pressure compression (or TC of Fig. 2.3) path using Prevost's Model.....261
4.8	Initial and final configurations of yield surfaces for TC simulation.....262
4.9	Measured vs. predicted stress-strain response for reduced triaxial compression (or RTC of Fig. 2.3) path using Prevost's model.....263
4.10	Initial and final configurations of yield surfaces for RTC simulation.....264
4.11	Measured vs. predicted stress-strain response for constant pressure extension (or TE of Fig. 2.3) path using Prevost's model.....265
4.12	Initial and final configurations of Yield Surfaces for TE simulation.....266
D.1	Measured vs. predicted stress-strain response for DCR 15 stress path using proposed model.....286
D.2	Measured vs. predicted stress-strain response for DCR 32 stress path using proposed model.....287

FIGURE	PAGE
D.3	Measured vs. predicted stress-strain response for DTR 58 stress path using proposed model.....288
D.4	Measured vs. predicted stress-strain response for DTR 75 stress path using proposed model.....289
D.5	Measured vs. predicted stress-strain response for GCR 15 stress path using proposed model.....290
D.6	Measured vs. predicted stress-strain response for GCR 32 stress path using proposed model.....291
D.7	Measured vs. predicted stress-strain response for R 45 (or pure torsion) stress path using proposed model.....292
D.8	Measured vs. predicted stress-strain response for GTR 58 stress path using proposed model.....293
D.9	Measured vs. predicted stress-strain response for GTR 75 stress path using proposed model.....294
D.10	Measured vs. predicted stress-strain response for GT 90 stress path using proposed model.....295
E.1	Measured and predicted response for axial compression test ($\sigma_3 = 400 \text{ kN/m}^2$) on Karlsruhe sand at 92.3% relative density.....297
E.2	Measured and predicted response for axial compression test ($\sigma_3 = 80 \text{ kN/m}^2$) on Karlsruhe sand at 99.0% relative density.....298
E.3	Measured and predicted response for axial compression test ($\sigma_3 = 200 \text{ kN/m}^2$) on Karlsruhe sand at 99.0% relative density.....299
E.4	Measured and predicted response for axial compression test ($\sigma_3 = 300 \text{ kN/m}^2$) on Karlsruhe sand at 99.0% relative density.....300
G.1	Measured vs. predicted stress-strain response for DCR 15 stress path using Prevost's model.....303
G.2	Measured vs. predicted stress-strain response for DCR 32 stress path using Prevost's model.....304
G.3	Measured vs. predicted stress-strain response for DTR 58 stress path using Prevost's model.....305

FIGURE	PAGE
G.4	Measured vs. predicted stress-strain response for DTR 75 stress path using Prevost's model.....306
G.5	Measured vs. predicted stress-strain response for GCR 15 stress path using Prevost's model.....307
G.6	Measured vs. predicted stress-strain response for GCR 32 stress path using Prevost's model.....308
G.7	Measured vs. predicted stress-strain response for R 45 stress path using Prevost's model.....309
G.8	Measured vs. predicted stress-strain response for GTR 58 stress path using Prevost's model.....310
G.9	Measured vs. predicted stress-strain response for GTR 75 stress path using Prevost's model.....311

KEY TO SYMBOLS

b	parameter controlling shape of dilation portion of yield surface
C_c, C_s	compression and swell indices
$d\bar{\epsilon}, d\bar{\epsilon}^e, d\bar{\epsilon}^p$	total, elastic, and plastic (small) strain increments
$d\bar{e}, d\bar{e}^e, d\bar{e}^p$	deviatoric components of $d\bar{\epsilon}, d\bar{\epsilon}^e$ & $d\bar{\epsilon}^p$ respectively
$d\bar{\epsilon}, d\bar{\epsilon}^e, d\bar{\epsilon}^p$	equal to $\sqrt{\frac{3}{2} d\bar{e}:d\bar{e}}$, $\sqrt{\frac{3}{2} d\bar{e}^e:d\bar{e}^e}$ & $\sqrt{\frac{3}{2} d\bar{e}^p:d\bar{e}^p}$ respectively
$d\epsilon_{kk}$	incremental volumetric strain
$d\epsilon_{kk}^e, d\epsilon_{kk}^p$	incremental elastic and plastic volumetric strains
$d\bar{s}$	deviatoric components of $d\bar{g}$
$d\bar{g}$	stress increment
D_r	relative density in %
\bar{e}	deviatoric components of strain $\bar{\epsilon}$
e_0	initial voids ratio
E	elastic Young's modulus
$f(\bar{g})$	failure or limit surface in stress space
$F(\bar{g})$	yield surface in stress space
$F_p(\bar{g})$	bounding surface in stress space
G	elastic shear modulus
$g(\theta)$	function of Lode angle θ used to normalize $\sqrt{J_2}$
I_1, I_2, I_3	first, second & third invariants of the stress tensor \bar{g}
$(I_1)_i$	initial magnitude of I_1 for virgin hydrostatic loading

I_0	intersection of yield surface with hydrostatic axis (the variable used to monitor its size)
$(I_0)_p$	magnitude of I_0 for the largest yield surface established by the prior loading
$\sqrt{J_2}$	square root of second invariant of \underline{s}
$\sqrt{J_2}^*$	equivalent octahedral shear stress = $\sqrt{J_2}/g(\theta)$
k	parameter controlling size of limit or failure surface
k_{mem}	maximum magnitude of k_{mob} established by the prior loading
k_{mob}	current mobilized stress ratio computed by inserting the current stress state in the function $f(\underline{q})$
K	elastic bulk modulus
K_u	dimensionless elastic modulus number
K_p	plastic modulus
\bar{K}_p	plastic modulus at conjugate point \bar{q}
$(K_p)_o$	plastic modulus at the origin of mapping
m	exponent to model curvature of failure meridian
\underline{n}	unit normal gradient tensor to yield surface
n	exponent to control field of plastic moduli interpolation function
n^*	magnitude of n applicable to compression stress space
N	slope of zero dilatancy line in $\sqrt{J_2}^*-I_1$ stress space
N_{REP}	number of load repetitions
p	mean normal pressure ($=I_1/3$)
p_a	atmospheric pressure
p_0 or p_0	initial mean pressure
q	shear stress invariant, = $\sqrt{(3J_2)} = \sqrt{(\frac{3}{2} s_{ij}s_{ij})}$
q^*	equivalent shear stress invariant, = $\sqrt{(3J_2)}/g(\theta)$

Q	parameter controlling shape of consolidation portion of yield surface
r	parameter to model the influence of σ_3 on E
R	parameter to model deviatoric variation of strength envelope
\underline{s}	deviatoric components of \underline{g}
S	slope of dilation portion of yield surface at the origin of $\sqrt{J_2^* - I_1}$ stress space
XN	slope of radial line in $\sqrt{J_2^* - I_1}$ stress space (below the zero dilation line of slope N) beyond which the effects of preconsolidation are neglected ($0 < X \leq 1$)
z	stress obliquity $\sqrt{J_2^* / I_1}$
β	scalar mapping parameter linking current stress state \underline{g} to image stress state $\underline{\bar{g}}$ on hardening control surface
β'	modified magnitude of β in proposed hardening option to account for preconsolidation effects
γ	reload modulus parameter for bounding surface hardening option
$\gamma_1, \gamma_2, \gamma_3$	reload modulus parameters for proposed cyclic hardening option
Γ	Lame's elastic constant
δ	distance from current stress state to conjugate stress state
δ_0	distance from origin of mapping to conjugate or image stress state
$\underline{\delta}$	Kronecker delta
$\underline{\epsilon}$	components of small strain tensor
$\bar{\epsilon}, \bar{\epsilon}^e, \bar{\epsilon}^p$	total, elastic, and plastic shear strain invariants, $\sqrt{\frac{3}{2} e_{ij} e_{ij}}$, etc.
ϵ_{kk}	total volumetric strain
$\epsilon_{kk}^e, \epsilon_{kk}^p$	elastic and plastic volumetric strains
θ	Lode's parameter

λ	plastic stiffness parameter for hydrostatic compression
μ	Lame's elastic constant
ν	Poisson's Ratio
$\underline{\sigma}$	components of Cauchy stress tensor
$\underline{\bar{\sigma}}$	stress tensor at conjugate point on bounding surface
$\sigma_1, \sigma_2, \sigma_3$	major, intermediate, and minor principal stresses
$\sigma_r, \sigma_z, \sigma_\theta$	radial, axial, and hoop stress components in cylindrical coordinates
ϕ	Mohr-Coulomb friction angle or stress obliquity
ϕ_c	Mohr-Coulomb friction angle observed in a compression test (i.e., one in which $\sigma_2 = \sigma_3$)
ϕ_e	Mohr-Coulomb friction angle observed in an extension test (i.e., one in which $\sigma_1 = \sigma_2$)
ϕ_{cv}	friction angle at constant volume or zero dilatancy
χ	ratio of the incremental plastic volumetric to shear strain ($= \sqrt{3} \, d\epsilon_{kk}^p / d\bar{\epsilon}^p$)

Abstract of Dissertation Presented to the Graduate School
of the University of Florida in Partial Fulfillment of the
Requirements for the Degree of Doctor of Philosophy

PLASTICITY THEORY FOR GRANULAR MEDIA

By

Devo Seereeram

May 1986

Chairman: Dr. Frank C. Townsend
Major Department: Civil Engineering

A special time-independent or elastic-plastic formulation is developed through qualitative and quantitative comparisons with experimental results reported in the literature. It does appear to provide a simple yet adequate model for a number of key aspects of the inelastic response of sands over a wide variety of loading paths. In its simplest form, the material model is purely stress dependent and exhibits no memory at all of prior inelastic deformation. Elementary procedures are presented for matching the limit or failure surface, the yield surface which passes through the current stress point for unloading as well as loading, and the associated scalar field of purely stress-dependent plastic moduli. Specific choices are presented for several sands of different origin and initial density.

Based on well-known experimental investigations, a hardening modification to the simple theory is proposed. The versatility of this novel proposal is demonstrated by predicting the cyclic hardening

phenomenon typically observed in a standard resilient modulus test and the influence of isotropic preconsolidation on a conventional triaxial test. Another more conventional bounding-surface hardening option is also described, and it is implemented to predict the results of a series of cyclic cavity expansion tests.

For comparative evaluation with the proposed theory, a study of the Prevost effective stress model is also undertaken. This multi-surface representation was chosen because it is thought of as one of the most fully developed of the existing soil constitutive theories.

CHAPTER 1 INTRODUCTION

1.1 The Role and Nature of Theory

In most fields of knowledge, from physics to political science, it is essential to construct a theory or hypothesis to make sense of a complex reality. The complex reality scrutinized in this dissertation is the load-deformation behavior of a statistically homogenous assemblage of unbound particles. More specifically, the mathematical theory of plasticity is used as the basis for developing a constitutive model for granular material. Such constitutive relations are of fundamental importance in a number of areas of science and technology including soil mechanics, foundation engineering, geophysics, powder processing, and the handling of bulk materials.

The mathematical theories of plasticity of this study should be clearly distinguished from the physical or microstructural plasticity theories which attempt to model the local interaction of the granules. A mathematical (or phenomenological) theory is only a formalization of known experimental results and does not inquire very deeply into their physical basis. It is essential, however, to the solution of problems in stress analysis and also for the correlation of experimental data (Drucker, 1950b).

To explain or model the complex phenomenon of particles crushing, distorting, sliding, and rolling past each other under load, a theory must simplify and abstract from reality. However, these simplifications and idealizations must lie within the realm of physically and mathematically permissible stress-strain relations. The test of any scientific theory is whether it explains or predicts what it is designed to explain or predict, and not whether it exactly mirrors reality. The most useful theory is the simplest one which will work for the problem at hand. A theory can consider only a few of the many factors that influence real events; the aim is to incorporate the most important factors into the theory and ignore the rest.

1.2 Statement of the Problem

The characterization of the complex stress-strain response of granular media is a subject which has generated much interest and research effort in recent years, as evidenced by the symposia organized by Cowin and Satake (1978), Yong and Ko (1980a), Pande and Zienkiewicz (1980), Vermeer and Luger (1982), Gudehus and Darve (1984), and Desai and Gallagher (1984), among others. This focusing of attention on constitutive models is a direct consequence of the increasing use of the finite element method to solve previously intractable boundary value problems. Solutions obtained from this powerful computer-based method are often precise to several significant digits, but this impressive degree of precision loses its significance if the governing equations, coupled with the constitutive assumptions or the imposed boundary conditions, are inappropriate idealizations of the physical problem.

Progress in the area of theoretical modelling of soil response has lagged conspicuously behind the state-of-the-art numerical solution techniques. An all-encompassing stress-strain model for soil media, or for that matter any other material, has yet to be formulated and opinions differ as to whether such a task is even remotely possible. An apparent drawback of all presently available constitutive relations is that each has been founded on data gathered from standard laboratory tests, and as Yong and Ko (1980b, p. 55) succinctly state, "the relationships developed therefrom have been obviously conditioned to respond to the soils tested as well as for the particular test system constraints, and therefore the parameters used and material properties sensed have been chosen to fit the test circumstance. Extension and projection into a more general framework for wider use do not appear to be sufficiently well founded."

Although the evolution of a fundamental set of constitutive equations will benefit foundation engineering as a science, this particular research effort was stimulated by the problem of rutting in pavement base courses--in particular, the existing U.S. Air Force runway system which is soon expected to be overloaded by a new generation of heavier aircraft. Dr. Salkind (1984), the director of the Air Force Office of Scientific Research (AFOSR), elucidates:

The relevance is extraordinarily high for this nation. There is the obvious deterioration of our highway system including potholes. The Air Force has 3700 miles of runways around the world designed for a 20 year life. Ninety-two percent are more than 20 years old and 25 percent are significantly deteriorated. The anticipated replacement cost with today's technology is \$1.9 billions. . . .The underlying methodology is empirical and should be put on a sound analytical basis. . . .The pavement system, consisting of supporting soil,

underpavement, and paving material should be analyzed for loads and moments (and loading spectrum) recognizing the differing response of the various layers with different material properties. A basic science need is the lack of measuring techniques for fundamental soil properties and descriptions of soil constitutive properties. Design is based on empirical values such as the penetration of a standard cone. As soil is a multi-phase mixture of solid particles, water, and air, the challenge is to define what are the basic fundamental properties (eg. soil "fabric" or spatial arrangement of particles) and how such properties change with loading (Personal communication, October 12).

Ever since the pioneering work of Drucker and Prager (1952), phenomenological plasticity theory has been developed and applied extensively to model the mechanical behavior of soil. Constitutive relations have grown increasingly complex as engineering mechanics have attempted to include the details of response for a broader spectrum of loading paths. However, it is not clear that some of these more sophisticated idealizations are better approximations of reality, or whether they do capture the key aspects of soil behavior. The present situation is complicated further by another problem: practicing geotechnical engineers, the group most qualified to evaluate the usefulness of these models, do not, for the most part, have a full and working knowledge of tensor calculus and basic plasticity precepts. They therefore tend to shun these potentially useful stress-strain relations in favor of the simpler elastic and quasi-linear theories.

1.3 Approach

Using concepts recently advanced by Drucker and Seereeram (1986), a new stress-strain model for granular material is introduced. This

representation incorporates those key aspects of sand behavior considered most important and relevant, while also attempting to overcome the conceptual difficulties associated with existing theories. Many aspects of conventional soil plasticity theory are abandoned in this novel approach:

1. The material is assumed to remain at yield during unloading in order to simulate inelastic response (either "virgin" or partially hardened) on reloading.
2. Plastic deformation is assumed possible at all stress levels (i.e., there is a vanishing region of elastic response for loading or reloading). The yield surface is not given by the traditional permanent strain offset or tangent modulus definitions, but by its tangent plane normal to the observed plastic strain increment vector.
3. The consistency condition does not play a central role in the determination of the plastic modulus. Instead, a scalar field of moduli in stress space is selected to give the plastic stiffness desired.
4. The limit surface is not an asymptote of or a member of the family of yield surfaces. These distinct surfaces intersect at an appreciable angle.
5. Hardening is controlled solely by changes in the plastic modulus. Therefore, the surface enclosing the partially or completely hardened region can be selected independently of the size and shape of the current yield surface.

In its most elementary form, the model ignores changes in state caused by the inelastic strain history. The field of plastic moduli

remains fixed and the yield surface expands and contracts isotropically to stay with the stress point. Supplementary features, including conventional work-hardening, bounding surface hardening, and cyclic hardening or softening, can be added as special cases by some simple and straightforward modifications to the basic hypotheses.

For comparative evaluation, a study of the Prevost (1978, 1980) pressure-sensitive isotropic/kinematic hardening theory is also undertaken. This model was chosen because it is thought of as the most complete analytical statement on elasto-plastic anisotropic hardening theories in soil mechanics (Ko and Sture, 1980).

1.4 Scope

Chapter 2 attempts to elucidate the fundamentals of plasticity theory from the perspective of a geotechnical engineer. It is hoped that this discussion will help the reader, particularly one who is unfamiliar with tensors and conventional soil plasticity concepts and terminology, to understand the fundamentals of plasticity theory and thus better appreciate the salient features of the new proposal.

Based on well-known observations on the behavior of sand, details of the new theory are outlined in Chapter 3. Specific choices are tendered for the analytical representations of 1) the yield surface, 2) the scalar field of plastic moduli (which implicitly specifies a limit or failure surface), and 3) the evolution of the yield surface. Several novel proposals are also embedded in these selections.

A procedure is outlined for computing the model constants from two standard experiments: a hydrostatic compression test and an axial compression test. Each parameter is calculated directly from the

stress-strain data, and the initialization procedure involves no trial and error or curve fitting techniques. Each parameter depends only on the initial porosity of the sand. What is particularly appealing is that all model constants can be correlated directly or conceptually to stress-strain or strength constants, such as friction angle and angle of dilation (Rowe, 1962), considered fundamental by most geotechnical engineers.

A number of hollow cylinder and solid cylinder test paths are used to demonstrate the predictive capacity of the simple "non-hardening" version of the theory. These tests include one series with a wide variety of linear monotonic paths, another consisting of axial compression paths on specimens prepared over an extended range of initial densities and tested under different levels of confining pressure, and still another sequence with more general load-unload-reload stress paths, including one test in which the direction of the shear stress is completely reversed. The range of the data permitted examination of the influence of density, if any, on the magnitudes of the model constants.

Although most of the predictions appeared satisfactory, many questions are raised concerning the reliability of the data and the probable limitations of the mathematical forms chosen for the yield surface and the field of plastic moduli.

Two hardening modifications to the simple theory are described. Unfortunately, both options sacrifice one important characteristic of the simple model: the ability to model "virgin" response in extension after a prior loading in compression, or vice-versa. The first, less realistic option is an adaptation of Dafalias and Herrmann's (1980)

bounding surface theory for clay, which is itself an outgrowth of the nonlinearly hardening model proposed by Dafalias and Popov (1975). Two modifications to the simple theory transform it to the first hardening option: 1) the largest yield surface established by the loading history is prescribed as a locus of "virgin" or prime loading plastic moduli (i.e., a bounding surface), and 2) for points interior to the bounding surface, an image point is defined as the point at which a radial line passing through the current stress state intersects the bounding surface. Then the plastic modulus at an interior stress state is rendered a function of the plastic modulus at the image point and the Euclidean distance between the current stress state and the image point. These constitutive equations are implemented in a finite element computer code to predict the results of a series of cyclic cylindrical cavity expansion tests.

Based on the observations of Poorooshasb et al. (1967) and Tatsuoka and Ishihara (1974b), a second, more realistic hardening option is proposed. It differs from the bounding surface formulation in that 1) the shape of the surface which encloses the "hardened" region differs from the shape of the yield surface, and 2) a special mapping rule for locating the conjugate or image point is introduced. The versatility of this proposed (cyclic) hardening option is demonstrated by predicting a) the influence of isotropic preconsolidation on an axial compression test, and b) the buildup of axial strain in a uniaxial cyclic compression test.

In Chapter 4 the Prevost (1978, 1980) model is described. Although this theory has been the focus of many studies, the writer believes that certain computational aspects of the hardening rule may have until now

been overlooked. These equations, appearing here for the first time in published work, were gleaned from a computer program written by the progenitors of the model (Hughes and Prevost, 1979).

Three experiments specify the Prevost model parameters: i) an axial compression test, ii) an axial extension test, and iii) a one-dimensional consolidation test, and although the initialization procedure was followed with great care, this model seemed incapable of realistically simulating stress paths which diverge appreciably from its calibration paths. Because of this serious limitation, no effort was expended beyond predicting one of the series of experiments used for verifying the proposed model.

CHAPTER 2
PRELIMINARY AND FUNDAMENTAL CONCEPTS

2.1 Introduction

It is the primary objective of this chapter to present and to discuss in a methodical fashion the key concepts which form the foundation of this dissertation. At the risk of composing this section in a format which is perhaps unduly elementary and prolix to the mechanist, the author strives herein to fill what he considers a conspicuous void in the soil mechanics literature: a discussion of plasticity theory which is comprehensible to the vast majority of geotechnical engineers who do not have a full and working knowledge of classical plasticity or tensor analysis.

The sequence in which the relevant concepts are introduced is motivated by the writer's background as a geotechnical engineer--accustomed to the many empirical correlations and conventional plane strain, limit equilibrium methods of analysis--venturing into the field of generalized, elasto-plastic stress-strain relations. The terms "generalized" and "elasto-plastic" will be clarified in the sequel. At the beginning, it should also be mentioned that, although an attempt will be made to include as many of the basic precepts of soil plasticity as possible, this chapter will give only a very condensed and selected treatment of what is an extensive and complex body of knowledge. In a

less formal setting, this chapter might have been titled "Plain Talk About Plasticity For The Soils Engineer."

2.2 Tensors

2.2.1 Background

Lack of an intuitive grasp of tensors and tensor notation is perhaps the foremost reason that many geotechnical engineering practitioners and students shun the theoretical aspects of work-hardening plasticity, and its potentially diverse computer-based applications in geomechanics.

In this chapter, the following terms and elementary operations are used without definition: scalar, vector, linear functions, rectangular Cartesian coordinates, orthogonality, components (or coordinates), base vectors (or basis), domain of definition, and the rules of a vector space such as the axioms of addition, scalar multiple axioms and scalar product axioms. Except where noted, rectangular Cartesian coordinates are used exclusively in this dissertation. This particular set of base vectors forms an orthonormal basis, which simply means that the vectors of unit length comprising the basis are mutually orthogonal (i.e., mutually perpendicular).

Quoting from Malvern (1969, p.7),

Physical laws, if they really describe the physical world, should be independent of the position and orientation of the observer. That is, if two scientists using different coordinate systems observe the same physical event, it should be possible to state a physical law governing the event in such a way that if the law is true for one observer, it is also true for the other.

Assume, for instance, that the physical event recorded is a spatial vector \underline{t} acting at some point P in a mass of sand, which is in equilibrium under a system of boundary forces. This vector represents some geometrical or physical object acting at P, and we can instinctively reason that this "tangible" entity, \underline{t} , does not depend on the coordinate system in which it is viewed. Furthermore, we can presume that any operations or calculations involving this vector must always have a physical interpretation. This statement should not be surprising since many of the early workers in vector analysis, Hamilton for example, actually sought these tools to describe mathematically real events. An excellent historical summary of the development of vector analysis can be found in the book published by Wrede (1972).

Having established that the entities typically observed, such as the familiar stress and strain vectors, are immutable with changes in perspective of the viewer, we must now ask: How does one formulate propositions involving geometrical and physical objects in a way free from the influence of the underlying arbitrarily chosen coordinate system? The manner in which this invariance requirement is automatically fulfilled rests on the representation of physical objects by tensors. To avoid any loss of clarity from using the word "tensor" prior to its definition, one should note that a vector is a special case of a tensor. There are several excellent references which deal with the subject of vector and tensor analysis in considerably more detail than the brief overview presented in the following. These include the books by Aklonis and Goldberg (1972), Hay (1953), Jaunzemis (1967), Malvern (1969), Synge and Schild (1949) and Wrede (1972).

Although the necessity to free our physical law from the arbitrariness implicit in the selection of a coordinate system has been set forth, it is important to realize that this assertion is meaningless without the existence of such coordinate systems and transformation equations relating them. The transformation idea plays a major role in the present-day study of physical laws. In fact, the use of tensor analysis as a descriptive language for theoretical physics is largely based on the invariant properties of tensor relations under certain types of transformations. For example, we can imagine that the vector \underline{t} was viewed by two observers, each using a different rectangular Cartesian coordinate system (say rotated about the origin with respect to each other). As a result, an alternative set of vector components was recorded by each scientist. Nonetheless, we should expect the length of the vector--a frame indifferent quantity--computed by both observers to be identical.

The transformation rules, which guarantee the invariant properties of vectors and tensors, are actually quite simple, but they are very important in deciding whether or not a quantity does indeed possess tensorial characteristics. To illustrate how a vector is converted from one rectangular Cartesian coordinate system to another, consider the following example in which the "new" coordinate components and base vectors are primed (') for distinction. The transformation from the old basis $(\underline{i}_1, \underline{i}_2, \underline{i}_3)$ to the new basis $(\underline{i}'_1, \underline{i}'_2, \underline{i}'_3)$ can be written in the matrix form

$$[\underline{i}'_1, \underline{i}'_2, \underline{i}'_3] = [\underline{i}_1, \underline{i}_2, \underline{i}_3] \begin{bmatrix} \cos(\underline{i}_1, \underline{i}'_1) & \cos(\underline{i}_2, \underline{i}'_1) & \cos(\underline{i}_3, \underline{i}'_1) \\ \cos(\underline{i}_1, \underline{i}'_2) & \cos(\underline{i}_2, \underline{i}'_2) & \cos(\underline{i}_3, \underline{i}'_2) \\ \cos(\underline{i}_1, \underline{i}'_3) & \cos(\underline{i}_2, \underline{i}'_3) & \cos(\underline{i}_3, \underline{i}'_3) \end{bmatrix}$$

(2.2.1.1)

where $\cos(\underline{i}_1, \underline{i}'_2)$, for example, represents the cosine of the angle between the base vectors \underline{i}_1 and \underline{i}'_2 . This is an ideal juncture to digress in order to introduce two notational conventions which save an enormous amount of equation writing.

The range convention states that when a small Latin suffix occurs unrepeated in a term, it is understood to take all the values 1,2,3. The summation convention specifies that when a small Latin suffix is repeated in a term, summation with respect to that term is understood, the range of summation being 1,2,3. To see the economy of this notation, observe that equation 2.2.1.1 is completely expressed as

$$\underline{i}'_m = Q_{mk} \underline{i}_k, \quad (2.2.1.2)$$

where Q_{mk} is equal to $\cos(\underline{i}_k, \underline{i}'_m)$. The index "m" in this equation is known as the free index since it appears only once on each side. The index "k" is designated the dummy index because it appears twice in the summand and implies summation over its admissible values (i.e., 1,2,3).

The corresponding transformation formulas for the vector components (t_r to t'_k) can now be derived from the information contained in equation 2.2.1.2 and the condition of invariance, which requires the vector representations in the two systems to be equivalent. That is,

$$\underline{t} = t_k \underline{i}_k = \underline{t}' = t'_m \underline{i}'_m. \quad (2.2.1.3)$$

Substituting the inverse of equation 2.2.1.2 (i.e., $\underline{i}_k = Q_{kr} \underline{i}'_r$) into equation 2.2.1.3 leads to

$$t_k Q_{kr} \underline{i}'_r = t'_r \underline{i}'_r,$$

or

$$(t'_r - t_k Q_{kr}) \underline{i}'_r = 0,$$

from which we see

$$t'_r = t_k Q_{kr}. \quad (2.2.1.4)$$

With the invariance discussion and the vector transformation example as background information, the following question can now be asked: What actually is a tensor? It is best perhaps to bypass the involved mathematical definition of a tensor and to proceed with a heuristic introduction (modified from Malvern, 1969, and Jaunzemis, 1967). The discussion will focus on the particular type of tensor in which we are most interested: second order (or second rank), orthogonal tensors.

Scalars and vectors are fitted into the hierarchy of tensors by identifying scalars with tensors of rank (or order) zero and vectors of rank (or order) one. With reference to indicial notation, we can say that the rank of a tensor corresponds to the number of indices appearing in the variable; scalar quantities possess no indices, vectors have one index, second order tensors have two indices, and higher rank tensors possess three or more indices. Every variable that can be written in index notation is not a tensor, however. Remember that a vector has to obey certain rules of addition, etc. or, equivalently, transform according to equation 2.2.1.4. These requirements for first order tensors (or vectors) can be generalized and extended for higher order tensors.

To introduce the tensor concept, let us characterize the state at the point P (of, say, the representative sand mass) in terms of the nature of the variable under scrutiny. If the variable can be described by a scalar point function, it is a scalar quantity which in no way depends on the orientation of the observer. Mass, density, temperature, and work are examples of this type of variable.

Suppose now that there exists a scalar $v^{(n)}$ (such as speed) associated with each direction at the point P, the directions being described by the variable unit vector \underline{n} . This multiplicity of scalars depicts a scalar state, and if we identify this scalar with speed, for instance, we can write

$$v^{(n)} = \underline{v} [\underline{n}] = v_i n_i \quad (2.2.1.5)$$

where $v^{(n)}$ is the component of speed in the nth direction, and the square brackets are used to emphasize that \underline{v} , the velocity vector, is a linear operator on \underline{n} . Deferring a more general proof until later, it can be said that the totality of scalars $v^{(n)}$ at a point is fully known if the components of \underline{v} are known for any three mutually orthogonal directions. At the point P, therefore, the scalar state is completely represented by a first order tensor, otherwise known as a vector.

The arguments for a second order tensor suggest themselves if one considers the existence of a vector state at P; that is, a different vector, $\underline{t}^{(n)}$, is associated with each direction \underline{n} . Two important examples of this type of tensor--the stress tensor and the strain tensor--are discussed in some detail in the following.

2.2.2 The Stress Tensor

An example of second order tensors in solid mechanics is the stress tensor. It is the complete set of data needed to predict the totality of stress (or load intensity) vectors for all planes passing through point P.

Recalling the routinely used Mohr circle stress representation, we generally expect different magnitudes of shear stress and normal stress to act on an arbitrary plane through a point P. The resultant stress

vector (or traction) $\underline{t}^{(n)}$ is unique on each of these planes and is a function of \underline{n} at the point P, where \underline{n} is the unit vector normal to a specified plane. In order to describe fully the state of stress at P, a relationship between the vectors $\underline{t}^{(n)}$ and \underline{n} must be established; in other words, we seek a vector function of a single vector argument \underline{n} . It turns out that we are in fact seeking a linear vector function, say \underline{g} , which is a rule associating the vector $\underline{t}^{(n)}$ with each vector \underline{n} in the domain of definition. A linear vector function is also called a linear transformation of the domain or a linear operator acting in the domain of definition of the function \underline{g} .

A second order extension of equation 2.2.1.5 is

$$\underline{t}^{(n)} = \underline{g} [\underline{n}], \quad (2.2.2.1)$$

where again the square brackets imply a linear operation. The linearity assumption of the function \underline{g} implies the following relationships:

$$\underline{g}[(\underline{n}_1 + \underline{n}_2)/|\underline{n}_1 + \underline{n}_2|] = \underline{g}[\underline{n}_1] + \underline{g}[\underline{n}_2] \quad (2.2.2.2)$$

for arbitrary unit vectors \underline{n}_1 and \underline{n}_2 , and

$$\underline{g}[\alpha \underline{n}] = \alpha \underline{g}[\underline{n}] \quad (2.2.2.3)$$

for arbitrary unit vector \underline{n} and real number α .

Geometrically, equation 2.2.2.2 means that the operator \underline{g} carries the diagonal of the parallelogram constructed on the vectors \underline{n}_1 and \underline{n}_2 into the diagonal of the parallelogram constructed on the vectors $\underline{t}_1 = \underline{g}[\underline{n}_1]$ and $\underline{t}_2 = \underline{g}[\underline{n}_2]$. Equation 2.2.2.3 means that if the length of the vector \underline{n} is multiplied by a factor α , then so is the length of the vector $\underline{t}^{(n)} = \underline{g}[\underline{n}]$.

Using a rectangular Cartesian coordinate system, the traction vector $\underline{t}^{(n)}$ and the unit normal vector \underline{n} can each be resolved into their

components $t_1^{(n)}$, $t_2^{(n)}$, $t_3^{(n)}$ and n_1 , n_2 , n_3 respectively. The linear relationship between \underline{t} and \underline{n} can be expressed in the matrix form

$$[t_1^{(n)}, t_2^{(n)}, t_3^{(n)}] = [n_1, n_2, n_3] \begin{bmatrix} \sigma_{11} & \sigma_{12} & \sigma_{13} \\ \sigma_{21} & \sigma_{22} & \sigma_{23} \\ \sigma_{31} & \sigma_{32} & \sigma_{33} \end{bmatrix}, \quad (2.2.2.4)$$

or alternatively, in the indicial notation,

$$t_i^{(n)} = \sigma_{ji} n_j, \quad (2.2.2.5)$$

where the components of the 3×3 matrix $\underline{\sigma}$ are defined as the stress tensor acting at point P. Note that the wavy underscore under symbols such as " $\underline{\sigma}$ " is used to denote tensorial quantities; however, in cases where indices are used, the wavy underscore is omitted.

In general, tensors can vary from point to point within the illustrative sand sample, representing a tensor field or a tensor function of position. If the components of the stress tensor are identical at all points in the granular mass, a homogenous state of stress is said to exist. The implication of homogeneity of stress (and likewise, strain) is particularly important in laboratory soil tests where such an assumption is of fundamental (but controversial) importance in interpreting test data (Saada and Townsend, 1980).

Second order tensors undergo coordinate transformations in an equivalent manner to vectors (see equation 2.2.1.4). For a pure rotation of the basis, the transformation formula is derived by employing a sequence of previous equations. Recall from equation 2.2.1.4 that

$$t'_r = t_k Q_{kr},$$

and by combining this equation with equation 2.2.2.5, we find that

$$t'_r = \sigma_{jk} n_j Q_{kr}. \quad (2.2.2.6)$$

Furthermore, \underline{n} in this equation can be transformed to \underline{n}' resulting in

$$t'_r = \sigma_{jk} Q_{js} n'_s Q_{kr}. \quad (2.2.2.7)$$

The left hand side of equation 2.2.2.7 can also be replaced by the linear transformation so that

$$\sigma'_{pr} n'_p = \sigma_{jk} Q_{js} n'_s Q_{kr},$$

which when rearranged yields

$$\sigma'_{pr} n'_p - \sigma_{jk} Q_{js} n'_s Q_{kr} = 0. \quad (2.2.2.8)$$

All the indices in equation 2.2.2.8 are dummy indices except "r"-- the free index. A step that frequently occurs in derivations is the interchange of summation indices. The set of equations is unchanged if the dummy index "p" is replaced by the dummy index "s." This manipulation allows us to rewrite equation 2.2.2.8 in the form

$$\sigma'_{sr} n'_s - \sigma_{jk} Q_{js} n'_s Q_{kr} = 0,$$

and by factoring out the common term n'_s , we obtain

$$(\sigma'_{sr} - \sigma_{jk} Q_{js} Q_{kr}) n'_s = 0.$$

From this equation, the tensor transformation rule is seen to be

$$\sigma'_{sr} = \sigma_{jk} Q_{js} Q_{kr}, \quad (2.2.2.9)$$

or in tensor notation,

$$\underline{\sigma}' = \underline{Q}^T \underline{\sigma} \underline{Q}. \quad (2.2.2.10)$$

It was previously stated (without verification) that a vector is completely defined once its components for any three mutually orthogonal directions are known. The reciprocal declaration for a second order tensor will therefore be that the components of a second order tensor are determined once the vectors acting on three mutually orthogonal planes are given. For the particular case of the stress tensor, this statement can be substantiated by inspecting the free body diagram of Figure 2.1 (note that this is not a general proof). Here, a soil prism

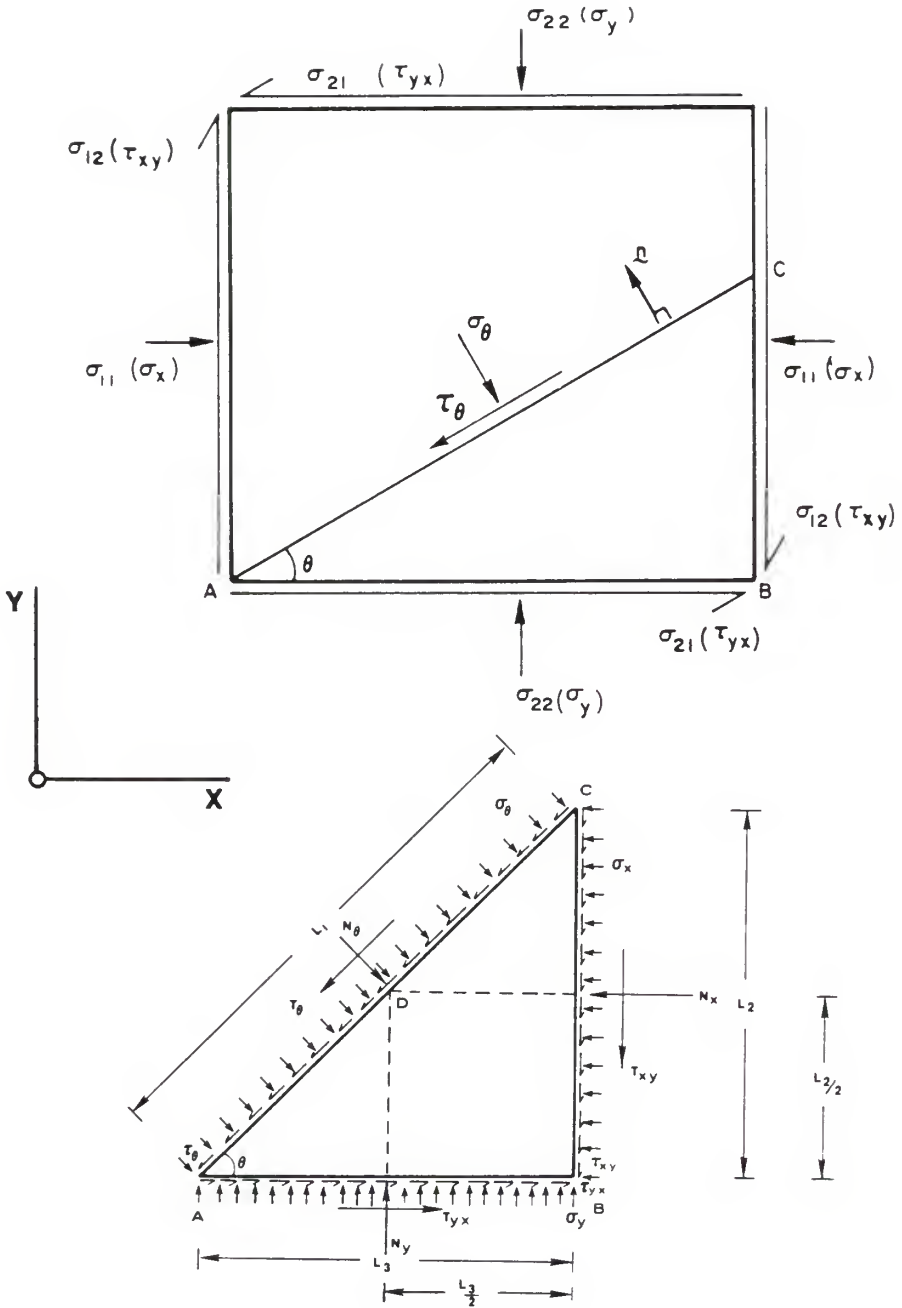


Figure 2.1 Representation of plane stress state at a "point"

is subject to a plane stress state, plane stress simply meaning there is no resultant stress vector on one of the three orthogonal planes; therefore, the non-zero stress components occupy a 2×2 matrix instead of the generalized 3×3 matrix. Generalized, in this context, refers to a situation where the full array of the stress tensor is considered in the problem, and when used as an adjective to describe a stress-strain relationship, the word tacitly relates all components of strain (or strain increment) to each stress (or stress increment) component for arbitrary loading programs.

Figure 2.1 shows the two-dimensional free body diagram of a material prism with a uniform distribution of stress vectors acting on each plane; note that the planes AB and BC are perpendicular. By taking moments about the point D, it can be shown that $\tau_{xy} = \tau_{yx}$, and this is known as the theorem of conjugate shear stresses, a relationship which is valid whenever no distributed body or surface couple acts on the element. This two dimensional observation can be generalized to three dimensions, where as a consequence, the 3×3 stress tensor matrix is symmetric. Symmetry implies that only six of the nine elements of the 3×3 matrix are independent.

By invoking force equilibrium in the x - and y -directions of Figure 2.1, the two resulting equations can be solved simultaneously for the unknowns τ_θ and σ_θ , thus verifying that the shear and the normal stress (or the stress vector in this case) on an arbitrary plane can be computed when the stress vectors on perpendicular planes are known. Extension of this two-dimensional result to three dimensions reveals that the components of three mutually perpendicular traction vectors,

acting on planes whose normals are the reference axes, comprise the rows of the stress tensor matrix.

Most geotechnical engineers are familiar with the Mohr-Coulomb strength theory for granular soils. This criterion specifies a limit state (or a locus in stress space where failure occurs with "infinite" deformations) based on a combination of principal stresses (σ_1 , σ_2 , and σ_3). As will be described in a later section on plasticity, even the more recently proposed failure criteria for soils are also only functions of the principal stresses. This is the motivation for presenting the following procedure for computing the principal stresses from the frame-dependent components of g .

A principal plane is a plane on which there are no shear stresses. This implies that the normal stress is the sole component of the traction vector acting on such a plane, and the geometrical interpretation is that the traction vector and the unit normal vector (\underline{n}) to the plane at a point both have the same line of action.

Mathematically, the principal plane requirement can be expressed as

$$\underline{t}^{(n)} = \Lambda \underline{n}, \quad (2.2.2.11)$$

or in indicial notation,

$$t_i^{(n)} = \Lambda n_i, \quad (2.2.2.12)$$

where Λ is the numerical value sought. Remember that there are, in general, three principal planes and therefore three principal values (Λ_1 , Λ_2 , and Λ_3).

Substituting equation 2.2.2.12 into equation 2.2.2.5 and rearranging leads to

$$\sigma_{ji} n_j - \Lambda n_i = 0. \quad (2.2.2.13)$$

As an aid to solving this equation for Λ , an extremely useful algebraic device, known as the Kronecker delta δ , is now introduced. It is a second order tensor defined as

$$\delta_{ij} = \begin{cases} 1 & \text{if } i = j \\ 0 & \text{if } i \neq j \end{cases} \quad (2.2.2.14)$$

By writing out the terms in long form, one may easily verify that

$$n_i = \delta_{ij} n_j \quad (2.2.2.15)$$

Equation 2.2.2.15 can now be substituted into equation 2.2.2.13 to give

$$\sigma_{ji} n_j - \Lambda \delta_{ij} n_j = 0,$$

or

$$(\sigma_{ji} - \Lambda \delta_{ij}) n_j = 0. \quad (2.2.2.16)$$

For clarity, equation 2.2.2.16 is expanded out to

$$\begin{aligned} (\sigma_{11} - \Lambda) n_1 + \sigma_{12} n_2 + \sigma_{13} n_3 &= 0 \\ \sigma_{21} n_1 + (\sigma_{22} - \Lambda) n_2 + \sigma_{23} n_3 &= 0, \\ \sigma_{31} n_1 + \sigma_{32} n_2 + (\sigma_{33} - \Lambda) n_3 &= 0 \end{aligned} \quad (2.2.2.17)$$

which may be organized in the matrix form

$$\begin{bmatrix} \sigma_{11} - \Lambda & \sigma_{12} & \sigma_{13} \\ \sigma_{21} & \sigma_{22} - \Lambda & \sigma_{23} \\ \sigma_{31} & \sigma_{32} & \sigma_{33} - \Lambda \end{bmatrix} \begin{Bmatrix} n_1 \\ n_2 \\ n_3 \end{Bmatrix} = \begin{Bmatrix} 0 \\ 0 \\ 0 \end{Bmatrix}, \quad (2.2.2.18)$$

and where it is seen to represent a homogenous system of three linear equations in three unknowns (n_1 , n_2 , and n_3) and contains the unknown parameter Λ . The fourth equation for solving this system is provided by the knowledge that

$$\underline{n} \cdot \underline{n} = n_i n_i = 1, \quad (2.2.2.19)$$

since \underline{n} is a unit vector.

Equation 2.2.2.16 has a nontrivial solution if and only if the determinant of the coefficient matrix in equation 2.2.2.18 is equal to

zero (see, for example, Wylie and Barrett, 1982, p.188). That is,

$$\begin{vmatrix} \sigma_{11} - \Lambda & \sigma_{12} & \sigma_{13} \\ \sigma_{21} & \sigma_{22} - \Lambda & \sigma_{23} \\ \sigma_{31} & \sigma_{32} & \sigma_{33} - \Lambda \end{vmatrix} = 0 \quad (2.2.2.20)$$

must be true for non-trivial answers.

This determinant can be written out term by term to give a cubic equation in Λ ,

$$\Lambda^3 - I_1 \Lambda^2 - I_2 \Lambda - I_3 = 0, \quad (2.2.2.21)$$

where the coefficients

$$I_1 = \sigma_{11} + \sigma_{22} + \sigma_{33} = \sigma_{kk}, \quad (2.2.2.22)$$

$$\begin{aligned} I_2 &= -(\sigma_{11}\sigma_{22} + \sigma_{22}\sigma_{33} + \sigma_{33}\sigma_{11}) + \sigma_{23}^2 + \sigma_{31}^2 + \sigma_{12}^2 \\ &= (\sigma_{ij}\sigma_{ij} - I_1^2) / 2, \end{aligned} \quad (2.2.2.23)$$

and

$$I_3 = \begin{vmatrix} \sigma_{11} & \sigma_{12} & \sigma_{13} \\ \sigma_{21} & \sigma_{22} & \sigma_{23} \\ \sigma_{31} & \sigma_{32} & \sigma_{33} \end{vmatrix}. \quad (2.2.2.24)$$

Since this cubic expression must give the same roots (principal stresses) regardless of the imposed reference frame, its coefficients--the numbers I_1 , I_2 , and I_3 --must also be independent of the coordinate system. These are therefore invariant with respect to changes in the perspective of the observer and are the so-called invariants of the stress tensor \underline{g} . The notation I_1 , I_2 , and I_3 are used for the first, second, and third invariants (respectively) of the stress tensor \underline{g} .

When provided with a stress tensor that includes off-diagonal terms (i.e., shear stress components), it is much simpler to compute the invariants as an intermediate step in the calculation of the principal stresses. Of course, writing the failure criterion directly in terms of the invariants is, from a computational standpoint, the most convenient approach. In any event, one should bear in mind that the stress

invariants and the principal stresses can be used interchangeably in the formulation of a failure criterion. The following discussion centers on a typical methodology for computing the principal stresses from the stress invariants.

Start by additively decomposing the stress tensor into two components: 1) a spherical or hydrostatic part ($p \delta_{ij}$), and 2) its deviatoric components (s_{ij}). The first of these tensors represents the average pressure or "bulk" stress (p) which causes a pure volumetric strain in an isotropic continuum. The second tensor, \underline{s} , is associated with the components of stress which bring about shape changes in an ideal isotropic continuum. The spherical stress tensor is defined as $p \delta_{ij}$, where p is the mean normal pressure ($\sigma_{kk}/3$ or $I_1/3$) and δ_{ij} is the Kronecker delta. Since, by definition, we know the spherical and deviatoric stress tensors combine additively to give the stress tensor, the components of the stress deviator (or deviatoric stress tensor) are

$$s_{ij} = \sigma_{ij} - p \delta_{ij} , \quad (2.2.2.25)$$

where compression is taken as positive. This particular sign convention applies throughout this dissertation.

The development of the equations for computing the principal values and the invariants of \underline{g} apply equally well to the stress deviator \underline{s} , with two items of note: a) the principal directions of the stress deviator are the same as those of the stress tensor since both represent directions perpendicular to planes having no shear stress (see, for example, Malvern, 1969, p.91), and b) the first invariant of the stress

deviator (denoted by J_1) is equal to zero. The proof of the latter follows:

$$\begin{aligned} J_1 &= s_{11} + s_{22} + s_{33} \\ &= \sigma_{11} - \frac{1}{3} I_1 + \sigma_{22} - \frac{1}{3} I_1 + \sigma_{33} - \frac{1}{3} I_1 = \sigma_{kk} - I_1, \end{aligned}$$

and by recalling equation 2.2.2.22, it is clear that

$$J_1 = 0. \quad (2.2.2.25)$$

From the last equation and equation 2.2.2.23, observe that the second invariant of the stress deviation (denoted by J_2) is simply

$$J_2 = (s_{ij}s_{ij}) + 2. \quad (2.2.2.26)$$

Denoting the third invariant of the stress deviation by J_3 , the cubic expression for the stress deviator \underline{s} , in analogy to equation 2.2.2.21 for the stress tensor \underline{g} , becomes

$$\Lambda^3 - J_2 \Lambda - J_3 = 0, \quad (2.2.2.27)$$

where the roots of Λ are now the principal values (or more formally, the eigenvalues) s_1 , s_2 , and s_3 of the stress deviator \underline{s} . Since the coefficient (i.e., J_1) of the quadratic term (Λ^2) is zero, the solution of equation 2.2.2.27 is considerably easier than that of equation 2.2.2.21. It is therefore more convenient to solve for the principal values of \underline{s} and then compute the principal values of \underline{g} using the identities

$$\sigma_1 = s_1 + p, \quad \sigma_2 = s_2 + p, \quad \text{and} \quad \sigma_3 = s_3 + p. \quad (2.2.2.28)$$

The direct evaluation of the roots, Λ , of equation 2.2.2.27 is not obvious until one observes the similarity of this equation to the trigonometric identity

$$\sin 3\theta = 3 \sin\theta - 4 \sin^3\theta.$$

Dividing through by four and rearranging shows the relevancy of this choice,

$$\sin^3\theta - \frac{3}{4} \sin\theta + \frac{1}{4} \sin 3\theta = 0. \quad (2.2.2.29)$$

Replacing Λ with $r \sin\theta$ in equation 2.2.2.27 gives

$$r^3 \sin^3\theta - J_2 r \sin\theta - J_3 = 0,$$

which when divided through by r^3 gives

$$\sin^3\theta - \frac{J_2}{r^2} \sin\theta - \frac{J_3}{r^3} = 0. \quad (2.2.2.30)$$

A direct correlation of this equation with equation 2.2.2.29 shows that

$$\frac{J_2}{r^2} = \frac{3}{4}$$

or

$$r = \pm \frac{2}{\sqrt{3}} \sqrt{J_2}, \quad (2.2.2.31)$$

and

$$\frac{J_3}{r^3} = -\frac{1}{4} \sin 3\theta,$$

or

$$\sin 3\theta = -\frac{4 J_3}{r^3}. \quad (2.2.2.32)$$

Substitution of the negative root of equation 2.2.2.31 into equation 2.2.2.32 leads to

$$\sin 3\theta = \left[\frac{3\sqrt{3}}{2} (J_3/\sqrt{J_2^3}) \right], \quad (2.2.2.33)$$

from which we find that

$$\theta = \frac{1}{3} \sin^{-1} \left[\frac{3\sqrt{3}}{2} (J_3/\sqrt{J_2^3}) \right], \quad (2.2.2.34)$$

where θ is known as the Lode angle or Lode parameter (Lode, 1926). As will be described in a later section on plasticity, the Lode angle is an attractive alternative to the J_3 invariant because of its insightful geometric interpretation in principal stress space. Physically, the

Lode angle is a quantitative indicator of the relative magnitude of the intermediate principal stress σ_2 with respect to σ_1 and σ_3 .

Owing to the periodic nature of the sine function, the angles 3θ , $3\theta + 2\pi$, and $3\theta + 4\pi$ all give the same sine in terms of the calculated invariants of the deviator in equation 2.2.2.33. If we further restrict 3θ to the range $\frac{\pm\pi}{2}$ (i.e., $-\frac{\pi}{6} \leq \theta \leq +\frac{\pi}{6}$), the three independent roots of the stress deviator are furnished by the equations (after Nayak and Zienkiewicz, 1972)

$$s_1 = -\frac{2}{\sqrt{3}} \sqrt{J_2} \sin(\theta + \frac{4}{3} \pi), \quad (2.2.2.35)$$

$$s_2 = -\frac{2}{\sqrt{3}} \sqrt{J_2} \sin(\theta), \quad (2.2.2.36)$$

and,

$$s_3 = -\frac{2}{\sqrt{3}} \sqrt{J_2} \sin(\theta + \frac{2}{3} \pi). \quad (2.2.2.37)$$

Finally, these relations can be combined with those of equation 2.2.2.28 to give the principal values of the stress tensor \underline{g} ,

$$\begin{Bmatrix} \sigma_1 \\ \sigma_2 \\ \sigma_3 \end{Bmatrix} = -\frac{2}{\sqrt{3}} \sqrt{J_2} \begin{Bmatrix} \sin(\theta + 4/3 \pi) \\ \sin \theta \\ \sin(\theta + 2/3 \pi) \end{Bmatrix} + \frac{1}{3} \begin{Bmatrix} I_1 \\ I_1 \\ I_1 \end{Bmatrix}. \quad (2.2.2.38)$$

To gain a clearer understanding of how the Lode angle θ accounts for the influence of the intermediate principal stress, observe from this equation that

$$\theta = \sin^{-1} \left[\frac{\sigma_1 + \sigma_3 - 2\sigma_2}{2\sqrt{3} J_2} \right], \quad -30^\circ \leq \theta \leq 30^\circ. \quad (2.2.2.39)$$

2.2.3. The Strain Tensor

The mathematical description of strain is considerably more difficult than the development just presented for stress. Nevertheless, a brief introduction to the small strain tensor is attempted herein,

while the interested reader should refer to a continuum mechanics textbook to understand better the concept and implications of finite deformation. This presentation has been modified from Synge and Schild (1949).

Most soils engineers are familiar with the geometrical measure of unit extension, e , which is defined as the change in distance between two points divided by the distance prior to straining or

$$e = (L_1 - L_0) \div L_0, \quad (2.2.3.1)$$

where L_0 and L_1 are respectively the distances between say particles P and Q before and after the deformation. If the coordinates of P and Q are denoted by $x_r(P)$ and $x_r(Q)$ respectively, we know that

$$L_0^2 = [x_r(P) - x_r(Q)] [x_r(P) - x_r(Q)] \quad (2.2.3.2)$$

from the geometry of distances.

Further, if the particles P and Q receive displacements $u_r(P)$ and $u_r(Q)$ respectively, the updated positions (using primed coordinates for distinction) are

$$x'_r(P) = x_r(P) + u_r(P), \quad (2.2.3.3)$$

and

$$x'_r(Q) = x_r(Q) + u_r(Q). \quad (2.2.3.4)$$

The notation $u_r(P)$ and $u_r(Q)$ indicates that the particles undergo displacements which are dependent on their position. Note that if the displacement vector, \underline{u} , is exactly the same for each and every particle in the medium, the whole body translates without deforming--a rigid body motion.

From equations 2.2.3.3 and 2.2.3.4, we find that

$$\begin{aligned} L_1^2 &= [x_r'(P) - x_r'(Q)] [x_r'(P) - x_r'(Q)], \\ &= [x_r(P) + u_r(P) - x_r(Q) - u_r(Q)] \times \\ &\quad [x_r(P) + u_r(P) - x_r(Q) - u_r(Q)], \end{aligned} \quad (2.2.3.5)$$

and subtracting equation 2.2.3.2 from this equation leads to

$$\begin{aligned} L_1^2 - L_0^2 &= [x_r(P) + u_r(P) - x_r(Q) - u_r(Q)] [x_r(P) + u_r(P) - \\ &\quad x_r(Q) - u_r(Q)] - [x_r(P) - x_r(Q)] [x_r(P) - x_r(Q)], \end{aligned}$$

which when reordered gives

$$\begin{aligned} L_1^2 - L_0^2 &= [u_r(Q) - u_r(P)] [u_r(Q) - u_r(P)] + \\ &\quad 2 [x_r(Q) - x_r(P)] [u_r(Q) - u_r(P)]. \end{aligned} \quad (2.2.3.6)$$

If attention is fixed on point P and an infinitesimally close particle Q, the description of the state of strain at P can be put in a more general form than the uniaxial unit extension measure. Since the distance between P and Q is assumed small, the term

$$[x_r(Q) - x_r(P)] [x_r(Q) - x_r(P)]$$

and its higher orders are negligible; a Taylor expansion about P is therefore approximately equal to

$$u_r(Q) - u_r(P) = \partial u_r / \partial x_s \Big|_P [x_s(Q) - x_s(P)]. \quad (2.2.3.7)$$

Substitution of this equation into equation 2.2.3.6 gives

$$\begin{aligned} L_1^2 - L_0^2 &= \partial u_r / \partial x_s \Big|_P [x_s(Q) - x_s(P)] \partial u_r / \partial x_t \Big|_P [x_t(Q) - x_t(P)] + \\ &\quad 2 [x_r(Q) - x_r(P)] \partial u_r / \partial x_m \Big|_P [x_m(Q) - x_m(P)]. \end{aligned} \quad (2.2.3.8)$$

Furthermore, we know approximately that

$$[x_r(Q) - x_r(P)] = L_0 n_r, \quad (2.2.3.9)$$

where n_r are the components of the unit vector directed from P to Q;

substitution of this relation into equation 2.2.3.8 gives

$$\begin{aligned}
L_1^2 - L_0^2 &= \partial u_r / \partial x_s |_P L_0 n_s \quad \partial u_r / \partial x_t |_P L_0 n_t + \\
&\quad 2 L_0 n_r \partial u_r / \partial x_m |_P L_0 n_m \\
&= L_0^2 \left[\partial u_r / \partial x_s |_P n_s \quad \partial u_r / \partial x_t |_P n_t + \right. \\
&\quad \left. 2 n_r \partial u_r / \partial x_m |_P n_m \right], \tag{2.2.3.10}
\end{aligned}$$

or

$$\begin{aligned}
\frac{L_1^2 - L_0^2}{L_0^2} &= \left[\partial u_r / \partial x_s |_P n_s \quad \partial u_r / \partial x_t |_P n_t + \right. \\
&\quad \left. 2 n_r \partial u_r / \partial x_m |_P n_m \right]. \tag{2.2.3.11}
\end{aligned}$$

If an assumption is made that the strain is small, $\partial u_r / \partial x_t |_P$ is small and hence the product

$$\partial u_r / \partial x_s |_P \quad \partial u_r / \partial x_t |_P$$

in the last equation is negligible. Therefore, for small strain

$$\frac{L_1^2 - L_0^2}{L_0^2} = 2 n_r \partial u_r / \partial x_m |_P n_m. \tag{2.2.3.12}$$

Moreover,

$$\begin{aligned}
\frac{L_1^2 - L_0^2}{L_0^2} &= \frac{L_1 - L_0}{L_0} \quad \frac{L_1 + L_0}{L_0} \\
&= \frac{L_1 - L_0}{L_0} \quad \frac{L_1 - L_0 + 2 L_0}{L_0} \\
&= \frac{L_1 - L_0}{L_0} \left[\frac{L_1 - L_0}{L_0} + 2 \right] \\
&= e (e + 2), \tag{2.2.3.13}
\end{aligned}$$

and with the assumption of small strain, e^2 is negligible, which implies that

$$\frac{L_1^2 - L_0^2}{L_0^2} \approx 2 e. \tag{2.2.3.14}$$

By equating the previous equation with equation 2.2.3.12, one finds that

$$e = n_r \left. \frac{\partial u_r}{\partial x_m} \right|_P n_m. \quad (2.2.3.15)$$

If the components of the small strain tensor at point P are now defined as

$$\epsilon_{rs} = \frac{1}{2} \left[\frac{\partial u_r}{\partial x_s} + \frac{\partial u_s}{\partial x_r} \right], \quad (2.2.3.16)$$

then the unit extension of every infinitesimal line emanating from P in the arbitrary direction \underline{n} is given by

$$e = \epsilon_{rs} n_r n_s. \quad (2.2.3.17)$$

Soil engineers may wonder how the traditional shear strain concept enters this definition of strain. It can be shown (see, for example, Malvern, 1969, p.121) that the off-diagonal terms of the tensor $\underline{\epsilon}$ are approximately equal to half the decrease, γ_{rs} , in the right angle initially formed by the sides of an element initially parallel to the directions specified by the indices r and s. This only holds for small strains where the angle changes are small compared to one radian.

Another important geometrical measure in studying soil deformation is the volume change or dilatation. The reader can easily verify that the volume strain is equal to the first invariant (or trace) of the strain tensor $\underline{\epsilon}$ (or in indicial notation, ϵ_{mm}).

In analogy to the stress deviator, the strain deviator (denoted by \underline{e}) is given by

$$e_{ij} = \epsilon_{ij} - \frac{1}{3} \epsilon_{mm} \delta_{ij}, \quad (2.2.3.18)$$

and since, like stress, strain is a symmetric second order tensor, the corresponding discussion for principal strains and invariants parallels

the previous development for the stress tensor. In analogy to the stress invariant $\sqrt{(3J_2)}$, the shear strain intensity is given by

$$\bar{\epsilon} = \sqrt{\frac{3}{2} e_{ij}e_{ij}}. \quad (2.2.3.19)$$

2.3 Stress-Strain Equations and Constitutive Theory

To solve statically indeterminate problems, the engineer utilizes the equations of equilibrium, the kinematic compatibility conditions, and a knowledge of the load-deformation response (or stress-strain constitution) of the engineering material under consideration. As an aside, it is useful to remind the soils engineer of two elementary definitions which are not part of the everyday soil mechanics vocabulary. Kinematics is the study of the motion of a system of material particles without reference to the forces which act on the system. Dynamics is that branch of mechanics which deals with the motion of a system of material particles under the influence of forces, especially those which originate outside the system under consideration.

For general applicability, the load-deformation characterization of the solid media is usually expressed in the form of a constitutive law relating the force-type measure (stress) to the measure of change in shape and/or volume (strain) of the medium. A constitutive law therefore expresses an exact correspondence between an action (force) and an effect (deformation). The correspondence is functional--it is a mathematical representation of the physical processes which take place in a material as it passes from one state to another. This is an appropriate point to interject and to briefly clarify the meaning of another word not commonly encountered by the soils engineer: functional.

Let us return to the sand mass which contains particle P and extend the discussion to include M discrete granules (P_i , $i = 1, 2, \dots, M$). Say the body of sand was subjected to a system of boundary loads which induced a motion of the granular assembly, while an observer, using a spatial reference frame \underline{x} , painstakingly recorded at N prescribed time intervals the location of each of the M particles. His data log therefore consists of the location of each particle M (\underline{x}_M) and the time at which each measurement was made (t'). At the current time t ($\geq t'$), we are interested in formulating a constitutive relationship which gives us the stress at point P, and in our attempt to construct a model of reality, we propose that such a relation be based on the MN discrete vector variables we have observed; i.e., the M locations \underline{x}_M (in the locality of point P) at N different times t' ($\leq t$). In other words, stress at P is a function of these MN variables. This function converges to the definition of a functional as the number of particles M and the discrete events in the time set t' approach infinity.

For our simplest idealization, we can neglect both history and time dependence, and postulate that each component of current stress \underline{g} depends on every component of the current strain tensor $\underline{\epsilon}$ and tender a stress-strain relationship of the form

$$\sigma_{ij} = C_{ijkl} \epsilon_{kl}, \quad (2.3.1)$$

or inversely,

$$\epsilon_{kl} = D_{klij} \sigma_{ij}, \quad (2.3.2)$$

where the fourth order tensors C_{ijkl} and D_{klij} (each with 81 components) are called the stiffness and compliance tensors respectively. Both of these constitutive tensors are discussed in detail later in this

section. Note that the number of components necessary to define a tensor of arbitrary order "n" is equal to 3^n .

Because the behavior of geologic media is strongly non-linear and stress path dependent, the most useful constitutive equations for this type of material are formulated in incremental form,

$$\dot{\sigma}_{ij} = C_{ijkl} \dot{\epsilon}_{kl}, \quad (2.3.3)$$

or conversely,

$$\dot{\epsilon}_{kl} = D_{klij} \dot{\sigma}_{ij}, \quad (2.3.4)$$

where the superposed dot above the stress and strain tensors denote a differentiation with respect to time. In these equations, \underline{C} and \underline{D} are now tangent constitutive tensors. The terms $\dot{\underline{\sigma}}$ and $\dot{\underline{\epsilon}}$ are the stress rate and strain rate respectively.

If the "step by step" stress-strain model is further idealized to be insensitive to the rate of loading, the incremental relationship may be written in the form

$$d\sigma_{ij} = C_{ijkl} d\epsilon_{kl}, \quad (2.3.5)$$

or inversely,

$$d\epsilon_{kl} = D_{klij} d\sigma_{ij}, \quad (2.3.6)$$

where $d\underline{\sigma}$ and $d\underline{\epsilon}$ are the stress increment and strain increment respectively, and \underline{C} and \underline{D} are independent of the rate of loading. Only rate-independent constitutive equations are considered in this thesis.

The formulation, determination, and implementation of these constitutive \underline{C} and \underline{D} tensors are the primary concern of this research.

In the formulation of generalized, rate independent, incremental stress-strain models, the objective is one of identifying the variables that influence the instantaneous magnitudes of the components of the stiffness (\underline{C}) or compliance (\underline{D}) tensors. Such a study bears resemblance

to many other specialized disciplines of civil engineering. The econometrician, for instance, may determine by a selective process that the following variables influence the price of highway construction in a state for any given year: cost of labor, cost of equipment, material costs, business climate, and a host of other tangible and intangible factors. The soils engineer, perhaps using the econometrician's techniques of regression analysis and his personal experience, can easily identify several factors which influence soil behavior. From our basic knowledge of soil mechanics, we might make the following preliminary list: 1) the void ratio or dry unit weight--perhaps the most important measure of overall stiffness and strength of the material; 2) the composition of the grains, which includes information on the mineral type (soft or hard), particle shape, angularity of particles, surface texture of particles, grain size distribution, etc.; 3) the orientation fabric description or anisotropy of the microstructure; 4) the stress history g^t or stress path, which may be used, for example, to indicate how close the current stress state is to the failure line, the number of cycles of loading, the degree of overconsolidation, etc.; 5) the magnitude and direction of the stress increment dg ; 6) the rate of application of the stress increment; and 7) the history of the strain ϵ^t , from which one may compute, for example, the current void ratio and magnitude of the cumulative permanent distortion.

In writing general mathematical formulations, it is convenient to lump all variables--except for g^t , ϵ^t , and dg --as a group known as the set of n internal variables q_i ($i = 1, 2, 3, \dots, n$). These internal variables represent the microstructural properties of the material. A

generalized, rate-independent, incremental stress-strain functional $\hat{d\varepsilon}$ can therefore be put in the form

$$d\varepsilon = d\hat{\varepsilon}(\underline{\sigma}^t, \underline{\varepsilon}^t, d\underline{\sigma}, \underline{q}_n). \quad (2.3.7)$$

This means that the components of the compliance (or stiffness) tensor depends on $\underline{\sigma}^t$, $\underline{\varepsilon}^t$, $d\underline{\sigma}$ (and its higher orders), and \underline{q}_n .

One basic difference between the econometrician's model and the mechanician's load-deformation model must be emphasized: the mechanician is dealing with dependent and independent variables which are physically significant, but the econometrician uses variables which may frequently be intangible. Therefore, in the selection of constitutive variables (such as stress and strain) and in the actual formulation of the stress-strain equations, certain physical notions (leading to mathematical constraints) must be satisfied. These conditions are embodied in the so-called axioms or principles of constitutive theory. An axiom is a well-established basis for theoretical development. Since geotechnical engineers are, for the most part, interested in isothermal processes, the principles linked to thermomechanical behavior are suppressed in the sequel.

The Axiom of Causality states that the motion of the material points of a body is to be considered a self-evident, observable effect in the mechanical behavior of the body. Any remaining quantities (such as the stress) that enter the entropy production and the balance equations--i.e., the equations of conservation of mass, balance of momentum, and conservation of energy--are the causes or dependent variables. In other words, there can occur no deformation (effect) without an external force (cause).

The Principle of Determinism is that the stress in a body is determined by the history of the motion of that body. This axiom excludes the dependence of the stress at a point P on any point outside the body and on any future events. This phenomenon is sometimes referred to as the Principle of Heredity.

In the purely mechanical sense, the Axiom of Neighborhood or Local Action rules out any appreciable effects on the stress at P that may be caused by the motion of points distant from P; "actions at a distance" are excluded from constitutive equations.

During the discussion of stress and strain, it was made quite clear that the tensor measures should be independent of the perspective of the observer. It is therefore natural to suggest a similar constraint for the constitutive equations: \underline{C} and \underline{D} must be form-invariant with respect to rigid motions (rotation and/or translation) of the spatial frame of reference. This is termed the Principle of Material Frame Indifference or Objectivity.

Finally, the Axiom of Admissibility states that all constitutive equations must be consistent with the basic principles of continuum mechanics; i.e., they are subject to the principles of conservation of mass, balance of momenta, conservation of energy, and the entropy inequality.

2.4 A Note on Stress and Strain in Granular Media

The concepts of stress and strain discussed in the previous sections are closely associated to the concept of a continuum, which effectivelly disregards the molecular structure of matter and treats the medium as if there were no holes or gaps. The following quotation from

Lambe and Whitman (1969, p.98) succinctly summarizes the applicability of the continuum stress measure to granular materials:

. . . when we speak of the stress acting at a point, we envision the forces against the sides of an infinitesimally small cube which is composed of some homogenous material. At first sight we may therefore wonder whether it makes sense to apply the concept of stress to a particulate system such as soil. However, the concept of stress as applied to soil is no more abstract than the same concept applied to metals. A metal is actually composed of many small crystals, and on the submicroscopic scale the magnitude of the forces vary randomly from crystal to crystal. For any material, the inside of the infinitesimally small cube is thus only statistically homogenous. In a sense all matter is particulate, and it is meaningful to talk about macroscopic stress only if this stress varies little over distances which are of the order of magnitude of the size of the largest particle. When we talk about stresses at a "point" within a soil, we often must envision a rather large "point."

Local strains within a statistically homogenous mass of sand are the result of distortion and crushing of individual particles, and the relative sliding and rolling velocities between particles. These local strains are much larger than the overall (continuum) strain described in section 2.2.3. The magnitude of the generated strain will, as mentioned before, depend on the composition, void ratio, anisotropic fabric, past stress history, and the stress increment. Composition is a term used in soil mechanics to refer to the average particle size, the surface texture and angularity of the typical grain, the grain size distribution, and the mineral type.

Figure 2.2 illustrates typical qualitative load-deformation response of loose and dense soil media subject to two conventional laboratory stress paths: hydrostatic compression, and conventional

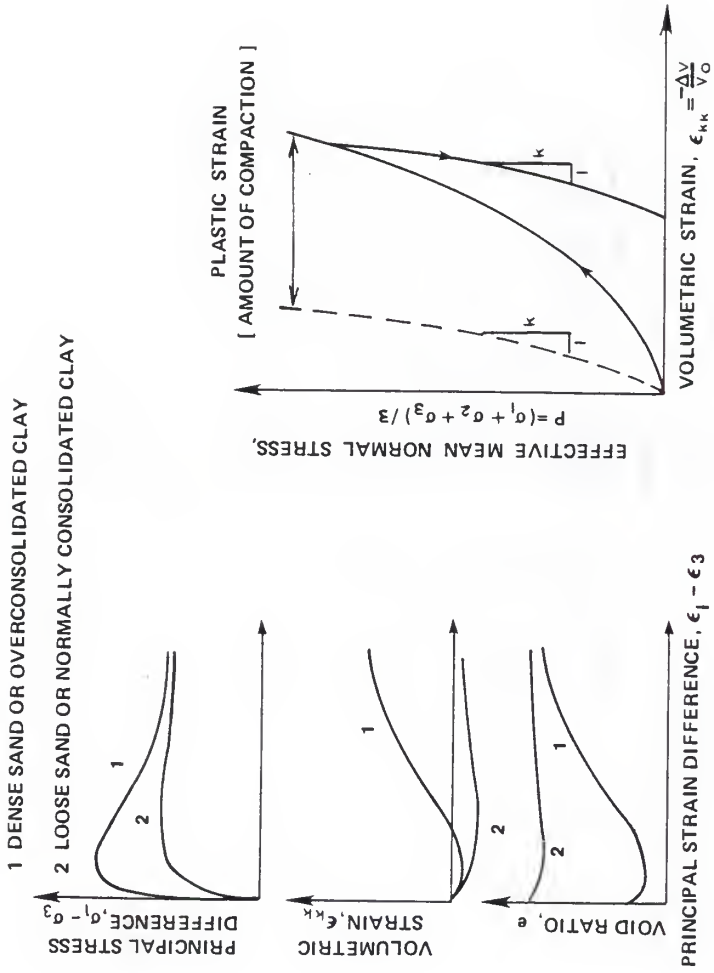


Figure 2.2 Typical stress-strain response of soil for a conventional 'triaxial' compression test (left) and a hydrostatic compression test (right)

triaxial compression. Figure 2.3 shows these paths together with an assortment of other "triaxial" stress paths used for research as well as routine purposes. In this context, note that the adjective "triaxial" is somewhat ambiguous since this particular test scenario dictates that the circumferential stress always be equal to the radial stress. The stress state is therefore not truly triaxial, but biaxial. As we can gather from Figure 2.2, the stress-strain behavior of soil is quite complicated, and in order to model approximately real behavior, drastic idealizations and simplifications are necessary. More complex details of soil response are mentioned in Chapter 3.

The major assumptions in most present idealizations are that: a) soil response is independent of the rate of loading, b) behavior may be interpreted in terms of effective stresses, c) the interaction between the mechanical and thermal processes is negligible, and d) the strain tensor can be decomposed into an elastic part ($\underline{\epsilon}^e$) and a plastic conjugate ($\underline{\epsilon}^p$) without any interaction between the two simultaneously occurring strain types,

$$\underline{\epsilon} = \underline{\epsilon}^e + \underline{\epsilon}^p, \quad (2.4.1)$$

or in incremental form,

$$d\underline{\epsilon} = d\underline{\epsilon}^e + d\underline{\epsilon}^p. \quad (2.4.2)$$

The elastic behavior ($\underline{\epsilon}^e$ or $d\underline{\epsilon}^e$) is modeled within the broad framework of elasticity theory, while the plastic part ($\underline{\epsilon}^p$ or $d\underline{\epsilon}^p$) is computed from plasticity theory. Both these theories will be elaborated later in this chapter.

With the introduction of the strain decomposition into elastic and plastic components, it is now important to emphasize the difference between irreversible strains and plastic strains for cyclic loading on

NAME OF TEST	Standard Designation	DESCRIPTION
Conventional Triaxial Compression	CTC	$\Delta\sigma_x = \Delta\sigma_z = 0; \Delta\sigma_y > 0$
Hydrostatic Compression	HC	$\Delta\sigma_x = \Delta\sigma_z = \Delta\sigma_y > 0$
Conventional Triaxial Extension	CTE	$\Delta\sigma_x = \Delta\sigma_z > 0; \Delta\sigma_y = 0$
Mean Normal Pressure Triaxial Compression	TC	$\Delta\sigma_x + \Delta\sigma_z + \Delta\sigma_y = 0;$ $\Delta\sigma_y > \Delta\sigma_x (= \Delta\sigma_z)$
Mean Normal Pressure Triaxial Extension	TE	$\Delta\sigma_x + \Delta\sigma_z + \Delta\sigma_y = 0;$ $\Delta\sigma_x = \Delta\sigma_z > \Delta\sigma_y$
Reduced Triaxial Compression	RTC	$\Delta\sigma_x = \Delta\sigma_z < 0; \Delta\sigma_y = 0$
Reduced Triaxial Extension	RTE	$\Delta\sigma_y < 0; \Delta\sigma_x = \Delta\sigma_z = 0$

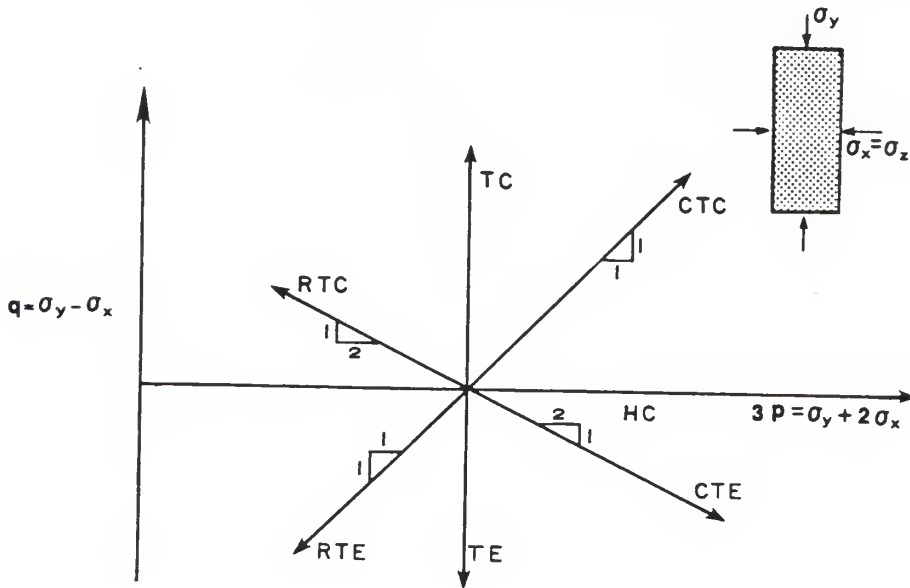


Figure 2.3 Typical stress paths used to investigate the stress-strain behavior of soil specimens in the triaxial environment

soils. Consider a uniaxial cyclic test consisting of a virgin loading, an unloading back to the initial hydrostatic state of stress, and a final reloading to the previous maximum deviatoric stress level. During the first virgin loading both elastic and plastic strains are generated, and these components may be calculated using an elastic and a plastic theory respectively. If at the end of this segment of the stress path we terminate the simulation and output the total, elastic, and plastic axial strains, one may be tempted to think that the plastic component represents the irrecoverable portion of the strain. However, when the stress path returns to the hydrostatic state, the hysteresis loop in Figure 2.4 indicates that reverse plastic strains are actually generated on the unload and a (small) portion of the plastic strain at the end of the virgin loading cycle is, in fact, recovered. This is an illustration of the Bauschinger effect (Bauschinger, 1887). Therefore, for such a closed stress cycle, the total strain can more generally be broken down into the three components:

$$\underline{\varepsilon} = \underline{\varepsilon}_{\text{irrev}}^{\text{p}} + \underline{\varepsilon}_{\text{rev}}^{\text{p}} + \underline{\varepsilon}^{\text{e}},$$

where $\underline{\varepsilon}_{\text{irrev}}^{\text{p}}$ is the irreversible plastic strain, $\underline{\varepsilon}_{\text{rev}}^{\text{p}}$ is the reverse plastic strain, and as before, $\underline{\varepsilon}^{\text{e}}$ denotes the elastic strain, which is by definition recoverable. Some complicated models of soil behavior, such as the one described in Chapter Four, allow for reverse plastic strains on such "unloading" paths. However, ignoring this aspect of reality, as is done in Chapter Three, can lead to very rewarding simplifications.

Three broad classes of continuum theories have evolved in the development and advancement of soil stress-strain models (Cowin, 1978):

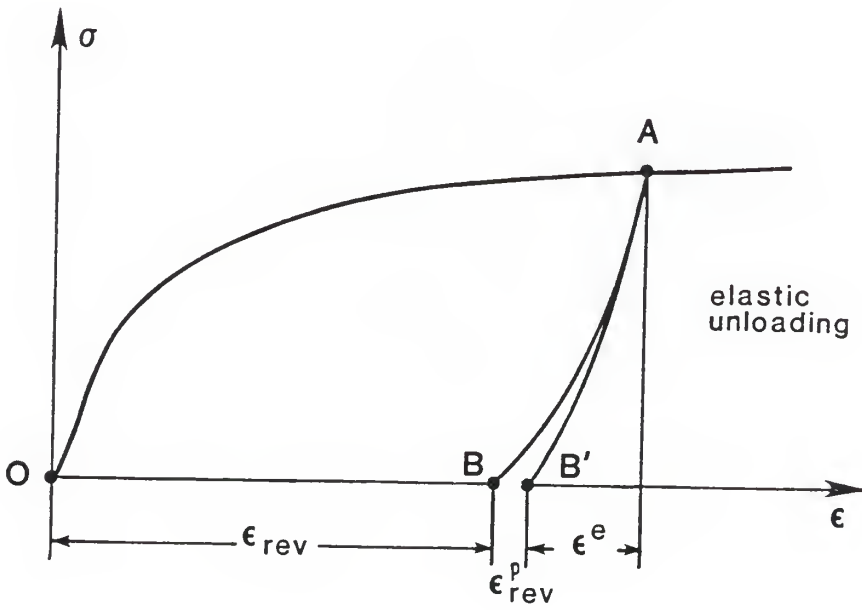
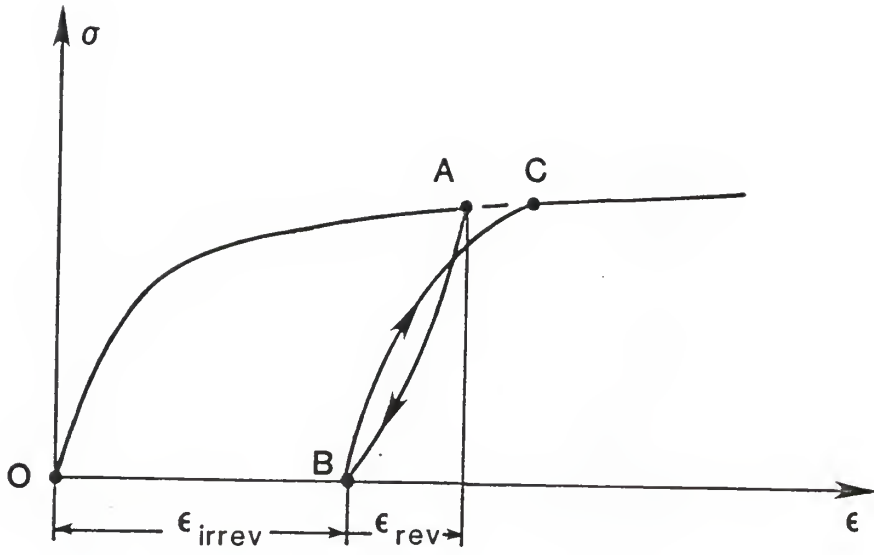


Figure 2.4 Components of strain: elastic, irreversible plastic, and reversible plastic

1) the kinematically ambiguous theories, 2) the phenomenological theories, and 3) the microstructural theories.

The kinematically ambiguous hypotheses employ the stress equations of equilibrium in conjunction with a failure criterion to form a system of equations relating the components of the stress tensor. This category is referred to as kinematically ambiguous because displacements and strains do not appear in and are therefore not computed from the basic equations of the theory. They assume the entire medium to be at a state of incipient yielding. A modern example of this type of formulation can be found in Cambou (1982).

A phenomenological continuum theory endeavors to devise constitutive relations based on experimentally observed stress-strain curves. It is presently the most popular class of the theories and it concentrates on the macroscopically discernible stress and strain measures. This theory does not inquire very deeply into the mechanisms which control the process of deformation. A controversial assumption of these phenomenological continuum theories, as applied to granular media, is that the laboratory tests, such as the standard triaxial test, achieve homogenous states of strain and stress. Many researchers are now seeking the answer to the question of when bifurcation of the deformation mode becomes acute enough to render interpretation of the supposedly "homogenous state" data troublesome (see, for example, Lade, 1982, and Hettler et al., 1984).

Microstructural theories attempt to incorporate geometric measures of local granular structure into the continuum theory. Local granular structure is also called fabric, which is defined as the spatial arrangement and contact areas of the solid granular particles and

associated voids. For clarity, fabric is subdivided into isotropic fabric measures (such as porosity, density, etc.) and anisotropic fabric measures (which are mentioned in the next section). In this dissertation, unless otherwise stated, the word fabric refers to anisotropic fabric. Perhaps the best known microstructural formulation is that proposed by Nemat-Nasser and Mehrabadi (1984).

2.5 Anisotropic Fabric in Granular Material

2.5.1 Introduction

The fabric of earthen materials is intimately related to the mechanical processes occurring during natural formation (or test sample preparation) and the subsequent application of boundary forces and/or displacements. Fabric evolution can be examined in terms of the deformations that occur as a result of applied tractions (strain-induced anisotropy), or the stresses which cause rearrangement of the microstructure (stress-induced anisotropy). Strains are influenced to some extent by the relative symmetry of the applied stress with respect to the anisotropic fabric symmetry (or directional stiffness). If straining continues to a relatively high level, it seems logical to expect that the initial fabric will be wiped out and the intensity and pattern of the induced fabric will align itself with the symmetry (or principal) axes of stress. Before introducing and discussing a select group of microscopic fabric measures, some of the commonly encountered symmetry patterns, caused by combined kinematic/dynamic boundary conditions, will be reviewed.

2.5.2 Common Symmetry Patterns

Triclinic symmetry implies that the medium possesses no plane or axis of symmetry. This fabric pattern is produced by complex deformations. Gerrard (1977) presents a simple example of how this most general and least symmetric system may arise. Consider the sketch in the upper left hand corner of Figure 2.5: triclinic symmetry develops as a result of the simultaneous application of compression in direction 1, differential restraint in directions 2 and 3, and shear stress components acting in directions 2 and 3 on the plane having axis 1 as its normal.

Monoclinic symmetry is characterized by a single plane of symmetry. Any two directions symmetric with respect to this plane are equivalent. An example of this symmetry group is shown in the lower left of Figure 2.5. The concurrent events leading to it are compression in direction 1, no deformation in the 2 and 3 directions, and a shear stress component acting in the 2-direction and on the plane with axis 1 as its normal.

A slight modification of the previous example permits a demonstration of a case of n-fold axis symmetry or cross-anisotropy. Exclusion of the shear stress component causes an axis of fabric symmetry to develop such that all directions normal to this axis are equivalent, bottom right of Figure 2.5.

The orthorhombic symmetry group can best be described by bringing to mind the true triaxial device. Here for example (top right of Figure 2.5), three mutually perpendicular planes of symmetry are produced by normal stresses of different magnitudes on the faces of the cubical sand specimen.

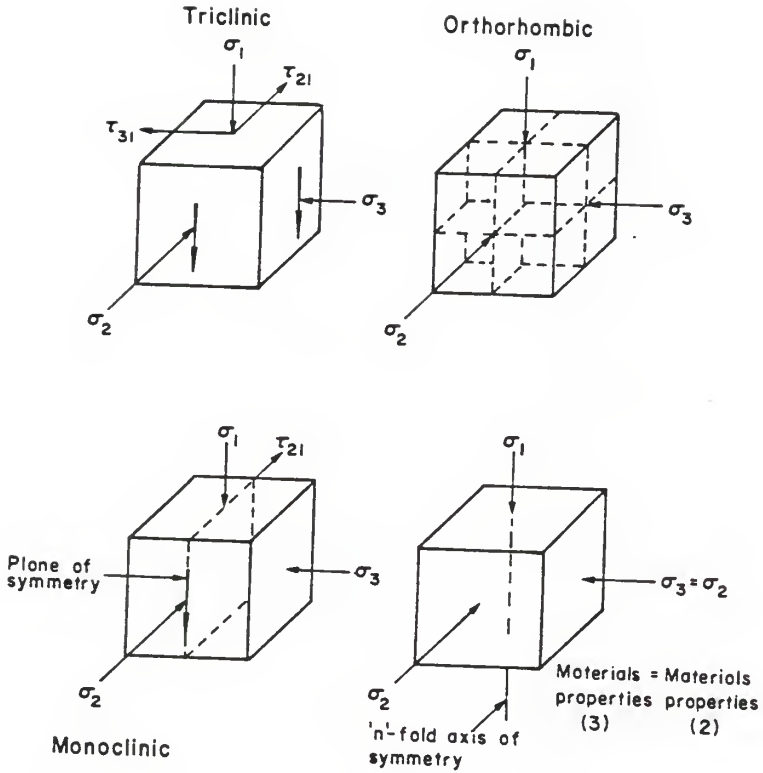


Figure 2.5 Common fabric symmetry types (after Gerrard, 1977)

Lastly, the rarest natural case is spherical symmetry or material isotropy which implies that all directions in the material are equivalent. However, because of its simplicity, isotropy is a major and a very common simplifying assumption in many of the current representations of soil behavior.

2.5.3 Fabric Measures

The selection of the internal variables, g_n , to characterize the mechanical state of a sand medium (see equation 2.3.7) has been a provocative subject in recent times (Cowin and Satake, 1978; and Vermeer and Luger, 1982). There is no doubt that the initial void ratio is the most dominant geometric measure, but as Cowin (1978) poses: "Given that porosity is the first measure of local granular structure or [isotropic] fabric, what is the best second measure of local granular structure or [anisotropic] fabric?" Trends suggest that the next generation of constitutive models will include this second measure. It is therefore worthwhile to review some of these variables.

An anthropomorphic approach is perhaps most congenial for introducing the reader to the concept of anisotropic fabric in granular material. Let us assume for illustrative purposes that, through a detailed experimental investigation, we have identified a microscopic geometric or physical measure (say variable X), which serves as the secondary controlling factor to the void ratio in interpreting the stress-strain response of sand. Some of the suggestions offered for the variable X are 1) the spatial gradient of the void ratio $\frac{\partial e}{\partial x}$ (Goodman and Cowin, 1972); 2) the orientation of the long axes of the grains (Parkin

et al., 1968); 3) the distribution of the magnitude and orientation of the inter-particle contact forces (Cambou, 1982); 4) the distribution of the inter-particle contact normals (see, for example, Oda, 1982); 5) the distribution of branches [note: a branch is defined as the vector connecting the centroids of neighboring particles, and it is thus possible to replace a granular mass by a system of lines or branches (Satake, 1978)]; 6) the mean projected solid path (Horne, 1964); and 7) mathematical representations in the form of second order tensors (Gudehus, 1968).

A commander (mother nature) of an army (the set representing the internal variable of the sand medium) stations her troops (variable X) in a configuration which provides maximum repulsive effort to an invading force (boundary tractions). The highest concentration of variable X will therefore tend to point in the direction of the imposed major principal stress. If the invading army (boundary tractions) withdraws (unloading), we should expect the general (mother nature) to keep her distribution of soldiers (X) practically unaltered. It is an experimental fact that there is always some strain recovery upon unloading, and this rebound is caused partly by elastic energy stored within individual particles as the soil was loaded and partly by inelastic reverse sliding between particles (Figure 2.4). Traditionally, it has been convenient to regard this unloading strain as purely elastic, but in reality, it stems from microstructural changes due to changes of the fabric and should be considered a dissipative thermodynamically irreversible process (Nemat-Nasser, 1982). Returning to our anthropomorphic description, we can therefore say that the general (mother nature) has an intrinsic command to modify slightly the

arrangement of her troops (X) once the offensive army (boundary tractions) decamps. The configuration of the defensive forces (distribution of X) after complete or partial withdrawal of the aggressor (complete or partial removal of the boundary loads) still, however, reflects the intensity and direction of the earlier attack (prior application of the system of boundary loads). This represents an induced fabric or stress-induced anisotropy in the granular material.

We can create additional scenarios with our anthropomorphic model to illustrate other features of fabric anisotropy. During the initial placement of the forces (initial distribution of the variable X during sample preparation or during natural formation of the soil deposit) under the general's command, there is a bias in this arrangement which is directly related to the general's personality (gravity as a law of nature). This is the so-called inherent anisotropy (Casagrande and Carillo, 1944) of soil which differs from the stress-induced anisotropy mentioned previously. Say the invading army (boundary tractions) attacks the defensive fortress (sand mass) with a uniform distribution of troops (uniform distribution of stress vectors), we will expect maximum penetration (strain) at the weakest defensive locations (smallest concentration of X), but our rational general (mother nature) should take corrective measures to prevent intrusion by the enemy forces (boundary tractions) through the inherently vulnerable sites (points of initially low X concentration). We can relate this situation to the effect of increasing hydrostatic pressure on an inherently cross-anisotropic sand specimen; the results of such a test carried out by Parkin et al. (1968) indicate that the ratio of the incremental horizontal strain to incremental vertical strain decreases from about 6

to 2.5. Increasing the hydrostatic pressure decreases the degree of anisotropy, but it does not completely wipe out the inherent fabric. We may infer that the general (mother nature) cannot reorient her forces at will since she is faced by the annoying internal constraints (particles obstructing each other) which plague most large and complex organizations (the microscopic world of particles sliding and rolling over each other).

It may seem logical to assume that if the demise of anisotropy is inhibited in some way, then so is its induction, but experimental evidence reported by Oda et al. (1980) indicates that the principal directions of fabric (i.e., principal directions of the distribution of X or the second order tensor representation) match the principal directions of the applied stress tensor during a virgin or prime loading, even with continuous rotation of the principal stress axes. There appears to be no lag effect. Data presented by Oda (1972) describing the evolution of the contact normal distribution suggests that fabric induction practically ceases once the material starts to dilate. However, no firm conclusions can be drawn until many tests have been repeated and verified by the soil mechanics community as a whole.

2.6 Elasticity

We now turn our attention to the mathematical models used to simulate the stress-strain response of soil. In this section, the essential features of the three types of elasticity-based stress-strain relations are summarized (Eringen, 1962): 1) the Cauchy type, 2) the Hyperelastic (or Green) type, and 3) the incremental (or Hypoelastic) type. Although, in the strict sense, elastic implies fully recoverable

response, it is sometimes convenient to pretend that total deformations are "elastic" and to disregard the elastic-plastic decomposition set forth in equations 2.4.1 and 2.4.2. This approach has some practical applications to generally monotonic outward loading paths. However, for unload-reload paths, this class of formulation will fail to predict the irrecoverable component of strain. Furthermore, one should not be misled into believing that elasticity theory should be used exclusively for predicting one-way loading paths because even in its most complicated forms, elasticity theory may fail to predict critical aspects of stress-strain behavior, many of which can be captured elegantly in plasticity theory.

2.6.1 Cauchy Type Elasticity

A Cauchy elastic material is one in which the current state of stress depends only on the current state of strain. Each stress component is a single-valued function of the strain tensor,

$$\sigma_{ij} = f_{ij}(\epsilon_{kl}), \quad (2.6.1.1)$$

where f_{ij} are nine elastic response functions of the material. Since the stress tensor is symmetric, $f_{kl} = f_{lk}$ and the number of these independent functions reduces from nine to six. The choice of the functions f_{ij} must also satisfy the Principle of Material Frame Indifference previously mentioned in section 2.3; such functions are called hemitropic functions of their arguments. The stress $\underline{\sigma}$ is an analytic isotropic function of $\underline{\epsilon}$ if and only if it can be expressed as

$$\sigma_{ij} = \phi_0 \delta_{ij} + \phi_1 \epsilon_{ij} + \phi_2 \epsilon_{im} \epsilon_{mj}, \quad (2.6.1.2)$$

where ϕ_0 , ϕ_1 , and ϕ_2 are functions only of the three strain invariants (see, for example, Eringen, 1962; p. 158).

For a first order Cauchy elastic model, the second order strain terms vanish ($\phi_2 = 0$) and ϕ_0 is a linear function of the first strain invariant ϵ_{mm} ,

$$\sigma_{ij} = (\alpha_0 + \alpha_1 \epsilon_{mm}) \delta_{ij} + \alpha_2 \epsilon_{ij}, \quad (2.6.1.3)$$

where α_0 , α_1 , and α_2 are response coefficients. At zero strain, $\alpha_0 \delta_{ij}$ is the initial spherical stress. Higher order Cauchy elastic models can be formulated by letting the response functions ϕ_0 , ϕ_1 , and ϕ_2 depend on strain invariant polynomials of corresponding order. For example, the second order Cauchy elastic material is constructed by selecting as the response functions

$$\phi_0 = a_1 \epsilon_{mm} + a_2 (\epsilon_{mm})^2 + a_3 \left(\frac{1}{2} \epsilon_{ij} \epsilon_{ij} \right),$$

$$\phi_1 = a_4 + a_5 \epsilon_{mm},$$

and

$$\phi_2 = a_6,$$

where a_1, a_2, \dots, a_6 are material constants (Desai and Siriwardane, 1984).

An alternative interpretation of the first order Cauchy model is presented in order to show the link between the elastic bulk and shear moduli (K and G respectively) and Lamé's constants (Γ and μ). For this material classification,

$$\sigma_{ij} = C_{ijkl} \epsilon_{kl},$$

where the components of C_{ijkl} are each a function of the strain components, or if isotropy is assumed, the strain invariants. Since both σ_{ij} and ϵ_{kl} are symmetric, the matrix C_{ijkl} is also symmetric in "ij" and in "kl." A generalization of the second order tensor

transformation formula (equation 2.2.2.9) to its fourth order analogue produces

$$C'_{ijkl} = Q_{ip} Q_{jq} Q_{kr} Q_{ls} C_{pqrs} \quad (2.6.1.4)$$

as the transformation rule for the "elastic" stiffness tensor \underline{C} . With the isotropy assumption, the material response must be indifferent to the orientation of the observer, and hence we must also insist that \underline{C} be equal to \underline{C}' . A fourth order isotropic tensor which obeys this transformation rule can be constructed from Kronecker deltas δ (see, for example, Synge and Schild, 1949, p.211); the most general of these is

$$C_{ijkl} = \Gamma \delta_{ij} \delta_{kl} + \mu \delta_{ik} \delta_{jl} + \nu \delta_{il} \delta_{jk}, \quad (2.6.1.5)$$

where Γ , μ , and ν are invariants. From the symmetry requirement,

$$C_{ijkl} = C_{ijlk}, \quad (2.6.1.6)$$

or

$$\Gamma \delta_{ij} \delta_{kl} + \mu \delta_{ik} \delta_{jl} + \nu \delta_{il} \delta_{jk} = \Gamma \delta_{ij} \delta_{lk} + \mu \delta_{il} \delta_{jk} + \nu \delta_{ik} \delta_{jl}, \quad (2.6.1.7)$$

and collecting terms,

$$(\mu - \nu) (\delta_{ik} \delta_{jl} - \delta_{il} \delta_{jk}) = 0, \quad (2.6.1.8)$$

which implies that $\mu = \nu$. With this equality, equation 2.6.1.5 simplifies to

$$C_{ijkl} = \Gamma \delta_{ij} \delta_{kl} + \mu (\delta_{ik} \delta_{jl} + \delta_{il} \delta_{jk}), \quad (2.6.1.9)$$

where Γ and μ are Lamé's elastic constants.

The incremental form of the first-order, isotropic, elastic stress-strain relation is therefore

$$\begin{aligned} d\sigma_{ij} &= [\Gamma \delta_{ij} \delta_{kl} + \mu (\delta_{ik} \delta_{jl} + \delta_{il} \delta_{jk})] d\epsilon_{kl} \\ &= \Gamma \delta_{ij} d\epsilon_{mm} + 2 \mu d\epsilon_{ij}. \end{aligned} \quad (2.6.1.10)$$

Multiplication of both sides of this equation by the Kronecker delta δ_{ij} results in

$$d\sigma_{kk} = 3 \Gamma d\epsilon_{mm} + 2 \mu d\epsilon_{mm}, \quad (2.6.1.11)$$

or

$$d\sigma_{kk}/3 d\epsilon_{mm} = K = \Gamma + \frac{2}{3} \mu, \quad (2.6.1.12)$$

where K is the elastic bulk modulus.

Substituting the identities

$$d\sigma_{ij} = ds_{ij} + \frac{1}{3} d\sigma_{kk} \delta_{ij}$$

and

$$d\epsilon_{ij} = de_{ij} + \frac{1}{3} d\epsilon_{kk} \delta_{ij}$$

into equation 2.6.1.10 results in

$$ds_{ij} + \frac{1}{3} d\sigma_{kk} \delta_{ij} = \Gamma \delta_{ij} d\epsilon_{mm} + 2 \mu (de_{ij} + \frac{1}{3} d\epsilon_{kk} \delta_{ij}),$$

and using equation 2.6.1.11 in this expression shows that

$$ds_{ij}/2 de_{ij} = G = \mu, \quad (2.6.1.13)$$

where G is the elastic shear modulus.

Combining equations 2.6.1.12 and 2.6.1.13 gives a more familiar form of the isotropic, elastic stiffness tensor, namely

$$C_{ijkl} = (K - \frac{2}{3} G) \delta_{ij} \delta_{kl} + G (\delta_{ik} \delta_{jl} + \delta_{il} \delta_{jk}). \quad (2.6.1.14)$$

Many researchers have adapted this equation to simulate, on an incremental basis, the non-linear response of soil; they have all essentially made K and G functions of the stress or strain level. Some of the better-known applications can be found in Clough and Woodward, 1967; Girijavallabhan and Reese, 1968; Kulhawy et al., 1969; and Duncan and Chang, 1970.

2.6.2 Hyperelasticity or Green Type Elasticity

Green defined an elastic material as one for which a strain energy function, W (or a complementary energy function, Ω) exists (quoted from Malvern, 1969, p. 282). The development of this theory was motivated by a need to satisfy thermodynamic admissibility, a major drawback of the Cauchy elastic formulation. Stresses or strains are computed from the energy functions as follows:

$$\sigma_{ij} = \frac{\partial W}{\partial \epsilon_{ij}}, \quad (2.6.2.1)$$

and conversely,

$$\epsilon_{ij} = \frac{\partial \Omega}{\partial \sigma_{ij}}. \quad (2.6.2.2)$$

For an initially isotropic material, the strain energy function, W , can be written out in the form (see, for example, Eringen, 1962)

$$\begin{aligned} W = W(\bar{I}_1, \bar{I}_2, \bar{I}_3) = & A_0 + A_1 \bar{I}_1 + A_2 \bar{I}_2 + A_3 \bar{I}_1^2 + A_4 \bar{I}_1^3 + \\ & A_5 \bar{I}_1 \bar{I}_2 + A_6 \bar{I}_3 + A_7 \bar{I}_1^4 + A_8 \bar{I}_1^2 \bar{I}_2 + \\ & A_9 \bar{I}_1 \bar{I}_3 + A_{10} \bar{I}_2^2, \end{aligned} \quad (2.6.2.3)$$

where \bar{I}_1 , \bar{I}_2 , and \bar{I}_3 are invariants of $\underline{\epsilon}$,

$$\bar{I}_1 = \epsilon_{kk}, \quad \bar{I}_2 = \frac{1}{2} \epsilon_{ij} \epsilon_{ij}, \quad \bar{I}_3 = \frac{1}{3} \epsilon_{km} \epsilon_{kn} \epsilon_{mn},$$

and A_k ($k=0,2,\dots,10$) are material constants determined from curve fitting. The stress components are obtained by partial differentiation,

$$\sigma_{ij} = \frac{\partial W}{\partial \bar{I}_1} \frac{\partial \bar{I}_1}{\partial \epsilon_{ij}} + \frac{\partial W}{\partial \bar{I}_2} \frac{\partial \bar{I}_2}{\partial \epsilon_{ij}} + \frac{\partial W}{\partial \bar{I}_3} \frac{\partial \bar{I}_3}{\partial \epsilon_{ij}} \quad (2.6.2.4)$$

$$= \phi_1 \delta_{ij} + \phi_2 \epsilon_{ij} + \phi_3 \epsilon_{im} \epsilon_{mj}, \quad (2.6.2.5)$$

where ϕ_i ($i=1,2,3$) are the response functions which must satisfy the condition $\partial \phi_i / \partial \bar{I}_j = \partial \phi_j / \partial \bar{I}_i$ in order to guarantee symmetry of the predicted stress tensor.

Different orders of hyperelastic models can be devised based on the powers of the independent variables retained in equation 2.6.2.3. If, for instance, we keep terms up to the third power, we obtain a second-order hyperelastic law. These different orders can account for various aspects of soil behavior; dilatancy, for instance, can be realistically simulated by including the third term of equation 2.6.2.3. Green's method and Cauchy's method lead to the same form of the stress-strain relationship if the material is assumed to be isotropic and the strains are small, but the existence of the strain energy function in hyperelasticity imposes certain restrictions on the choice of the constitutive parameters. These are not pursued here, but the interested reader can find an in-depth discussion of these constraints in Eringen (1962). Also, detailed descriptions--including initialization procedures--for various orders of hyperelastic models can be found in Saleeb and Chen (1980), and Desai and Siriwardane (1984).

2.6.3 Hypoelasticity or Incremental Type Elasticity

This constitutive relation was introduced by Truesdell (1955) to describe a class of materials for which the current state of stress depends on the current state of strain and the history of the stress $\underline{\sigma}^t$ (or the stress path). The incremental stress-strain relationship is usually written in the form

$$d\underline{\sigma} = \underline{f}(\underline{\sigma}, d\underline{\epsilon}), \quad (2.6.3.1)$$

where \underline{f} is a tensor valued function of the current stress $\underline{\sigma}$, and the strain increment $d\underline{\epsilon}$. The principle of material frame indifference (or objectivity) imposes a restriction on \underline{f} : it must obey the transformation

$$\underline{Q} \underline{f}(\underline{\sigma}, d\underline{\epsilon}) \underline{Q}^T = \underline{f}(\underline{Q} \underline{\sigma} \underline{Q}^T, \underline{Q} d\underline{\epsilon} \underline{Q}^T) \quad (2.6.3.2)$$

for any rotation Q of the spatial reference frame. When \underline{f} satisfies this stipulation, it is, as mentioned in the previous section, a hemitropic function of \underline{g} and $d\underline{g}$. A hemitropic polynomial representation of \underline{f} is

$$\begin{aligned} d\underline{g}' = \underline{f}(\underline{g}, d\underline{g}) = & \alpha_0 \operatorname{tr}(d\underline{g}) \underline{\delta} + \alpha_1 d\underline{g} + \alpha_2 \operatorname{tr}(d\underline{g}) \underline{g}' + \\ & \alpha_3 \operatorname{tr}(\underline{g}' d\underline{g}) \underline{\delta} + \frac{1}{2} \alpha_4 (d\underline{g} \underline{g}' + \underline{g}' d\underline{g}) + \alpha_5 \operatorname{tr}(d\underline{g}) \underline{g}'^2 + \\ & \alpha_6 \operatorname{tr}(\underline{g}' d\underline{g}) \underline{g}' + \alpha_7 \operatorname{tr}(\underline{g}'^2 d\underline{g}) \underline{\delta} + \\ & \frac{1}{2} \alpha_8 (d\underline{g} \underline{g}'^2 + \underline{g}'^2 d\underline{g}) + \alpha_9 \operatorname{tr}(\underline{g}' d\underline{g}) \underline{g}'^2 + \\ & \alpha_{10} \operatorname{tr}(\underline{g}'^2 d\underline{g}) \underline{g}' + \alpha_{11} \operatorname{tr}(\underline{g}'^2 d\underline{g}) \underline{g}'^2, \end{aligned} \quad (2.6.3.3)$$

where \underline{g}' is the nondimensional stress $\underline{g}/2\mu$ (μ being the Lamé shear modulus of equation 2.6.1.10), α_k ($k = 0, 2, \dots, 11$) are the constitutive constants (see, for example, Eringen, 1962, p.256), and "tr" denotes the trace operator of a matrix (i.e., the sum of the diagonal terms). The constants α_k are usually dimensionless analytic functions of the three invariants of \underline{g}' , and these are determined by fitting curves to experimental results.

Various grades of hypoelastic idealizations can be extracted from equation 2.6.3.3. This is accomplished by retaining up to and including certain powers of the dimensionless stress tensor \underline{g}' . A hypoelastic body of grade zero is independent of \underline{g}' , and in this case, the general form simplifies to

$$d\underline{g}' = \underline{f}(\underline{g}, d\underline{g}) = \alpha_0 \operatorname{tr}(d\underline{g}) \underline{\delta} + \alpha_1 d\underline{g}. \quad (2.6.3.4)$$

Comparing this equation with the first order Cauchy elastic model (equation 2.6.1.10) shows that

$$\alpha_0 = \frac{\Gamma}{2\mu} \quad \text{and} \quad \alpha_1 = 1.$$

Similarly, a hypoelastic constitutive equation of grade one can be elicited from the general equation by keeping only the terms up to and including the first power of $\underline{\sigma}'$,

$$\underline{d\sigma}' = \underline{f}(\underline{\sigma}, d\underline{\epsilon}) = \alpha_0 \operatorname{tr}(d\underline{\epsilon}) \underline{\delta} + \alpha_1 d\underline{\epsilon} + \alpha_2 \operatorname{tr}(d\underline{\epsilon}) \underline{\sigma}' + \alpha_3 \operatorname{tr}(\underline{\sigma}' d\underline{\epsilon}) \underline{\delta} + \frac{1}{2} \alpha_4 (d\underline{\epsilon} \underline{\sigma}' + \underline{\sigma}' d\underline{\epsilon}).$$

By a similar procedure, the description can be extended up to grade two, with the penalty being the task of fitting a larger number of parameters to the experimental data. These parameters must be determined from representative laboratory tests using curve fitting and optimization techniques, which often leads to uniqueness questions since it may be possible to fit more than one set of parameters to a given data set.

Romano (1974) proposed the following special form of the general hypoelastic equation to model the behavior of granular media:

$$d\sigma_{ij} = [\alpha_0 d\epsilon_{mm} + \alpha_3 \sigma_{pq} d\epsilon_{pq}] \delta_{ij} + \alpha_1 d\epsilon_{ij} + [\alpha_2 d\epsilon_{mm} + \alpha_6 \sigma_{rs} d\epsilon_{rs}] \sigma_{ij}. \quad (2.6.3.5)$$

This particular choice ensures that the predicted stress increment is a linear function of the strain increment; in other words, if the input strain increment is doubled, then so is the output stress increment. Imposing linearity of the incremental stress-strain relation is one way of compelling the stress-strain relation to be rate-independent; a more general procedure for specifying rate independence will be described in the section on plasticity theory.

Davis and Mullenger (1978), working from Romano's equation, have developed a model which can simulate many aspects of real soil behavior. Essentially, they have used well-established empirical stress-strain

relations and merged them with concepts from plasticity to arrive at restrictions on and the interdependency of the constitutive parameters.

2.7 Plasticity

Having outlined the theories used to compute the elastic, or sometimes pseudo-elastic component $d\epsilon^e$ of the total strain increment $d\epsilon$, the next topic deals with the computation of its plastic conjugate $d\epsilon^p$. This section prefaces the mathematical theory of plasticity, a framework for constitutive laws, which until 1952 (Drucker and Prager, 1952) remained strictly in the domain of metals. Over the past three decades, the role of elastic-plastic constitutive equations in soil mechanics has grown in importance with the development of sophisticated computers and computer-based numerical techniques. These tools have significantly increased the geotechnical engineer's capacity to solve complicated boundary value problems. The three main ingredients for these modern solution techniques are computer hardware, numerical schemes, and stress-strain equations, and, of these, the development of constitutive laws for soils has lagged frustratingly behind.

The fundamentals of plasticity theory still remain a mystery to many geotechnical engineers. It is very likely that a newcomer to this field will find considerable difficulty in understanding the literature, usually written in highly abstruse language. The chief objective of this section is to provide some insight into plasticity theory by highlighting the basic postulates, with special emphasis on their applicability and applications to soil mechanics.

In brief, plasticity theory answers these questions:

- a) When does a material plastically flow or yield? Or more directly, how do we specify all possible stress states where plastic deformation starts? The answer to this question lies in the representation of these stress states by yield surfaces. Also underlying this discussion are the definitions of and the possible interpretations of yield.
- b) Once the material reaches a yield stress state, how are the plastic strains computed? And, if the stress path goes beyond the initial yield surface (if an initial one is postulated), what happens to the original yield surface (if anything)? The first question is addressed in the discussion on the flow rule (or the incremental plastic stress-strain relation), while the second is treated in the discussion on hardening rules.

2.7.1 Yield Surface

Perhaps the best starting point for a discussion of plasticity is to introduce, or rather draw attention to, the concept of a yield surface in stress space. At the outset, it should be noted that yield is a matter of definition, and only the conventional interpretations will be mentioned in this chapter. The reader is, however, urged to keep an open mind on this subject since a different perspective, within the framework of a new theory for sands, will be proposed in Chapter 3.

Since strength of materials is a concept that is familiar to geotechnical engineers, it is used here as the stimulus for the introduction to yield surfaces. Figure 2.6 shows a variety of uniaxial rate-insensitive stress-strain idealizations. In particular, Figures

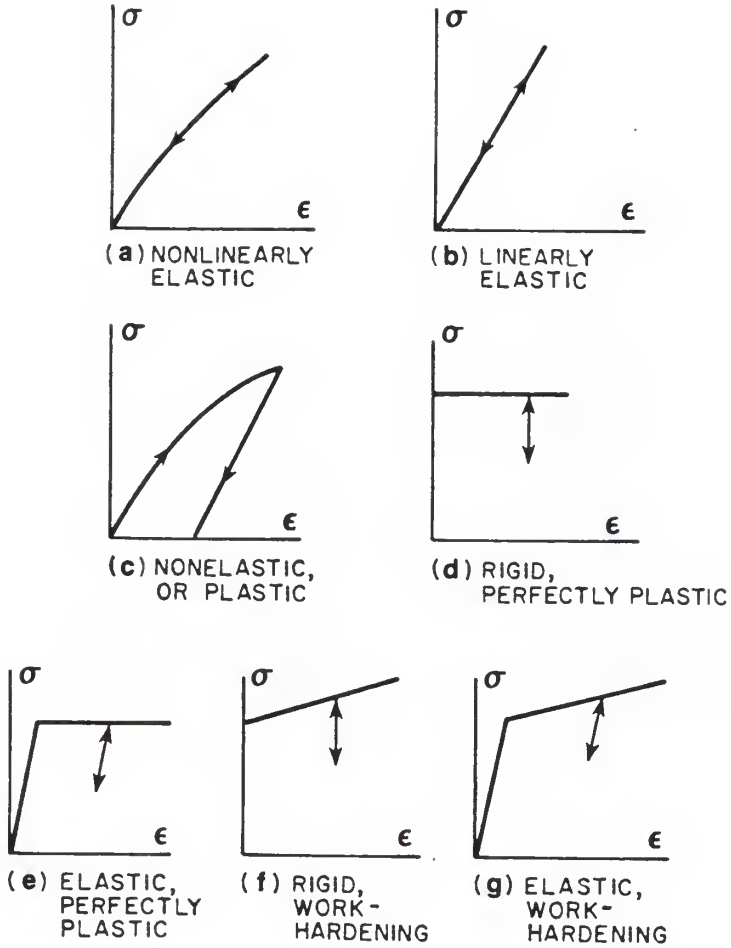


Figure 2.6 Rate-independent idealizations of stress-strain response

2.6 (d) and (e) show examples of perfectly plastic response, and one may infer from this that, for homogenous stress fields, yield and failure are equivalent concepts for this simplest idealization of plastic response.

In the calculation of the stability of earth structures, the Mohr-Coulomb failure criterion is typically used to estimate the maximum loads a structure can support. That is, when this load is reached, the shear stress to normal stress ratio is assumed to be at its peak value at all points within certain zones of failure. This method of analysis is known as the limit equilibrium method. Using the classification set forth in section 2.4, it is a kinematically ambiguous theory in that no strains are predicted. Another common method of analysis is the wedge analysis method. This is a trial and error procedure to find the critical failure plane, a failure plane being a plane on which the full strength of the material is mobilized and the critical plane being the one that minimizes the magnitude of the imposed load.

A feature common to both the limiting equilibrium and the wedge analysis methods is the need to provide a link between the shear and normal stress at failure. A constitutive law, which is a manifestation of the internal constitution of the material, provides this information. More generally, the kinematically ambiguous theories for a perfectly plastic solid must specify the coordinates of all possible failure points in a nine dimensional stress space. Mathematically, this is accomplished by writing a failure function or criterion in the form $F(\sigma_{ij}) = 0$; many well-established forms of the yield function are previewed in the following.

The Mohr-Coulomb frictional failure criterion states that shear strength increases linearly with increasing normal stress, Figure 2.7. For states of stress below the failure or limit or yield line, the material may be considered rigid [Fig. 2.6 (d)] or elastic [Fig. 2.6 (e)]. For a more general description, it is necessary to extend the two-dimensional yield curve of Figure 2.7 to a nine-dimensional stress space. Although such a space need not be regarded as having an actual physical existence, it is an extremely valuable concept because the language of geometry may be applied with reference to it (Synge and Schild, 1949). The set of values $\sigma_{11}, \sigma_{12}, \sigma_{13}, \sigma_{21}, \sigma_{22}, \sigma_{23}, \sigma_{31}, \sigma_{32}$ and σ_{33} , is called a point, and the variables σ_{ij} are the coordinates. The totality of points corresponding to all values of say N coordinates within certain ranges constitute a space of N dimensions denoted by V_N . Other terms commonly used for V_N are hyperspace, manifold, or variety.

Inspection of, say, the equation of a sphere in rectangular cartesian coordinates (x,y,z),

$$F(x,y,z) = (x - a)^2 + (y - b)^2 + (z - c)^2 - k^2 = 0$$

where a, b, and c are the center coordinates and k is the radius, is a simple way of showing that the nine-dimensional equivalent of a stationary surface in stress space may be expressed as

$$F(\sigma_{ij}) = 0. \quad (2.7.1.1)$$

A surface in four or more dimensions is called a hypersurface. The theoretician must therefore postulate a mechanism of yield which leads directly to the formulation of a yield surface in stress space or he must fit a surface through observed yield points.

Rigorously speaking, a yield stress (or point) is a stress state which marks the onset of plastic or irrecoverable strain and which may

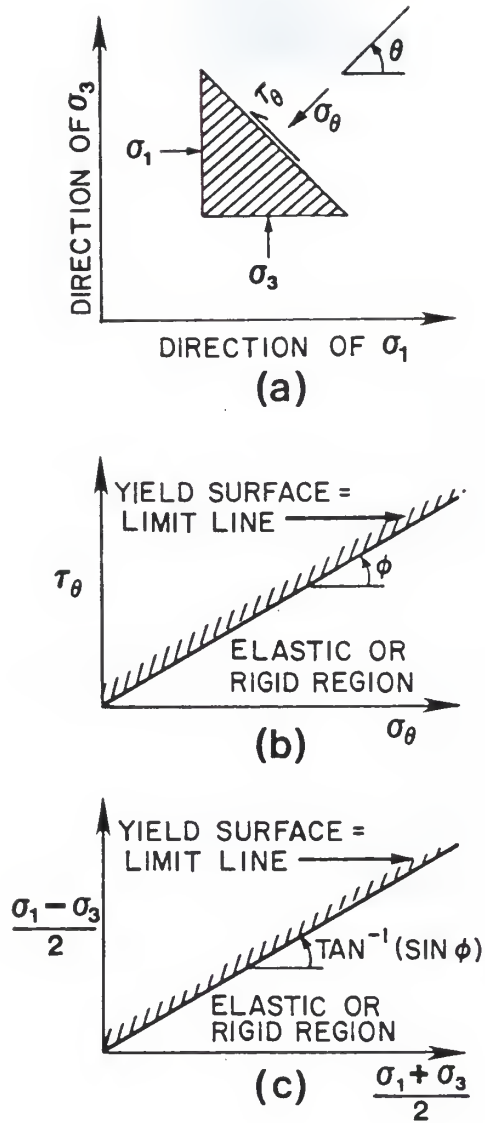


Figure 2.7 Two dimensional picture of Mohr-Coulomb failure criterion

lie within the failure surface. Yield surfaces specify the coordinates of the entirety of yield stress states. These (not necessarily closed) surfaces bound a region in stress space where the material behavior is elastic. But an all-important practical question still looms: How can we tell exactly where plastic deformation begins? Is the transition from elastic to elastic-plastic response distinct? At least for soils, it is not that simple a task. The stress-strain curves continuously turn, and plastic deformation probably occurs to some extent at all stress states for outward loading paths. However, for the perfectly plastic idealization, there should be no major difficulty since the limit states are usually easy to identify.

Among the techniques used to locate the inception of yield are:

- a) for materials like steel with a sharp yield point, the yield stress is usually taken as the plateau in stress that occurs just after the yield point;
- b) for soft metals like aluminium, the yield stress is defined as the stress corresponding to a small value of permanent strain (usually 0.2%);
- c) a large offset definition may be chosen which more or less gives the failure stress;
- d) a tangent modulus definition may be used, but it must be normalized if mean stress influences response; and
- e) for materials like sand which apparently yield even at low stress levels, a Taylor-Quinney (1931) definition is used. This and some of the alternative definitions are illustrated in Figure 2.8.

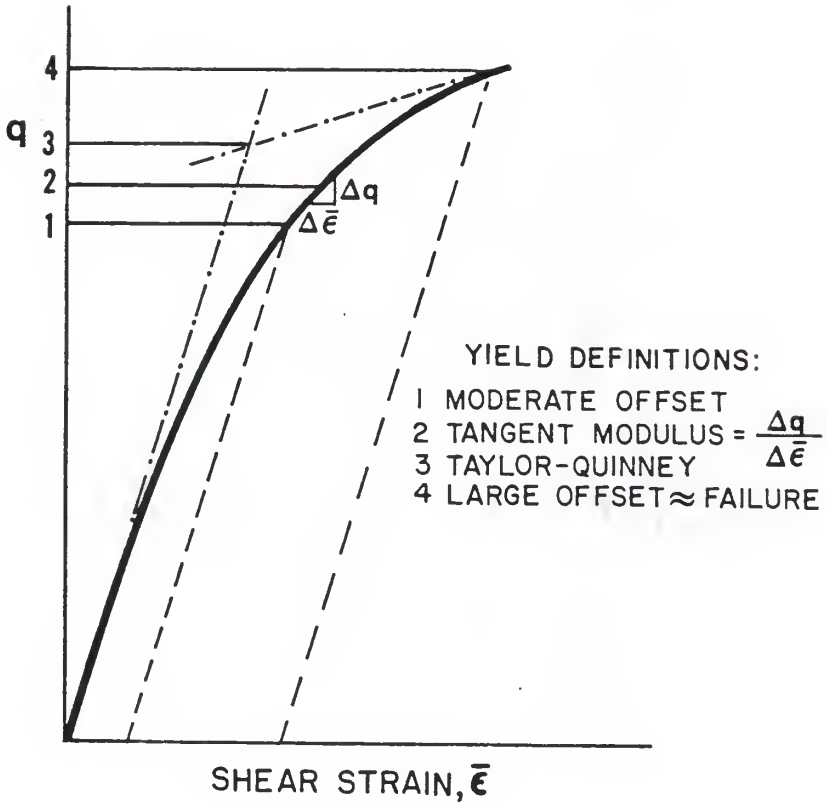


Figure 2.8 Commonly adopted techniques for locating the yield stress

Soil mechanics will identify the Taylor-Quinney definition with the Casagrande procedure (Casagrande, 1936) for estimating the preconsolidation pressure of clays.

Defining a yield surface using the methods outlined above usually leads to one with a shape similar to that of the failure or limit surface. However, in Chapter 3, an alternative approach will be suggested for determining the shape of the yield surface based on the observed trajectory of the plastic strain increment--for sands, these surfaces have shapes much different from the typical failure or yield surfaces.

2.7.2 Failure Criteria

If an existing testing device had the capability to apply simultaneously the six independent components of stress to a specimen, the yield function $F(\sigma_{ij}) = 0$ could be fitted to a comprehensive data set. Unfortunately, such equipment is not available at present, and most researchers still rely on the standard triaxial test (Bishop and Henkel, 1962). However, if the material is assumed to be isotropic, as is usually done, then the number of independent variables in the yield function reduces from six to three; i.e., the three stress invariants or three principal stresses replace the six independent components of $\underline{\sigma}$. In other words, material directions are not important, only the intensity of the stress is. Therefore, by ignoring anisotropy, all that the theoretician needs is a device, like the cubical triaxial device, which can vary σ_1 , σ_2 , and σ_3 independently.

Another implication of the isotropy assumption is that stress data can be plotted in a three dimensional stress space with the principal

stresses as axes. This stress space is known as the Haigh-Westergaard stress space (Hill, 1950). Working in this stress space has the pleasant consequence of an intuitive geometric interpretation for a special set of three independent stress invariants. In order to see them, the rectangular coordinate reference system $(\sigma_1, \sigma_2, \sigma_3)$ must be transformed to an equivalent cylindrical coordinate system (r, θ, z) as described in the following.

Figure 2.9 depicts a yield surface in Haigh-Westergaard (or principal) stress space. The hydrostatic axis is defined by the line

$$\sigma_1 = \sigma_2 = \sigma_3,$$

which is identified with the axis of revolution (z). For cohesionless soils (no tensile strength), the origin of stress space is also the origin of this axis. A plane perpendicular to the hydrostatic axis called a deviatoric or octahedral plane and is given by

$$\sigma_1 + \sigma_2 + \sigma_3 = \text{constant}.$$

When this constant is equal to zero, the octahedral plane passes through the origin of stress space and is then known as a π plane.

If we perform a constant pressure test (paths TC or TE of Figure 2.4), the stress point follows a curve on a fixed deviatoric plane for the entire loading. Such stress paths provide a useful method for probing the shape and/or size of the yield surface's π -plane projection for different levels of mean stress. Polar coordinates (r, θ) are used to locate stress points on a given deviatoric plane.

By elementary vector operations, the polar coordinates r , θ , and z can be correlated to each of the stress invariants $\sqrt{J_2}$, θ and I_1 , which were previously defined in equations 2.2.2.26, 2.2.2.39, and 2.2.2.22

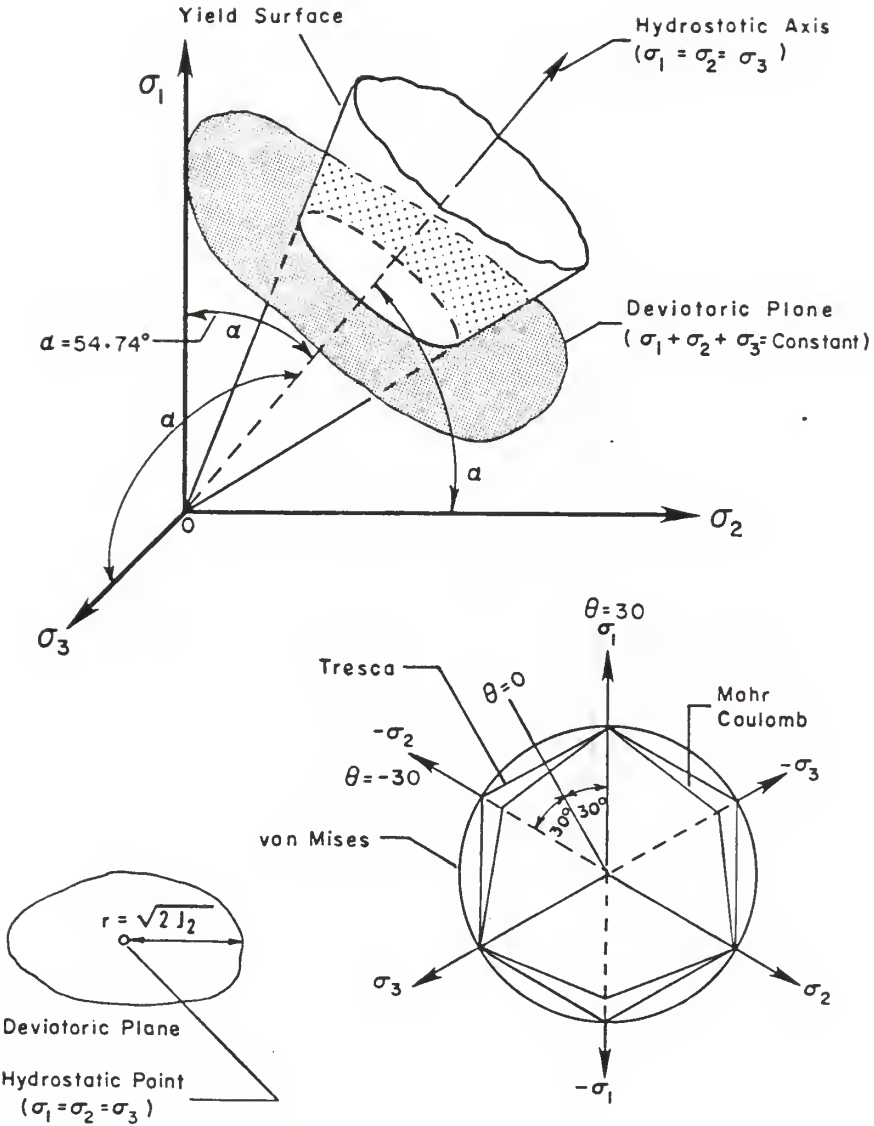


Figure 2.9 Yield surface representation in Haigh-Westergaard stress space

respectively. A measure of the shear stress intensity is given by the radius

$$r = \sqrt{(2J_2)} \quad (2.7.2.1)$$

from the hydrostatic point on the octahedral plane to the stress point.

The polar angle shown in Figure 2.9 is the same as the Lode angle θ . It provides a quantitative measure of the relative magnitude of the intermediate principal stress (σ_2). For example,

$$\sigma_2 = \sigma_3 \quad (\text{compression tests}) \quad \rightarrow \quad \theta = +30^\circ$$

$$\sigma_1 = \sigma_2 \quad (\text{extension tests}) \quad \rightarrow \quad \theta = -30^\circ$$

and

$$\sigma_1 + \sigma_3 = 2 \sigma_2 \quad (\text{torsion tests}) \quad \rightarrow \quad \theta = 0^\circ.$$

Lastly, the average pressure, an important consideration for frictional materials, is proportional to the perpendicular distance "d" from the origin of stress space to the deviatoric plane;

$$d = I_1/\sqrt{3}, \quad (2.7.2.2)$$

where I_1 is the first invariant of $\underline{\sigma}$.

For isotropic materials, the yield function (equation 2.7.1.1) may therefore be recast in an easily visualized form (Figure 2.9)

$$F(I_1, \sqrt{J_2}, \theta) = 0. \quad (2.7.2.3)$$

Some of the more popular failure/yield criteria for isotropic soils and metals are reviewed in the following.

The much used Mohr-Coulomb failure criterion (Coulomb, 1773) for soils is usually encountered in practice as

$$\frac{(\sigma_1 - \sigma_3)}{(\sigma_1 + \sigma_3)} = \sin \phi = k, \quad (2.7.2.4)$$

where ϕ is a constant termed the angle of internal friction. The symbol "k" is used as a generic parameter in this section to represent the size

of yield surfaces. This criterion asserts that plastic flow occurs when the shear stress to normal stress ratio on a plane reaches a critical maximum. If the equations which express the principal stresses in terms of the stress invariants (equation 2.2.2.38) are substituted into equation 2.7.2.4, the Mohr-Coulomb criterion can be generalized to (Shield, 1955)

$$F = \frac{I_1}{3} \sin \phi + \sqrt{J_2} \left\{ \frac{\sin \theta \sin \phi}{\sqrt{3}} - \cos \theta \right\} = 0. \quad (2.7.2.5)$$

A trace of this locus on the π plane is shown in Figure 2.9. The surface plots as an irregular hexagonal pyramid with its apex at the origin of stress space for non-cohesive soils.

Also depicted in this figure are the well-known Tresca and Mises yield surfaces used in metal plasticity. Mises (1928) postulated a yield representation of the form

$$F = \sqrt{J_2} - k = 0, \quad (2.7.2.6)$$

and physically, this criteria can be interpreted to mean that plastic flow commences when the load-deformation process produces a critical strain energy of distortion (i.e., strain energy neglecting the effects of hydrostatic pressure and volume change).

Tresca (1864), on the other hand, hypothesized that a metal will flow plastically when the maximum shear stress on any plane through the point reaches a critical value. In the Mohr's circle stress representation, the radius of the largest circle $[(\sigma_1 - \sigma_3)/2]$ is the maximum shear stress. Replacing the principal stresses with the stress invariants gives the following alternative form for the Tresca criterion:

$$F = \frac{-1}{\sqrt{3}} \sqrt{J_2} \left[\sin \left(\theta + \frac{4}{3} \pi \right) - \sin \left(\theta + \frac{2}{3} \pi \right) \right] - k = 0,$$

which, upon expansion of the trigonometric terms, simplifies to

$$F = \sqrt{J_2} \cos \theta - k = 0. \quad (2.7.2.6)$$

A noticeable difference between the Mises or Tresca criterion and the Mohr-Coulomb criterion is the absence of the variable I_1 in the former. This reminds us that yielding of metals is usually not considered to be dependent on hydrostatic pressure, as the experiments of Bridgman (1945) have demonstrated.

Drucker and Prager (1952) modified the Mises criterion to account for pressure-sensitivity and proposed the form

$$F = \frac{\sqrt{J_2}}{I_1} - k = 0. \quad (2.7.2.8)$$

To match the Drucker-Prager and Mohr-Coulomb yield points in compression space ($\sigma_2 = \sigma_3$), one must use

$$k = \frac{2 \sin \phi}{\sqrt{3} (3 - \sin \phi)}, \quad (2.7.2.9)$$

but, to obtain coincidence in extension space ($\sigma_1 = \sigma_2$),

$$k = \frac{2 \sin \phi}{\sqrt{3} (3 + \sin \phi)} \quad (2.7.2.10)$$

must be specified. Although the development of the Drucker-Prager yield function was motivated mainly by mathematical convenience, it has been widely applied to soil and rock mechanics. However, there is considerable evidence to indicate that the Mohr-Coulomb law provides a better fit to experimental results (see, for example, Bishop, 1966).

Scrutiny of sketches of the previously defined yield surfaces in principal stress space (see Figure 2.9) reveals that they are all "open" along the hydrostatic stress axis. Therefore, for an isotropic compression path, no plastic strains will be predicted. This

contradicts the typical behavior observed along such paths, Figure 2.2. Recognizing this deficiency, Drucker et al. (1957) capped the Drucker-Prager cone with a sphere to allow for plastic yielding for generally outward but non-failure loading paths. The equation for the spherical cap (of radius k) centered on the origin of stress space can be derived by rearranging equation 2.2.2.23,

$$F(\sigma_{ij}) = \sigma_{ij}\sigma_{ij} - k^2 = I_1^2 - 2 I_2 - k^2 = 0. \quad (2.7.2.11)$$

As a result of the development of more sophisticated testing devices, sensing equipment, and data capture units, more reliable and reproducible stress-strain data is becoming available. This has quite naturally led to the development of many new mathematical representations of yielding in soils. Most notably, Lade and Duncan (1975), using a comprehensive series of test data obtained from a true triaxial device (Lade, 1973), have suggested that failure is most accurately modeled by the function

$$F = (I_1^3/I_3) (I_1/p_a)^m - k = 0, \quad (2.7.2.12)$$

where I_3 is the third stress invariant defined in equation 2.2.2.24, p_a is the atmospheric pressure in consistent units, and m is a constant to model deviation from purely frictional response. A spherical cap was subsequently added by Lade (1977) to "close" this "open-ended" function along the hydrostatic axis.

Another recent proposal, based on a sliding model, was put forward by Matsuoka and Nakai (1974). They defined the spatial mobilized plane as the plane on which soil particles are most mobilized on the average in three dimensional stress space. Only for special cases when any two of the three principal stresses are equal does this criterion coincide with the Mohr-Coulomb criterion. Based on the postulate that the

shear/normal stress ratio on the spatial mobilized plane governs failure, Matsuoka and Nakai have derived the following failure criterion:

$$F = \sqrt{\left[\frac{I_1 I_2 - 9 I_3}{9 I_3} \right]} - k = 0. \quad (2.7.2.13)$$

The mobilized plane concept is essentially a three-dimensional extension of the Mohr-Coulomb criterion that takes into account the relative weight of the intermediate principal stress.

Even more recently, Desai (1980) has shown that the Mises, Drucker-Prager, Lade, and Matsuoka surfaces are all special cases of a general third-order tensor invariant polynomial he proposed. Using statistical analyses, he found that the failure criterion

$$F = [I_2 + (I_1 I_3)^{1/3}] - k = 0 \quad (2.7.2.14)$$

gave the best fit to experimental data sets on Ottawa sand and an artificial soil. Research in this field is presently very active, and as more high quality data becomes available, it is anticipated that even more proposals for failure/yield functions will emerge in the near future.

2.7.3 Incremental Plastic Stress-Strain Relation, and Prager's Theory

A material at yield signals the onset of plastic strain, and this section describes the computation of the resulting plastic strain increment. By definition, plasticity theory excludes any influence of the rate of application of the stress increment on the predicted plastic strain increment, and as will be shown later, this leads to restrictions on the possible forms of the stress-strain relation.

In analogy to the flow lines and equipotential lines used in seepage analysis, the existence of a plastic potential, G , in stress space can be postulated such that (Mises, 1928)

$$d\epsilon_{ij}^p = \Lambda \frac{\partial G}{\partial \sigma_{ij}}, \quad \Lambda > 0 \quad (2.7.3.1)$$

where Λ is a scalar factor which controls the magnitude of the generated plastic strain increment, and G is a surface in stress space (like the yield surface) that dictates the direction of the plastic strain increment. More specifically, the plastic strain increment is perpendicular to the level surface $G(\sigma_{ij}) = 0$ at the stress point.

To get a better grasp of equation 2.7.3.1, the soils engineer may think of the function G as a fixed equipotential line in a flow net problem. The partial derivatives $\partial G / \partial \sigma_{ij}$ specify the coordinate components of a vector pointing in the direction perpendicular to the equipotential. This direction is, in fact, the direction of flow (along a flow line) of a particle of water instantaneously at that spatial point. Supplanting now the spatial coordinates (x, y, z) of the seepage problem with stress axes $(\sigma_x, \sigma_y, \sigma_z)$, while keeping the potential and flow lines in place, illustrates the mathematical connection between the movement of a particle of water and the plastic deformation of a soil element. The plastic geometrical change of a soil element is in a direction perpendicular to the equipotential surface $G(\sigma_{ij}) = 0$. At different points in the flow problem, the particles of water move at speeds governed by Darcy's law; therefore, it is possible to construct a scalar point function which gives the speed at each location. In an equivalent manner, the scalar multiplier Λ in equation 2.7.3.1 determines the speed (or equivalently, the magnitude of the incremental

deformation) of the soil particle at different locations in stress space. For example, the closer the stress point is to the failure line, a larger magnitude of Λ (with a corresponding larger magnitude of $d\epsilon^P$) is expected. Therefore, in the crudest sense, the two elements of plasticity theory which immediately confront us are: a) the specification of the direction of the plastic strain increment through a choice of the function $G(\sigma_{ij})$, and b) the computation of the magnitude of $d\epsilon^P$. There are, of course, other important questions to be answered, such as "What does the subsequent yield surface look like?", and these will be treated in later sections and chapters.

Mises (1928) made the assumption that the yield surface and the plastic potential coincide and proposed the stress-strain relation

$$d\epsilon_{ij}^P = \Lambda \frac{\partial F}{\partial \sigma_{ij}}. \quad (2.7.3.2)$$

This suggests a strong connection between the flow law and the yield criterion. When this assumption is made, the flow rule (equation 2.7.3.1) is said to be associated and equation 2.7.3.2 is called the normality rule. However, if we do not insist upon associating the plastic potential with the yield function (as suggested by Melan, 1938), the flow rule is termed non-associated. The implications of the normality rule, it turns out, are far reaching, and as a first step to an incisive understanding of them, Prager's (1949) treatment of the incremental plastic stress-strain relation will be summarized.

The first assumption is designed to preclude the effects of rate of loading, and it requires the constitutive equation

$$d\epsilon^P = \hat{d}\epsilon^P (\underline{g}, d\underline{g}, q_n)$$

to be homogenous of degree one in the stress increment $d\sigma$. Recall that homogeneity of order n ensures that

$$d\epsilon^P = d\hat{\epsilon}^P(\underline{\sigma}^t, \Lambda d\sigma, q_n) = \Lambda^n d\hat{\epsilon}^P(\underline{\sigma}^t, d\sigma, q_n), \quad (2.7.3.3)$$

where Λ is a positive constant.

A simple example will help clarify this seemingly complex mathematical statement. Suppose an axial stress increment of 1 psi produced an axial plastic strain increment of .01 %; this means that if Λ is equal to 2, and $n = 1$, the stress increment of 2 psi ($\Lambda \times 1$ psi) will predict a plastic strain increment of .02% ($\Lambda \times .01\%$). Ideally then, the solution should be independent of the stress increment, provided the stiffness change is negligible over the range of stress spanned by the stress increment.

The simplest option, which ensures homogeneity of order one, is the linear form

$$d\epsilon_{ij}^P = D_{ijkl} d\sigma_{kl}, \quad (2.7.3.4)$$

where \underline{D} is a fourth order plastic compliance tensor, the components of which may depend on the stress history $\underline{\sigma}^t$, the strain history $\underline{\epsilon}^t$, the fabric parameters, etc., but not on the stress increment $d\sigma$. This is referred to as the linearity assumption.

The second assumption, the condition of continuity, is intended to eliminate the possibility of jump discontinuities in the stress-strain curve as the stress state either penetrates the elastic domain (i.e., the yield hypersurface) from within or is unloaded from a plastic state back into the elastic regime. To guarantee a smooth transition from elastic to elastic-plastic response and vice-versa, a limiting stress increment vector, $d\sigma^t$, tangential to the exterior of the yield surface must produce no plastic strain (note: the superscript "t" used here is

an abbreviation for the word tangential and should not be interpreted to imply history). As a consequence, an infinitesimal change of stress, $d\underline{\sigma}$, added to a body at yield [i.e., $F(\underline{\sigma}) - k = 0$ is satisfied] gives rise to three possibilities:

$$a). \frac{\partial F}{\partial \underline{\sigma}} : d\underline{\sigma} < 0 \rightarrow \text{pure elastic response (unloading)} \quad (2.7.3.5)$$

$$b). \frac{\partial F}{\partial \underline{\sigma}} : d\underline{\sigma} = 0 \rightarrow \text{pure elastic response (neutral loading)} \quad (2.7.3.6)$$

or

$$c). \frac{\partial F}{\partial \underline{\sigma}} : d\underline{\sigma} > 0 \rightarrow \text{elastic \& plastic response (loading)}. \quad (2.7.3.7)$$

The notation ":" is the double contraction operator used here to compactly denote the scalar product $\frac{\partial F}{\partial \sigma_{ij}} d\sigma_{ij}$ (see, for instance, Malvern, 1969).

A further implication of the continuity condition can be deduced by decomposing an arbitrary stress increment $d\underline{\sigma}$ into its components normal ($d\underline{\sigma}^n$) and tangential ($d\underline{\sigma}^t$) to the yield surface,

$$d\underline{\sigma} = d\underline{\sigma}^t + d\underline{\sigma}^n.$$

Since the incremental stress-strain relation is linear, we can superpose the individual effects of $d\underline{\sigma}^t$ and $d\underline{\sigma}^n$ to obtain the combined effect of $d\underline{\sigma}$. But we know that $d\underline{\sigma}^t$ constitutes a neutral loading and generates no plastic strain. Therefore, plastic loading is attributed only to the normal component ($d\underline{\sigma}^n$) of $d\underline{\sigma}$,

$$d\underline{\varepsilon}^p \propto |d\underline{\sigma}^n| = d\underline{\sigma} : \underline{n} = d\underline{\sigma} : \nabla F / |\nabla F|, \quad (2.7.3.8)$$

where \underline{n} is the unit tensor normal to the yield surface, ∇ is a vector

differential operator which means, for example, that for the scalar function $F(x,y,z) = 0$,

$$\nabla F = \frac{\partial F}{\partial x} \underline{i} + \frac{\partial F}{\partial y} \underline{j} + \frac{\partial F}{\partial z} \underline{k}.$$

In his presentation of the restrictions imposed by the uniqueness condition, Prager (1949) made use of the following boundary value problem: given the instantaneous mechanical state in a body together with a system of infinitesimal added surface tractions, find the corresponding stress increments throughout the body. A reasonable demand is that plasticity theory predict a unique solution to the problem. But let us assume that the boundary value problem admits two solutions. Say these two solutions resulted in a difference between the predicted stress increments at a given point of the body equal to $\Delta(d\underline{\sigma})$, and similarly, differences in elastic and plastic strain increments equal to $\Delta(d\underline{\epsilon}^e)$ and $\Delta(d\underline{\epsilon}^p)$ respectively. Now, since the two solutions correspond to the same increment of surface tractions on a body of volume V , the principle of virtual work requires that

$$\int_V [\Delta(d\underline{\sigma}) : \{ \Delta(d\underline{\epsilon}^e) + \Delta(d\underline{\epsilon}^p) \}] dV = 0, \quad (2.7.3.9)$$

with the integrand being positive definite. By virtue of Hooke's law, the quantity

$$\Delta(d\underline{\sigma}) : \Delta(d\underline{\epsilon}^e)$$

will always be positive definite so proof of the uniqueness condition is actually a proof that the quantity

$$\Delta(d\underline{\sigma}) : \Delta(d\underline{\epsilon}^p) \quad (2.7.3.10)$$

is positive definite.

In considering equation 2.7.3.10, three cases must be examined:

a) both solutions result in unloading, b) both solutions involve

loading, and c) one solution is an unloading event while the other is a plastic loading process. For the first case, $d\epsilon^p$ is zero for both instances and equation 2.7.3.10 vanishes trivially. To investigate the second case, we label the two "loading" solutions as $d\mathbf{g}^{(1)}$ and $d\mathbf{g}^{(2)}$ and require that the plastic strain increment be directed such that equation 2.7.3.10 is always positive. The limiting scenario occurs when $d\mathbf{g}^{(1)}$ and $d\mathbf{g}^{(2)}$ are both tangential to the yield surface but directed in an opposite sense. Therefore, the only provision which will ensure this is a plastic strain increment directed along the outward normal to the yield surface--i.e., the normality condition. The arguments for case 3 parallel those for case 2, and we can conclude that a sufficient condition for uniqueness of a boundary value problem is that the flow rule be associated and that normality of the plastic strain increment apply,

$$d\epsilon_{ij}^p \propto \frac{\nabla F}{|\nabla F|}. \quad (2.7.3.11)$$

By merging the linearity, the continuity, and the uniqueness conditions--equations 2.7.3.4, 2.7.3.8, and 2.7.3.11 respectively-- the flow rule takes the form

$$d\epsilon^p = \frac{1}{K_p} \frac{\nabla F}{|\nabla F|} \{ \frac{\nabla F}{|\nabla F|} : d\mathbf{g} \}, \quad K_p > 0 \quad (2.7.3.12)$$

where, for reasons which will become apparent later, the scalar K_p (the generalized plastic modulus) is used instead of its inverse. Equation 2.7.3.12 is valid only if the stress state resides on a yield surface [i.e., $F(\underline{\sigma}) = 0$] and a plastic loading event is taking place ($\underline{n} : d\mathbf{g} > 0$).

For non-associative flow, equation 2.7.3.12 is modified to

$$d\epsilon^p = \frac{1}{K_p} \frac{\nabla G}{|\nabla G|} \left\{ \frac{\nabla F}{|\nabla F|} : dg \right\}, \quad K_p > 0 \quad (2.7.3.13)$$

where G is the plastic potential, a surface distinct from the yield surface F .

Frequently in the literature on plasticity, the quantity

$$L = \frac{1}{K_p} \left\{ \frac{\nabla F}{|\nabla F|} : dg \right\} \quad (2.7.3.14)$$

is synthesized as a single term and designated the loading function or loading index "L." With this terminology, the flow rule is then encountered as

$$d\epsilon_{ij}^p = L m_{ij}, \quad (2.7.3.15)$$

where m_{ij} are the components of the unit gradient tensor to the plastic potential G .

If incremental plastic deformation takes place, the stress point, which was initially on a yield surface, must move to another plastic state. This means that the updated stress point must reside on another yield surface or a transformed version of the initial one. In this chapter, discussion is restricted to subsequent yield surfaces which evolve from the initial one. In Chapter 4, the other option--the multiple yield surface concept--is described in detail.

During plastic loading, the material remains at yield as it moves from one plastic state $F(g) = 0$ to another, $F(g + dg) = 0$. When this requirement is met, the consistency condition is said to be satisfied. To stay with the stress point, the yield surface may undergo a size change, or a shape change, or translate, or rotate, or undergo any combination of these processes. No change in the initial yield surface

is the perfectly plastic idealization: the yield surface is also the limit surface. In conventional plasticity, changes in the yield surface occur only when the material undergoes plastic deformation ($\dot{\eta}:d\mathbf{g} > 0$), but Drucker and Seereeram (1986) recently proposed a new concept whereby the yield surface also changes during unloading ($\dot{\eta}:d\mathbf{g} < 0$). Such an evolutionary rule is implemented in Chapter 3.

Remembering that the yield surface encloses the elastic (or "stiffer") region, we may interpret these yield surface transmogrifications as a specification of how the "hard" region in stress space evolves during loading. These are the hardening rules of plasticity. Anyone who has ever bent a wire hanger or a paper clip and then tried to bend it back to its original shape can attest to the phenomenon of hardening. Hardening of a material can also mean that more work per unit volume is required to alter the plastic state. The implications of this particular interpretation are profound, and they are treated in the next section.

2.7.4 Drucker's Stability Postulates

It is now appropriate to introduce one of the cornerstones of modern plasticity theory: Drucker's stability postulates (Drucker, 1950a, 1950b, 1951, 1956, 1958, 1966). Emanating from these basic postulates is a classification of material behavior which results in normality of $d\mathbf{e}^P$ at a smooth point on and convexity of the yield surface.

The meaning of work hardening in the case of an axial compression test is simply that the stress is a monotonically increasing function of strain. This is considered stable response. Drucker (1950a) observed, however, that the definition of work hardening is not such a simple

picture for more general states of stress and paths of loading where some components of stress may increase, while others may decrease. There, working from the notion of the stability of simple rigid bodies, he advanced a definition of intrinsic material stability using the sign of the work done by the addition of and the addition and removal of a small stress increment. This is commonly referred to as "stability in the small" to distinguish it from a later postulate he called "stability in the large", wherein a finite disturbance was considered.

Imagine a material element with a homogenous state of stress \underline{g} and strain $\underline{\epsilon}$. Let an external agency, entirely separate and distinct from the agency which caused the existing state of stress and strain, apply small surface tractions which alter the stress state at each point by $d\underline{g}$ and produce correspondingly small strain increments $d\underline{\epsilon}$. Next, assume this external agency slowly removes the added surface tractions, and in the process recovers the elastic strain increment $d\underline{\epsilon}^e$. In layman terms, a small external load is used to probe the stability of an existing "system"; if the body "runs away" with any small probe, or if upon removal of the probe the material rebounds past its original position, the system is said to be unstable. Stability therefore implies that positive work is done by the external agency during the application of the set of stresses,

$$d\underline{g}:d\underline{\epsilon} > 0, \quad (2.7.4.1)$$

and that the net work performed by it over the cycle of application and removal is zero or positive,

$$d\underline{g}:(d\underline{\epsilon} - d\underline{\epsilon}^e) = d\underline{g}:d\underline{\epsilon}^p \geq 0. \quad (2.7.4.2)$$

It is emphasized that the work referred to is not the total work done by all the forces acting, but only the work done by the added set

on the displacements which result. The latter postulate (equation 2.7.4.2) can be rephrased: work hardening means that useful energy over and above the elastic energy cannot be extracted from the material and the system of forces acting upon it. If equation 2.7.4.2 is to hold for any outward $d\bar{g}$, then it is obvious that $d\bar{\epsilon}^p$ must be normal to the yield surface.

Drucker (1951) extended his postulates by considering the external agency to apply a finite set of surface tractions to the body with its initial stress state \bar{g}^* residing within the yield surface at a reference time $t = 0$. The external agency first causes the stress state to move to a point \bar{g} (at time t) exactly on the yield surface. Then, it gives rise to an infinitesimal loading increment $d\bar{g}$ (with a corresponding $d\bar{\epsilon}^p$), over an arbitrarily short interval Δt , which now moves the point to a neighboring point outside of or on the yield surface. Finally, the external agency removes the stress increment $d\bar{g}$ and returns to \bar{g}^* (at time t^*) along an elastic path. The net work done (dW_{net}) by the external agency over the cycle is assumed to be positive, and it is equal to the total work during the cycle (dW_t) minus the work (dW_o) that would have been done during the cycle by the initial stress \bar{g}^* ,

$$dW_t = \int_0^t (\bar{g}:d\bar{\epsilon}^e) dt + \int_t^{t+\Delta t} [\bar{g}:(d\bar{\epsilon}^e + d\bar{\epsilon}^p)] dt + \int_{t+\Delta t}^t (\bar{g}^*:d\bar{\epsilon}^e) dt. \quad (2.7.4.3)$$

However, the net elastic work during the cycle is zero so this equation simplifies to

$$dW_t = \int_t^{t+\Delta t} (\bar{g}:d\bar{\epsilon}^p) dt, \quad (2.7.4.4)$$

and similarly, we can show that

$$dW_o = \int_t^{t+\Delta t_*} (\underline{\sigma} : d\underline{\epsilon}^P) dt. \quad (2.7.4.5)$$

Therefore,

$$dW_{net} = dW_t - dW_o = \int_t^{t+\Delta t} [(\underline{\sigma} - \underline{\sigma}^*) : d\underline{\epsilon}^P] dt > 0, \quad (2.7.4.6)$$

and so by Drucker's definition, the following must hold:

$$(\underline{\sigma} - \underline{\sigma}^*) : d\underline{\epsilon}^P > 0. \quad (2.7.4.7)$$

With this "stability in the large" restriction, convexity of the yield surface can be demonstrated from simple geometric considerations: all vectors $\underline{\sigma} - \underline{\sigma}^*$ must lie to one side of the hyperplane which is normal to the strain increment vector $d\underline{\epsilon}^P$, and this must hold for all points on the yield hypersurface, thus proving convexity. Drucker (1956) has also shown that stability is a necessary condition for uniqueness.

2.7.5 Applicability of the Normality Rule to Soil Mechanics

The essential difference between a plastic material and an assemblage of two bodies with a sliding friction contact is the necessary volume expansion which accompanies the latter in shear (Drucker, 1954). This volume expansion will be predicted by a pressure sensitive yield surface using the normality assumption. Experimental studies on sand response all generally agree that normality of the shear strain component is almost satisfied on the octahedral plane. However, the observed volumetric component of the plastic strain increment, $d\epsilon_{kk}^P$, has been found to be inconsistent with that specified by normality to a conventionally defined yield surface--i.e., one using a moderate or

Taylor-Quinney definition of yield (see, for example, the study by Lade and Duncan, 1975).

Two options are usually suggested to correct for this discrepancy: the first and more complicated approach is to determine a plastic potential function G , which is entirely distinct from and unrelated to the yield surface. The second and perhaps more appealing approach is to modify the normal vector $\partial F/\partial g$ to bring it into agreement with the direction of $d\epsilon^P$. As a first step to explaining the second alternative, observe from equation 2.7.3.2 that

$$d\epsilon_{kk}^P = \Lambda \frac{\partial F}{\partial \sigma_{kk}} \quad (2.7.7.1)$$

and

$$de_{ij}^P = \Lambda \frac{\partial F}{\partial s_{ij}} \quad (2.7.7.2)$$

respectively.

In order to bring the gradient $\partial F/\partial g$ in line with the observed trajectory of $d\epsilon^P$, the volumetric component $d\epsilon_{kk}^P$ and the deviatoric components are modified by the scalar factors A_1 and A_2 ,

$$d\epsilon_{kk}^P = \Lambda A_1 \frac{\partial F}{\partial \sigma_{kk}} \quad (2.7.7.3)$$

and

$$de_{ij}^P = \Lambda A_2 \frac{\partial F}{\partial s_{ij}}. \quad (2.7.7.4)$$

To clarify the influence of these factors, these equations are restated in terms of 'triaxial' stress parameters,

$$\frac{dv^P}{v} = \Lambda A_1 \frac{\partial F}{\partial p}, \quad (2.7.7.5)$$

and

$$d\bar{\epsilon}^P = \frac{2}{3} (d\epsilon_1^P - d\epsilon_3^P) = \Lambda A_2 \frac{\partial F}{\partial q}, \quad (2.7.7.6)$$

where dv^P/v is the plastic volume strain and $d\bar{\epsilon}^P$ is the plastic equivalent shear strain. Figure 2.10 is a geometric interpretation of these equations. Figure 2.10 (a) corresponds to the normality rule (i.e., $A_1 = A_2 = 1$) and Figure 2.10 (b) shows how the volumetric and deviatoric components are modified to change both the magnitude and direction of the resulting plastic strain increment vector. Lastly, Figure 2.10 (c) illustrates how the magnitude of the plastic strain increment vector may be changed without altering its direction.

Restrictions on the selection of the two factors A_1 and A_2 imposed by stability considerations have been discussed by Jain (1980).

Stability in the small (equation 2.7.4.2),

$$d\underline{\sigma} : d\underline{\epsilon}^P = dp \, d\epsilon_{kk}^P + ds : d\underline{\epsilon}^P \geq 0,$$

or for this special case,

$$d\sigma_{mn} \, d\epsilon_{mn}^P = A \left[dp \, A_1 \frac{\partial F}{\partial \sigma_{kk}} + ds_{ij} \, A_2 \frac{\partial F}{\partial s_{ij}} \right] \geq 0, \quad (2.7.7.7)$$

requires a frictional system to dissipate energy regardless of whether it expands or contracts. Since shear distortions are considered to be the result of frictional sliding and therefore dissipative, A_2 must always be positive. On the other hand, the modifying factor A_1 is permitted to take on a negative value. This means that the spherical stress can extract energy from the system, but the choice of A_1 must still ensure that total energy is dissipated (i.e., equation 2.7.7.7 must still hold). Examples of models which incorporate these parameters can be found in the papers by Prevost (1978), Desai and Siriwardane (1980), and Sture et al. (1984).

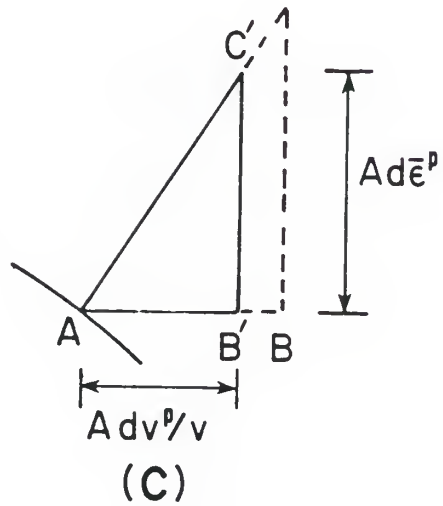
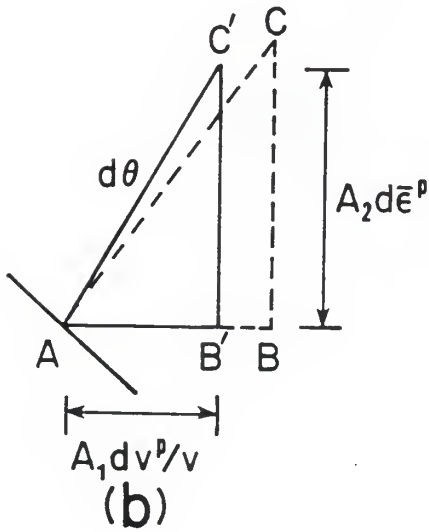
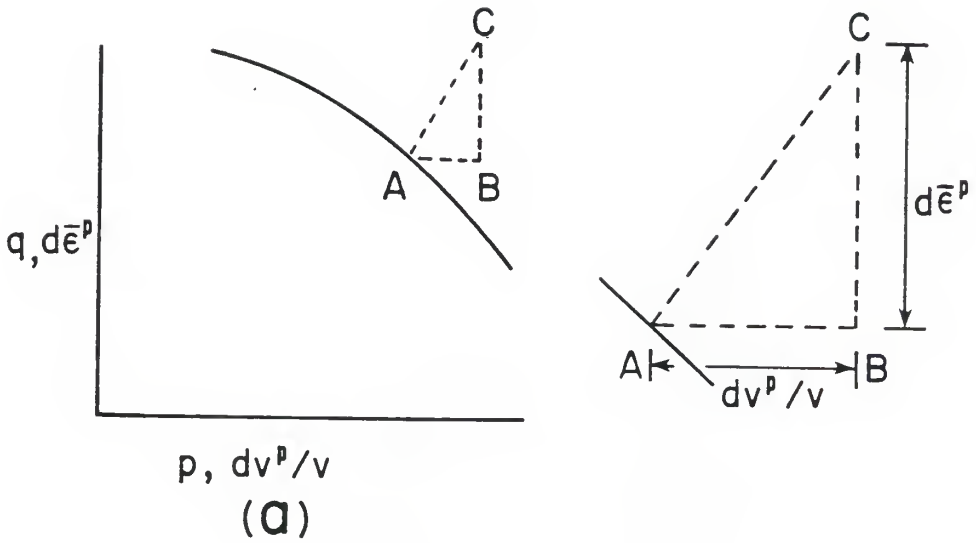


Figure 2.10 Diagrams illustrating the modifying effects of the coefficients A_1 and A_2 : (a) $A_1 = A_2 = 1$; (b) $A_1 \neq A_2$; (c) $A_1 = A_2 = A$ (after Jain, 1980)

2.7.6 Isotropic Hardening

Based on physical postulates and experimental stress probes, various rules have been suggested to describe the metamorphosis (or hardening) of the yield surface. Of these, the simplest idealization is that of isotropic hardening (Hill, 1950). To illustrate this concept, consider a hypothetical isotropic material with a circular initial yield curve (or surface) centered at the origin of principal stress space and of some initial radius k_0 , Figure 2.11. Also assume the existence of an outer concentric failure or limiting or bounding surface of fixed radius k_f . Although this is an inappropriate representation of yielding in engineering materials, its visual and mathematical features are ideal for demonstration. It is used almost exclusively in this section as a vehicle for introducing other related concepts.

For a uniaxial compression stress path, Figure 2.11, the stress point moves up the σ_1 axis and meets the initial yield surface where $\sigma_1 = k_0$, point A. As the stress point continues up this axis, the initial surface expands uniformly about the origin to stay with the stress point; the current radius of the circle k is equal to σ_1 . Note also that, from the geometry of this yield surface, the only non-zero component of plastic strain is ϵ_1^P . If loading continues until $\sigma_1 = k_f$, the material fails (i.e., $K_p \rightarrow 0$), but if the path terminates at some pre-failure stress $\sigma_1 = k^*$, point B in Figure 2.11, and is followed by an (elastic) unloading back to the origin O, the expanded yield surface of radius k^* remains as memory of the prior loading. Now, if σ_2 is increased while maintaining σ_1 at zero stress, the material yields or flows plastically only if σ_2 reaches and then exceeds a magnitude of k^* . Expansion of the yield surface takes place as before when $\sigma_2 > k^*$.

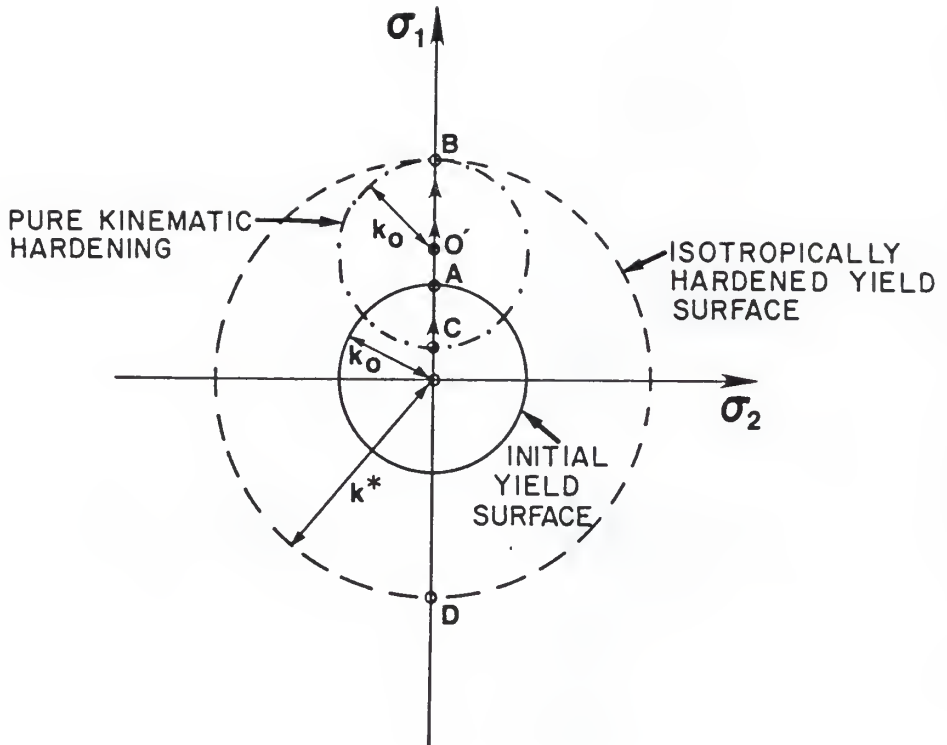


Figure 2.11 Schematic illustration of isotropic and kinematic hardening

Thus, in effect, isotropic hardening means that the material hardens equally well in all directions--it remains isotropic despite the hardening.

How might isotropic hardening correspond to reality? If the material under investigation is a soil, we may assume that hardening takes place primarily as a result of compaction, and that the anisotropic realignment of the microstructure is insignificant. Reduction in the porosity represents an all around (or isotropic) hardening (or strengthening) of the material. However, if the hardening is not due to an all around effect like porosity changes or if the anisotropic fabric induction is consequential, then we must keep track of the material directions and account for anisotropy within the framework of plasticity theory. Because of the important role isotropic hardening rules play in soil mechanics today, these are discussed in some detail before introducing the specific rules designed for anisotropic (or kinematic) hardening.

If the stress tensor appears as the only independent variable in the equation for the yield surface, the configuration of the current yield surface, as given by say the size of the isotropically expanding or expanded circle, is determined solely by the stress history. This particular choice is the basis for the stress hardening theories. Prager (1949) proposed, however, that the mechanical state of a material, as manifested by its yield surface, should, in addition to \underline{g} , also depend on the components of the plastic strain $\underline{\epsilon}^P$, $F(\underline{g}, \underline{\epsilon}^P) = 0$. Applying this postulate to the illustrative isotropic hardening model implies that the radius, k , should depend on $\underline{\epsilon}^P$, $F[\underline{g}, k(\underline{\epsilon}^P)] = 0$. With

this additional constraint, the consistency condition takes on added importance since the differential

$$dF = \frac{\partial F}{\partial \sigma_{ij}} d\sigma_{ij} + \frac{\partial F}{\partial \epsilon_{rs}^p} d\epsilon_{rs}^p = 0 \quad (2.7.6.1)$$

must be satisfied during plastic loading. Substituting the flow rule (equation 2.7.3.12) into this equation makes the consequence of the restriction more transparent,

$$\frac{\partial F}{\partial \sigma_{ij}} d\sigma_{ij} + \frac{\partial F}{\partial \epsilon_{mn}^p} \frac{1}{K_p} \frac{\partial F}{\partial \sigma_{mn}} \frac{1}{|\nabla F|^2} \left\{ \frac{\partial F}{\partial \sigma_{pq}} d\sigma_{pq} \right\} = 0,$$

from which the scalar term $(\partial F / \partial \sigma_{ij}) d\sigma_{ij}$ may then be factored out to show that

$$K_p = - \frac{\partial F}{\partial \epsilon_{mn}^p} \frac{\partial F}{\partial \sigma_{mn}} \frac{1}{|\nabla F|^2}, \quad (2.7.6.2)$$

or for the illustrative example,

$$K_p = - \frac{\partial F}{\partial k} \frac{\partial k}{\partial \epsilon_{mn}^p} \frac{\partial F}{\partial \sigma_{mn}} \frac{1}{|\nabla F|^2}. \quad (2.7.6.3)$$

Therefore, the plastic modulus can be computed directly from equation 2.7.6.3 if one can postulate an equation linking the size of the yield surface (k) with the plastic strain ϵ^p , or its invariants if material isotropy is assumed. Even more generally, any number of identifiable plastic internal variables q_n (including ϵ^p) may be used to characterize the state of the material, $F(g, q_n) = 0$. The name plastic internal variable (PIV) is selected in order to emphasize its association with plasticity in particular, while the name internal variables is associated with inelasticity in general (Dafalias, 1984). Examples of PIVs include the plastic strain tensor, the plastic work, and a scalar measure of cumulative plastic strain; many authors prefer to identify the (non-plastic) internal variables of soil as the

porosity, and the numerous fabric measures such as the orientation of the particles and their contact planes. The evolution of g_n is given by

$$dg_n = L r_n,$$

where L is the loading index defined in equation 2.7.3.14, and r_n are functions of the state variables (Lubliner, 1974). If, for example, g_1 represents $\underline{\epsilon}^P$, then r_1 is the unit normal to the yield surface \underline{n} in associative plasticity. The generalization of equation 2.7.6.2 is therefore

$$K_p = - \frac{\partial F}{\partial g_n} r_n \frac{1}{|\nabla F|}.$$

Perhaps the three most popular plastic internal variables used in soil plasticity are the plastic volumetric strain ϵ_{kk}^P , the plastic work

$$W_p = \int (\sigma_{ij} d\epsilon_{ij}^P) dt, \quad (2.7.6.4)$$

and the arc length of the deviatoric plastic strain \underline{e}^P

$$\eta = \int \sqrt{(de_{ij}^P de_{ij}^P)} dt. \quad (2.7.6.5)$$

When plastic work appears as the state variable, the formulation is classified as a work-hardening theory. Similarly, if one or a combination of the invariants or arc lengths of $\underline{\epsilon}^P$ or its deviation \underline{e}^P are employed, the material is said to be strain-hardening. Concepts similar to that of work hardening were employed as early as the 1930's by Taylor and Quinney (1931) and Schmidt (1932). The arc length was used as a state variable by Odqvist (1933). However, in these earlier works, the total strain $\underline{\epsilon}$ was used instead of the plastic strain $\underline{\epsilon}^P$. This was clearly inappropriate because elastic strains occurring within the yield surface could alter it. With regards to modern soil plasticity, the reader is referred to Lade's work (Lade and Duncan, 1975) to find an application of a work-hardening theory and to Nova and

Wood's (1979) for a strain-hardening description. Mroz (1984) has surveyed the many specialized forms of these plastic internal variables or hardening parameters, with emphasis on their applications to soil mechanics.

Models based on the concept of density or volumetric hardening utilize the irreversible plastic volumetric strain as the state variable, $F(\underline{g}, \epsilon_{kk}^p) = 0$; examples of this approach can be found in Drucker, Gibson, and Henkel (1957); Schofield and Wroth (1968); Roscoe and Burland (1968); DiMaggio and Sandler (1971); and Sandler, DiMaggio, and Baladi (1976). With this choice of state variable, equation 2.7.6.3 specializes to

$$K_p = - \frac{\partial F}{\partial k} \frac{dk}{d\epsilon_{mm}^p} \frac{1}{3} \frac{\partial F}{\partial p} \frac{1}{|\nabla F|^2} \quad (2.7.6.6)$$

where p is the mean stress.

One may wonder how the size of the yield surface k may be analytically linked to the plastic volumetric strain ϵ_{mm}^p . This is illustrated by alluding to an isotropically hardening spherical yield surface. Consider the typical stress-strain response of soil in hydrostatic compression, Figure 2.2, and observe from Figure 2.12 that the radius of the yield surface (k) is equal to $\sqrt{3} p$ for this stress path. The latter information could have also been retrieved directly from equation 2.7.2.2. It is well known in soil mechanics that the pressure-volume response along this path can be reasonably approximated by the equation

$$p = p_0 \exp(\lambda \epsilon_{kk}^p), \quad (2.7.6.7)$$

or alternatively,

$$k = k_0 \exp(\lambda \epsilon_{kk}^p), \quad (2.7.6.8)$$

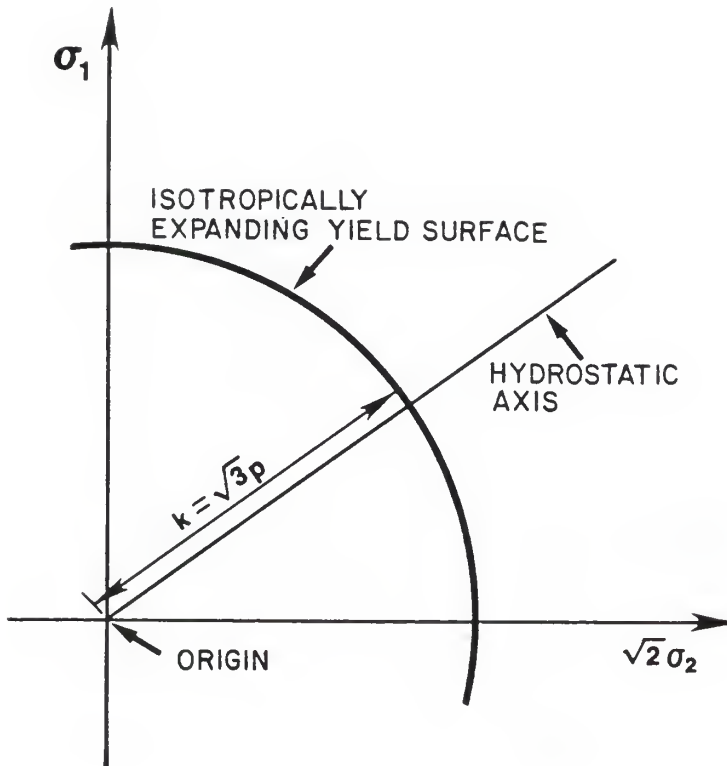


Figure 2.12 Two dimensional view of an isotropically hardening yield sphere for hydrostatic loading

where p (or k) and p_0 (or k_0) are the current and the initial sizes respectively, and λ is a constant which characterizes the plastic compressibility of the material. Higher magnitudes of λ imply a stiffer (or denser) sand. Soils engineers will perhaps recognize this equation as being an alternative expression for the linear voids ratio vs. log mean stress plot.

From equation 2.7.6.7, we find that

$$\frac{dp}{d\varepsilon_{kk}^D} = \lambda p_0 \exp(\lambda \varepsilon_{kk}^D) = \lambda p, \quad (2.7.6.9)$$

and for this particular empirical stress-strain relation, the plastic modulus (derived from equation 2.7.6.6) is

$$K_p = - \frac{1}{|\nabla F|^2} \frac{3 (\partial F)^2}{\partial p} \lambda p. \quad (2.7.6.10)$$

Notice that $K_p \rightarrow 0$ as $\partial F / \partial p \rightarrow 0$, which means that plastic flow is isochoric (volume preserving) at failure. Normally consolidated clays and loose sands generally exhibit this phenomenon.

Three types of hardening rules have been described: stress-hardening, work-hardening, and strain-hardening. With work- and strain-hardening, the plastic modulus is computed from the consistency condition, but nothing has yet been said about the stress-hardening theory. Because of its applicability to the proposed formulation in Chapter 3, it is embedded in the ideas presented there.

Recently, Drucker and Palgen (1981, p.482) reminded us that "the temptation to think of the special form $F(\underline{g}, \underline{\varepsilon}^D) = 0$ as a good first approximation to reality must be resisted. Writing

$$dF = 0 = \frac{\partial F}{\partial \sigma_{ij}} d\sigma_{ij} + \frac{\partial F}{\partial \varepsilon_{mn}^D} d\varepsilon_{mn}^D$$

and replacing

$$\frac{\partial F}{\partial \sigma_{ij}} d\sigma_{ij} \text{ by } - \frac{\partial F}{\partial \epsilon_{mn}^p} d\epsilon_{mn}^p$$

generally leads to an undesirable and misleading constraint." They proposed that the plastic modulus may be entirely stress dependent--that is, the state of the material (i.e., the yield surface and the plastic modulus) is given solely by the state of stress. In Chapter 3, it will be shown that "freeing" the plastic modulus from the consistency condition does, in fact, lead to a simpler and more elegant approach.

2.7.7 Anisotropic Hardening

Kinematic hardening is a term introduced by Prager (1955) to describe his proposition that the yield surface rigidly translates in stress space. It is easy to visualize this movement and its connotation by considering again the hypothetical elastic-plastic material with the circular yield surface, Figure 2.11. If after the unloading from $\sigma_1 = k^*$ to zero stress was followed by a complete reversal of σ_1 , the isotropic hardening idealization would not predict any plastic strains until σ_1 reaches and then goes beyond $-k^*$. Experimental evidence suggests that this is not true: Bauschinger (1887) found that if a metal specimen is compressed beyond its elastic limit, then its yield stress in tension is lowered. This mode of response was anticipated earlier by Wiedemann (1860) and has been confirmed more recently by many experimental investigations. See, for example, Naghdi, Essenburg, and Koff (1958); Ivey (1961); and Phillips and Weng (1975).

To capture the essence of the Bauschinger effect, Prager (1955) assumed that the yield surface translates without deforming to follow

the stress point, the direction of translation being the direction of $d\underline{\xi}^P$. With such an idealization, yielding would be predicted at point C in Figure 2.11 on an unload following a loading from O to B. This is in striking contrast to point D, which would have been predicted for the isotropic hardening theory. Therefore, in order to characterize more generally a yield surface, not only should its size k be monitored, but also its center coordinate $\underline{\xi}$, $F(\underline{g}, \underline{\xi}, k) = 0$. The consistency condition is now more generally written as

$$dF = \frac{\partial F}{\partial \underline{g}} : d\underline{g} + \frac{\partial F}{\partial \underline{\xi}} : d\underline{\xi} + \frac{\partial F}{\partial k} dk = 0, \quad (2.7.7.1)$$

or $F(\underline{g} + d\underline{g}, \underline{\xi} + d\underline{\xi}, k + dk) = 0$ must be satisfied during plastic loading.

Yield surfaces may simultaneously change their size and center coordinate, and these are said to follow an isotropic/kinematic hardening rule. If the center coordinate $\underline{\xi}$ is some scalar magnitude multiplied by the Kronecker delta δ_{ij} , the material remains isotropic, but in general, the translation of the yield surface takes induced anisotropy into account and reflects the history of loading.

As mentioned before, Prager (1955) assumed that the yield surface's center translates in a direction parallel to the plastic strain increment vector $d\underline{\xi}^P$. However, in the application of this hardening rule, a problem arises: although the yield surface remains rigid in nine-dimensional stress space, it may not appear rigid in subspaces. To overcome this difficulty, Ziegler (1959) proposed that the surface translates in the direction of a radius connecting its center with the stress point [i.e., $d\underline{\xi} \propto (\underline{g} - \underline{\xi})$]. Based on experimental observations, Phillips (Phillips and Weng, 1975) has postulated that the yield surface

translates in the direction of the stress increment (i.e., $d\bar{\epsilon} \propto d\bar{g}$), while simultaneously changing its shape to manifest no cross effect. He accomplished this by pulling in the "rear" of the yield surface as it moved along the trajectory of the stress path. Baltov and Sawczuk (1965) described an analytical hardening rule in which the yield surface rotates in addition to translating and isotropically hardening.

Virtually all of these anisotropic hardening rules have been employed in soil plasticity. Prevost (1978), in describing an early version of his pressure-sensitive model, gives options for using all but the rotation and shape transformation hardening. Anandarajah et al. (1984) describe a special application wherein the yield surface is permitted to rotate about the origin as well as isotropically expand. A similar approach was also adopted by Ghaboussi and Momen (1982). Poorooshasb, Yong, and Lelievre (1982) describe a graphical procedure for obtaining the shape of the deviatoric section of the yield surface for complicated paths of loading. The possible variations on the hardening law are endless, and for additional discussion of research on hardening, the reader is referred to Naghdi (1960).

A second option for specifying the plastic modulus as a function of stress history is to assume that there are a field of nesting (i.e., non-intersecting) yield surfaces in stress space, each of which has a plastic modulus associated with it (Mroz, 1967, and Iwan, 1967). Depending upon the loading, a yield surface will translate and/or change its size such that its resulting motion may engage an interior or exterior member of the family of yield surfaces. To avoid intersecting adjacent members, the active yield surface must follow a Mroz kinematic hardening rule; this is implemented and described more fully in Chapter

4. The plastic modulus in the nested surface models varies in a piecewise linear manner, and has memory of the loading history built into the current configuration of the yield surfaces. Variations on the multi-surface approach, including smooth variation of the plastic modulus, are described in detail in Chapter 4.

2.7.8 Incremental Elasto-Plastic Stress-Strain Relation

When elastic and plastic strain increments are occurring simultaneously, the constitutive equations must be organized in a compact but general form for computational purposes. The equation for the total strain increment (equation 2.4.2) is

$$d\underline{\underline{\epsilon}} = d\underline{\underline{\epsilon}}^e + d\underline{\underline{\epsilon}}^p,$$

and if the test simulation is stress-controlled (i.e., $d\underline{\underline{\sigma}}$ is input), both these components can be computed explicitly. Elastic increments are computed by combining equations 2.6.1.12 and 2.6.1.13,

$$\begin{aligned} d\underline{\underline{\epsilon}}_{ij}^e &= d\underline{\underline{\epsilon}}_{ij}^e + \frac{1}{3} d\underline{\underline{\epsilon}}_{mm}^e \delta_{ij} \\ &= (ds_{ij} + 2G) + \frac{1}{3} (d\sigma_{kk} + 3K) \delta_{ij}, \end{aligned} \quad (2.7.8.1)$$

which may then be put in the alternative form:

$$d\underline{\underline{\epsilon}}^e = \underline{\underline{D}}^e d\underline{\underline{\sigma}}, \quad (2.7.8.2)$$

where $\underline{\underline{D}}^e$ is the fourth order, incremental, elastic compliance tensor,

$$D_{ijkl}^e = \frac{2G - 3K}{18 KG} \delta_{ij} \delta_{kl} + \frac{1}{4G} (\delta_{ik} \delta_{jl} + \delta_{il} \delta_{jk}). \quad (2.7.8.3)$$

Plastic strain increments are computed from the flow rule (equation 2.7.3.13), and when combined with equation 2.7.8.2, the total strain increment is

$$d\underline{\underline{\epsilon}} = \underline{\underline{D}}^e d\underline{\underline{\sigma}} + \frac{1}{K_p} \frac{\nabla G}{|\nabla G|} \left\{ \frac{\partial F}{\partial \underline{\underline{\sigma}}} : d\underline{\underline{\sigma}} \right\}. \quad (2.7.8.4)$$

If, however, a strain increment was specified, as in a finite element routine, the inverse of this incremental stress-strain relation will be needed. The algebraic operations involved in this inversion are carried out in the following. First multiply both sides of equation 2.7.8.4 by the inverse of the \underline{D}^e matrix or \underline{C}^e ,

$$\underline{C}^e d\underline{\varepsilon} = d\underline{\sigma} + \underline{C}^e \frac{1}{K_p} \frac{\nabla \underline{G}}{|\nabla \underline{G}|} \frac{1}{|\nabla \underline{F}|} \{\partial \underline{F} : d\underline{\sigma}\}, \quad (2.7.8.5)$$

and if we replace $(\nabla \underline{G} / |\nabla \underline{G}|)$ and $(\nabla \underline{F} / |\nabla \underline{F}|)$ by their unit tensor notation \underline{m} and \underline{n} respectively,

$$\underline{C}^e d\underline{\varepsilon} = d\underline{\sigma} + \underline{C}^e \frac{1}{K_p} \underline{m} \{\underline{n} : d\underline{\sigma}\}. \quad (2.7.8.6)$$

The next step is to multiply both sides of this equation by the tensor \underline{n} ,

$$\underline{n} : \underline{C}^e d\underline{\varepsilon} = \underline{n} : d\underline{\sigma} + \underline{n} : \underline{C}^e \frac{1}{K_p} \underline{m} \{\underline{n} : d\underline{\sigma}\},$$

and from this result, we find that

$$\frac{1}{K_p} \underline{n} : d\underline{\sigma} = \frac{\underline{n} : \underline{C}^e d\underline{\varepsilon}}{K_p + \underline{n} : \underline{C}^e : \underline{m}},$$

which when substituted into equation 2.7.8.6 gives

$$\underline{C}^e d\underline{\varepsilon} = d\underline{\sigma} + \frac{(\underline{C}^e : \underline{m}) (\underline{n} : \underline{C}^e)}{K_p + (\underline{n} : \underline{C}^e : \underline{m})} d\underline{\varepsilon}, \quad (2.7.8.7)$$

or

$$d\underline{\sigma} = \left[\underline{C}^e + \frac{(\underline{C}^e : \underline{m}) (\underline{n} : \underline{C}^e)}{K_p + (\underline{n} : \underline{C}^e : \underline{m})} \right] d\underline{\varepsilon} = \underline{C} d\underline{\varepsilon}. \quad (2.7.8.8)$$

If the flow rule is associated (i.e., $\underline{m} = \underline{n}$), the elastic-plastic stiffness matrix \underline{C} is symmetric, but if \underline{m} is not equal to \underline{n} (i.e., non-associative flow) the matrix loses its major symmetry and leads to increased computation costs in numerical applications. For

completeness, the independent components of the symmetric elastic-plastic stiffness tensor \underline{C} of the incremental stress-strain relation

$$\begin{Bmatrix} d\sigma_{11} \\ d\sigma_{22} \\ d\sigma_{33} \\ d\sigma_{23} \\ d\sigma_{31} \\ d\sigma_{12} \end{Bmatrix} = \begin{bmatrix} C_{11} & C_{12} & C_{13} & C_{14} & C_{15} & C_{16} \\ C_{21} & C_{22} & C_{23} & C_{24} & C_{25} & C_{26} \\ C_{31} & C_{32} & C_{33} & C_{34} & C_{35} & C_{36} \\ C_{41} & C_{42} & C_{43} & C_{44} & C_{45} & C_{46} \\ C_{51} & C_{52} & C_{53} & C_{54} & C_{55} & C_{56} \\ C_{61} & C_{62} & C_{63} & C_{64} & C_{65} & C_{66} \end{bmatrix} \begin{Bmatrix} d\varepsilon_{11} \\ d\varepsilon_{22} \\ d\varepsilon_{33} \\ d\varepsilon_{23} \\ d\varepsilon_{31} \\ d\varepsilon_{12} \end{Bmatrix}$$

are written out in long form:

$$C_{11} = \Gamma + 2\mu + F [(\Gamma n_{kk} + 2\mu n_{11})^2]$$

$$C_{12} = \Gamma + F [(\Gamma n_{kk} + 2\mu n_{11})(\Gamma n_{kk} + 2\mu n_{22})]$$

$$C_{13} = \Gamma + F [(\Gamma n_{kk} + 2\mu n_{11})(\Gamma n_{kk} + 2\mu n_{33})]$$

$$C_{14} = F [(\Gamma n_{kk} + 2\mu n_{11})(2\mu n_{23})]$$

$$C_{15} = F [(\Gamma n_{kk} + 2\mu n_{11})(2\mu n_{13})]$$

$$C_{16} = F [(\Gamma n_{kk} + 2\mu n_{11})(2\mu n_{12})]$$

$$C_{22} = \Gamma + 2\mu + F [(\Gamma n_{kk} + 2\mu n_{22})^2]$$

$$C_{23} = \Gamma + F [(\Gamma n_{kk} + 2\mu n_{22})(\Gamma n_{kk} + 2\mu n_{33})]$$

$$C_{24} = F [(\Gamma n_{kk} + 2\mu n_{22})(2\mu n_{23})]$$

$$C_{25} = F [(\Gamma n_{kk} + 2\mu n_{22})(2\mu n_{13})]$$

$$C_{26} = F [(\Gamma n_{kk} + 2\mu n_{22})(2\mu n_{12})]$$

$$C_{33} = \Gamma + 2\mu + F [(\Gamma n_{kk} + 2\mu n_{33})^2]$$

$$C_{34} = F [(\Gamma n_{kk} + 2\mu n_{33})(2\mu n_{23})]$$

$$C_{35} = F [(\Gamma n_{kk} + 2\mu n_{33})(2\mu n_{13})]$$

$$C_{36} = F [(\Gamma n_{kk} + 2\mu n_{33})(2\mu n_{12})]$$

$$C_{44} = \mu + F [4 (\mu n_{23})^2]$$

$$C_{45} = F [(2 \mu n_{23})(2 \mu n_{13})]$$

$$C_{46} = F [(2 \mu n_{23})(2 \mu n_{12})]$$

$$C_{55} = \mu + F [4 (\mu n_{13})^2]$$

$$C_{56} = F [(2 \mu n_{13})(2 \mu n_{12})]$$

$$C_{66} = \mu + F [4 (\mu n_{12})^2]$$

where

$$F = - \frac{1}{K_p + \Gamma (n_{kk})^2 + 2 \mu}.$$

CHAPTER 3
PROPOSED PLASTICITY THEORY FOR GRANULAR MEDIA

3.1 Introduction

A constitutive model for sand is proposed within the framework of a rather special time-independent or elastic-plastic theory recently put forward by Drucker and Seereeram (1986). In its simplest form, the material model exhibits no memory of prior plastic deformation, although modifications can be easily devised to account for more complicated aspects of real behavior. This elementary form, with no account of hardening, lies at the extreme end of a spectrum of idealizations where the conventional work-hardening theories are at the other extreme and the "bounding surface" type formulations are intermediate.

The key features of the theory as applied to sand are

1. The material remains at yield during unloading as well as loading (Figure 3.1).
2. Yielding is defined as any plastic deformation, no matter how small, and not by the traditional moderate offset or Taylor-Quinney (1931) definition (Figure 3.2).
3. Material behavior at each state of stress is assumed to be stable in the small for any direction of motion of the stress point. This implies that the plastic strain increment ($d\varepsilon^P$) is

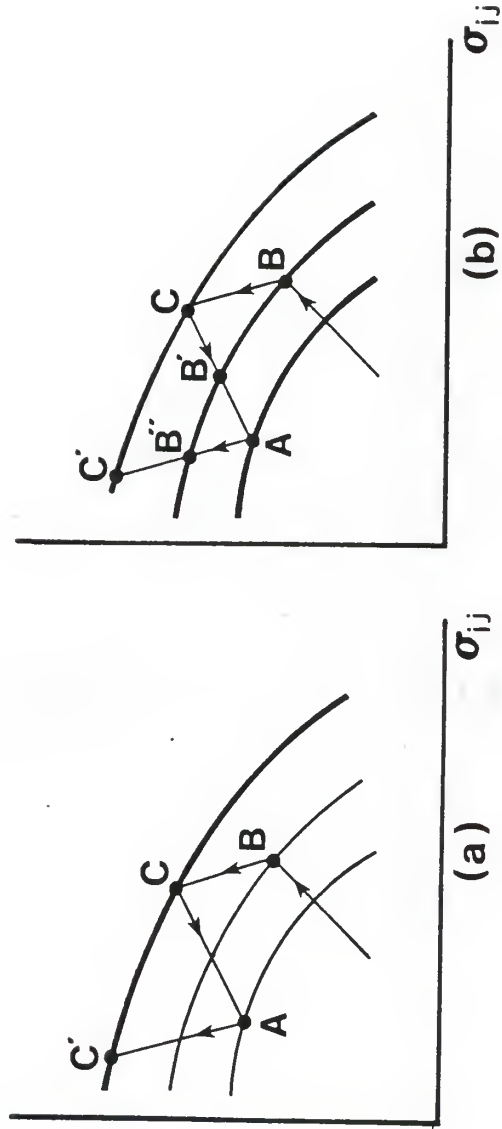


Figure 3.1 In conventional plasticity (a) path CAC' is purely elastic; in the proposed formulation (b) path $CB'A$ is elastic but $AB'B'C'$ is elastic-plastic (after Drucker and Seegeram, 1986)

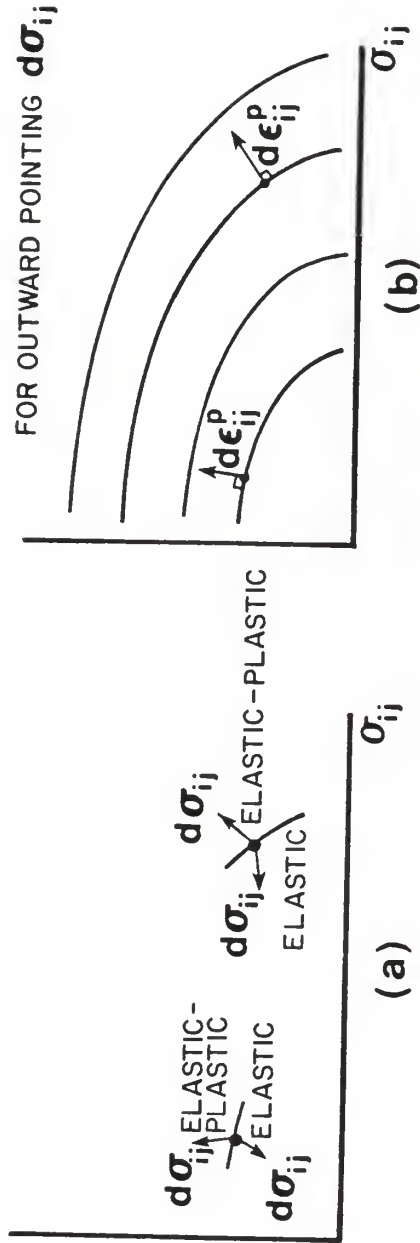


Figure 3.2 The current yield surface passes through the current stress point and locally separates the domain of purely elastic response from the domain of elastic-plastic response (after Drucker and Seegeram, 1986)

normal to the yield surface (Figure 3.2) and is calculated as

$$d\bar{\epsilon}^P = \frac{1}{K_p} \underline{n} (\underline{n}:d\underline{g}), \quad (3.1.1)$$

where K_p is the plastic modulus, \underline{n} is the unit normal to the yield surface, and $d\underline{g}$ is the stress increment (cf. equation 2.7.3.12).

4. Unlike many formulations, the consistency condition is automatically satisfied, and plays no role in the determination of the plastic modulus K_p . For the non-hardening version proposed here, K_p depends solely on the current stress state, whereas with the hardening modification, stress history effects are manifested by the evolution of an independent hardening control surface. This surface is generally not coincident with a yield surface.
5. In the simplest version, with no history dependence, the nested family of yield surfaces and scalar field of plastic moduli do not change; i.e., there is no hardening and cyclic response is immediately stable.
6. The yield surfaces are chosen so that the normal to each is constant in direction along a radial line from the origin (Figure 3.3).
7. The scalar field of plastic moduli in stress space varies from a continually increasing maximum plastic stiffness in pure hydrostatic loading to zero as the stress point approaches a stationary failure or limit surface (Figure 3.3).

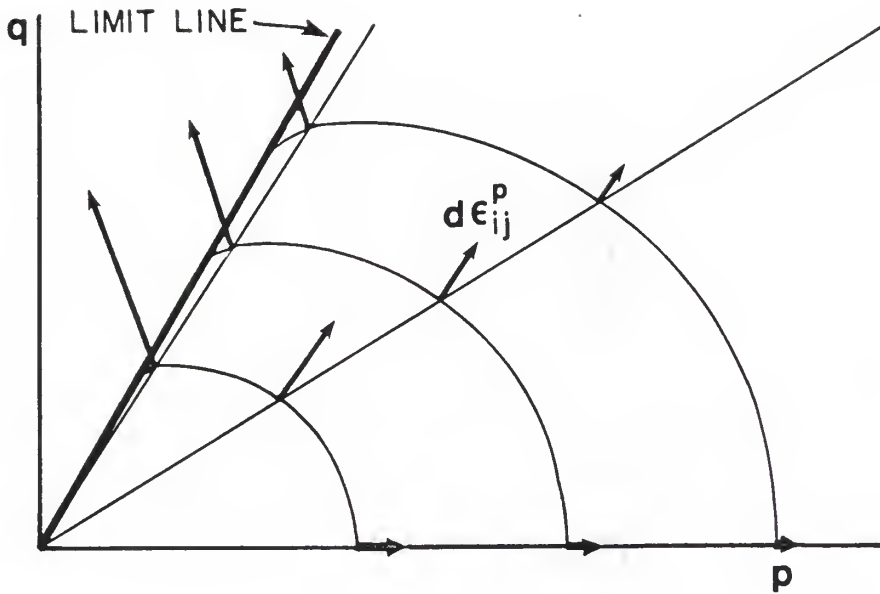


Figure 3.3 Pictorial representation for sand of the nested set of yield surfaces, the limit line, and the field of plastic moduli, shown by the $d\epsilon_{ij}^p$ associated with a constant value of $n_{pq} \frac{d\sigma_{pq}}{\sigma_{pq}}$ (after Drucker and Seereeram, 1986)

8. The limit or failure surface is also not a member of the family of yield surfaces; it intersects them at an appreciable angle (Figure 3.3).
9. No purely elastic domain of stress exists.

The first part of this chapter describes those aspects of sand behavior that suggest the use of such an unorthodox theory. Then, using well-established experimental observations on sand, detailed analytical forms are tendered for the set of yield surfaces, the scalar field of plastic moduli (which implicitly defines a limit surface), and the rule to ensure that the yield surface follows the stress point.

At the outset, it must be emphasized that these selections were not instituted after a systematic rejection of other alternatives, but they evolved during the course of development as certain features were incorporated and others, deemed less important, were deleted. It is therefore quite possible for a potential user to match data equally well or even better with an alternative set of choices. The structure of the theory does not hinge on these details.

After the analytical forms for the yield surface and the field of plastic moduli are presented, a description of the initialization procedure follows, with emphasis on the physical significance of each parameter and its expected variation with initial porosity. All model constants are then identified with a corresponding stress-strain or strength parameter (or concept) in common use by geotechnical engineers. The slope of the zero dilation line (or the friction angle at constant volume) is taken as independent of initial void ratio as found experimentally. Each of the other parameters depends only on the initial density. Two standard laboratory tests specify the material

parameters: a hydrostatic compression test and a uniaxial compression test with a small unload-reload loop to assess the elastic properties. Calculation of each of the eight constants--two elastic and six plastic--of the simple model is straightforward and can be carried out expeditiously with the aid of only a hand calculator; the procedure involves no heuristic, or curve fitting, or optimization techniques. In fact, if the elastic and plastic strains are already separated and if typical values for two less critical plastic parameters are chosen in advance, the procedure will take as little as ten minutes.

A comparison of calculated results and experiments, for a series of hollow cylinder and triaxial tests over a range of confining pressures and on materials of different origin and initial density, demonstrates the realism of the simple idealization for a wide variety of stress paths.

Two hardening modifications to the simple theory also are presented. The first is an adaptation of Dafalias and Herrmann's (1980) bounding surface theory for clays, the key characteristics of which are i) the largest yield surface established by the prior loading history acts as a boundary of "virgin" plastic moduli, and ii) a radial mapping rule is used to locate conjugate points on the boundary surface for interior stress states. These constitutive equations are implemented in a finite element routine to solve a boundary value problem of growing interest in soil mechanics, especially in the field of insitu testing, and one for which measured data was available: the expansion of a vertically embedded cylindrical cavity.

Based on the documented behavior of sand, a second more realistic hardening option is then proposed. It differs from the previous one in

that i) the hardening control surface does not resemble the yield surface, and ii) a new interpolation function for the reload modulus is implemented. The versatility of this novel formulation is explored by simulating a) the influence of isotropic preloading on an axial compression test, and b) the buildup of axial strain in a cyclic stress controlled uniaxial test.

Finally, advantages and limitations of the model are indicated; a difficulty does arise for somewhat unusual inward loading paths which start near the failure surface.

3.2 Material Behavior Perceived as Most Essential and Relevant

Those aspects of the behavior of sand (or of any material) that are identified as key aspects will vary greatly with the problems of prime interest. Furthermore, any representation of the actual complex inelastic behavior of a material is a matter of background and taste. Drastic idealization is necessary and so tends to be controversial even in those rare instances when ample experimental data are available.

For example, in the consideration of geomaterials, just as for metal polymers and composites, the simplest model suitable for generally increasing load will differ radically from the simplest model suitable for cyclic loading between fixed limits of stress or strain. The simplest model that covers both types of loading will not match some aspects of each very closely.

Adequacy of representation clearly is a matter of viewpoint and judgement. The aspects selected here as the key aspects of the inelastic behavior of sands are

1. The existence of an essentially path-independent (stationary) limit or failure surface that bounds the reachable states of stress (Figure 3.4). This surface more or less resembles the Mohr-Coulomb criterion on the octahedral plane, but it may exhibit some degree of curvature (or deviation from a pure friction criterion) on meridional (or q - p) sections. Studies by Wu, Loh, and Malvern (1963), Bishop (1966), and more recently, by Matsuoka and Nakai (1974), Lade and Duncan (1975), Desai (1980), and Podgorski (1985) are among the many on which this assumption is based.
2. A generally outward path of loading from a state of hydrostatic pressure to the limit or failure surface will induce inelastic volume contraction to start. The incremental inelastic volume change will go to zero at a stress point fairly close to but clearly below failure. Then as the stress increases toward failure (peak stress) in a stable manner, there will be appreciable continuing dilation. The stress-strain data of Figure 3.5, taken from a recent conference paper by Hettler et al. (1984), illustrates this phenomenon for axial compression tests on sand specimens over a range of initial densities.
3. The response to partial unloading is dominantly elastic, while the response to reloading is dominantly inelastic as well as elastic (Figure 3.6). It is this inelastic response on reloading at stress levels (defined by q/p) below those reached on the prior loading that led many years ago to proposals of nested set of yield surfaces with an innermost surface of small diameter and more recently to bounding surface models.

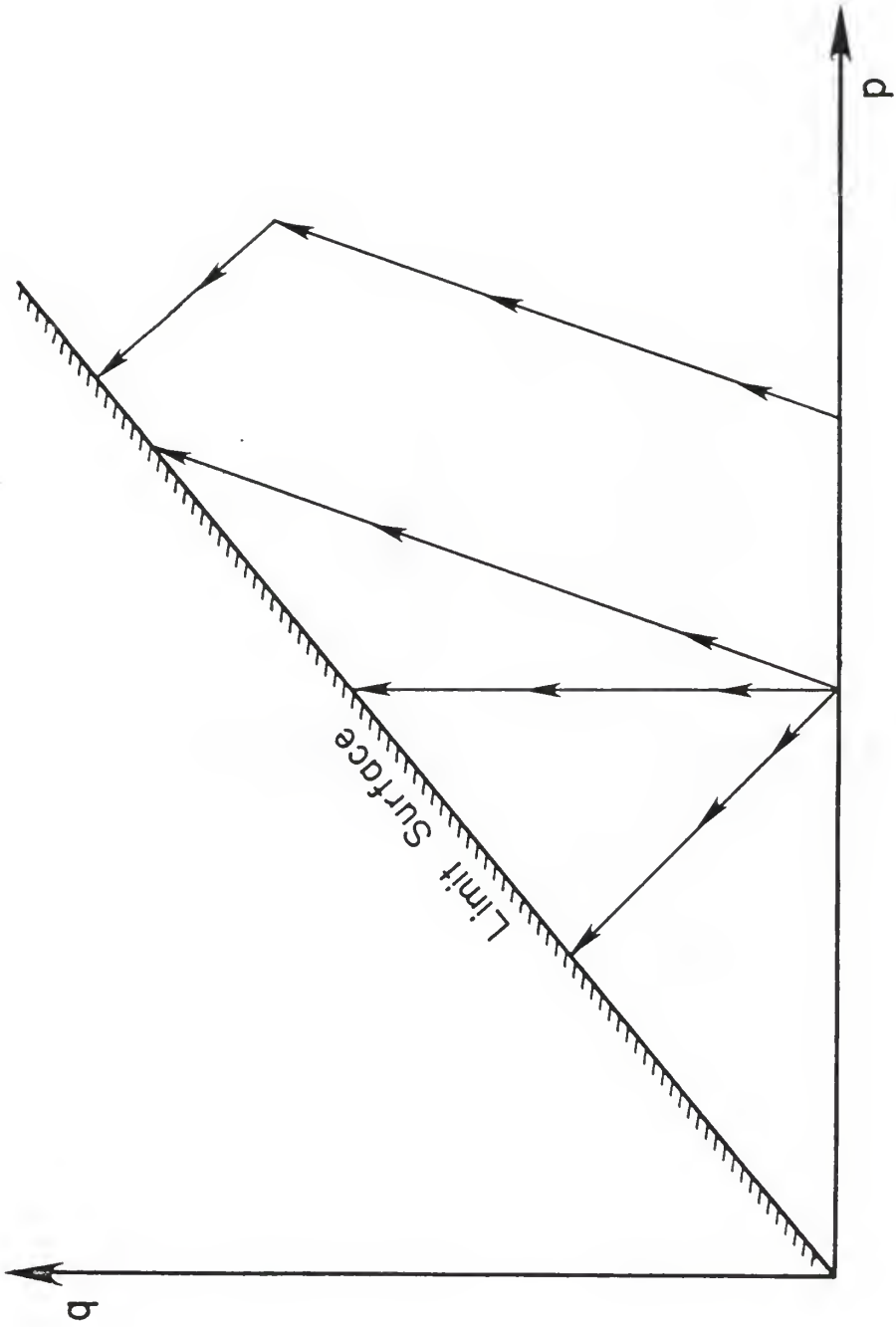


Figure 3.4 Path independent limit surface as seen in q-p stress space

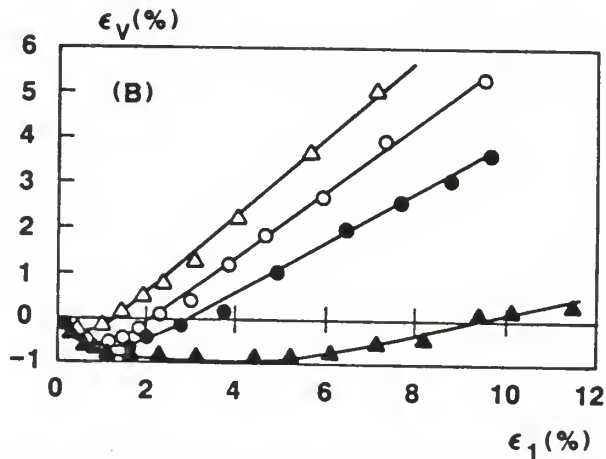
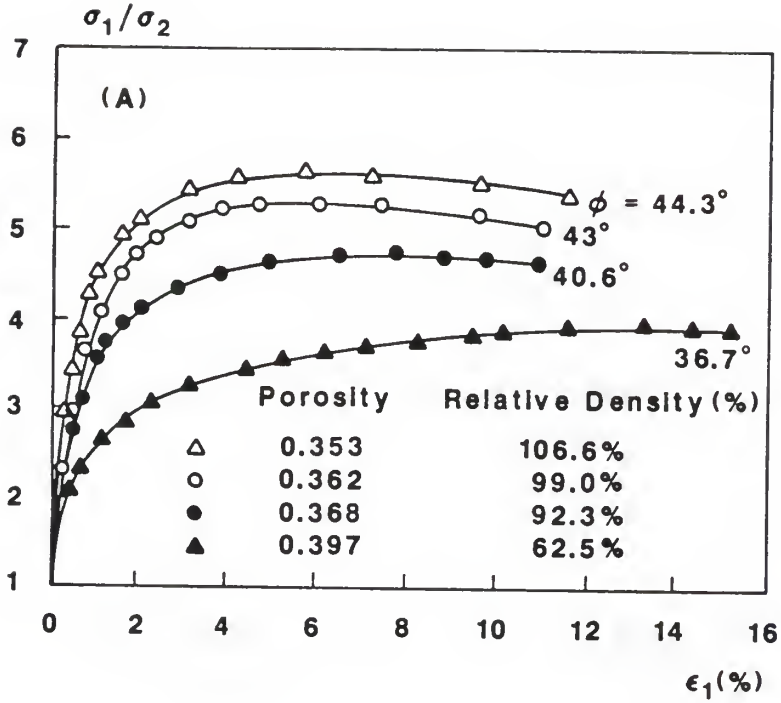


Figure 3.5 Axial compression stress-strain data for Karlsruhe sand over a range of porosities, and at a constant confinement pressure of 50 kN/m^2 (after Hettler et al., 1984)

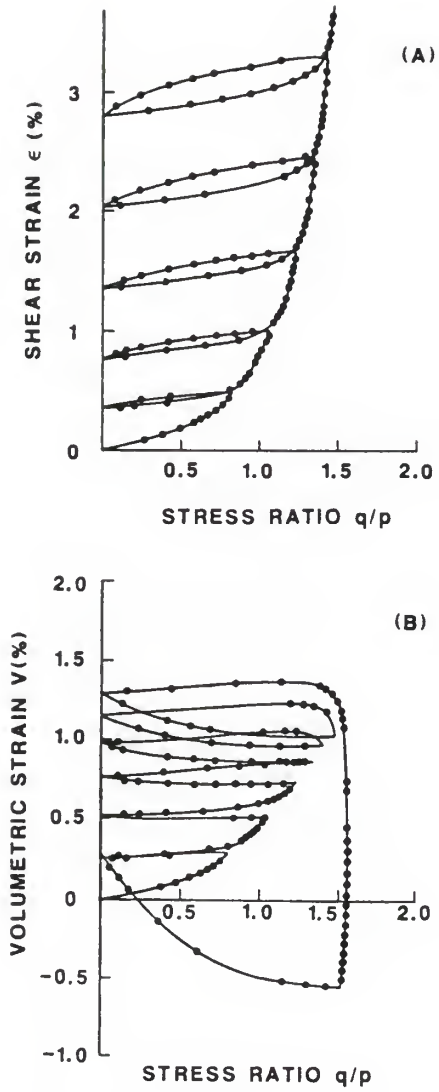


Figure 3.6 Stress-strain response for a cyclic axial compression test on loose Fuji River sand (after Tatsuoka, 1972)

4. The inelastic response in subsequent extension testing is not altered much by moderate prior inelastic deformation in the compression test regime, as the data of Tatsuoka and Ishihara (1974a) in Figure 3.7 suggests.
5. The ratios of the components of the increments of inelastic strain remain fairly constant along each radial or proportional ($q/p = \text{constant}$) loading path in stress space. Data presented by Poorooshasb et al. (1966) (Figure 3.8), and Tatsuoka (1972) substantiate this contention. Implicit in this premise is the existence of a radial, path-independent zero dilation line, and experimental studies by Kirkpatrick (1962) and Habib and Luong (1978) have confirmed the existence of such a line.
6. At a given stress point, the ratios of the components of the inelastic strain increments are the same for all outward loading paths through the point (Poorooshasb et al., 1966) (Figure 3.9). This aspect of sand behavior has not always been found. For example, in comparing constant pressure shear paths and radial loading paths, Tatsuoka (1972) noticed some degree of stress path influence on the direction of the plastic strain increment. But this divergence he found was more pronounced at lower (and thus less critical) stress levels.
7. Except at very high magnitudes of stress where particle crushing becomes important, the stress-strain response of sand in hydrostatic compression is of the "locking" type: the incremental pressure-volume response becomes stiffer with increasing levels of bulk stress (Figure 2.2).

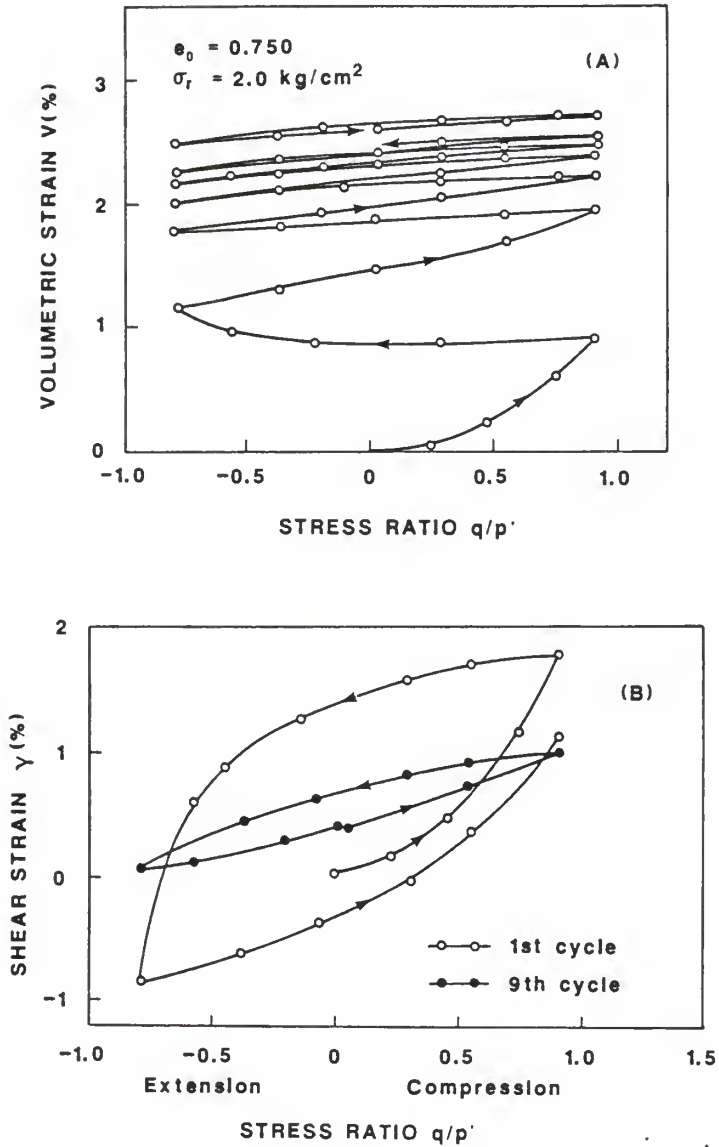


Figure 3.7 Medium amplitude axial compression-extension test on loose Fuji River sand (after Tatsuoka and Ishihara, 1974a)

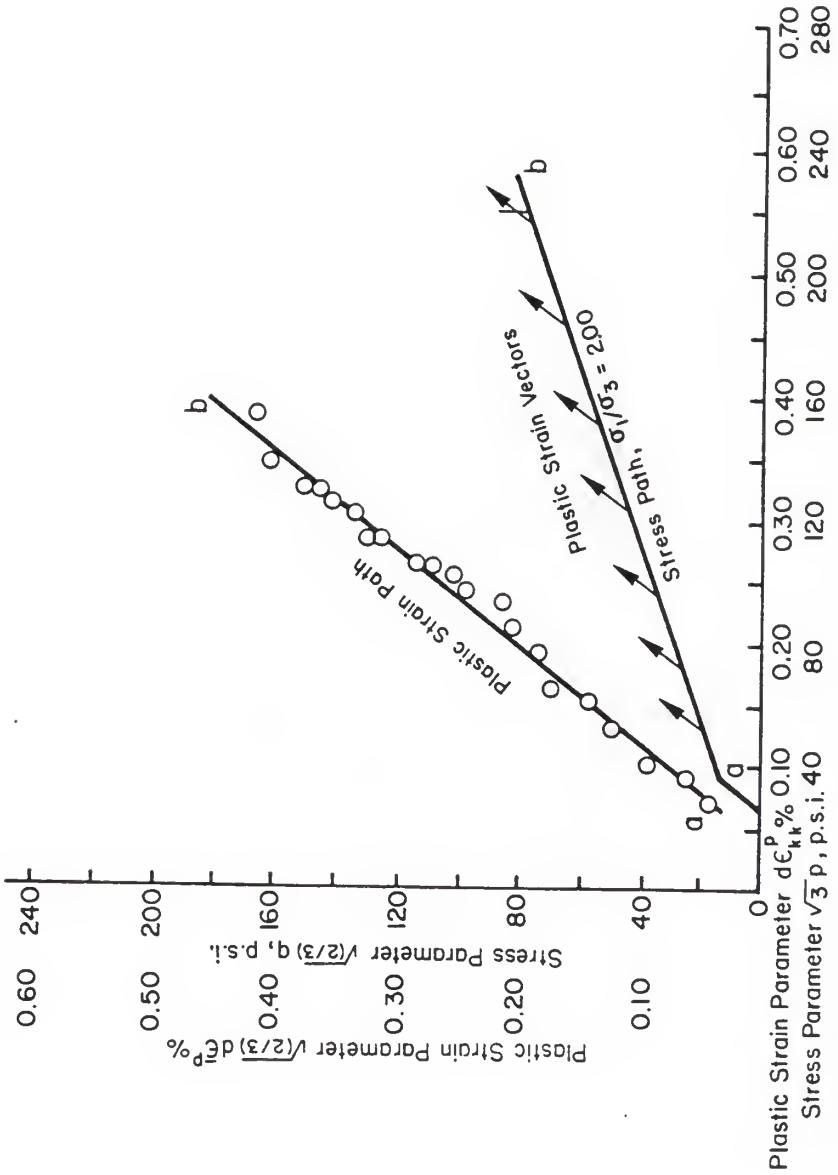


Figure 3.8 Plastic strain path obtained from an anisotropic consolidation test (after Porooshah et al., 1966)

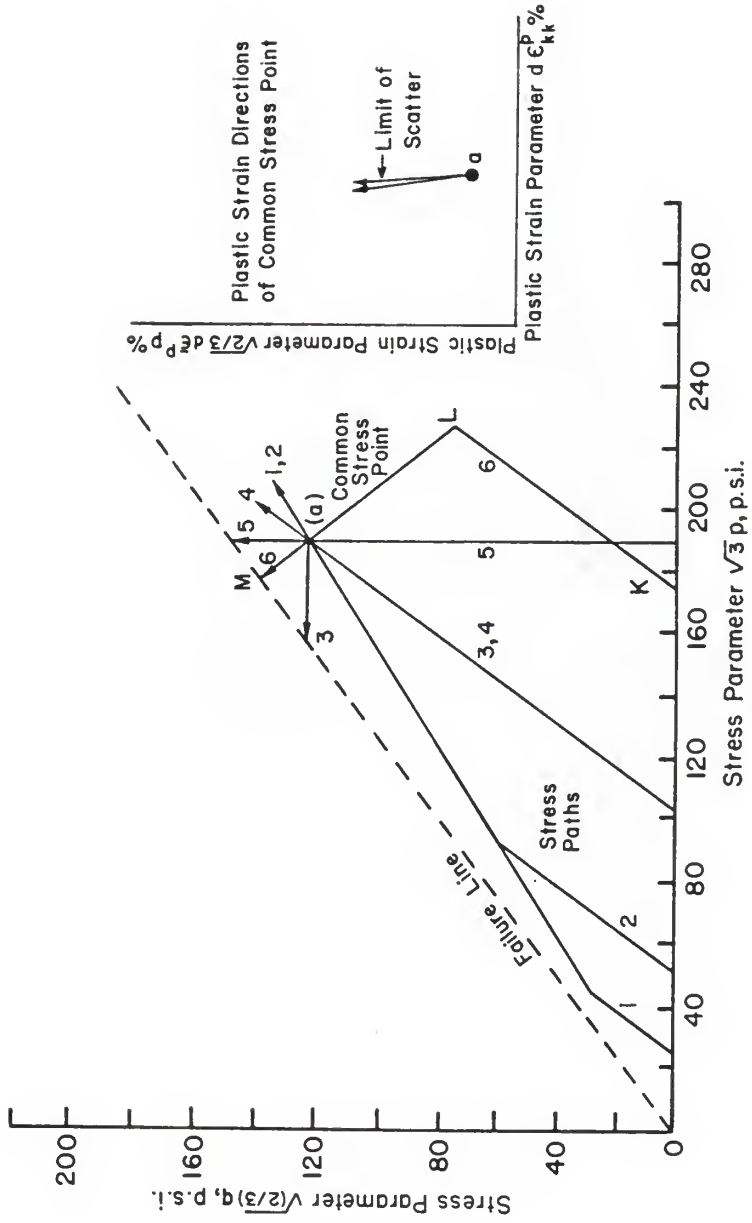


Figure 3.9 Plastic strain direction at common stress point (after Poorooshasb et al., 1966)

8. At a constant all-around pressure, the overall stiffness of the sand decreases as the intensity of the shear stress increases.

Much of the recent literature on constitutive relations for granular media, quite appropriately, is devoted to the proper characterization of the state of the material and the change in state. However, as a first approximation, the simple form of the proposal implemented here postulates that the state of the material is unchanged by the inelastic deformation. This hypothesis is a special case of what Cherian et al. (1949), in their study of commercially pure aluminium, termed orthorecovery: the reloading curve, for the uniaxial case, is finitely displaced from and parallel to the original curve (Figure 3.10).

In the application to sands, such a formulation does automatically give those key aspects of the inelastic behavior labelled 3, 4, and 6. Simple and appropriate choices of the scalar field of plastic moduli and the field of yield surfaces permit matching the failure surface (aspect 1) and produce the type of inelastic behavior labelled 2, 5, 7 and 8.

3.3 Details of the Yield Function And Its Evolution

The analytical representation of the yield surface is guided strongly by experimental observations, and to a lesser extent by some certain very helpful mathematical simplifications. But before going into these details, it is instructive to remind the reader that yielding, in this context, is the existence of a plastic strain increment vector (Figure 3.2) no matter how small and is not defined by the traditional offset or Taylor-Quinney (1931) methods.

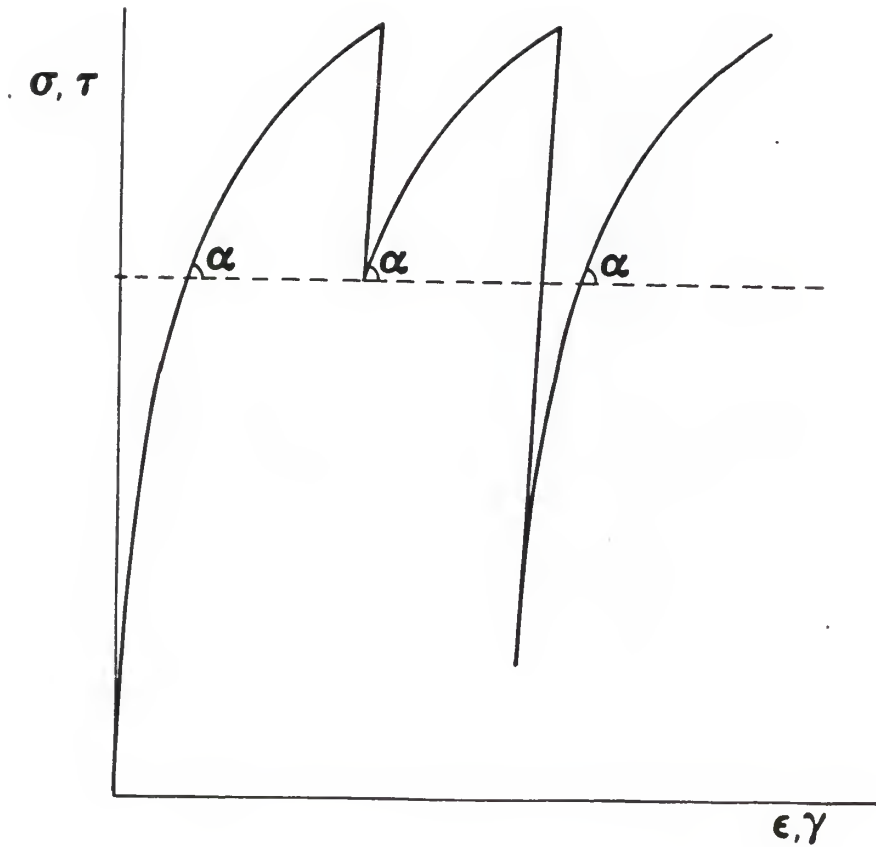


Figure 3.10 Successive stress-strain curves for uniaxial stress or shear are the initial curve translated along the strain axis in simplest model (after Drucker and Seereeram, 1986)

3.3.1 Isotropy

The soil is assumed to be isotropic, and thus the yield function may be expressed solely in terms of the stress invariants. A cylindrical coordinate system in Haigh-Westergaard (or principal) stress space is particularly attractive because a simple geometrical interpretation can be attached to each of the following invariants:

$$I_1 = \sigma_{kk} = 3 p, \quad (3.3.1.1)$$

$$\sqrt{J_2} = \sqrt{\left(\frac{1}{2} s_{ij} s_{ij}\right)} = q/\sqrt{3}, \text{ and} \quad (3.3.1.2)$$

$$\theta = \sin^{-1} \left[\frac{\sigma_1 + \sigma_3 - 2 \sigma_2}{2 \sqrt{3 J_2}} \right], \quad -30^\circ \leq \theta \leq 30^\circ. \quad (3.3.1.3)$$

These invariants were defined previously in equations 2.2.2.22, 2.2.2.26, and 2.2.2.39 respectively, and are repeated and renumbered here for easy reference.

With such an isotropic representation, the general six dimensional form of the yield surface simplifies to (cf. equation 2.7.2.3)

$$F(I_1, \sqrt{J_2}, \theta) = 0. \quad (3.3.1.4)$$

This depiction is reduced further to two dimensions by normalizing $\sqrt{J_2}$ with a function of θ , say $g(\theta)$, to obtain a modified octahedral shear stress,

$$\sqrt{J_2}^* = \sqrt{J_2} / g(\theta) = q^* / \sqrt{3}. \quad (3.3.1.5)$$

The function $g(\theta)$ is such that $g(30^\circ) = 1$ and it determines the shape of the π -section. For instance the Mohr-Coulomb relation, equation 2.7.2.5, gives

$$g(\theta) = \frac{\cos(30^\circ) - \{[\sin(30^\circ) \sin \phi]/\sqrt{3}\}}{\cos \theta - \{(\sin \theta \sin \phi)/\sqrt{3}\}}$$

which defines a straight line with corners occurring at $\theta = \pm 30^\circ$ as shown in Figure 2.9. To avoid these corners, continuous functions are chosen such that

$$\frac{dg(\theta)}{d\theta} = 0 \quad \text{at} \quad \theta = \pm 30^\circ.$$

Such functions can be written in polynomial or trigonometric form.

Taking $g(30^\circ) = 1$ and $g(-30^\circ) = R$, Willam and Warnke (1974) suggest an elliptic expression of the form

$$g(\theta) = \frac{(1-R^2) A + (2R-1) \sqrt{[(2+B)(1-R^2) + 5R^2 - 4R]}}{(2+B)(1-R^2) + (1-2R)^2} \quad (3.3.1.6)$$

where

$$A = \sqrt{3} \cos \theta - \sin \theta,$$

$$B = \cos 2\theta - \sqrt{3} \sin 2\theta,$$

and R specifies the ratio of the radius $[\sqrt{(2J_2)}]$ in extension to that in compression. For convexity, R must lie in the range

$$0.5 \leq R \leq 2.$$

Selecting

$$R = \frac{3 - \sin \phi}{3 + \sin \phi} \quad (3.3.1.7)$$

in the function $g(\theta)$ ensures that the smooth deviatoric locus matches the Mohr-Coulomb criterion in compression and extension. Equation

3.3.1.7 may be derived directly from equations 2.7.2.9 and 2.7.2.10.

Although this choice is made here for convenience, other magnitudes of R may generally be determined from experiment. Furthermore, observe that with $R = 1$, the yield surface becomes a Drucker-Prager (1952) or extended von Mises criterion.

A simpler alternative to equation 3.3.1.6 was proposed by Gudehus (1973),

$$g(\theta) = \frac{2R}{(1+R) - (1-R) \sin 3\theta}, \quad (3.3.1.8)$$

but this function suffers from the unrealistic constraint that R must be greater than 0.77 (or $\phi < 23^\circ$) to ensure convexity.

With the introduction of this modified second invariant $\sqrt{J_2^*}$, the form of the isotropic yield surface is now written as

$$F(I_1, \sqrt{J_2^*}) = 0. \quad (3.3.1.9)$$

3.3.2 Zero Dilation Line

An important aspect of the theory is the existence of a zero dilation radial line in $\sqrt{J_2^*}$ - I_1 (or q - p) space, say of slope N in $\sqrt{J_2^*}$ - I_1 space,

$$\frac{\sqrt{J_2^*}}{I_1} = N. \quad (3.3.2.1)$$

Ascribing special significance to this locus is not without merit because many laboratory investigations on the behavior of sand have confirmed its existence. Perhaps most noteworthy, Habib and Luong (1978) and Luong (1980), using a number of careful experiments, have studied this phenomenon which they termed the "characteristic state." It is similar and probably identical to the "phase transformation line" observed by Ishihara et al. (1975) in saturated undrained experiments.

From their extensive tests, Habib and Luong (1978) concluded that the characteristic state of a soil is associated with

1. a zero volumetric strain rate ($\dot{\epsilon}_{kk} = 0$),
2. a unique stress level (q/p) where net interlocking ceases and effective disruption of interlocking starts,
3. a relatively low distortion deformation ($\bar{\epsilon}$),

4. an independence of the initial porosity and the grain size distribution, and
5. an absence of the influence of fabric anisotropy and stress history.

In addition, their data shown in Figure 3.11 suggests that the projection of the characteristic state curve on the q - p plane is practically a straight line passing through the origin of stress space, even though the limit envelope may be highly non-linear along the pressure axis. This may be verified by locating the points on the volumetric strain vs. axial strain plots (bottom of Figure 3.11) where the incremental volumetric strain is zero and then finding the corresponding points on the σ_1/σ_3 vs. axial strain plot at the top of Figure 3.11; these zero dilation points all approximately give the same stress level (σ_1/σ_3). Other data presented by Habib and Luong (1978) suggests that the deviatoric variation of the zero dilation line mathematically built into equation 3.3.2.1 does not agree with reality. This equation suggests that the mobilized friction angles at the point of zero dilatancy in compression and extension are the same, or that the deviatoric traces of the zero dilation and the failure loci are concentric. Figure 3.12 presents data from Habib and Luong's (1978) paper which indicates this is not strictly true: $\phi = 24.6^\circ$ in extension vs. 32.5° in compression. If in later applications this turns out to be a serious limitation of the model, it may be very easily remedied by selecting an experimentally determined magnitude of R to normalize the zero dilation line in $\sqrt{J_2^*}$ - I_1 stress space and another magnitude to normalize the failure locus. Such an improvement will require at least one additional material parameter.

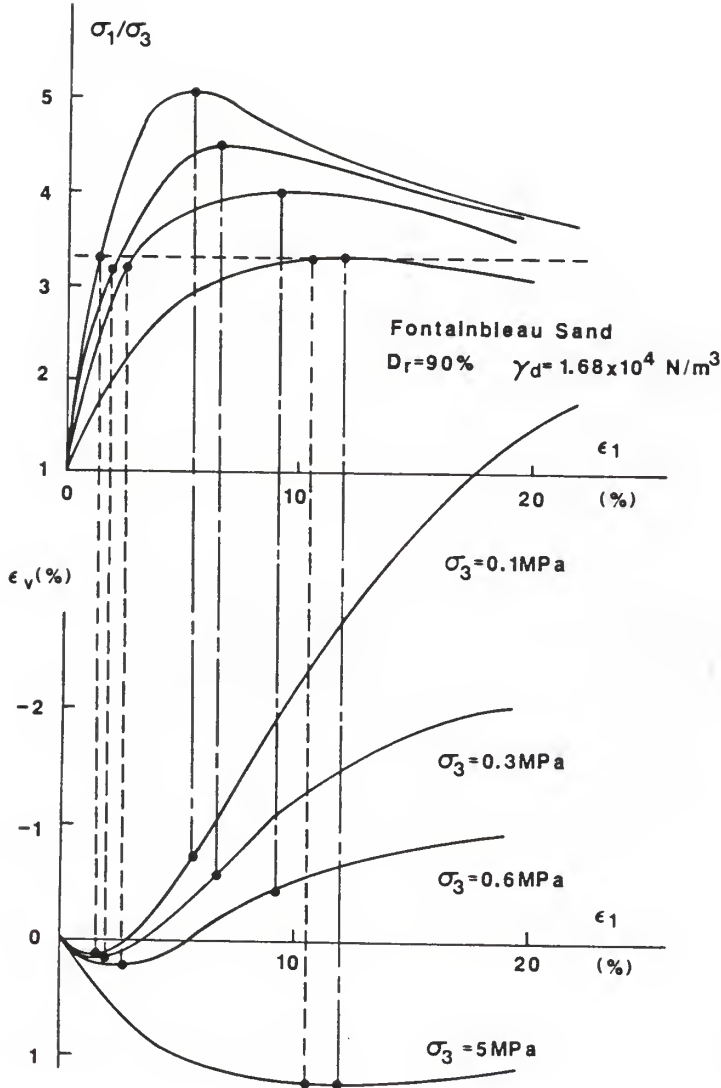


Figure 3.11 Constant q/p ratio (as given by constant σ_1/σ_3 ratio) at zero dilation as observed from axial compression stress-strain curves on dense Fontainebleau sand. Note that the peak stress ratio decreases with increasing pressure (after Habib and Luong, 1978)

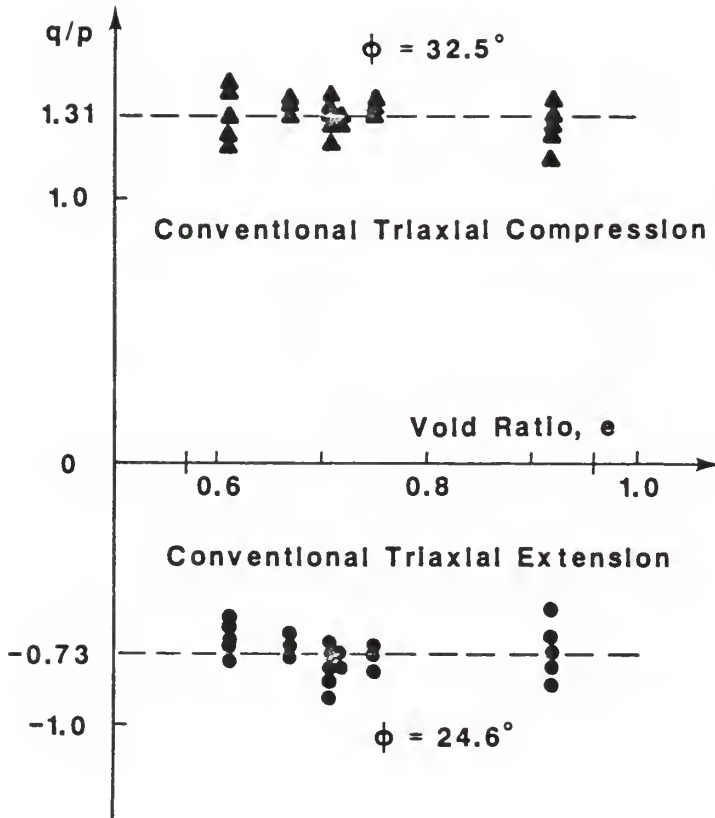


Figure 3.12 Characteristic state friction angles in compression and extension are different, suggesting that the Mohr-Coulomb criterion is an inappropriate choice to model the zero dilation locus (after Habib and Luong, 1978)

For comparison, the differences between the concept of characteristic state and the more familiar critical state concept (Schofield and Wroth, 1968) are highlighted in Table 3.1.

Two analytic functions are used to describe the yield surface: one for the region below the zero dilation line, in the sub-characteristic domain, and another for the region between the zero dilation line and the limit line, in the super-characteristic domain. These two portions of the yield surface are chosen to be continuous and differentiable at the zero dilation locus.

3.3.3 Consolidation Portion of Yield Surface

From the isotropy assumption, pure plastic volumetric strain must be predicted for an isotropic compression path. Therefore, a smooth yield surface must intersect the hydrostatic axis perpendicularly, and by a similar reasoning, it must also be parallel to the hydrostatic axis at the zero dilation line.

Figure 3.13 shows plots of smooth yield surfaces back-fitted from the trajectory of plastic strain increments observed from a series of axial compression tests on Ottawa sand (Poorooshasb et al., 1966).

Guided by these pictures, the meridional section of the yield surface below the zero dilation line ($\sqrt{J_2^*/I_1} \leq N$) was chosen to be an ellipse

$$F = I_1^2 - 2(I_0/Q) I_1 + [(Q-1)/N]^2 J_2^* + I_0^2 [(2/Q)-1] = 0, \quad (3.3.3.1)$$

where I_0 is its point of intersection with the I_1 axis, and Q is a parameter which controls the major to minor axis ratio of the ellipse.

Figure 3.14 shows a plot of this yield surface in q^* - p space; note the mathematical interpretation of the parameter Q in this figure. Figure 3.15 gives an alternate view of the yield surface on the triaxial plane

Table 3.1 Comparison of the Characteristic State and Critical State Concepts

PROPERTY	CHARACTERISTIC STATE	CRITICAL STATE
1. Volume variation	$\dot{\epsilon}_v = 0$ at any \dot{q}	$\dot{\epsilon}_v = 0$ at $\dot{q} = 0$
2. Shear Strain, $\bar{\epsilon}$	low (prior to failure)	indeterminate (at failure)
3. Deformation	small	large
4. Void Ratio (e)	any e	e_{critical}
5. Grain Structure	maximum "locking" effect	uncertain
6. Loading	monotonic or cyclic	monotonic, asymptotic
7. Behavior	transitory	asymptotic
8. Definition	threshold demarcating contractancy and dilatancy domains	idealized concept of soil
9. Experimental Determination	direct therefore easy	by extrapolation therefore delicate

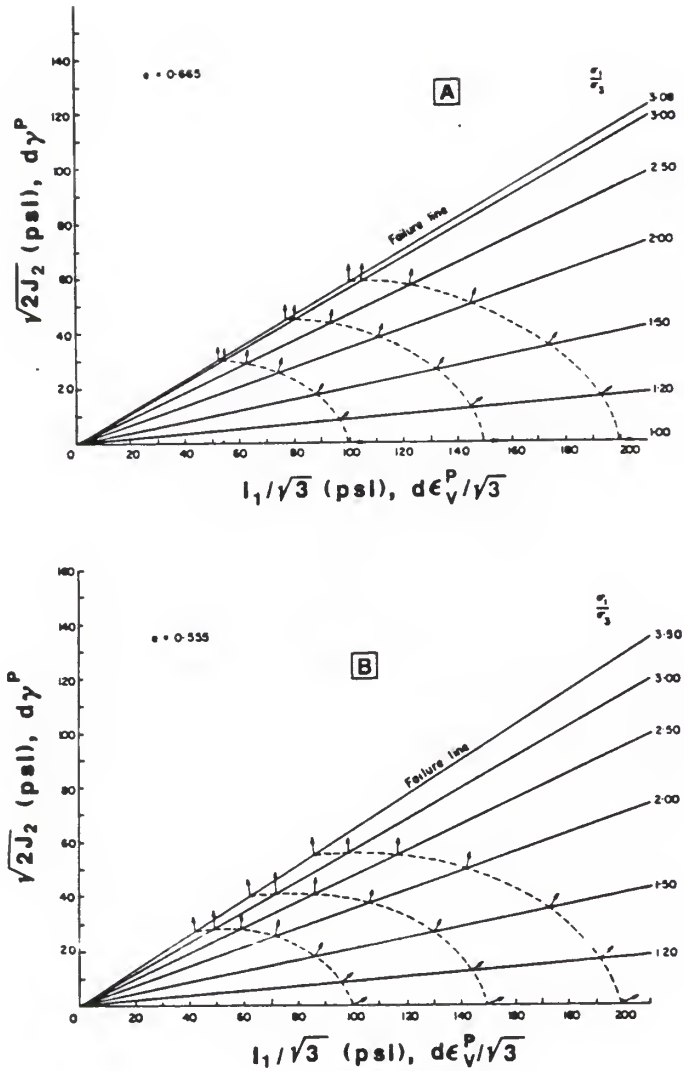
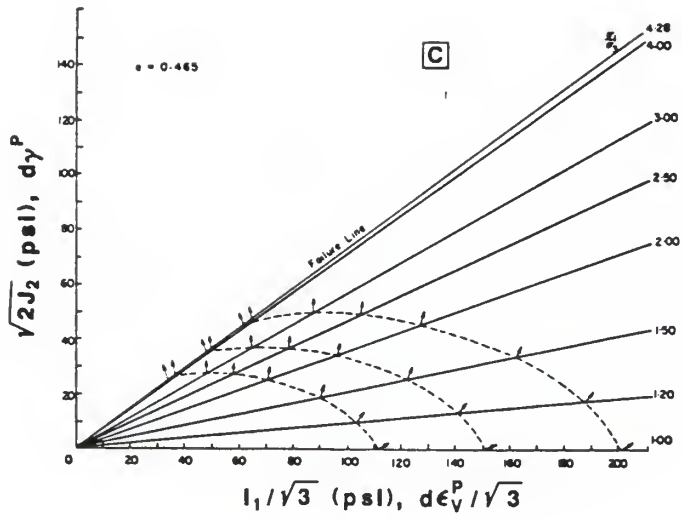


Figure 3.13 Establishment of the yield surfaces from the inclination of the plastic strain increment observed along axial compression paths on Ottawa sand at relative densities of (a) 39% ($e=0.665$), (b) 70% ($e=0.555$), and (c) 94% ($e=0.465$) (after Poorooshasb et al., 1966)



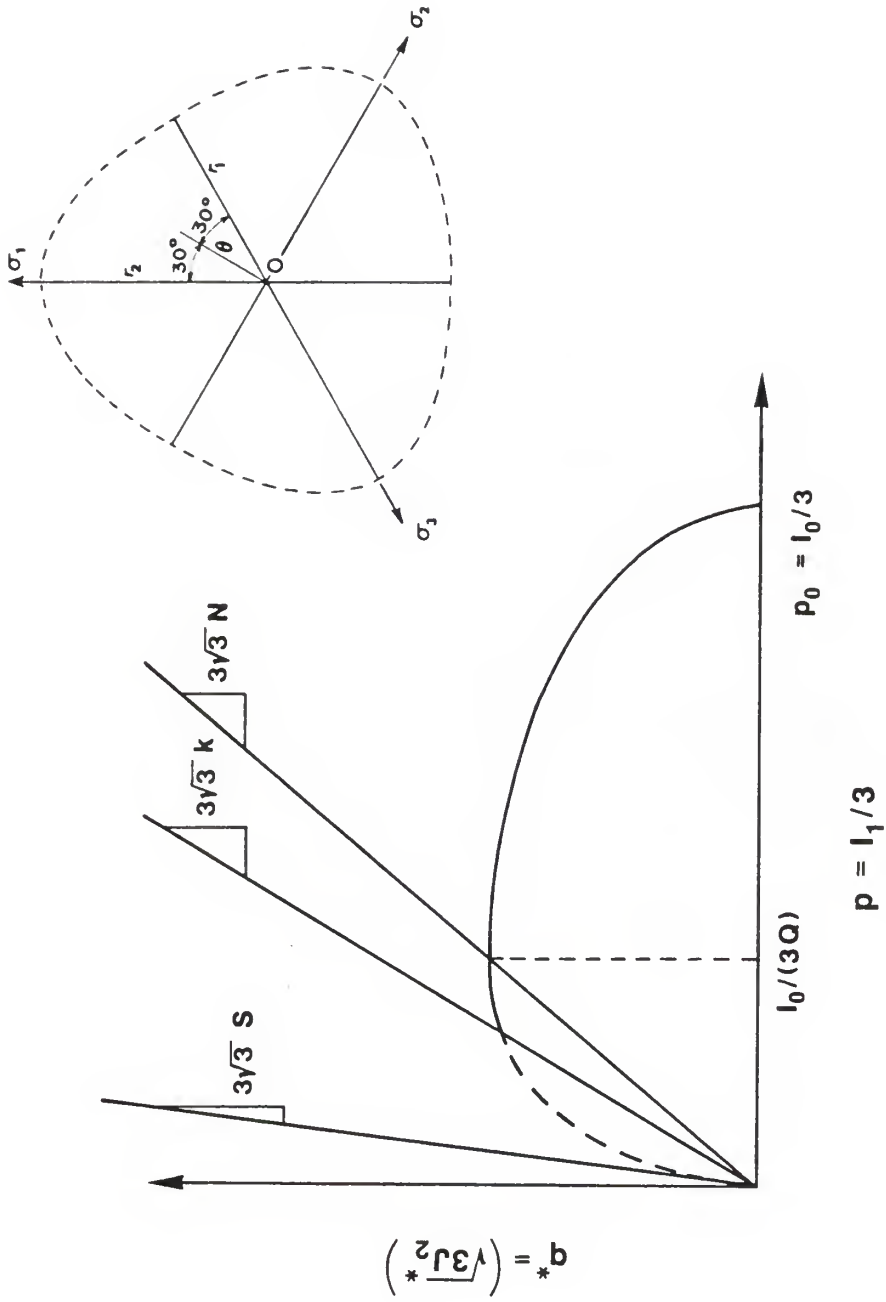


Figure 3.14 Typical meridional (q^*-p) and octahedral sections (inset) of the yield surface

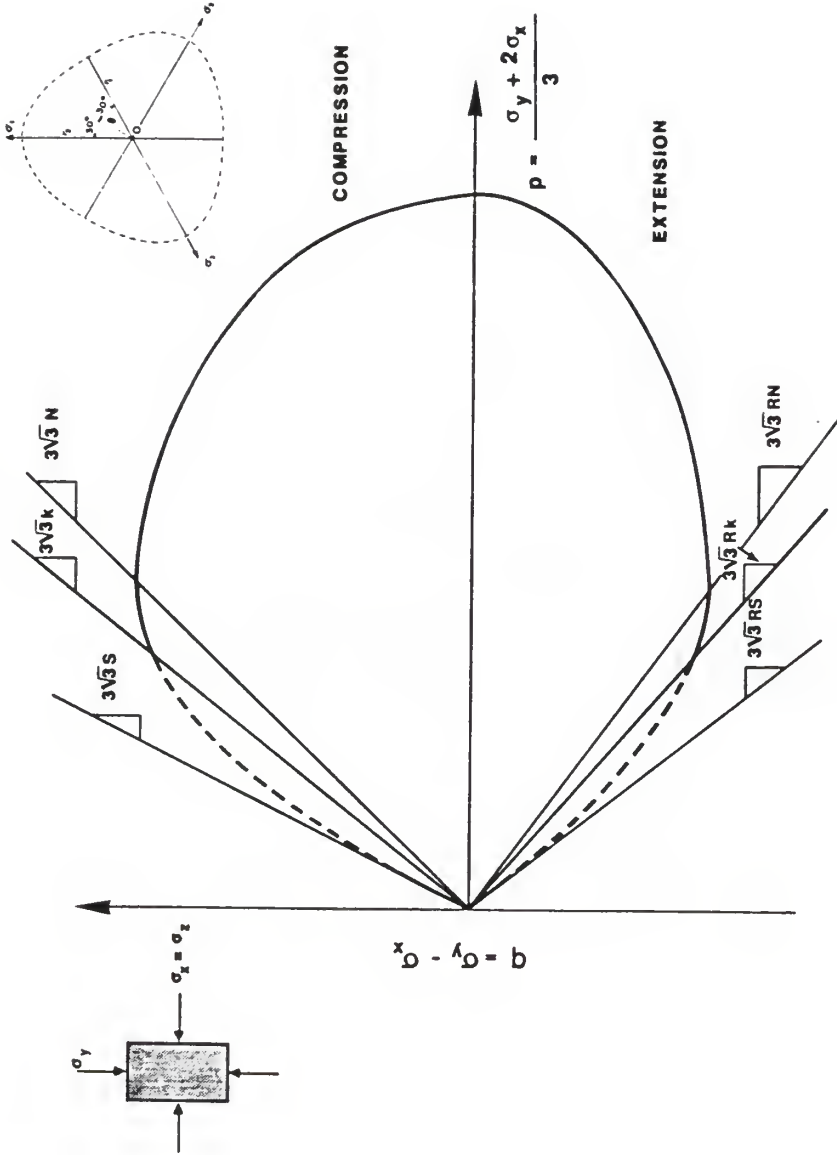


Figure 3.15 Trace of the yield surface on the triaxial q - p plane

with material reference coordinates. This choice of the yield function is by no means original. Roscoe and Burland (1968) derived a particular form of this equation for their modified Cam-Clay theory in which the parameter Q was fixed at a magnitude of two so that

$$F = I_1^2 - I_0 I_1 + (1/N)^2 J_2^* = 0. \quad (3.3.3.2)$$

However, in this work, Q is retained as a material parameter to enhance the simple model's ability to predict the compaction phenomenon.

Magnitudes of Q reckoned from Poorooshasb's plots (Figure 3.13) are 1.75, 1.77, and 2.06 for Ottawa sand at 39%, 70%, and 94% relative density respectively, so if only a crude estimate is desired, it is not unrealistic to assume $Q = 2$. Theoretically and in general, however,

$$1 \leq Q \leq \infty. \quad (3.3.3.3)$$

3.3.4 Dilation Portion of Yield Surface

The yield surface's meridional segment above the zero dilation line intersects the limit or failure curve at an angle which has no obvious physical basis (Figure 3.3). This angle plays no role in theory and therefore offers no useful mathematical link between the yield surface and the limit surface. Nevertheless, the limit line does serve to delineate the real from the unreachable part of the dilation portion of the yield surface since the analytical form of the yield surface does not terminate abruptly at the limit line. In Figure 3.14, the real part of the dilation portion of the yield surface is the solid curve bounded by the zero dilation and limit lines, while the unreachable part is the dashed portion beyond the limit line.

A second order polynomial in $\sqrt{J_2^*} - I_1$ stress space was developed specifically for this portion of the surface. Constraints were imposed

to ensure that i) the surface passes through the origin of $\sqrt{J_2^*} - I_1$ stress space at a specified slope S , and ii) its first partial derivatives merge continuously with the half-ellipse at the zero dilation line. The first requirement is an artifact of an earlier phase in the study (Seereeram et al., 1985) when it was thought that the slopes of the limit line and the yield surface should coincide at points on the limit line. However, in the version here, the slope S is fixed at a slope much steeper than the limit line to give more leverage in choosing the dilation portion of the yield surface to model plastic flow.

The proposed yield surface for the dilation domain ($\sqrt{J_2^*}/I_1 > N$) is

$$F = I_1^2 + b J_2^* + \left[\frac{S}{N^2} - \frac{2}{N} - S b \right] I_1 \sqrt{J_2^*} + (I_0/Q) \left[\frac{1}{N} - bN \right] [\sqrt{J_2^*} - S I_1] = 0, \quad (3.3.4.1)$$

where b is a dimensionless material parameter. A detailed derivation of this equation and the restriction on the parameter " b " are presented in Appendix A.

From limited experience with this new yield surface, a preselected magnitude of S equal to 1.5 appears to work well. For reference, note that the slope of the limit line ($\sqrt{J_2^*}/I_1$ at failure) is typically in the range 0.20 to 0.35.

The constant b is constrained to be less than $\frac{1}{N^2}$, and the discriminant of equation 3.3.4.1,

$$\left[\frac{S}{N^2} - \frac{2}{N} - Sb \right]^2 - 4b, \quad (3.3.4.2)$$

identifies the canonical form of the surface. With $S = 1.5$, the back-computed dilation portion of the yield surface usually turns out to be elliptical.

For completeness, the yield surface gradient tensor equations are included in Appendix B.

3.3.5 Evolutionary Rule for the Yield Surface

To remain at yield during loading and unloading, the yield surface is assumed to contract and expand isotropically to stay with the stress point. This rule was selected because it produces many desirable features, among which are

1. successive yield surfaces remain similar, as the data of Figure 3.13 suggest;
2. a unique zero dilation line is preserved for all loading paths, and more generally, the ratio of the components of the plastic strain increment vector remain constant for radial lines;
3. mathematical tractability; and
4. it can be readily modified to give "bounding surface" type hardening rules.

Since, in this theory, no elastic domain is postulated, plastic strains can occur at any stress level, and there are no restricted (or elastic) zones to impede the movement of the yield surface. The size of the yield surface is given by its intersection I_0 with the hydrostatic axis (Figure 3.14). Once the current state of stress is known, I_0 can be solved for directly from equation 3.3.3.1 if the stress point is below the zero dilation line, or from equation 3.3.4.1 if it is above. Thus, in effect, the consistency condition is automatically satisfied. If it is postulated that the yield surface does not follow the stress

point on unloading, this evolutionary rule degenerates to that of a conventional stress-hardening theory of plasticity.

The equations for updating I_0 are presented in Appendix C.

3.4 Choice of the Field of Plastic Moduli

The expected magnitude and variation of the plastic modulus along three lines in $\sqrt{J_2^*}-I_1$ stress space dictated the choice of the field of plastic moduli:

1. the hydrostatic axis,
2. the zero dilation line, and
3. the failure or limit line.

Each of these three loading paths is now explored in sequence.

Consider a pure hydrostatic or spherical loading on an isotropic material with a yield function $F(\sqrt{J_2}, I_1) = 0$. Since such a path must produce only volumetric strain, $\partial F/\partial I_1$ is the only non-zero gradient component, and the flow rule (equation 3.1.1) therefore specializes to

$$d\epsilon_{kk}^p = \frac{1}{K_p} \frac{\partial F/\partial I_1 (\partial F/\partial I_1 dI_1)}{(\partial F/\partial I_1)^2} = \frac{1}{K_p} dI_1. \quad (3.4.1)$$

A comparison of this equation with its elastic analogue (equation 2.6.1.12),

$$d\epsilon_{kk}^e = \frac{1}{3K} d\sigma_{kk},$$

shows that the plastic modulus K_p is analogous to three times the elastic bulk modulus (K) for hydrostatic compression.

Following a similar development, we find that at a point of zero dilation,

$$\partial F/\partial I_1 = 0,$$

$$\partial F / \partial \sqrt{J_2} \neq 0,$$

and therefore

$$de_{ij}^p = \frac{1}{K_p} \frac{\partial F / \partial \sqrt{J_2} s_{ij} (\partial F / \partial \sqrt{J_2}) (s_{mn} ds_{mn})}{4 J_2 (\partial F / \partial \sqrt{J_2})^2} = \frac{1}{K_p} \frac{s_{ij} s_{mn} ds_{mn}}{2 J_2},$$

from which we then see that

$$\sqrt{\frac{1}{2} de_{ij}^p de_{ij}^p} = \frac{1}{K_p} \frac{s_{mn} ds_{mn}}{2 \sqrt{J_2}} = \frac{1}{K_p} d(\sqrt{J_2}),$$

or

$$d\bar{\epsilon}^p = \sqrt{\frac{3}{2} de_{ij}^p de_{ij}^p} = \frac{1}{K_p} dq. \quad (3.4.2)$$

Comparing this equation with its elastic analog (equation 2.6.1.13)

shows that K_p is comparable to twice the elastic shear modulus (G) at the zero dilation line. Mathematically, this means that at the point of zero dilatancy

$$\frac{1}{K_p} = \frac{1}{dq/d\bar{\epsilon}} - \frac{1}{2G}, \quad (3.4.3)$$

where $dq/d\bar{\epsilon}$ is the tangent modulus. Note that this is a general result not contingent on any particular choice of the yield surface.

The final case considers the magnitude of the plastic modulus at the failure line. At this locus, the material fails in the sense that the incremental plastic strains are supposedly "infinite." Therefore, in order to approach asymptotically this response at the limit state, the plastic modulus must approach zero at all points on this line (see equation 3.1.1).

The plastic modulus functions as a bulk modulus for hydrostatic loading, a shear modulus at the zero dilation line for shear loading, and a "failure" modulus (zero) on the limit surface.

With this background, a specific form is now derived for the plastic modulus on the hydrostatic axis, and an interpolation rule is then adopted to model its approach to zero at the limit surface.

The plastic modulus on the hydrostatic axis increases with mean pressure. A familiar pressure-volume relationship along this axis is assumed (cf. equation 2.7.6.7)

$$I_1 = (I_1)_i \exp(\lambda \epsilon_{kk}^p), \quad (3.4.4)$$

where $(I_1)_i$ is the magnitude of I_1 at the start of a virgin hydrostatic loading, and λ is a plastic stiffness constant. Soils engineers will recognize this equation as an alternative statement of the typical linear voids ratio vs. log mean pressure relationship. In incremental form

$$dI_1 = (I_1)_i \lambda d\epsilon_{kk}^p \exp(\lambda \epsilon_{kk}^p) = \lambda I_1 d\epsilon_{kk}^p, \quad (3.4.5)$$

which, by comparison with equation 3.4.1, shows that the plastic modulus K_p is equal to λI_1 , a linear stress-dependent function.

It is reasonable to expect the plastic stiffness to decrease monotonically from its bulk modulus magnitude (λI_1) on the hydrostatic axis to zero on the fixed limit surface

$$f(\underline{g}) = k. \quad (3.4.6)$$

A simple and not unreasonable rule for this decrease is

$$K_p = \lambda I_1 \{1 - [f(\underline{g})/k]\}^n, \quad (3.4.7)$$

in which the exponent "n" is regarded as a material constant.

Geometrically, this interpolation function forces the equi-plastic modulus loci on the octahedral plane in principal stress space to resemble the π -section of the selected failure criterion $f(\underline{g})$. As will be described later in the initialization procedure, the observed plastic

(shear) modulus at the zero dilation line provides the necessary information for computing the exponent "n" directly.

Any desired frictional failure criterion $f(\underline{\sigma})$ may be inserted in equation 3.4.7. The form chosen here is

$$\frac{\sqrt{J_2^*}}{I_1} = k. \quad (3.4.8)$$

Because one of the sands used in the evaluation had a significantly curved (along the pressure axis) failure envelope, the straight line representation was modified to

$$\frac{\sqrt{J_2^*}}{I_1} (I_1/p_a)^m = k, \quad (3.4.9)$$

to allow for non-linear pressure dependence. The exponent "m" in this equation is a material parameter that describes the degree of curvature, and p_a is atmospheric pressure in consistent units. The modifying factor $(I_1/p_a)^m$ was proposed by Lade (1977). So, in general, two parameters, "k" and "m", characterize the strength of the material, but, as discussed earlier, the parameter "R" in equation 3.3.1.6 may also be considered a model constant if no a priori assumptions are made about matching the compression and extension radii with a Mohr-Coulomb or any other criterion.

3.5 Elastic Characterization

Two elastic stress-strain relations are employed. The simpler idealization is used for simulations within a limited range of mean stress, while the more complicated option is used for stress paths which cover a wider range.

In the first alternative, the elasticity of the material is assumed to be isotropic and linear, while anisotropy and nonlinear effects are attributed to plastic deformation. The incremental elastic stress-strain relation is

$$d\epsilon_{kk}^e = d\sigma_{kk} / (3 K), \text{ and} \quad (3.5.1)$$

$$d\epsilon_{\underline{e}}^e = d\underline{s} / (2 G), \quad (3.5.2)$$

where K and G are the elastic bulk and shear moduli respectively, and $d\epsilon_{kk}^e$ and $d\epsilon_{\underline{e}}^e$ are the trace and deviatoric components respectively of the elastic strain increment $d\epsilon^e$.

For the second more complicated option, it is assumed that i) the material is elastically isotropic, and ii) the Young's modulus E depends on the minor principal stress σ_3 , as proposed by Janbu (1963). That is,

$$E = K_u p_a (\sigma_3/p_a)^r \quad (3.5.3)$$

where K_u is a dimensionless modulus number, and r is an exponent to regulate the influence of σ_3 on E . As suggested by Lade (1977), Poisson's ratio ν for sands is assumed equal to 0.2.

It is recognized that these elastic stress-strain relations are the simplest of choices, and if a more complete elastic characterization of sand is desired, degradation effects and shear stress dependency must also be included. Examples of these more sophisticated elastic idealizations have been presented by Ghaboussi and Momen (1982) and Loret (1985).

3.6 Parameter Evaluation Scheme

A hydrostatic compression test and an axial compression test furnish the data to initialize the simple model. But, since it is customary to consolidate hydrostatically a specimen prior to axial

compression, one such set of experiments can provide the necessary calibration data. Quite naturally, the initialization procedure will require more tests if certain aspects of the simple model are to be improved. For example, if the stress-dependent elastic characterization or the curved failure envelope options are included, data must be obtained from a series of, say, three axial compression tests over an appropriate range of confining pressures. Furthermore, if precise matching of the failure or the zero dilation locus on the deviatoric plane is warranted, an axial extension test or equivalent will also be needed.

Before going into the details of the parameter evaluation scheme, this is an ideal juncture to emphasize an important innate aspect of the simple theory: if the failure envelope is a straight line, the representation predicts exactly the same plastic strains for parallel stress paths which all emanate from points on the hydrostatic axis. Therefore, for instance, the theory will predict identical q/p vs. $\bar{\epsilon}^D$ (or q/p vs. ϵ_{kk}^D) curves for a series of conventional axial compression paths covering a range of confining pressures. Data will be presented later which demonstrates this intrinsic trait of the simple theory.

Material parameters are divided into three conceptually distinct groups:

1. The elastic constants: K_u and r , or K and G .
2. The plastic stiffness/strength parameters which serve to define the scalar field of plastic moduli: λ , n , and k .
3. The parameters governing the shape of the yield surface, or alternatively, the parameters governing the direction of the

plastic strain increment vector (n_{ij}) and the extent of plastic loading ($n_{ij}d\sigma_{ij}$): N , Q and b .

3.6.1 Elastic Constants

The elastic Young's modulus is determined from an unloading segment in the axial compression test,

$$E = (1 + \nu) \frac{\Delta q}{\Delta \bar{\epsilon}}, \quad (3.6.1.1)$$

where Δq is the deviatoric load reduction, $\Delta \bar{\epsilon}^e$ is the recoverable (or resilient) shear strain, and ν is Poisson's ratio assumed equal to 0.2. For the more complicated option in which E depends on the minor principal stress (equation 3.5.3), the modulus exponent r and $\log(K_u)$ are the slope and intercept respectively of a straight line fit to a plot of $\log(E/p_a)$ vs. $\log(\sigma_3/p_a)$. This data is most conveniently obtained from the unloading loops of a series of axial compression tests at different levels of confining stress (σ_3).

3.6.2 Field of Plastic Moduli Parameters

The parameter λ is matched to the stiffness of the material in hydrostatic compression (equation 3.4.4). It is simply the slope of a plot of $\log[I_1/(I_1)_i]$ vs. ϵ_{kk}^D for an isotropic consolidation test, or in terms of conventional geotechnical parameters,

$$\lambda = \log_e(10) \frac{1 + e_0}{C_c - C_s}, \quad (3.6.2.1)$$

where e_0 is the initial voids ratio, and C_c and C_s are the compression and swell indices respectively. As an aid in separating the elastic and

plastic volumetric strains, note that direct integration of equation 3.5.3 gives

$$\epsilon_{kk}^e = \frac{3(1-2\nu)(p_a)^{r-1}}{K_u(1-r)} [p^{1-r} - p_{\text{initial}}^{1-r}] \quad (3.6.2.2)$$

for a hydrostatic compression path.

The strength parameter k is the peak stress ratio $\sqrt{J_2^*/I_1}$ determined from an axial compression or any other shear path to failure. In terms of more familiar strength constants,

$$3\sqrt{3}k = (q/p)_{\text{peak}} = 6 \sin \phi_c / (3 - \sin \phi_c), \quad (3.6.2.3)$$

where ϕ_c is the friction angle computed from a compression test (cf. equation 2.7.2.9).

If the curved failure surface option is used, the exponent m and $\log(k)$ are the slope and intercept respectively of a straight line fit to a plot of $\log(\sqrt{J_2^*/I_1})_{\text{peak}}$ vs. $\log(p_a/I_1)$ for a number of tests.

At the point of zero dilatancy on the q/p vs. $\bar{\epsilon}^D$ stress-strain curve, a) the mean stress p , b) the stress ratio q/p , and c) the tangent modulus $dq/d\bar{\epsilon}$ are used to compute the slope of the zero dilation line,

$$N = \frac{(q/p)}{3\sqrt{3}} \quad (\text{at } d\epsilon_{kk}^D = 0). \quad (3.6.2.4)$$

The result is then combined with $p \Big|_{d\epsilon_{kk}^D=0}$ and $K_p \Big|_{d\epsilon_{kk}^D=0}$ (computed from equation 3.4.3) to calculate the exponent n of the interpolation function as

$$n = \log(K_p/3\lambda p) + \log(1 - \frac{N}{k}). \quad (3.6.2.5)$$

Choosing n exactly as given in this equation guarantees that the plastic stiffness at the zero dilation line will be matched. But in order to obtain a better overall fit to the data, it may be desirable to alter

this constant somewhat. In equation 3.6.2.5, $K_p/3\lambda p$ is the ratio of the plastic stiffness at the zero dilation line to that on the hydrostatic axis. For a given N/k ratio, the exponent n may be interpreted as a measure of the stiffness of the stress-strain curve. Higher magnitudes of n produce a softer response.

3.6.3 Yield Surface or Plastic Flow Parameters

The constants Q and b (with a preselected slope of $S = 1.5$) govern the direction of the plastic strain increment. For a compression shear test [$g(\theta) = 1$],

$$\chi = \sqrt{3} \frac{d\epsilon_{kk}^p}{d\epsilon^p} = 6 \frac{(\partial F / \partial I_1)}{(\partial F / \partial J_2^*)} \quad (3.6.3.1)$$

Substituting the explicit forms of the partial derivatives for the consolidation surface (listed in Appendix B) into this identity gives

$$1 - 2 \left[1 - \frac{z(Q-1)^2}{6\chi N^2} \right] + \frac{(Q-1)^2 z^2}{N^2} + \left[1 - \frac{(Q-1)^2 z}{6\chi N^2} \right]^2 (2Q - Q^2) = 0, \quad (3.6.3.2)$$

where z is the mobilized stress ratio $\sqrt{J_2^*}/I_1$. Similarly, for the dilation surface, it can be shown that

$$b = \frac{1}{(z-S)^2} [6\chi(2z - S + C z^2) + C S + 1], \quad (3.6.3.3)$$

where

$$C = [(S/N^2) - (2/N)].$$

Therefore, by recording the pointwise incremental plastic volumetric/shear strain ratio χ and the corresponding mobilized stress ratio z along an axial compression path, the parameter b can be solved for directly using equation 3.6.3.3, while Q must be solved for iteratively from equation 3.6.3.2. The back-computed magnitudes of Q

and b have been found not to change much from point to point indicating that reasonable choices were made for both portions of the yield surface.

3.6.4 Interpretation of Model Parameters

An attempt is made in Table 3.2 to attach the simplest possible geotechnical interpretation to each model constant. Table 3.3 summarizes the likely trends in the magnitudes of these parameters with increasing relative density. Later, in the evaluation of the model, there will be an opportunity to compare these expected trends with calculated parameters for a range of densities.

3.7 Comparison of Measured and Calculated Results Using the Simple Model

Three data sets are used to demonstrate the range of applicability (in terms of the loading paths) of the simple model. First, a recent series of hollow cylinder tests reported by Saada et al. (1983) is used to assess the model performance along different linear monotonic paths. Each of these paths emanate from the same point on the hydrostatic axis ($p = 30$ psi) and move out in principal stress space at different Lode angles (θ), while the intermediate principal stress or the mean pressure is held constant.

The second test sequence was extracted from a recent paper by Hettler et al. (1984). It consists of a comprehensive series of axial compression tests on sands at different densities and all-around pressures. This data is considered very reliable because it has been reproduced by other researchers using alternative testing devices (see, for example, Goldscheider, 1984, and Lanier and Stutz, 1984). Since

Table 3.2 Simple Interpretation of Model Constants

MODEL PARAMETER	GEOTECHNICAL INTERPRETATION
k	Friction angle, ϕ
m	Degree of curvature of the Mohr-Coulomb failure envelope
N	Friction angle at constant volume, ϕ_{cv}
λ	Slope of voids ratio (e) vs. log mean stress (p) plot, or compression index
b	Magnitude of positive angle of dilation [see Rowe (1962) for a development of the theory of stress-dilatancy]
Q	Magnitude of negative angle of dilation
K_u and r	Elastic constants which vary with confining pressure
n	Stiffness of the shear stress-shear strain (q vs. $\bar{\epsilon}$) curve.

Table 3.3 Expected Trends in the Magnitude of Key Parameters With Relative Density

PARAMETER	EXPECTED TREND WITH INCREASING RELATIVE DENSITY
Q	increases, implying less compaction per unit shear strain
b	increases, implying greater dilatancy per unit shear strain
N	unchanged, as implied by characteristic state theory
n	decreases slightly, modelling a less ductile response
k	increases, higher strength due to greater degree of interlocking
m	increases, deviation from pure frictional behavior becomes more pronounced as interlocking contribution to shear resistance increases
λ	increases, stiffer response in hydrostatic compression due to denser configuration of particles
K_u	increases, stiffer elastic response because denser packing results in lower inter-particle contact stresses
r	decreases, lower interparticle contact forces result in a smaller fraction of the granules being crushed

these tests covered a wide range of densities, it was also possible to compare the calculated material parameters with the trends suggested in Table 3.3.

Thirdly, a comparison of measured and simulated response for a special series of load-unload-reload stress paths (Tatsuoka and Ishihara, 1974a and 1974b) shows, at least in a qualitative sense, the realistic nature of the simple representation for much more complicated stress histories.

3.7.1 Simulation of Saada's Hollow Cylinder Tests

Figure 3.16 depicts the state of stress in a typical hollow cylinder device. All tests paths were stress controlled and were either constant intermediate principal stress (i.e., constant $\sigma_r = \sigma_\theta$) or constant mean pressure shear paths. Fifteen trajectories were considered in principal stress space. When dealing with such an assortment of stress paths, it is always convenient to introduce a compact but unmistakably clear notation, and Saada's (Saada et al., 1983) convention is adopted here. The letters "D" or "C" appear first in the test designation and they refer to loading conditions with constant intermediate principal stress or constant mean stress respectively. The letters "C" or "T" follow and they indicate whether the axial stress (σ_z) was in relative compression or tension respectively. If a shear stress ($\tau_{z\theta}$) was applied, the letter "R" is appended to "C" or "T." The number which comes after the letters is the fixed angle (in degrees) between the major principal stress (σ_1) and the vertical (or z) direction; this is shown as the angle β in Figure 3.17. These angles were nominally 0° [with Lode angle $\theta = 30^\circ$ (compression

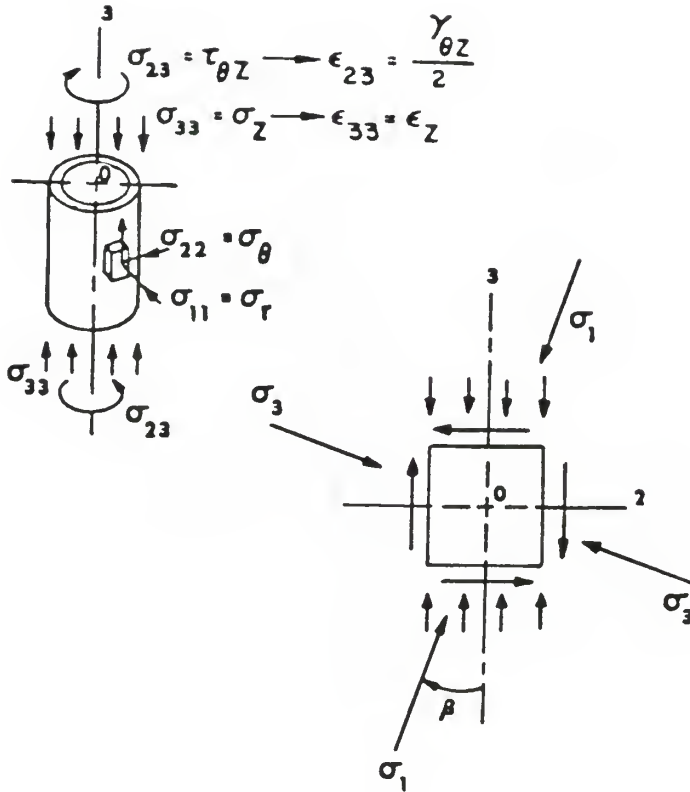


Figure 3.16 Stress state in "thin" hollow cylinder

tests)], 15° ($\theta \approx 27^\circ$), 32° ($\theta \approx 15^\circ$), 45° [$\theta = 0^\circ$ (pure torsion)], 58° ($\theta \approx -15^\circ$), 75° ($\theta \approx -27^\circ$), and 90° [$\theta = -30^\circ$ (extension tests)]. So, for example, a GTR 58 test is one in which a) the incremental application of the stress components ensures no change in mean stress (G), b) the axial stress is in tension relative to the initial hydrostatic state (T), c) a torque is applied (R), d) the angle between σ_1 and the vertical axis is constant and equal to 58 degrees (Lode's parameter $\theta \approx -15^\circ$). Wherever possible, the more familiar test path nomenclature of Figure 2.3 is juxtaposed with this specialized test designation. Figure 3.17 depicts the trajectories of these shear paths in Mohr's stress space, and with reference to Figure 2.3, all test paths are included except the CTE.

Reid-Bedford sand, at a relative density of 75%, was the material tested in all experiments. Its physical characteristics have been described elsewhere (Seereeram et al., 1985).

In accordance with the recommended initialization procedure, all but the elastic parameters were determined from the axial compression and hydrostatic compression paths of Saada's series of tests. The elastic constants had to be estimated from Linton's (1986) unloading triaxial tests because Saada monotonically sheared (to failure) all of his specimens. Two solid cylindrical axial compression tests, at confining pressures of 35 and 45 psi, were also extracted from Linton's thesis to supplement Saada's data.

Table 3.4 lists the computed parameters. Figures 3.18 and 3.19 show the measured and fitted response for the hydrostatic compression and axial compression paths respectively. Very close agreement is observed in both cases. Figures 3.20 and 3.21 show measured and

Table 3.4 Model Constants for Reid-Bedford Sand at 75% Relative Density

PARAMETER	MAGNITUDE
<u>Elastic Constants</u>	
Modulus number, K_u	2400
Modulus exponent, r	0.50
<u>Yield Surface Parameters</u>	
Slope of zero dilation line, N	0.218
Shape controlling parameter of consolidation portion of yield surface, Q	2.6
Shape controlling parameter of dilation portion of yield surface, b	15.0
<u>Field of Plastic Moduli Parameters</u>	
Plastic compressibility parameter, λ	280
Strength parameter, k (note: no curvature in failure meridian assumed)	.300
Exponent to model decrease of plastic modulus, n	2

Note: all plastic parameters were computed from the monotonic hydrostatic and axial compression (@30 psi) experiments of Saada et al. (1983). The elastic constants were computed from the data of Linton (1986).

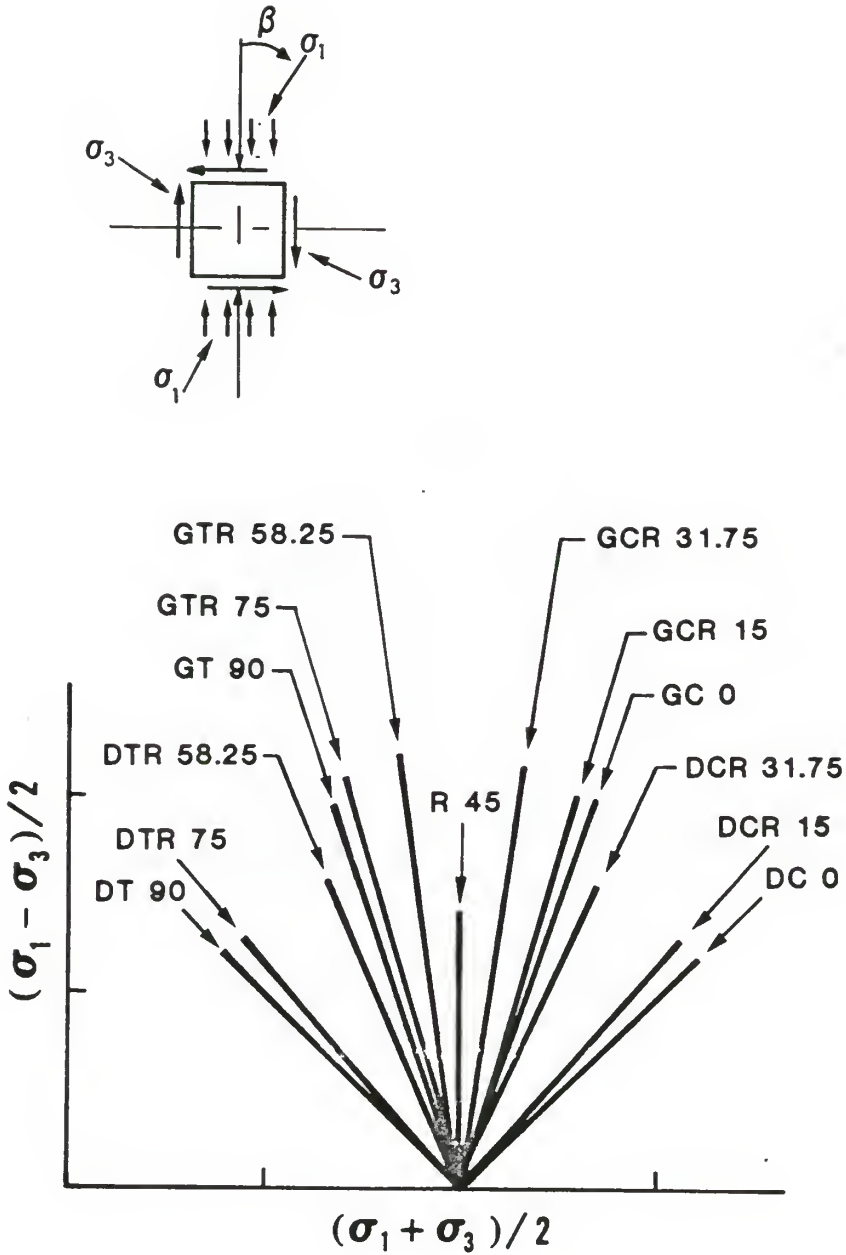


Figure 3.17 Saada's hollow cylinder stress paths in Mohr's stress space (after Saada et al., 1983)

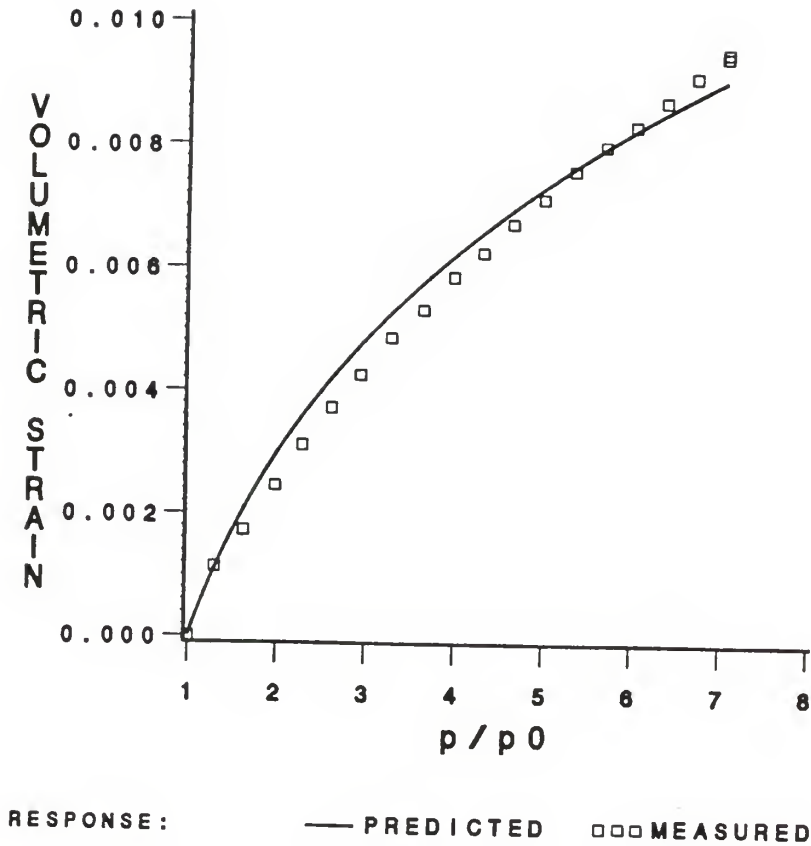


Figure 3.18 Measured vs. fitted response for hydrostatic compression (HC) test using proposed model ($p_0 = 10$ psi)

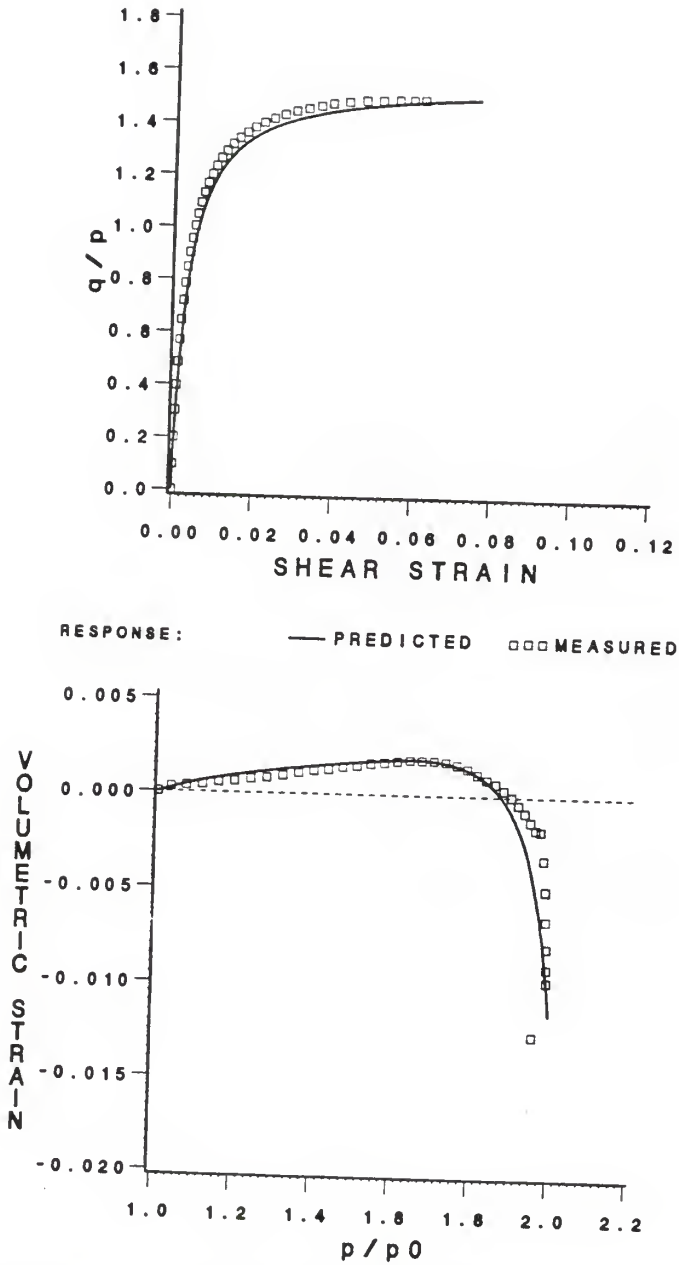


Figure 3.19 Measured vs. fitted response for axial compression test (DC 0 or CTC of Figure 2.3) @30 psi using proposed model

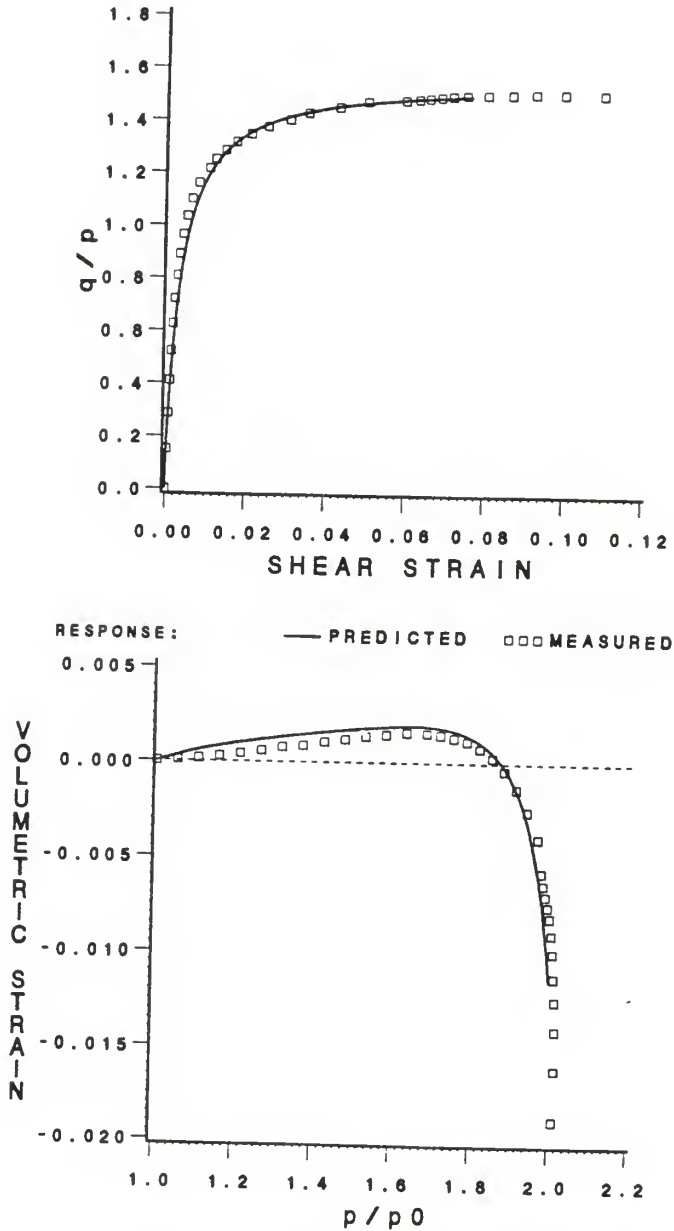


Figure 3.20 Measured vs. predicted response for axial compression test (DC 0 or CTC of Figure 2.3) @35 psi using proposed model

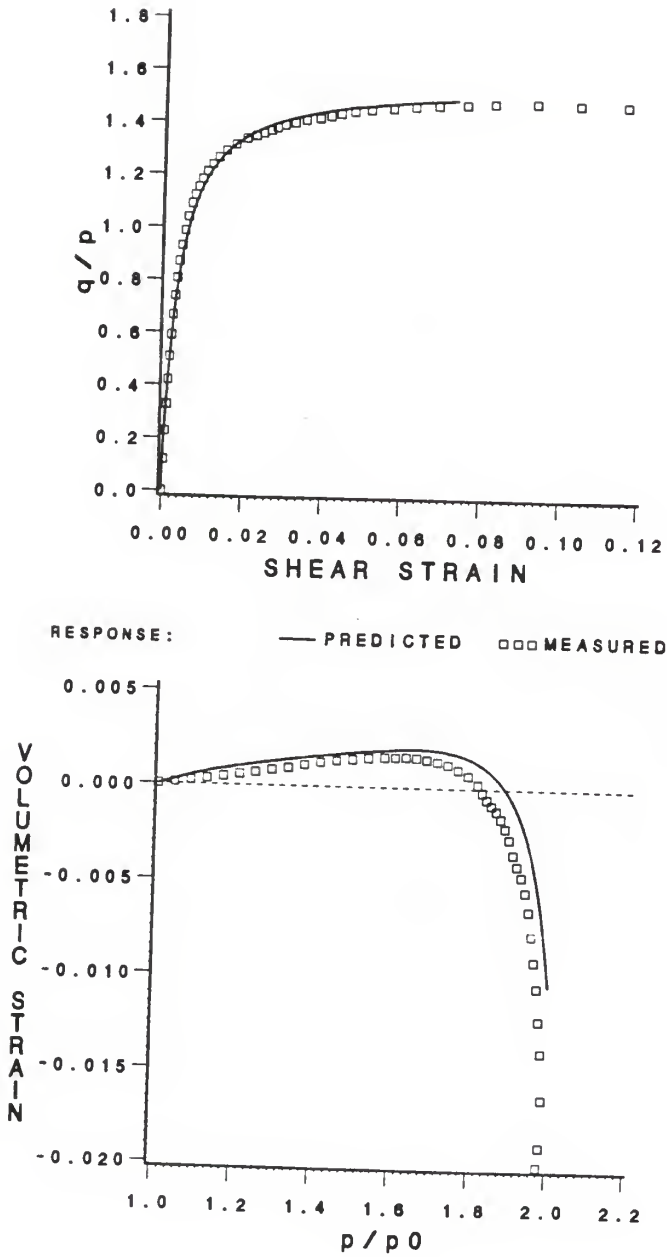


Figure 3.21 Measured vs. predicted response for axial compression test (DC 0 or CTC of Figure 2.3) @45 psi using proposed model

predicted response for the axial compression paths on the solid cylindrical specimens at confining pressures of 35 and 45 psi respectively. Again the correspondence is good. However, it appears that the observed volumetric compression in the solid cylinder tests is slightly less than that recorded in the hollow cylinder test (see Figure 3.19).

Predictions for the RTC and TC stress paths (of Figure 2.3) are given in Figures 3.22 and 3.23. Although the predictions here are not as precise as the previous axial compression paths, they are satisfactory considering the radical departure from the axial compression trajectory used in fitting the parameters.

Lode's parameter θ in all of the previous experiments were the same ($\theta = 30^\circ$). When the stress path moves on another meridional plane, as shown by the prediction of the axial extension test ($\theta = -30^\circ$) in Figure 3.24, the agreement is far less impressive. Even though the strength asymptote appears to be reasonably matched, the pre-peak model response is too stiff, and the large compression strains observed just prior to failure are not predicted. Close inspection of the remainder of the hollow cylinder predictions compiled in Appendix D uncovers two distinct trends: i) as the trajectory of the stress path moves away from compression toward extension, the simulations worsen in that the calculated shear stress-shear strain and volumetric compressive response become stiffer than the measured data, and ii) the strength asymptote is underpredicted for the tests where the angle between the vertical direction and the major principal stress is close to 32° , while it is overpredicted near 75° . Seereeram et al. (1985) have attempted to explain the second discrepancy by correlating (anisotropic) strength

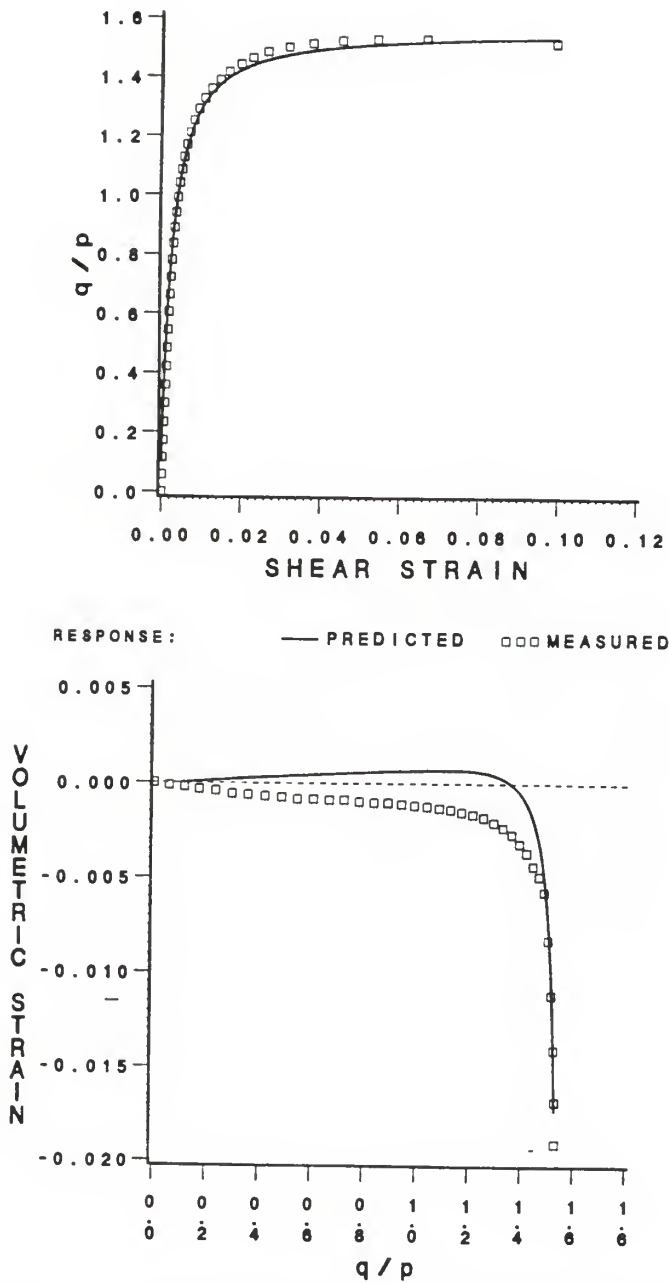


Figure 3.22 Measured vs. predicted response for constant mean pressure compression shear test (GC 0 or TC of Figure 2.3) using proposed model

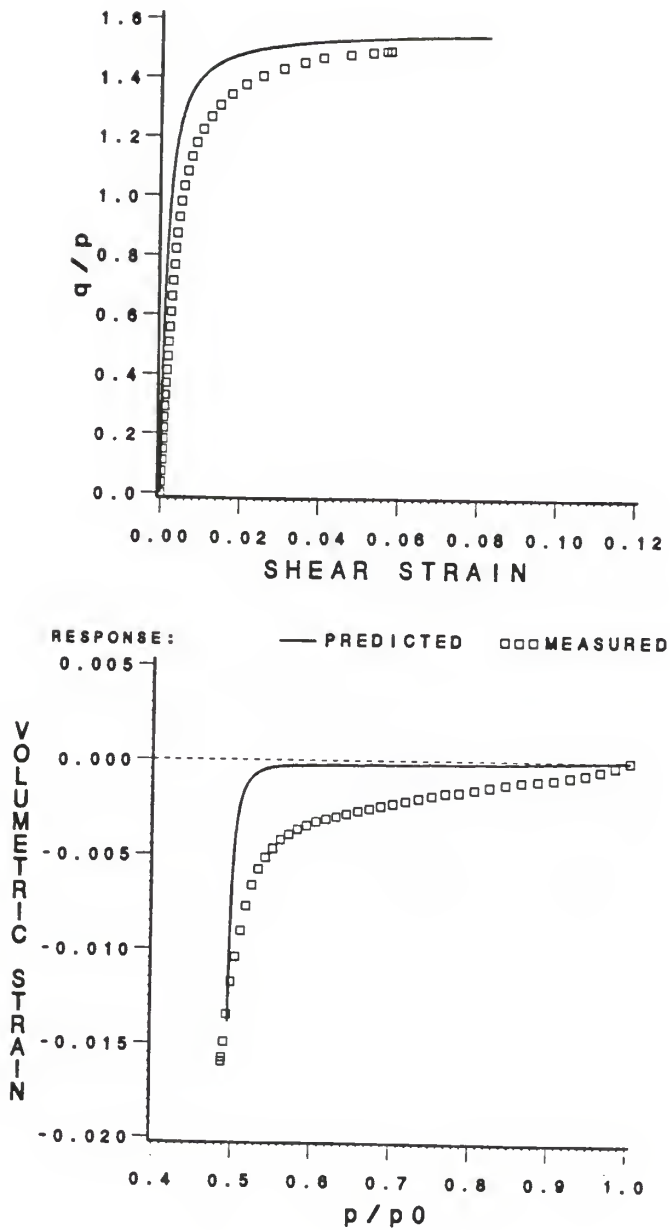


Figure 3.23 Measured vs. predicted response for reduced triaxial compression test (RTC of Figure 2.3) using proposed model

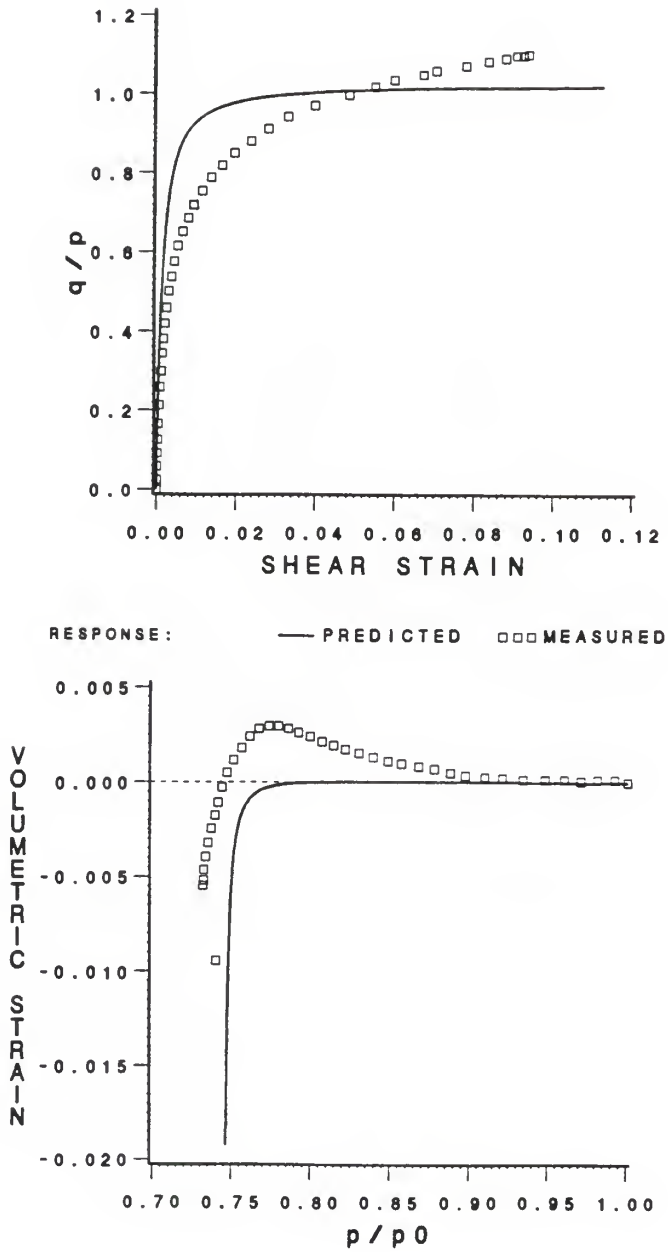


Figure 3.24 Measured vs. predicted response for axial extension test (DT 90 or RTE of Figure 2.3) using proposed model

with the angle between the principal fabric axes and those of the slip-line field. An important point to emphasize is that all the constant pressure shear paths, including the pure torsion test, trace identical curves in $q^* - p$ stress space, and so generate exactly the same predicted response.

Because of the well-known experimental difficulties associated with extension tests (Jamal, 1971, and Lade, 1982), it is perhaps premature to conclude from this single series of tests that the formulation is unsuitable for loading paths which are far removed from compression stress space. In fact, axial extension tests and constant pressure extension tests reported by Tatsuoka and Ishihara (1974a) and Luong (1980), respectively, contradict Saada's data and seem to be consistent with what the simple model will give.

As part of this research, an experiment was devised specifically to investigate the volume change phenomenon during an axial extension test. A solid cylindrical specimen, of height to diameter ratio of unity as suggested by Lade (1982), was equipped with LVDTs (Linear Variable Differential Transducers) at the center third of a water-saturated sample. During extension shear, volume changes were measured by the LVDTs and the conventional burette readings, and the results of this study are pictured in Figure 3.25. Superposed on this plot are a) the observed volumetric response as recorded by the LVDTs and the burette, b) Saada's hollow cylinder extension test data, and c) the model prediction. Based on this graphic evidence, it does indeed seem premature to criticize the model's performance in simulating extension volume strains. The reader is therefore urged to withhold judgement on this aspect until the soil mechanics community can concur on what is

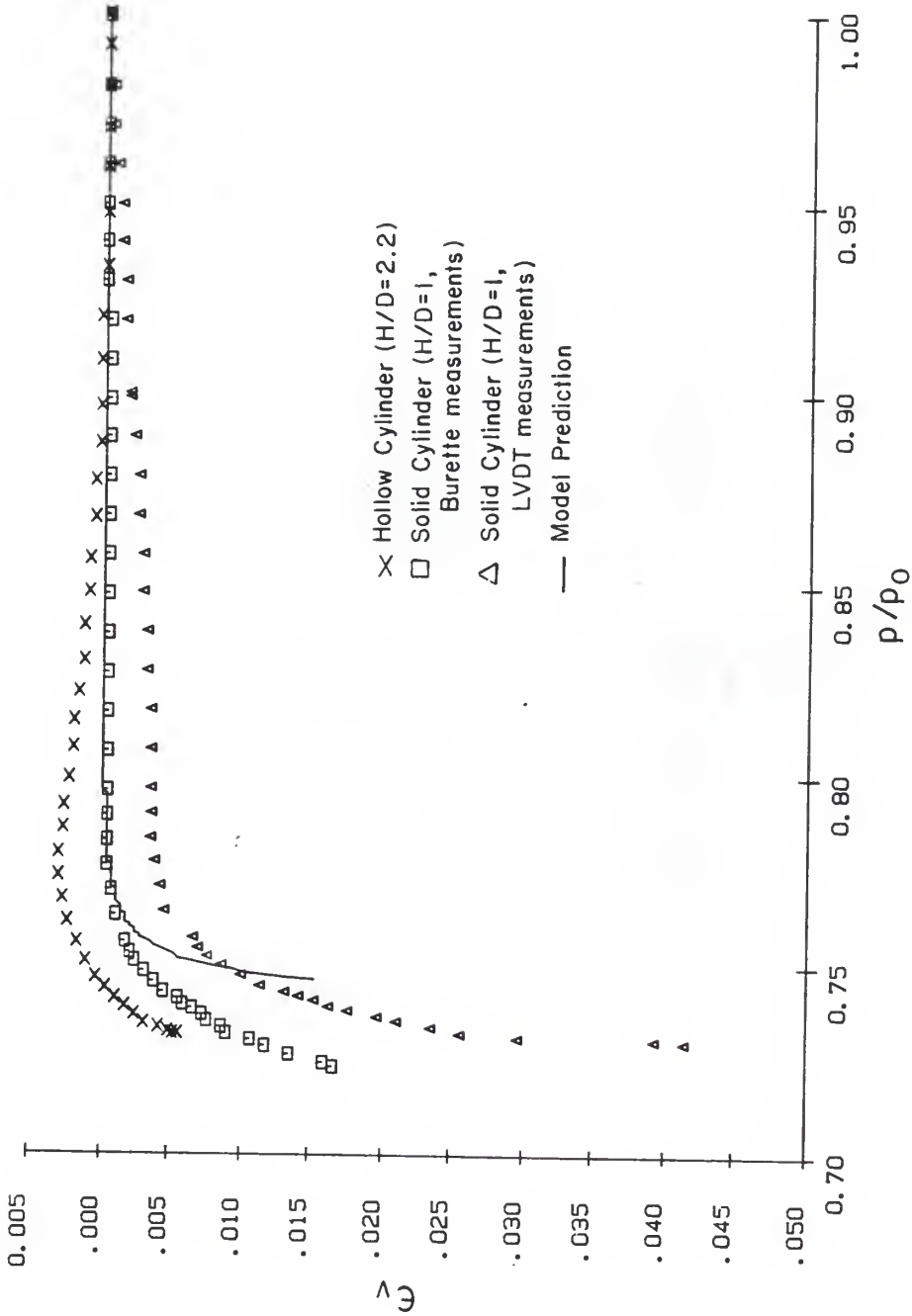


Figure 3.25 Volume change comparison for axial extension test (hollow cylinder data after Saada et al., 1983)

real behavior for extension tests. This statement is in the spirit of Professor Scott's epilog in his recent Terzaghi lecture (Scott, 1985) where he called for the development of an international data bank of test results on soils.

If we do not withhold judgement and assume that the behavior recorded by Saada is real and that the material is reasonably isotropic, then the data suggests that both the shape of the consolidation portion of the yield surface and the plastic moduli interpolation rule in extension differ markedly from compression. There is evidence, however, to indicate that the sand specimens used in Saada's experiments were anisotropic. Many researchers have verified that, at least on the octahedral plane, the strength of nearly isotropic soil approximates a Mohr-Coulomb type failure criterion. Podgorski (1985) has recently surveyed these isotropic failure criteria. Therefore, if such a criterion is taken for granted, and if the soil is indeed isotropic, the computed strength parameter should be approximately constant and independent of the path of loading. To test this hypothesis, three well-known isotropic failure criteria were used to evaluate Saada's data, and the results are presented in Table 3.5. Clearly, looking for instance only at the "G" tests to rule out the possibility of nonlinear pressure effects, inherent anisotropy has a significant influence on the strength and there is no reason not to expect it to also have an effect on the stress-strain response. Anisotropy could therefore be the cause of the discrepant axial extension prediction, and if this is true, as the author believes likely, it renders Saada's data an unsuitable proving ground for the proposed theory.

Table 3.5 Computed Isotropic Strength Constants for Saada's Series of Hollow Cylinder Tests

Reference:	$[(\underline{I}_1^3) - 27] (\underline{I}_1)^{.056}$ $\begin{matrix} I_3 \\ p_a \end{matrix}$ (Lade, 1977) ^a	$[-(\underline{I}_1 \underline{I}_2) - 9]$ I_3 (Matsuoka, 1974)	Friction Angle (Shield, 1955)
<u>Constant Intermediate Principal Stress Tests</u>			
DC 0 (or CTC of Fig. 2.3)	30.6	4.45	36.71
RTC (of Fig. 2.3)	28.2	4.43	36.67
DCR 15	34.7	5.00	40.39
DCR 32	45.9	7.74	49.69
DTR 58	26.7	5.81	42.74
DTR 75	23.9	5.34	39.49
DT 90 (or RTE of Fig. 2.3)	29.6	6.64	42.34
<u>Constant Mean Normal Pressure Tests</u>			
GC 0 (or TC of Fig. 2.3)	31.7	4.73	37.57
GCR 15	40.2	5.83	42.89
GCR 32	66.1	11.22	55.02
R 45 (or pure torsion)	40.4	8.22	49.32
GTR 58	23.9	5.15	41.00
GTR 75	17.9	3.91	35.49
GT 90 (or TE of Fig. 2.3)	25.6	5.63	40.00

3.7.2 Simulation of Hettler's Triaxial Tests

The physical characteristics of the two sands used in this study--one a medium-grained sand from Karlsruhe, Germany, and the other a fine-grained dune sand from Holland--are described by Goldscheider (1984) and Hettler et al. (1984).

In the first series of tests, the medium grained Karlsruhe sand was used to prepare four specimens at a relative density (D_r) of 99.0%. These samples were sheared to failure in axial compression with constant confining pressures of 50, 80, 200, and 300 kN/m² respectively, and this data is given in Figure 3.26. Notice here that the failure envelope is straight (constant σ_1/σ_3 ratios) and the stress-strain curves are neatly normalized.

The second phase of the program consisted of tests in which the confining pressure was kept constant at 50 kN/m², while the relative density of the prepared specimens was varied. Stress-strain data for this test sequence was obtained at relative densities of 62.5%, 92.3%, 99.0%, and 106.6%; see Figure 3.5. Accompanying these data sets on Karlsruhe sand were the results of a hydrostatic consolidation test (at 99% relative density) and an axial compression test (at 92.3% relative density) with an all-around stress of 400 kN/m². Hettler took care to point out that the specimens were initially isotropic by noting the equality of the normal strain components during hydrostatic compression.

The final series of Hettler's experiments were carried out on three specimens of Dutch dune sand, each prepared at an initial relative density of 60.9%. These samples were sheared in axial compression under ambient pressures of 50, 200, and 400 kN/m² respectively. Unlike the medium-grained sand from Karlsruhe, the failure meridian of this

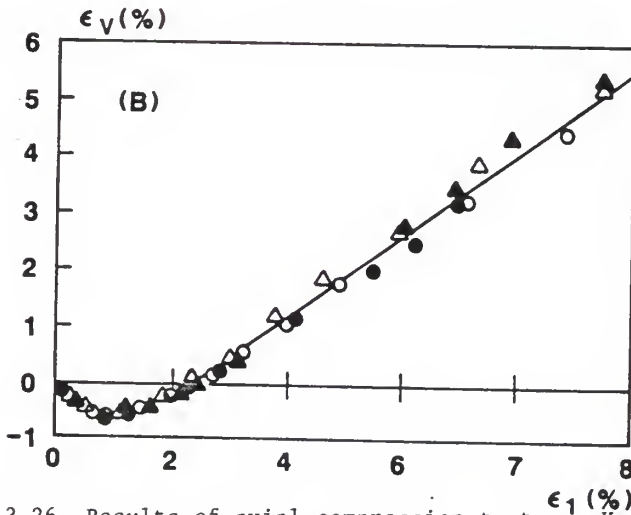
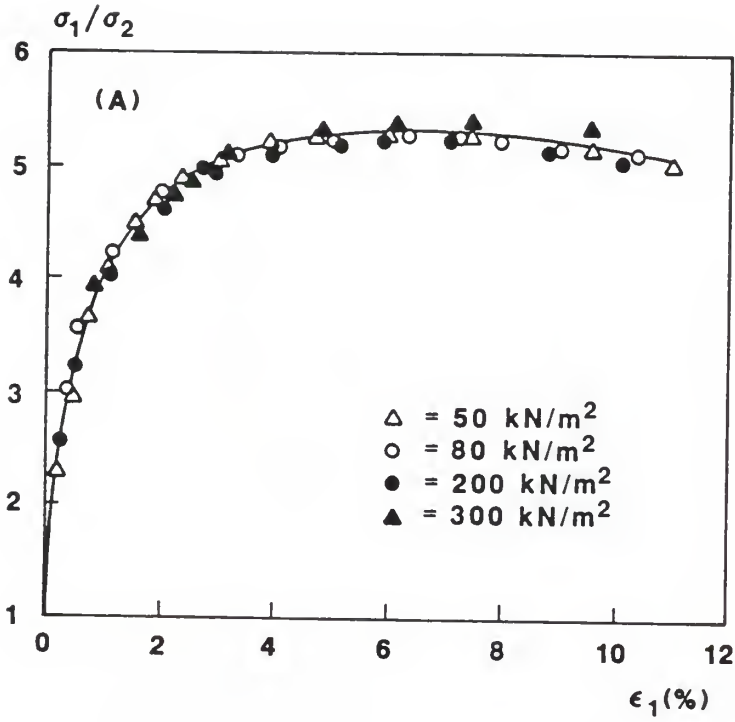


Figure 3.26 Results of axial compression tests on Karlsruhe sand at various confining pressures and at a relative density of 99% (after Hettler et al., 1984)

fine-grained sand was curved as exhibited in Figure 3.27 by the unequal σ_1/σ_3 ratios at failure.

The model parameters for each sand were initialized and these are summarized in Table 3.6. Other than the parameters "Q" and "b" (which control the shape of the yield surface), this list of model constants reflects the general trends with increasing relative density suggested in Table 3.3. Since no unloading data was presented by Hettler et al. (1984), the elastic shear moduli were reckoned, using an ad-hoc procedure suggested by Lade and Oner (1984), to be twice that of the initial slopes of the shear stress vs. shear strain (q vs. $\bar{\epsilon}$) data. And except for the Karlsruhe sand at a relative density of 99%, hydrostatic consolidation tests were also not available, so it was necessary to estimate the density hardening parameters (λ) in all but this one case.

As mentioned previously in section 3.6, the representation gives the same plastic response for each of a series of parallel stress paths emanating from the hydrostatic axis if the failure envelope is straight. However, if the failure envelope is curved, or if the plastic bulk modulus increases non-linearly with hydrostatic pressure, this statement would not be true. Hettler's data indicate that in cases where the failure envelope is straight, see Figure 3.5 for example, the stress-strain curves can indeed be normalized. Therefore, in such cases, all verifications could just as well be placed on one plot. However, this was not taken advantage of in preparing the figures. But, for economy of presentation, the predictions given in the body of the dissertation for Karlsruhe sand (i.e., the sand with the normalizable data) are only at one level of confining pressure, 50 kN/m², while the remainder have been included for reference in Appendix E.

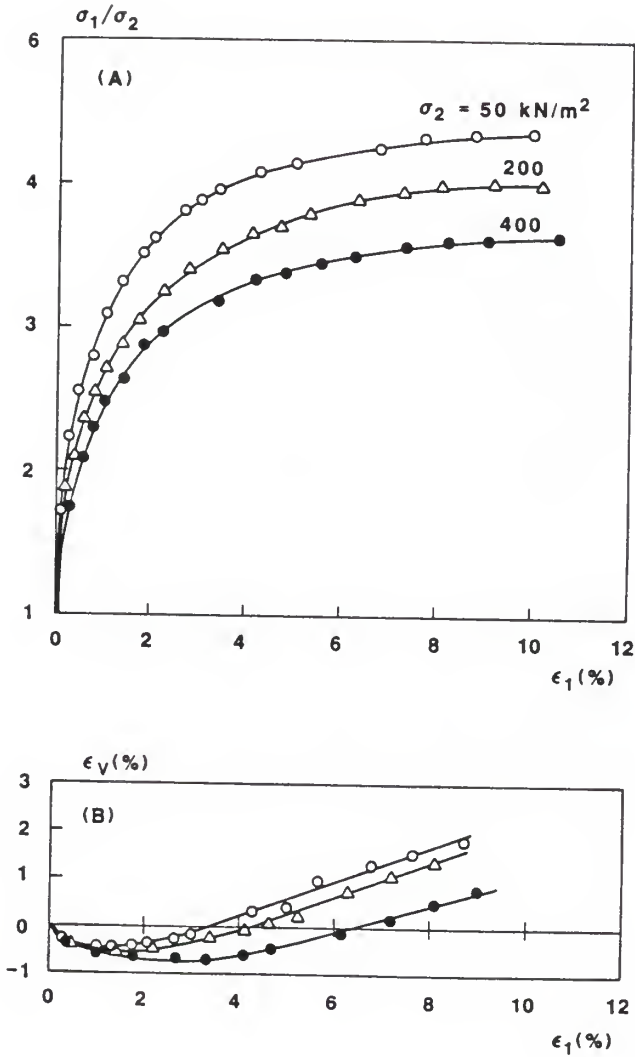


Figure 3.27 Results of axial compression tests on Dutch dune sand at various confining pressures and at a relative density of 60.9% (after Hettler et al., 1984)

Table 3.6 Model Parameters for Karlsruhe Sand and Dutch Dune Sand

PARAMETER	MEDIUM GRAINED Relative Density		KARLSRUHE SAND Relative Density		DUTCH DUNE SAND Relative Density
	62.5%	92.3%	99.0%	106.6%	60.9%
<u>Field of Plastic Moduli Constants</u>					
k	.2868	.3195	.3390	.3503	.3400
m	-	-	-	-	.0601
n	2.2	2.0	2.0	1.9	2.6
λ	300	500	530	550	300
<u>Plastic Flow or Yield Surface Parameters</u>					
N	.265	.265	.265	.265	.230
Q	1.8	1.4	1.3	1.5	1.8
b	12.9	11.4	11.1	11.6	14.8
<u>Elastic Constants</u>					
K_u	1070	1810	2100	2200	1332
r	.70	.65	.62	.57	.668

Note: The slope of the yield surface at the origin of $\sqrt{J_2}$ - I_1 stress space, S, is assumed equal to 1.5 in all cases. Also note that these parameters were computed from the data of Hettler et al. (1984).

Figures 3.28-3.32 are, in sequence, plots of the calculated results superposed with the experimental data points for the hydrostatic compression test at 99% relative density, and the axial compression paths on samples of relative densities 62.5%, 92.3%, 99.0%, and 106.6%. Correspondence between measured and predicted response is remarkably accurate in all cases. This is particularly encouraging because the data are known to be of high quality. The model's intrinsic ability to simulate this wide cross-section of densities over a range of confining pressures is testimony to its rationality.

Figures 3.33-3.35 are the predictions of the axial compression tests on the fine-grained dune sand with the curved failure envelope. These are also impressive considering the "non-normalizable" nature of the data.

3.7.3 Simulation of Tatsuoka and Ishihara's Stress Paths

Figure 3.36 shows the type "A" and type "B" triaxial stress paths of Tatsuoka and Ishihara (1974b), and Figures 3.37 and 3.38 are plots of the corresponding stress-strain curves they recorded for these paths. The material tested was loose Fuji River sand, the physical characteristics of which have been described by Tatsuoka and Ishihara (1974b). Both these loading paths consist of a series of axial compression paths which are offset at increasing increments of confining stress for the type "A" case and at decreasing levels for the type "B."

To a fairly close approximation, all of the axial shear paths for the type "A" loading program appear to produce somewhat parallel stress-strain curves (Figure 3.37b). This observation lends credence to the idea that, at least along these paths and for this type and

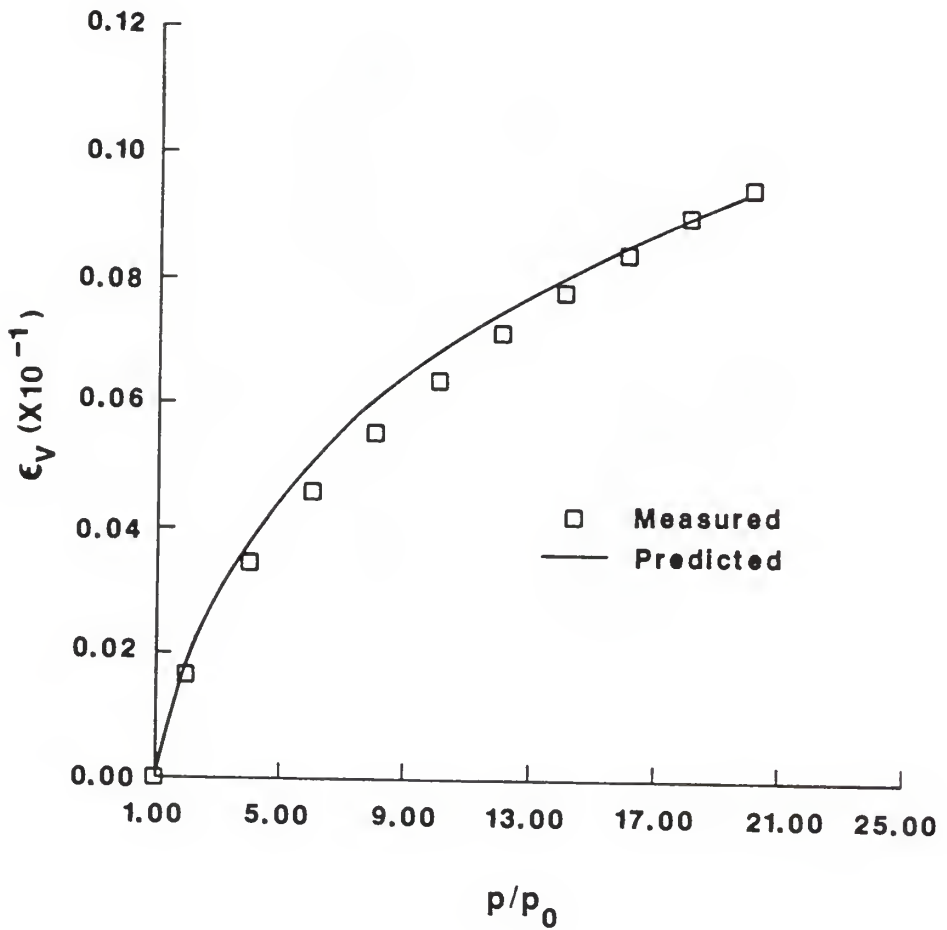


Figure 3.28 Measured and predicted response for hydrostatic compression test on Karlsruhe sand at 99% relative density (measured data after Hettler et al., 1984)

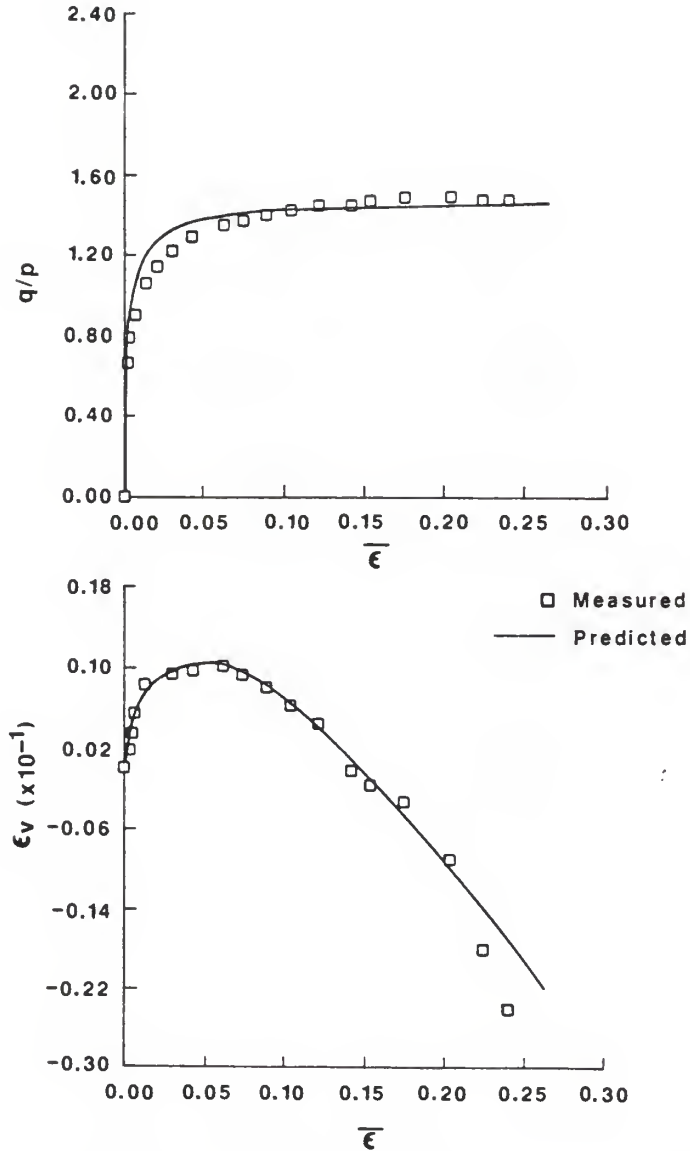


Figure 3.29 Measured and predicted response for axial compression test ($\sigma_3 = 50 \text{ kN/m}^2$) on Karlsruhe sand at 62.5% relative density (measured data after Hettler et al., 1984)

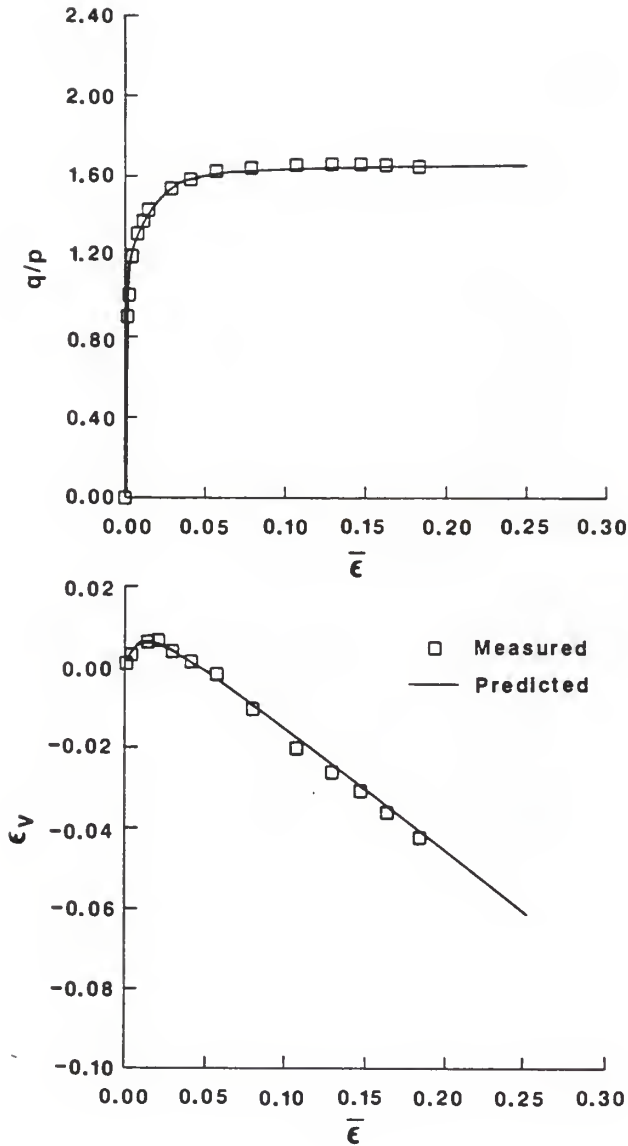


Figure 3.30 Measured and predicted response for axial compression ($\sigma_3 = 50 \text{ kN/m}^2$) on Karlsruhe sand at 92.3% relative density (measured data after Hettler et al., 1984)

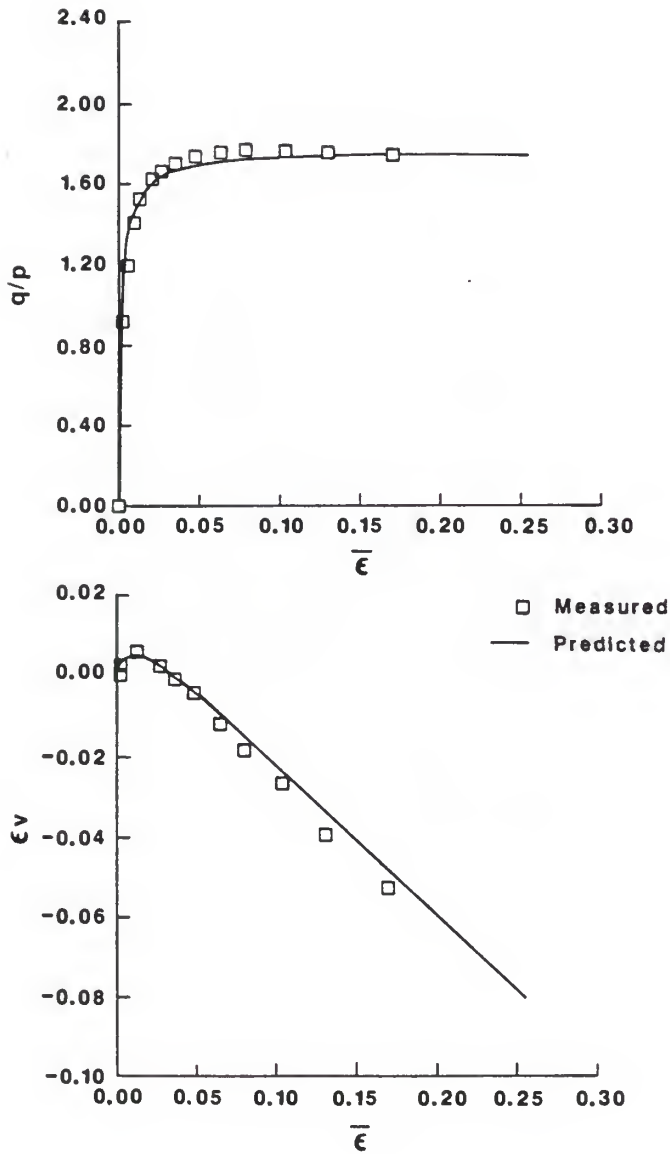


Figure 3.31 Measured and predicted response for axial compression test ($\sigma_3 = 50 \text{ kN/m}^2$) on Karlsruhe sand at 99.0% relative density (measured data after Hettler et al., 1984)

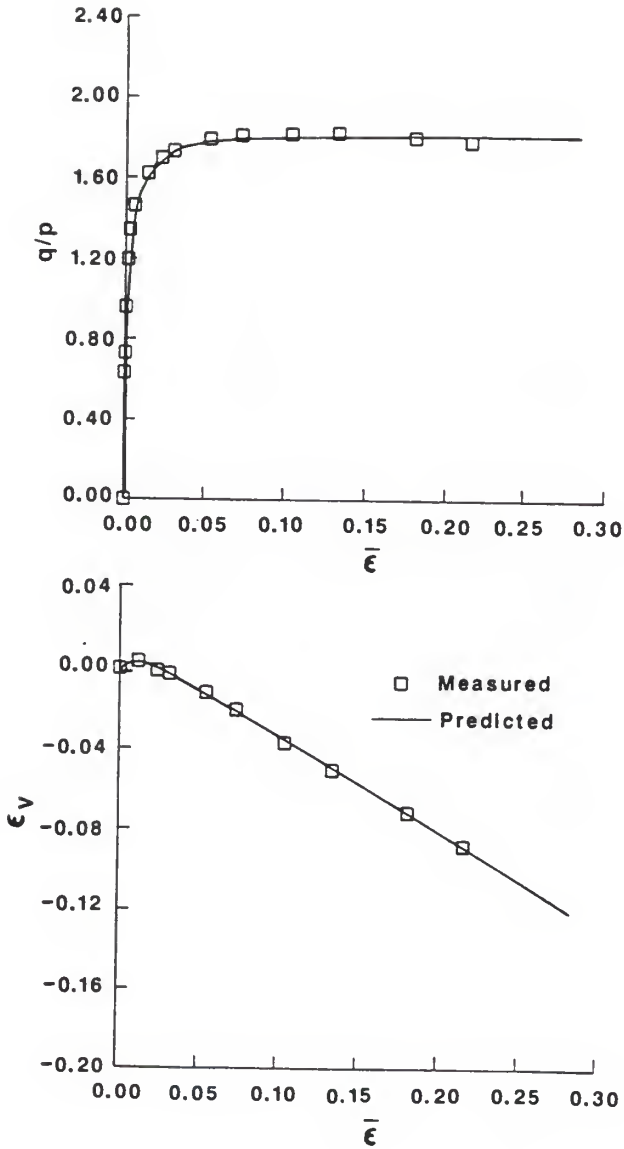


Figure 3.32 Measured and predicted response for axial compression test ($\sigma_3 = 50 \text{ kN/m}^2$) on Karlsruhe sand at 106.6% relative density (measured data after Hettler et al., 1984)

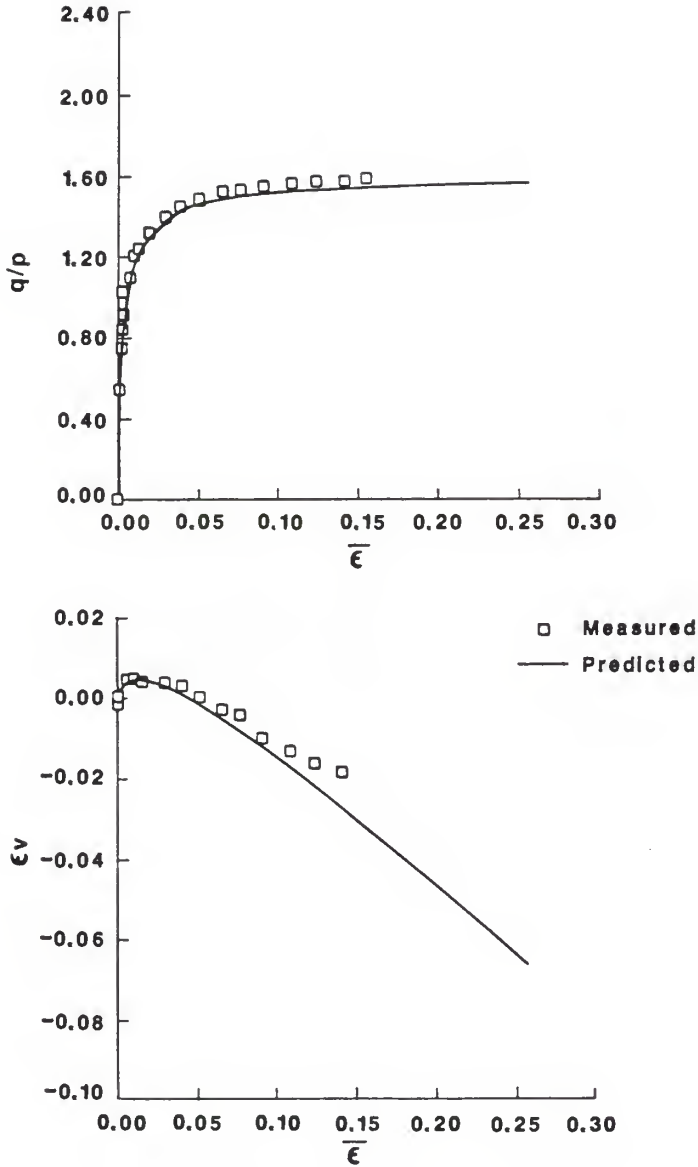


Figure 3.33 Measured and predicted response for axial compression test ($\sigma_3 = 50 \text{ kN/m}^2$) on Dutch dune sand at 60.9% relative density (measured data after Hettler et al., 1984)

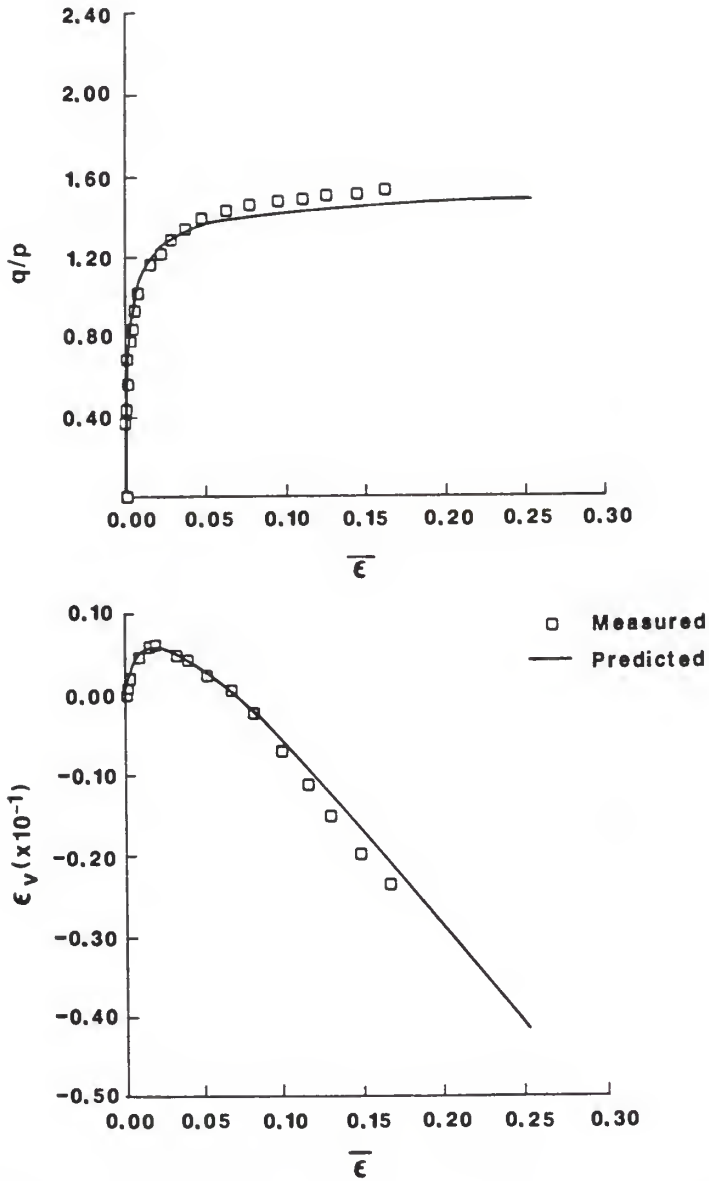


Figure 3.34 Measured and predicted response for axial compression test ($\sigma_3 = 200 \text{ kN/m}^2$) on Dutch dune sand at 60.9% relative density (measured data after Hettler et al., 1984)

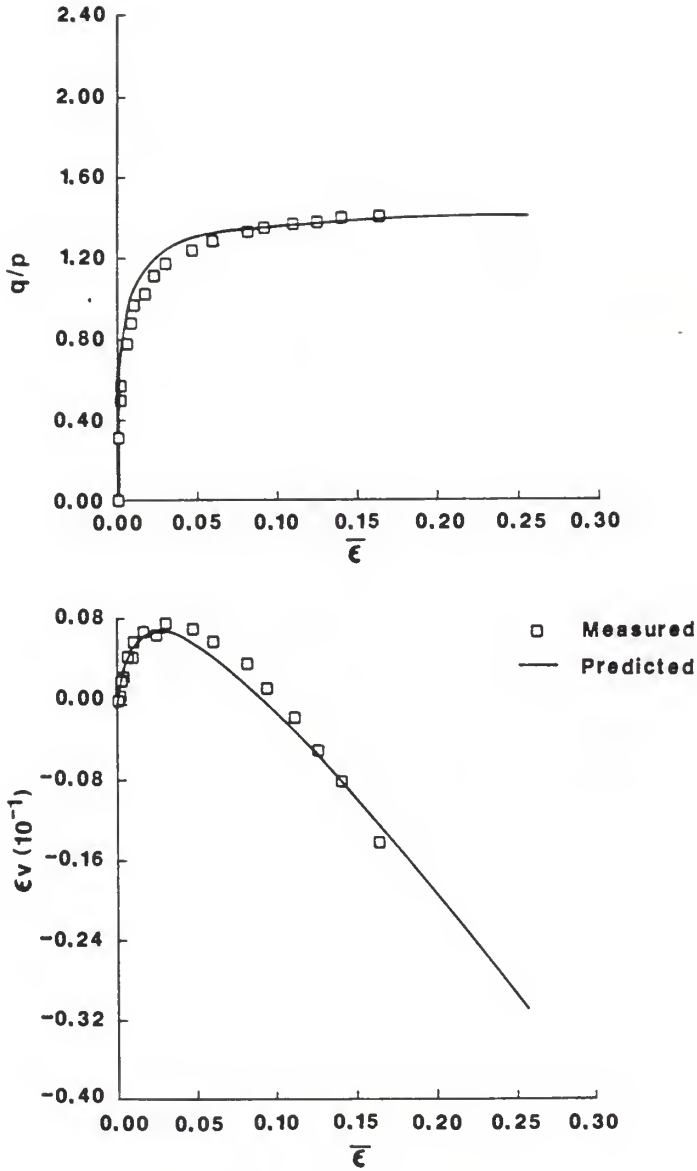


Figure 3.35 Measured and predicted response for axial compression test ($\sigma_3 = 400 \text{ kN/m}^2$) on Dutch dune sand at 60.9% relative density (measured data after Hettler et al., 1984)

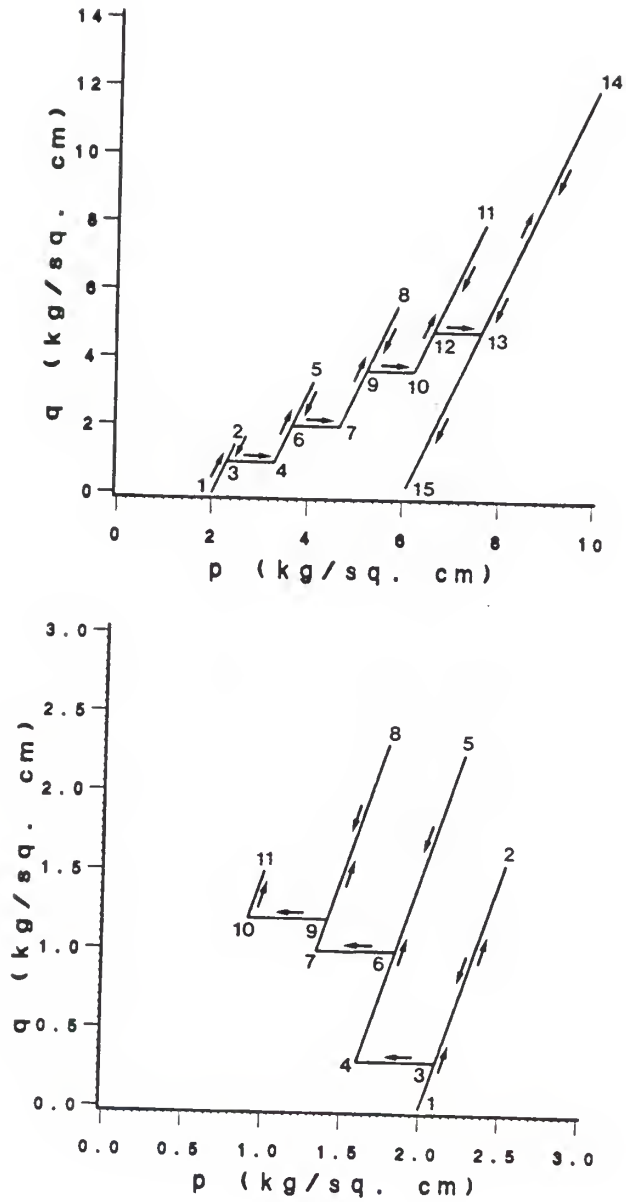


Figure 3.36 Type "A" (top) and type "B" (bottom) stress paths of Tatsuoka and Ishihara (1974b)

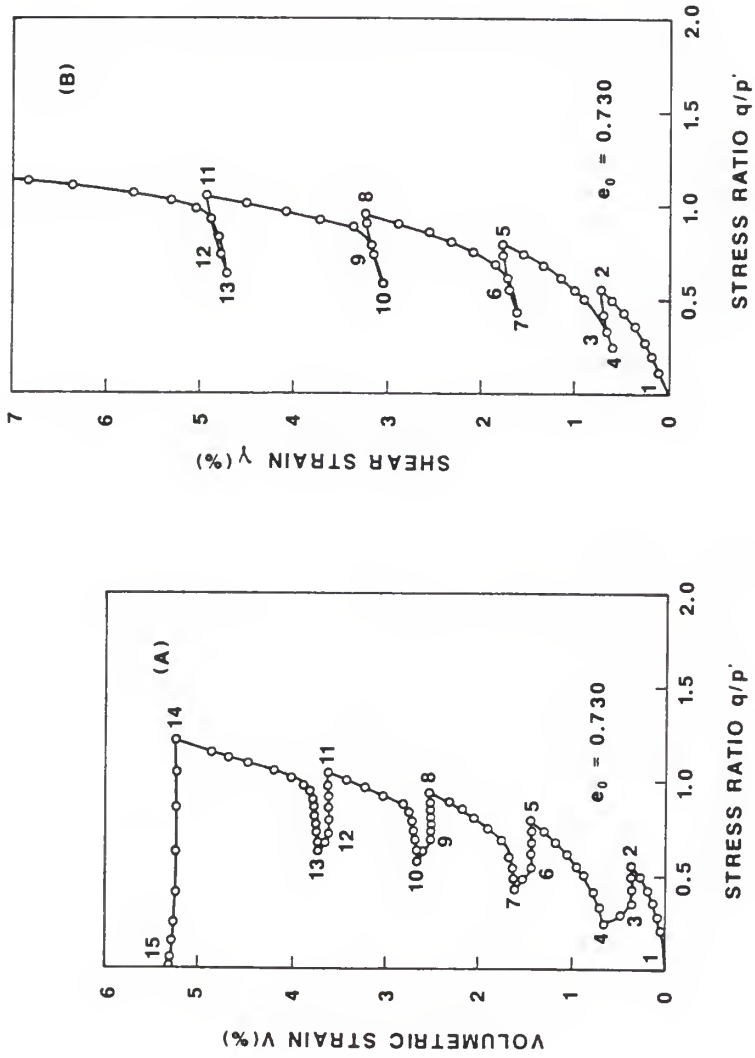


Figure 3.37 Observed stress-strain response for type "A" loading path on loose Fuji River sand (after Tatsuoka and Ishihara, 1974b)

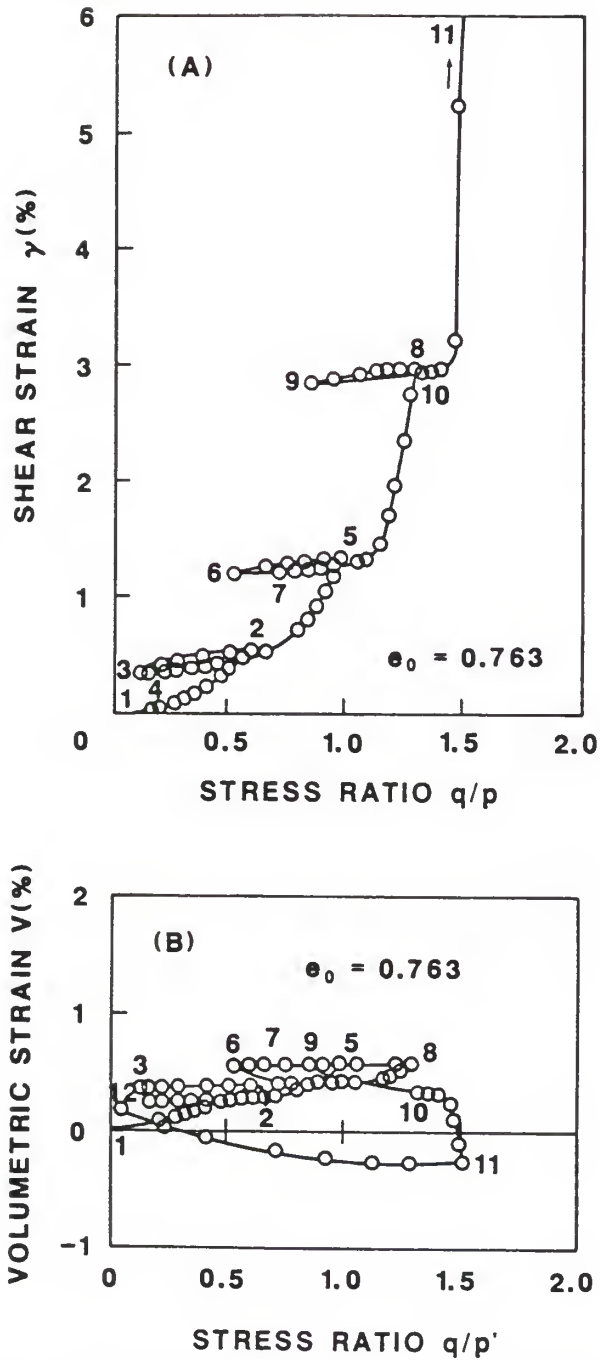


Figure 3.38 Observed stress-strain response for type "B" loading path on loose Fuji River sand (after Tatsuoka and Ishihara, 1974b)

density of sand, hardening may be neglected without sacrificing too much modelling power. Using the data of this plot and the results of a hydrostatic compression test presented by Tatsuoka (1972), the model parameters for this loose sand were computed and are listed in Table 3.7.

The predicted curves for the type "A" loading path are shown in Figure 3.39, and except for the shear strain direction during the incremental hydrostatic loadings from points 3 to 4, 6 to 7, 9 to 10, and 12 to 13, this prediction agrees qualitatively with the measured data. Induced anisotropy is believed to be the cause of the wrong direction predicted by the isotropic model for the small hydrostatic segments.

Quantitatively, the model response is about twice as stiff as the measured data, and this problem stems from the choice of the interpolation rule that controls the field of plastic moduli. In its present form, it is not capable of precisely matching stress-strain curves in which the tangent modulus decreases significantly well below the zero dilation line. Furthermore, by looking at the shape of the stress-strain curve in Figure 3.37 (b), it is difficult to imagine that failure should occur at a q/p ratio of 1.55.

To gain greater control over the rate at which K_p decreases, the interpolation rule may be improved as follows. The plastic modulus at each point on the zero dilation line can be taken as some fraction of its corresponding magnitude on the hydrostatic axis, and its reduction between these two radial lines may be governed by one exponent, while a different exponent may be used to control its approach to zero (at the failure line) beyond the zero dilation line. But before doing all this

Table 3.7 Model Parameters for Loose Fuji River Sand

PARAMETER	MAGNITUDE
<u>Elastic Constants</u>	
Modulus number, K_u	1816
Modulus exponent, r	.513
<u>Yield Surface Parameters</u>	
Slope of zero dilation line, N	0.281
Shape controlling parameter of consolidation portion of yield surface, Q	2.50
Shape controlling parameter of dilation portion of yield surface, b	11.0
<u>Field of Plastic Moduli Parameters</u>	
Plastic compressibility parameter, λ	135
Strength parameter, k (note: no curvature in failure meridian assumed)	.298
Exponent to model decrease of plastic modulus, n	2

Note: these parameters were computed from data reported by Tatsuoka (1972) and Tatsuoka and Ishihara (1974b)

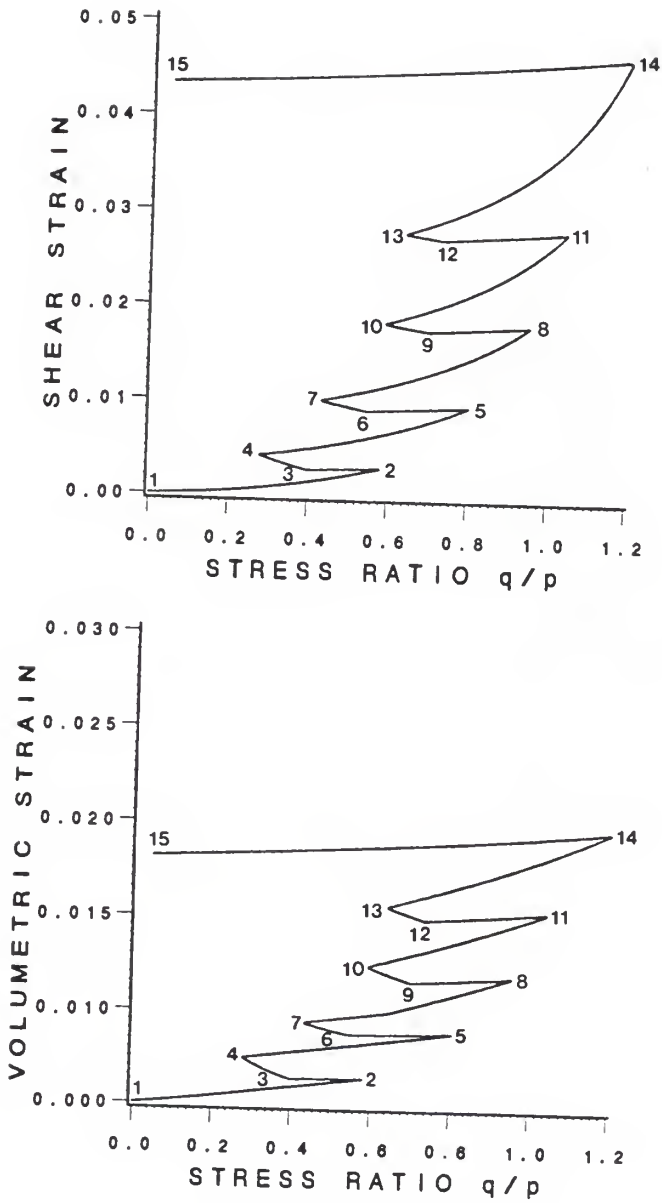


Figure 3.39 Simulation of type "A" loading path on loose Fuji River sand using the simple representation

work, it is important to verify that the observed response is indeed real because the simple form of the interpolation rule was quite adequate for matching Hettler's tests on sands of similar relative density (Hettler et al., 1984); see, for example, Figures 3.29, 3.33, 3.34, and 3.35.

For the type "B" loading path (Figure 3.36b), hardening appears to be more pronounced, but as the simulation depicted in Figure 3.40 suggests, the qualitative nature of the simple representation is again not a poor first approximation.

As shown earlier in Figure 3.7, Tatsuoka and Ishihara (1974a) also performed medium amplitude axial compression-extension cycles on this loose Fuji River sand. And as they concluded from their study, ". . . the memory of previous stress history experienced during the cycle in extension [compression] does not appear in the subsequent triaxial compression [extension], and therefore, the sample shows yielding from the outset as if it were in a virgin state." Figure 3.41 shows a simulation of this path using the parameters of Table 3.7, and for the first cycle, the "no-hardening" postulate (Drucker and Seegeram, 1986) does seem relevant. After many cycles, too much strain will be predicted if hardening is completely ignored. But, for materials subject to many cycles of loading, as in highway base courses, the parameters governing the stiffness of the fixed field of plastic moduli may be derived from the cyclically stabilized stress-strain curve to give more realistic predictions of the accumulation of permanent deformation.

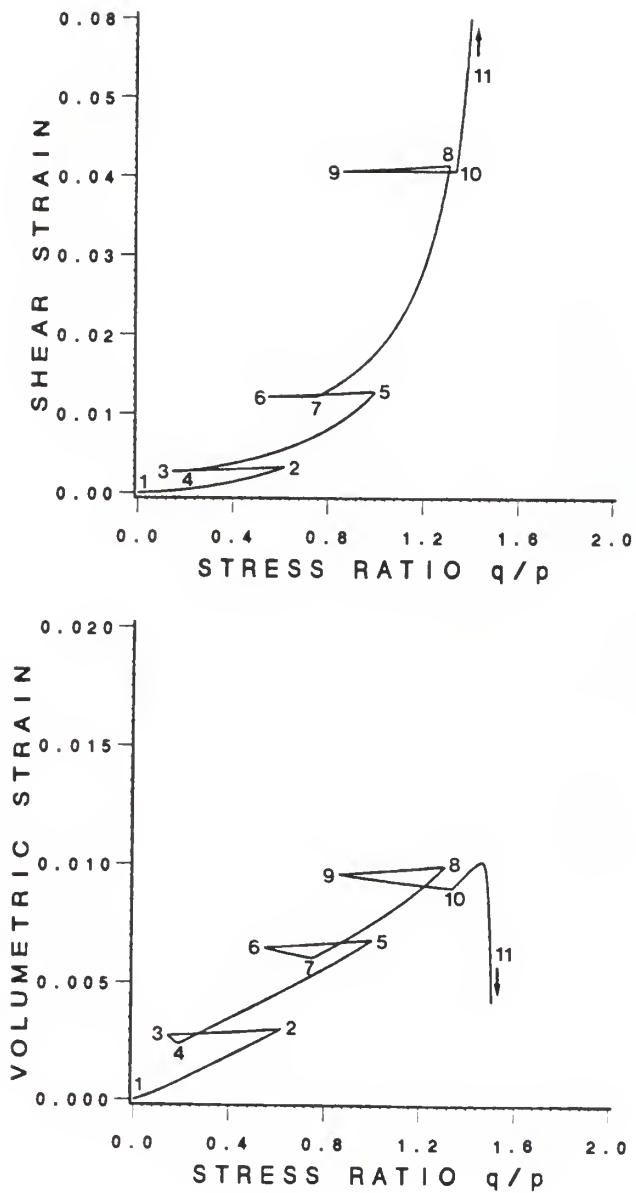


Figure 3.40 Simulation of type "B" loading path on loose Fuji River sand using the simple representation

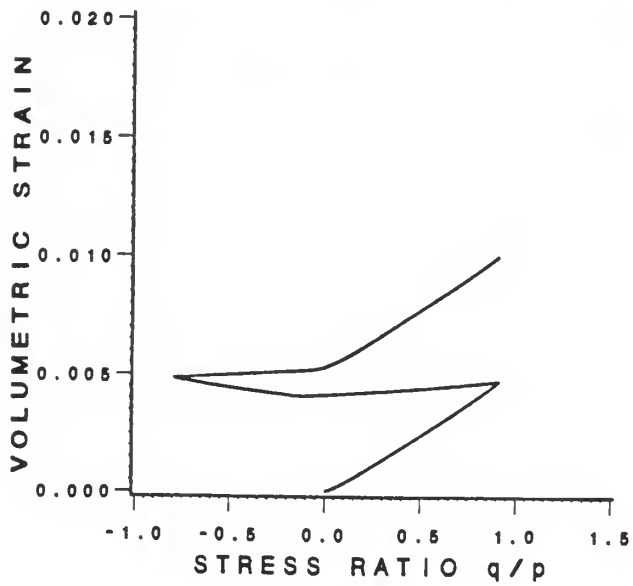
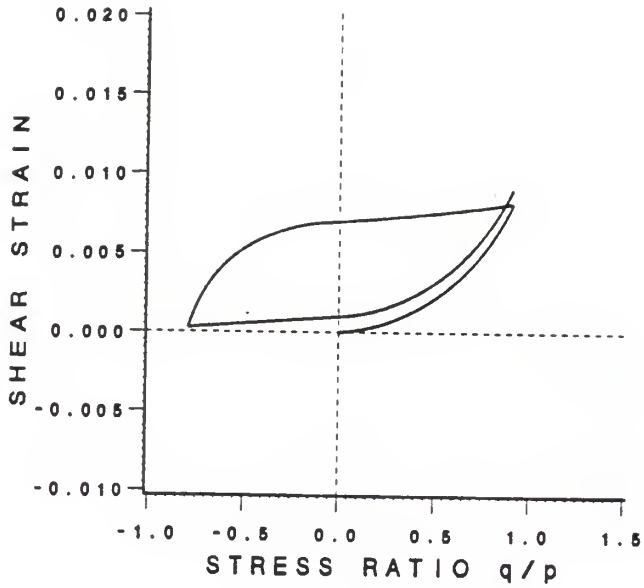


Figure 3.41 Simulation of compression-extension cycle on loose Fuji River sand using the simple representation

3.8 Modifications to the Simple Theory to Include Hardening

Two hardening options are implemented. The first is similar in many respects to the bounding surface proposal of Dafalias and Herrmann (1980). The key difference is that the plastic modulus here is given solely as a function of stress. This bounding surface adaptation is incorporated in a finite element computer program to predict a series of cyclic cavity expansion tests.

Although the first option could simulate inelastic reloading response for reloading paths which more or less retrace their unloading paths, the shape specified for the hardened region does not resemble the shapes intimated by the experimental stress probes of Poorooshasb et al. (1967) and Tatsuoka and Ishihara (1974b). A second option is then proposed to take these well-known observations into account. This new theory is used to predict the influence of isotropic preloading on an axial compression test and the build-up of permanent strain in a cyclic triaxial test.

Unfortunately, both hardening options sacrifice the ability to predict "virgin" response in extension after an excursion in compression stress space.

3.8.1 Conventional Bounding Surface Adaptation

In the cyclic context, the term hardening could refer to the increase in the size of the elastic region or to the increase in the plastic tangent modulus at a given stress or both (Drucker and Palgen, 1982). This first modification, which originates from the bounding surface concept of Dafalias and Popov (1975), involves only an increase in the plastic modulus. Given the loading history, the objective is

therefore first to identify the shape and size of the hardened region in stress space, or the totality of points where the purely stress-dependent plastic moduli are higher than the magnitudes they would assume for virgin loading, and then to specify the plastic moduli at each of these interior points. In general, the hardening control surface may not resemble the yield surface; if it does, it is a bounding surface as defined in the theory of Dafalias and Popov (1975).

For simplicity, the hardened region is assumed to have a shape similar to the yield surface (Figure 3.15) and a size equal to the largest yield surface established by the prior loading. Thus, the hardening control surface is really a conventional bounding surface ($F_p = 0$), within which the yield surface ($F = 0$) moves. For virgin loading, the bounding surface and yield surface coincide.

The essence of the bounding surface concept is that for any stress state \underline{g} within the boundary surface or hardened domain $F_p = 0$, a corresponding image point $\bar{\underline{g}}$ on F_p can be specified using an appropriate mapping rule. Having established $\bar{\underline{g}}$, the plastic modulus is rendered an increasing function of i) the Euclidean distance between the actual stress state (\underline{g}) and the image stress state ($\bar{\underline{g}}$), and ii) the plastic modulus \bar{K}_p at $\bar{\underline{g}}$. Dafalias and Herrmann (1980) employed the radial mapping rule illustrated in Figure 3.42 such that

$$K_p = \hat{K}_p [\bar{K}_p, \delta, \delta_0, (K_p)_0], \quad (3.8.1.1)$$

where $(K_p)_0$ is the plastic modulus at $\delta = \delta_0$. To ensure a smooth transition from reloading to virgin or prime loading, the function \hat{K}_p must guarantee that $K_p = \bar{K}_p$ when $\delta = 0$. This mapping rule also requires that the limit line be straight to avoid mapping to points outside it.

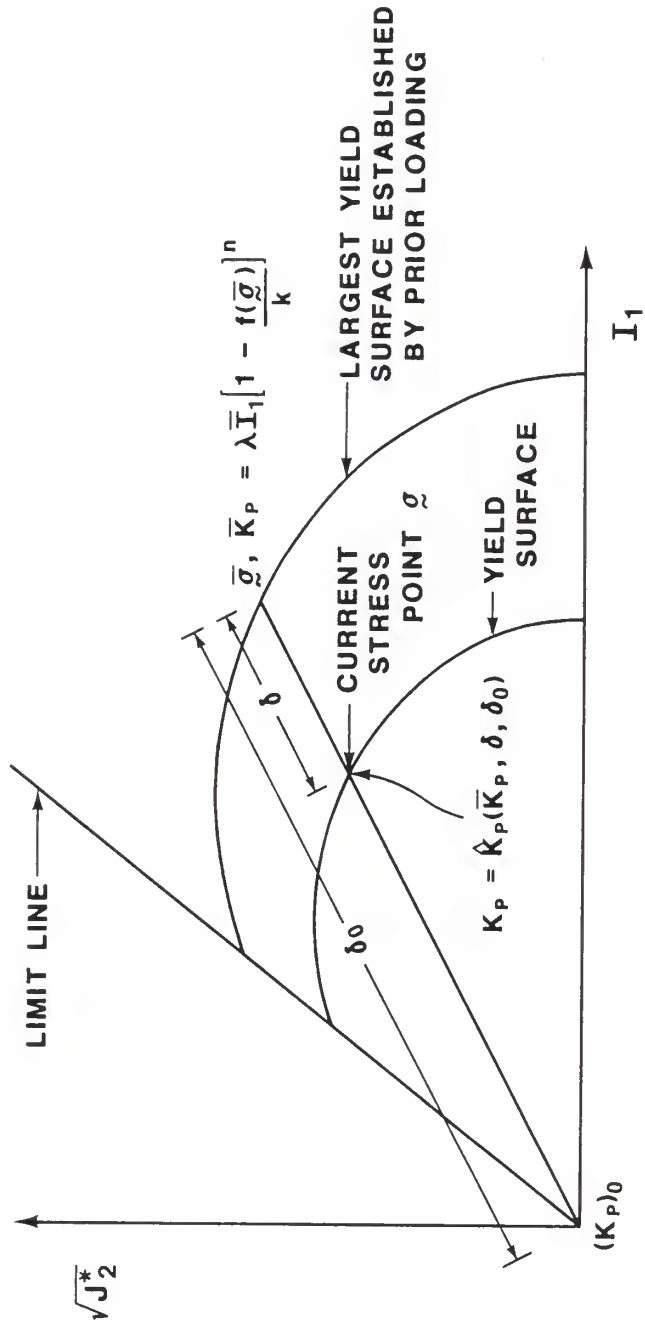


Figure 3.42 Conventional bounding surface adaptation with radial mapping rule

Since a radial line connects the current stress state (\underline{g}) with the image state ($\bar{\underline{g}}$), we can write

$$\bar{\underline{g}} = \beta \underline{g}, \quad \beta \geq 1, \quad (3.8.1.2)$$

where β is a positive scalar. The equations for computing the mapping quantity β directly from the current state of stress and the size of the bounding surface are presented in Appendix F.

The Euclidean distance between the origin and the image point (δ_0), and the distance between the current stress state and the image point (δ) are

$$\delta_0 = \beta \sqrt{(\sigma_{ij}\sigma_{ij})} \quad (3.8.1.3)$$

and

$$\delta = (\beta - 1) \sqrt{(\sigma_{ij}\sigma_{ij})}, \quad (3.8.1.4)$$

respectively.

Therefore, once β is computed from a knowledge of the size of the boundary surface $(I_0)_p$ and the current stress point, the stress state $\bar{\underline{g}}$ can be located and used to compute the "virgin" bounding plastic modulus \bar{K}_p . For this stress-dependent formulation only $\bar{\underline{g}}$ is needed to calculate \bar{K}_p .

To complete the formulation, a specific form for the function \hat{K}_p (equation 3.8.1.1) must now be selected. Zienkiewicz and Mroz (1984) proposed the form

$$K_p = \bar{K}_p [\delta_0 / (\delta_0 - \delta)]^\gamma = \bar{K}_p \beta^\gamma, \quad (3.8.1.5)$$

which is adopted here because it adds only one more parameter (γ) to the existing list. If γ is constant, plastic response is cyclically stable, but in general, it may be considered a function of the number of load repetitions, etc. to simulate cyclic hardening or softening. Notice from equation 3.8.1.5 that $K_p \rightarrow \infty$ as $\delta \rightarrow \delta_0$.

On the hydrostatic axis, observe that

$$\beta = (I_0)_p / I_1,$$

where $(I_0)_p$ is the size (or intersection with the hydrostatic axis) of the boundary surface. By using the plastic modulus formula (equation 3.4.7) and the previous equation, the plastic modulus at the bound on the hydrostatic axis is found to be

$$\bar{K}_p = \lambda (I_0)_p = \lambda \beta I_1. \quad (3.8.1.6)$$

Substituting this equation into the mapping function (equation 3.8.1.5) gives

$$K_p = \lambda I_1 (\beta)^{\gamma+1} = \lambda I_1 [(I_0)_p / I_1]^{\gamma+1}, \quad (3.8.1.7)$$

which in turn yields the following equation for the plastic volumetric strains generated on spherical reloading:

$$\epsilon_{kk}^p = \frac{1}{\lambda x} (A^x - B^x), \quad A > B \quad (3.8.1.8)$$

where

$$A = [I_1 / (I_0)_p] \text{ at the end of reloading,}$$

$$B = [I_1 / (I_0)_p] \text{ at the start of reloading,}$$

$$\epsilon_{kk}^p = \text{plastic volumetric strain caused by reloading from B to A,}$$

and

$$x = \gamma + 1.$$

This equation provides a simple method for initializing γ .

Although one might exist, the writer was not able to find a closed-form solution for "x" ($= \gamma + 1$) in equation 3.8.1.8, so a trial and error procedure was adopted.

3.8.2 Prediction of Cavity Expansion Tests

With two additional refinements, the version of the bounding surface theory described in the previous section has been implemented in a finite element routine to predict a series of cavity expansion tests (Seereeram and Davidson, 1986). The first improvement is the freedom accorded the parameter R (of equation 3.3.1.6) to match the deviatoric shape of the failure surface. It is no longer forced to coincide with the Mohr-Coulomb criterion in extension. Instead, R is now a material constant which is calculated directly from the (generally unequal) friction angles observed in compression (ϕ_c) and extension (ϕ_e) tests,

$$R = [\sin \phi_e / \sin \phi_c] [(3 - \sin \phi_c) / (3 + \sin \phi_e)]. \quad (3.8.2.1)$$

A second modification was effected to predict a softer response in extension tests, as the data of Saada et al. (1983) suggests. To accomplish this, the exponent "n" of the plastic modulus equation (equation 3.4.7) was made a function of Lode's parameter θ ,

$$n = n^* / g(\theta), \quad (3.8.2.2)$$

where n^* is the exponent applicable to compression tests and $g(\theta)$ is as defined in equation 3.3.1.6. This change causes the shape of the iso-plastic moduli contours on the deviatoric plane to differ from the trace of the specified failure locus.

In retrospect, the writer must admit that these modifications were perhaps not necessary; they do not seem to have as much an impact on the predictions as originally thought. Therefore, in future studies, consideration should be given to omitting both of them.

A self-boring pressuremeter probe, implanted in a large-scale triaxial chamber, provided the necessary experimental data for this study (Davidson, 1983). The soil tested, Reid-Bedford Sand, was the

same as that investigated by Saada et al. (1983) and Linton (1986), except that the relative density was about 7% higher.

Table 3.8 summarizes from Davidson (1983) essential information regarding the five pressuremeter tests analyzed. Included in this table are the initial vertical and horizontal stresses, and the elastic stress-strain and strength parameters [derived from the data using the elastic-perfectly frictional "plastic" method of interpretation proposed by Hughes et al. (1977)]. Notice that tests #2 and #3 as well as tests #4 and #5 were nominally replicate experiments. The reproducibility of these data (later see Figures 3.45 and 3.46 for example) gave the writer the needed confidence to proceed with such a rigorous solution.

Selection of the material parameters for the pressuremeter simulations was not a simple task because the element tests of Saada et al. (1983) and Linton (1986) may not manifest the real behavior of Reid-Bedford sand. Table 3.9 lists the model parameters used in the finite element analysis, and these were selected on the following basis:

1. The strength parameter k used in all simulations was computed from an average of the friction angles listed in Table 3.8.
2. A unique (constant) elastic shear modulus was input for each numerical prediction, and these were calculated directly from the small unload-reload loop common to all pressuremeter tests (Table 3.8 provides this information).
3. The material constants N , Q , b , and n were assumed to be the same as that for Reid-Bedford sand at 75% relative density (see Table 3.4). Judging from Table 3.5, these parameters do not seem to be affected much by changes in the relative density.

Table 3.8 Summary of Pressuremeter Tests in Dense Reid-Bedford Sand

	TEST IDENTIFICATION				
	#1	#2	#3	#4	#5
Initial relative density D_r (%)	83.2	84.8	85.8	83.2	81.1
Initial vertical stress (kPa)	45.5	155.	157.	265.	265.
Initial horizontal stress (kPa)	20.7	46.2	51.7	84.8	92.4
Observed lift-off pressure (kPa)	35.9	46.2	51.7	84.8	92.4
Estimated shear modulus (MPa)	45.6	55.2	55.2	82.7	82.7
Friction angle, ϕ	39.5°	41.7°	41.3°	41.2°	39.2°

Note: Tests # 2 and #3 as well as #4 and # 5 were intended to be replicate experiments

Table 3.9 Model Constants Used to Simulate Pressuremeter Tests

PARAMETER	MAGNITUDE
<u>Elastic Constants</u>	
Elastic shear modulus, G for test #1	45610 kPa
for tests #2 & #3	55160 kPa
for tests #4 & #5	82740 kPa
(extracted from Table 3.7)	
Poisson's ratio, ν	0.2
<u>Flow Parameters</u>	
Slope of zero dilation line, N	.218
Shape controlling parameter of consolidation portion of yield surface, Q	2.60
Shape controlling parameter of dilation portion of yield surface, b	15.0
<u>Plastic Modulus Parameters</u>	
Plastic compressibility parameter, λ	580
Strength parameter, k	.325
Parameter to model curvature of failure meridian, m	0
Shape hardening controlling exponent n	2
<u>Non-standard Parameters</u>	
Ratio of radius of failure surface in extension to compression, R	.7
Bounding surface reload modulus parameter, γ	15

Note: the parameters G and k were calculated from data reported by Davidson (1983), λ and γ from Linton (1986), and the remainder from Saada et al. (1983).

Note that in this theory the slope of the zero dilation line, N , does not vary at all with porosity.

4. The reload modulus parameter γ was reckoned from a series of unload-reload hydrostatic compression tests reported by Linton (1986). Also calculated from Linton's experiments was the plastic bulk modulus parameter λ ; it was found to be about twice as large as that computed from a similar test by Saada (see Table 3.4 and Figure 3.18). However, because Linton repeated many tests, using different types and combinations of strain measuring devices, all of which gave consistent results, his characterization was chosen.
5. Finally, the parameter R was estimated from the constant mean pressure compression and extension tests (GC 0 and GT 90) of the series of experiments reported by Saada et al. (1983).

Figure 3.43 gives the nodal point and element information of the finite element idealization of the expanding cavity problem. Observe from this figure that the radius of the pressuremeter's cavity is equal to 40.8 mm, and the distance from the centerline of the cavity to the lateral boundary of the chamber is equal to 607 mm. Also, note the assumption of plane strain for the boundary conditions and the fact that the lateral periphery of the calibration chamber does not move. Studies by Laier et al. (1975), Hartmann and Schmertmann (1975), and Hughes et al. (1977) support the hypothesis that the pressuremeter cavity expands under conditions of axial symmetry and plane strain.

The numerical results of the five tests are superposed with the experimentally measured data in Figures 3.44 to 3.48. Cavity strain in these plots is defined as the average radial displacement of three

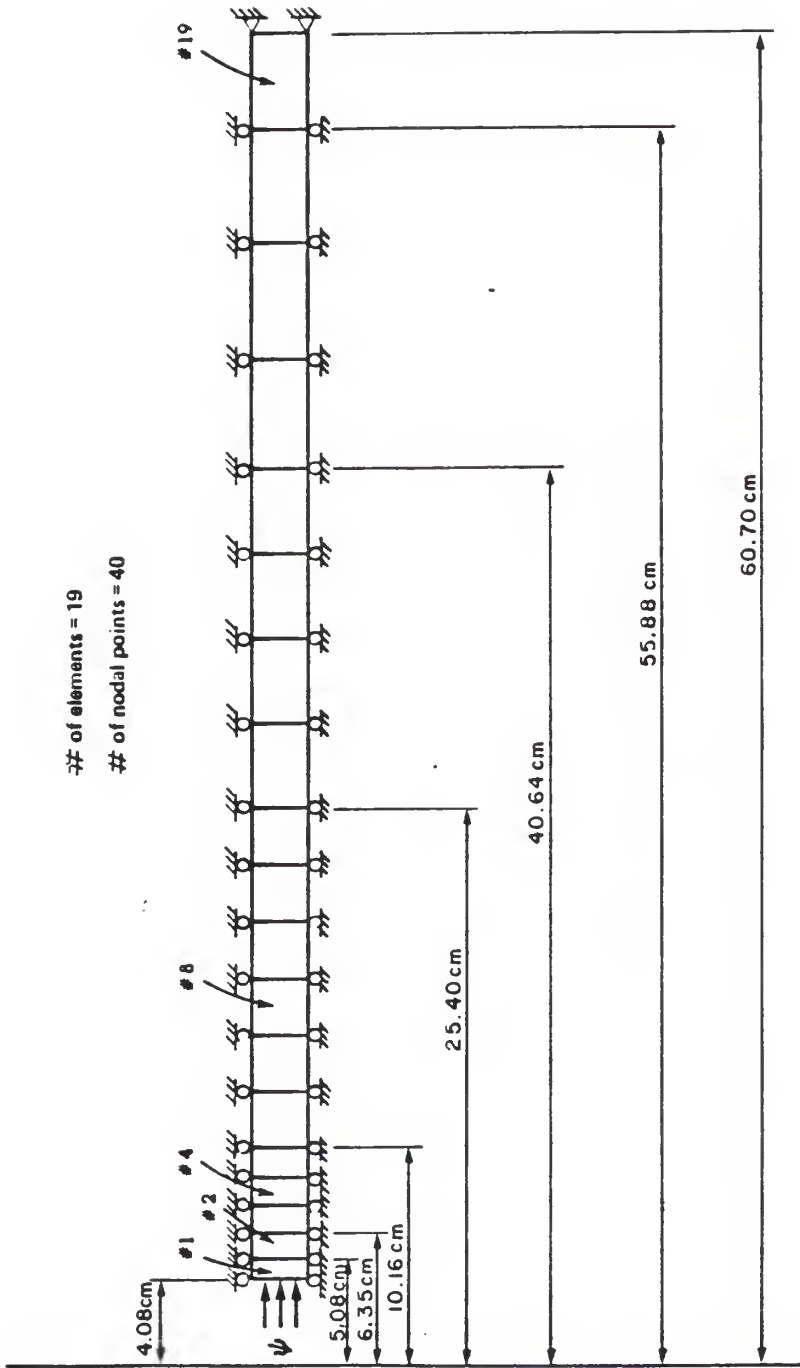


Figure 3.43 Finite element mesh used in pressuremeter analysis (after Seereram and Davidson, 1986)

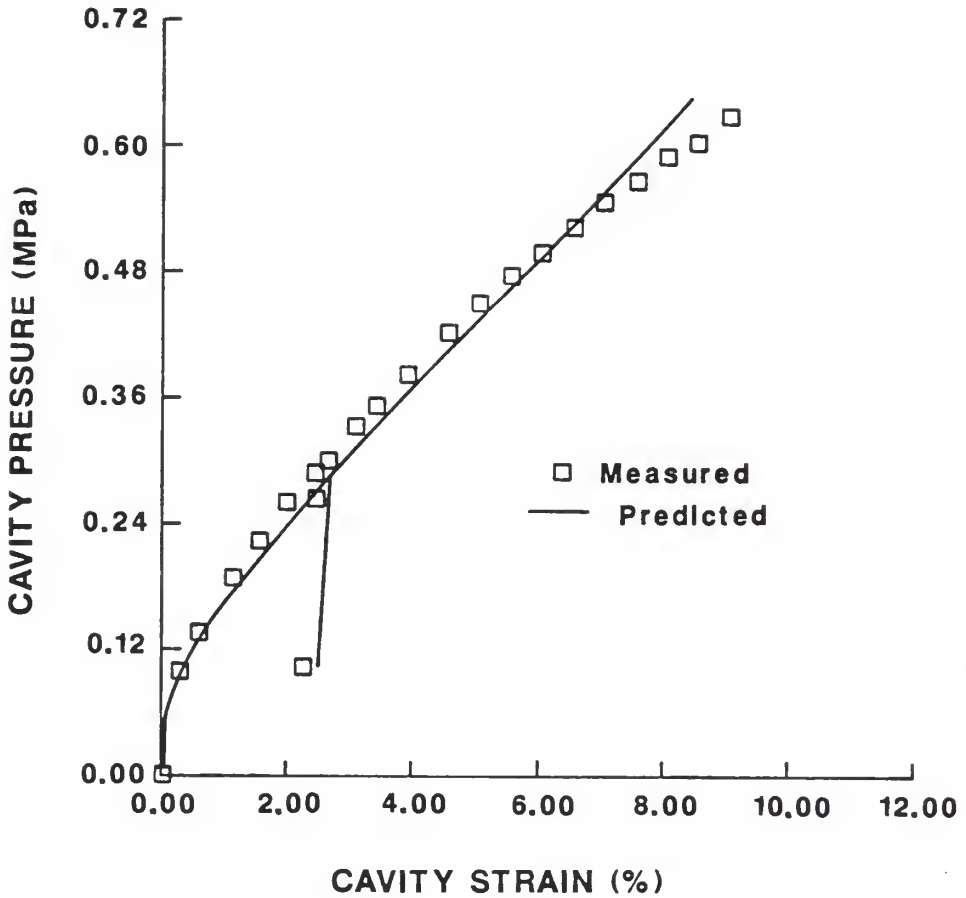


Figure 3.44 Measured vs. predicted response for pressuremeter test #1 (after Seereeram and Davidson, 1986)

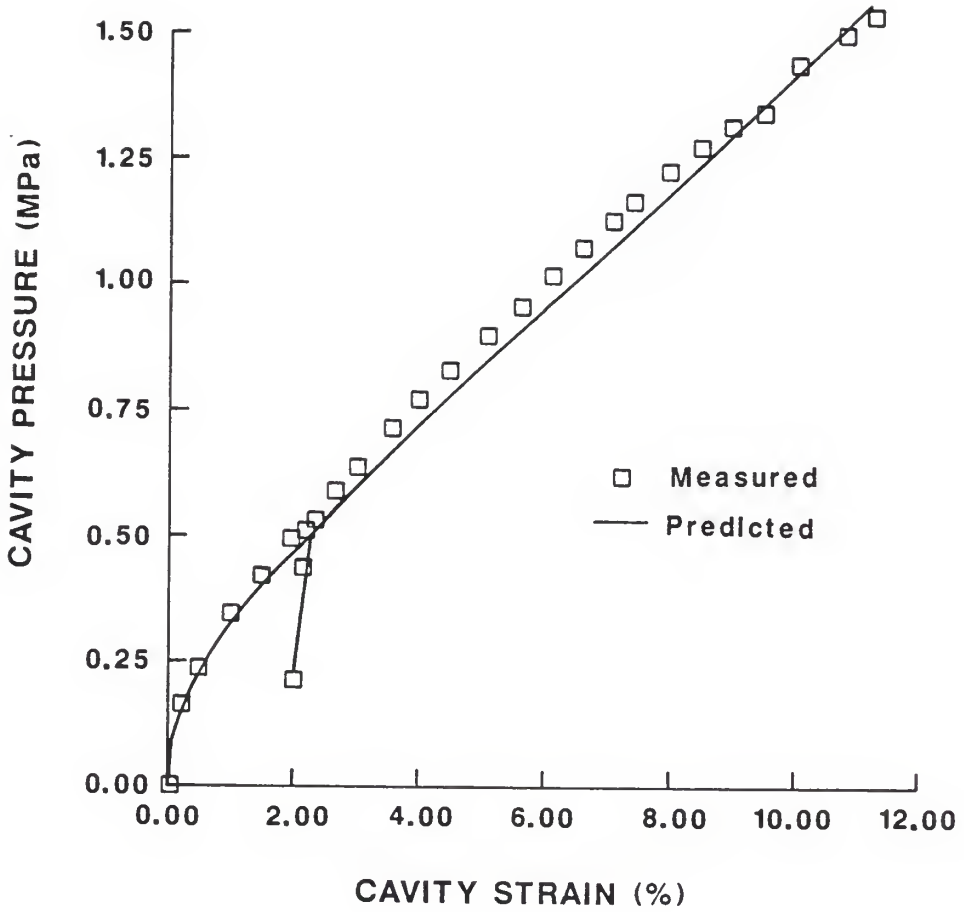


Figure 3.45 Measured vs. predicted response for pressuremeter test #2 (after Seereeram and Davidson, 1986)

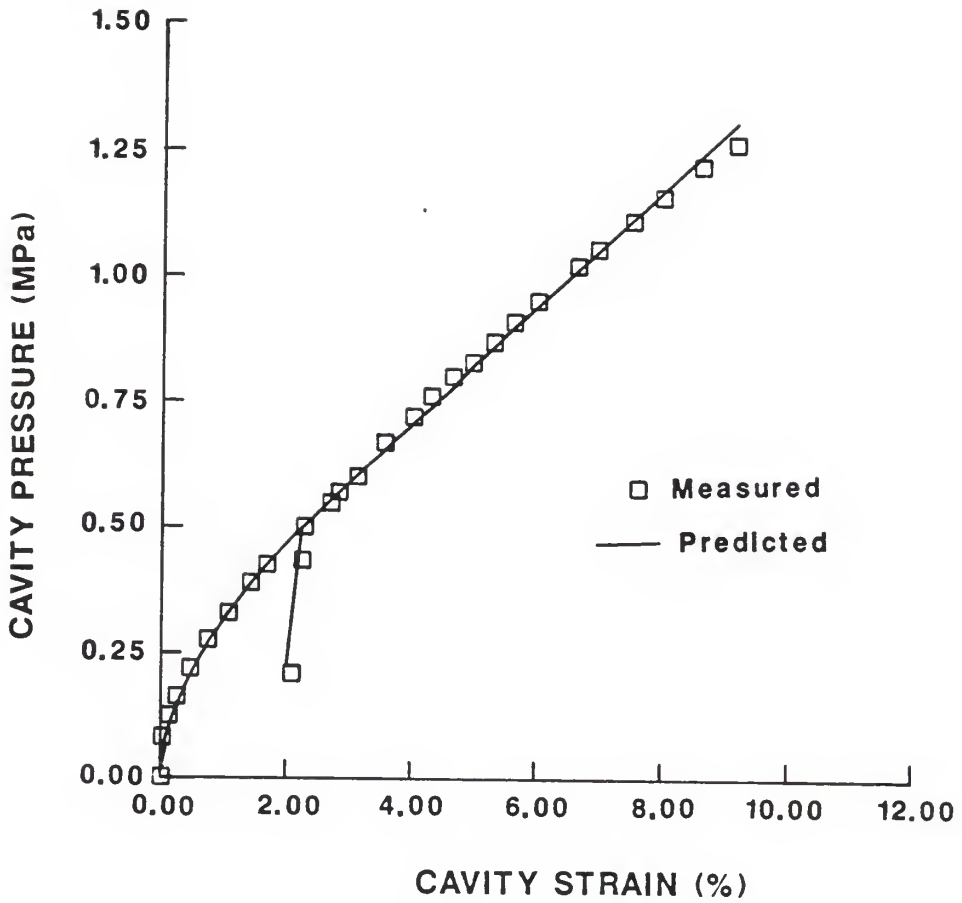


Figure 3.46. Measured vs. predicted response for pressuremeter test #3 (after Seereeram and Davidson, 1986)

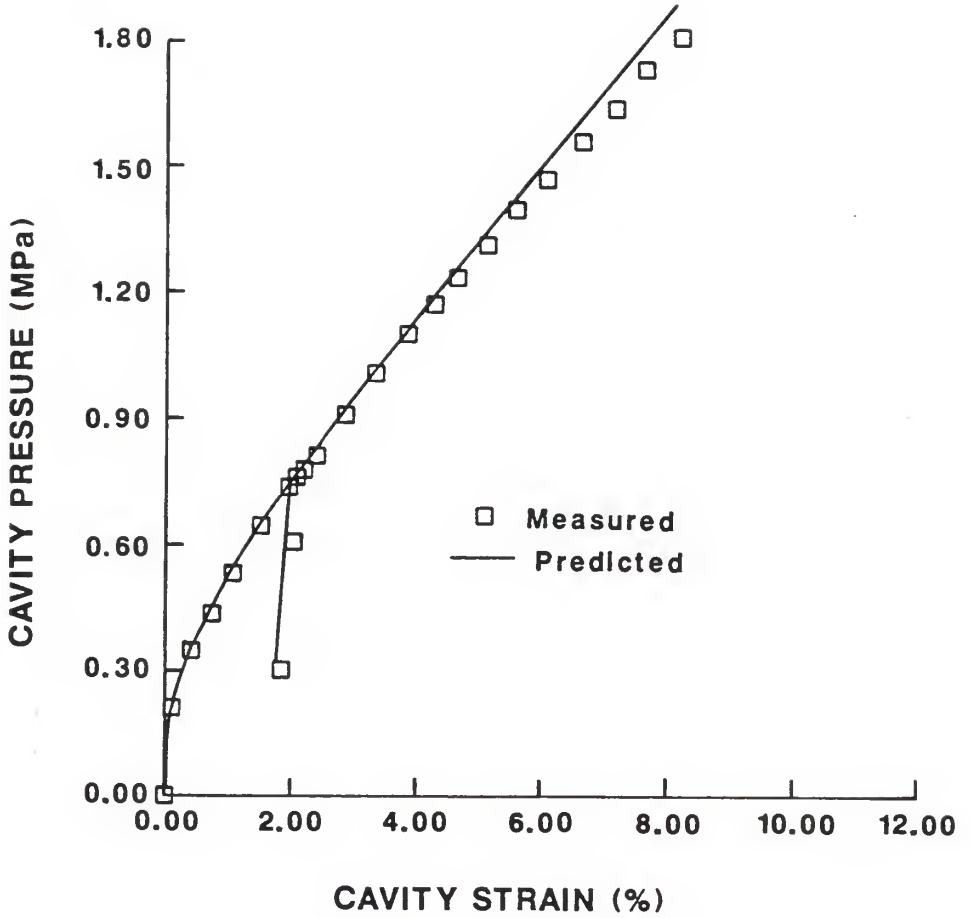


Figure 3.47 Measured vs. predicted response for pressuremeter test #4 (after Seereeram and Davidson, 1986)

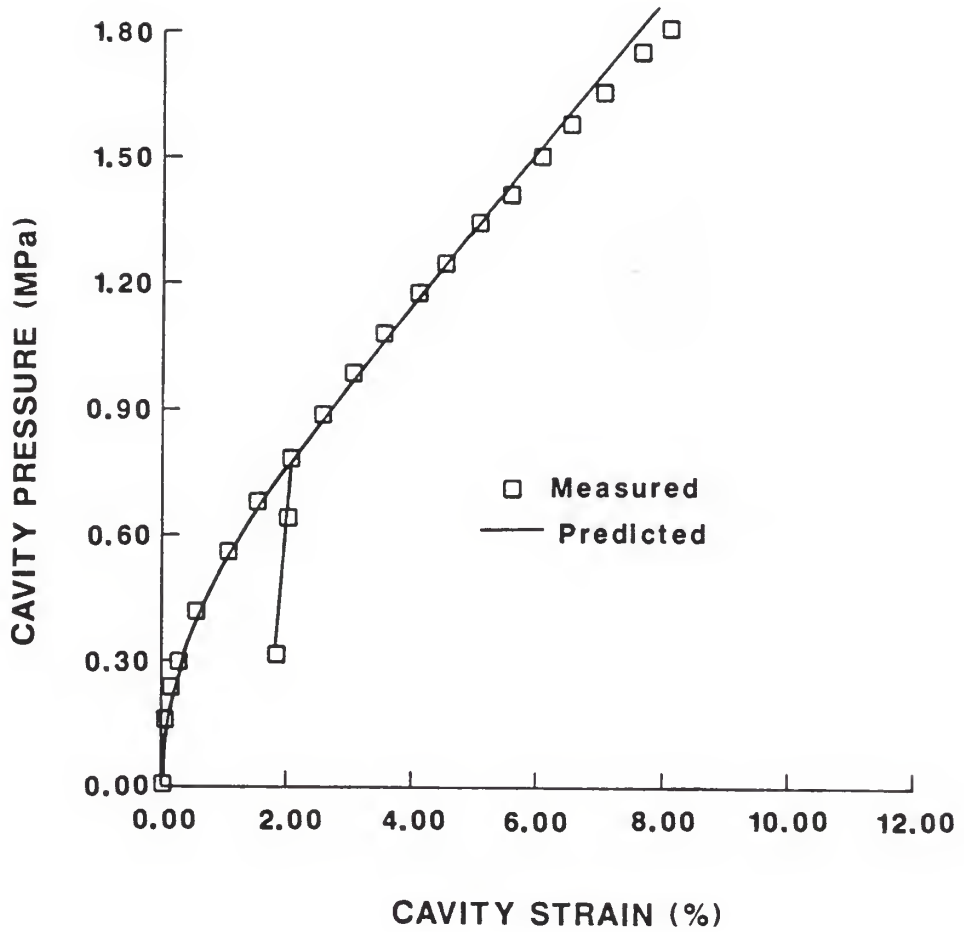


Figure 3.48 Measured vs. predicted response for pressuremeter test #5 (after Seereeram and Davidson, 1986)

symmetrically positioned "feeler" arms, divided by the radius of the undeformed cavity. In each prediction, 200 load steps were used for the initial loading, 50 steps for the small unloading, and 300 steps for the final loading.

The remarkably close agreement between the measured and predicted curves suggests that a) the constitutive idealization is indeed a good approximation to reality for this test path, b) the assumption of plane strain is valid, c) the pressure-expansion tests are free of any major sources of experimental error, and d) the conventional procedure for computing the friction angle ϕ from pressuremeter data, as outlined in Davidson (1983), is rational.

Detailed results, originating from the finite element output, permitted an inspection of the typical predicted stress path and the stress distribution in the zone of influence of the expanding cylindrical cavity. In the graphs that follow, σ_r , σ_z , and σ_θ denote respectively the radial, axial, and circumferential components of the stress tensor in cylindrical coordinates. Figure 3.49 shows the typical variation of the principal stresses with monotonically increasing cavity pressure. The variation of the predicted Lode angle θ , an indicator of the relative magnitude of the intermediate principal stress, is also shown on this plot. Its significance becomes apparent when related to Figure 3.50, which shows the variation of plastic stiffness in selected elements. Notice that the material response is softest when the Lode angle is minus 30° , or alternatively, when $\sigma_r = \sigma_z$ ($\sigma_1 = \sigma_2$). This spectacular drop in stiffness is a direct consequence of the connection imposed between the exponent "n" and the Lode angle θ in equation 3.8.2.2. The stiffness increases as the Lode angle increases toward a

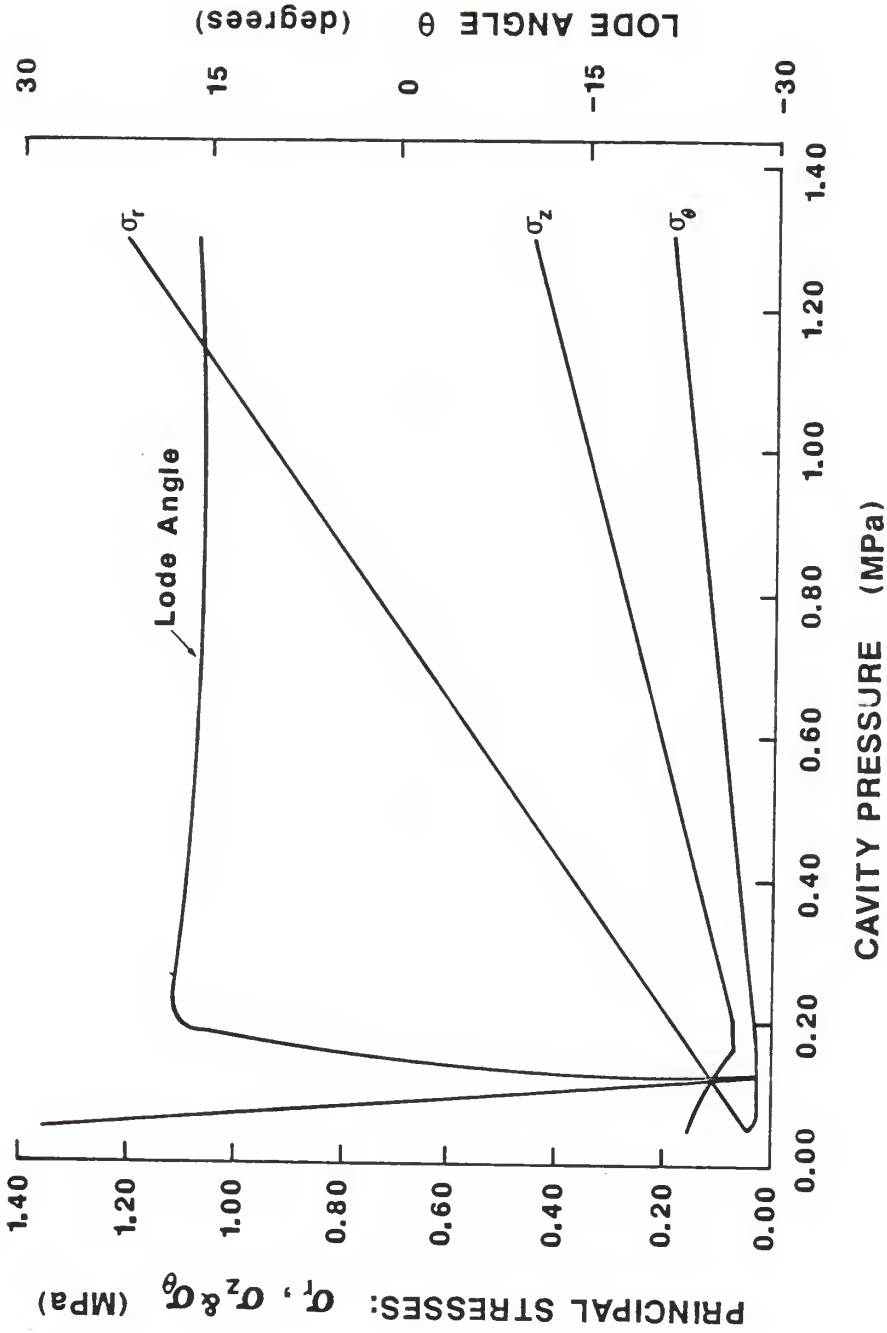


Figure 3.49 Variation of principal stresses and Lode angle with cavity pressure for element #1 and pressuremeter test #2 (after Seeceream and Davidson, 1986)

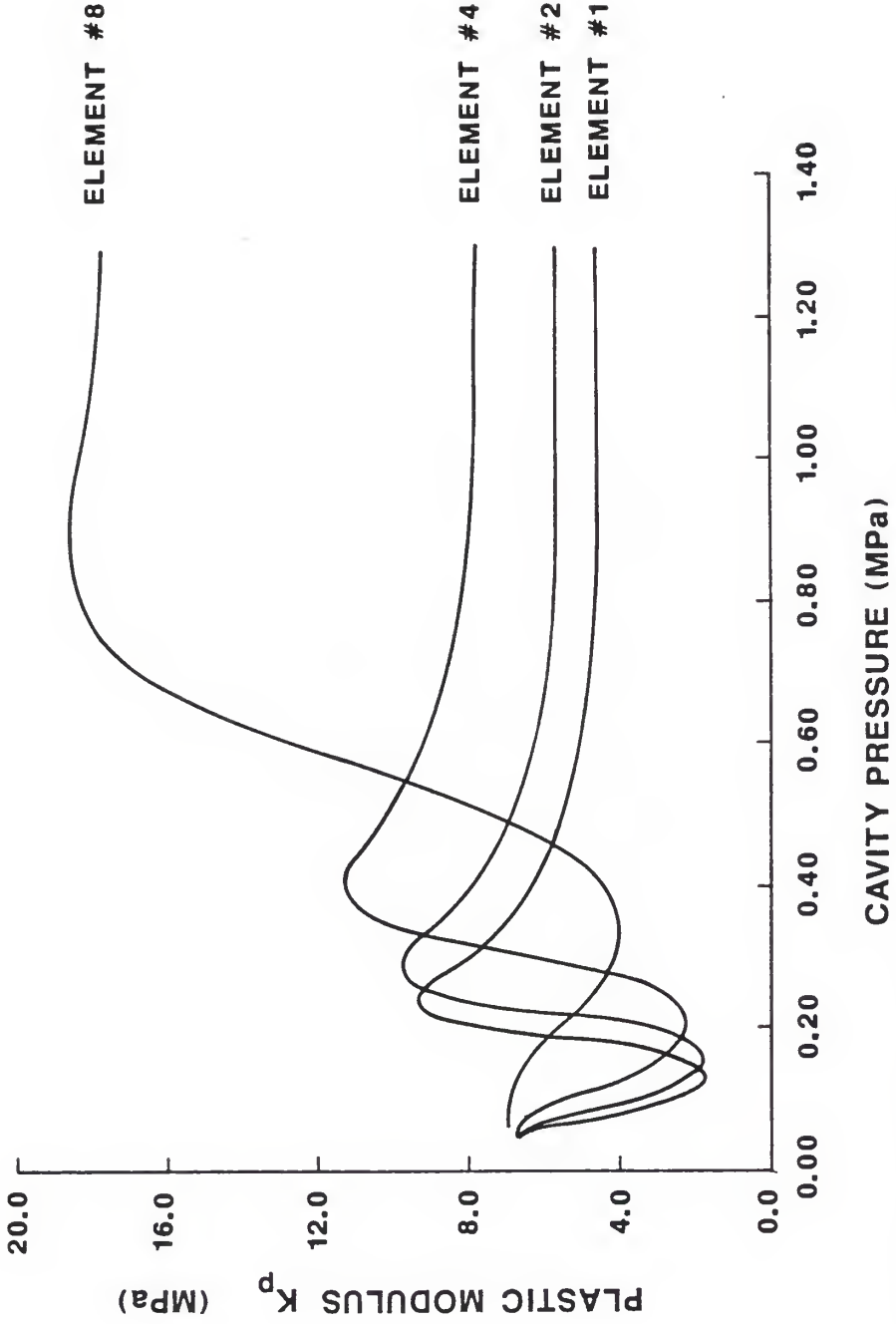


Figure 3.50 Variation of plastic modulus with cavity pressure for pressuremeter test #2 (after Seereeram and Davidson, 1986)

steady magnitude of about $+15^\circ$, and once there, the plastic modulus decreases again.

Figure 3.51 gives a different view of the stress path in which its relative position with respect to the zero dilatancy line and the failure envelope is emphasized. It appears that, for this particular boundary condition, the soil element does not undergo plastic dilation, but compacts as it is being sheared. Also note from this figure that the reloading path more or less retraces the unloading path, and so the actual shape of the bounding surface does not really matter--virgin response reinitiates at the point of unloading.

The importance of minimizing disturbance to the surrounding soil is emphasized in Figure 3.52, which shows the distribution of principal stresses with radial distance from the cavity wall. Very high stress gradients exist in the small annular region of soil within a few centimeters of the probe. Any significant remoulding in this region due to the field drilling procedure may result in meaningless pressure-expansion data.

3.8.3 Proposed Hardening Modification

Recall that a hardening control surface is defined here as a surface which encloses the totality of points where the purely stress-dependent plastic moduli are higher than their virgin loading magnitudes. As pointed out previously, experimental studies indicate that the shape of the hardening control surface does not resemble the shape of the yield surface relevant to the simple theory. Poorooshasb et al. (1967) and Tatsuoka and Ishihara (1974b) have found, using a

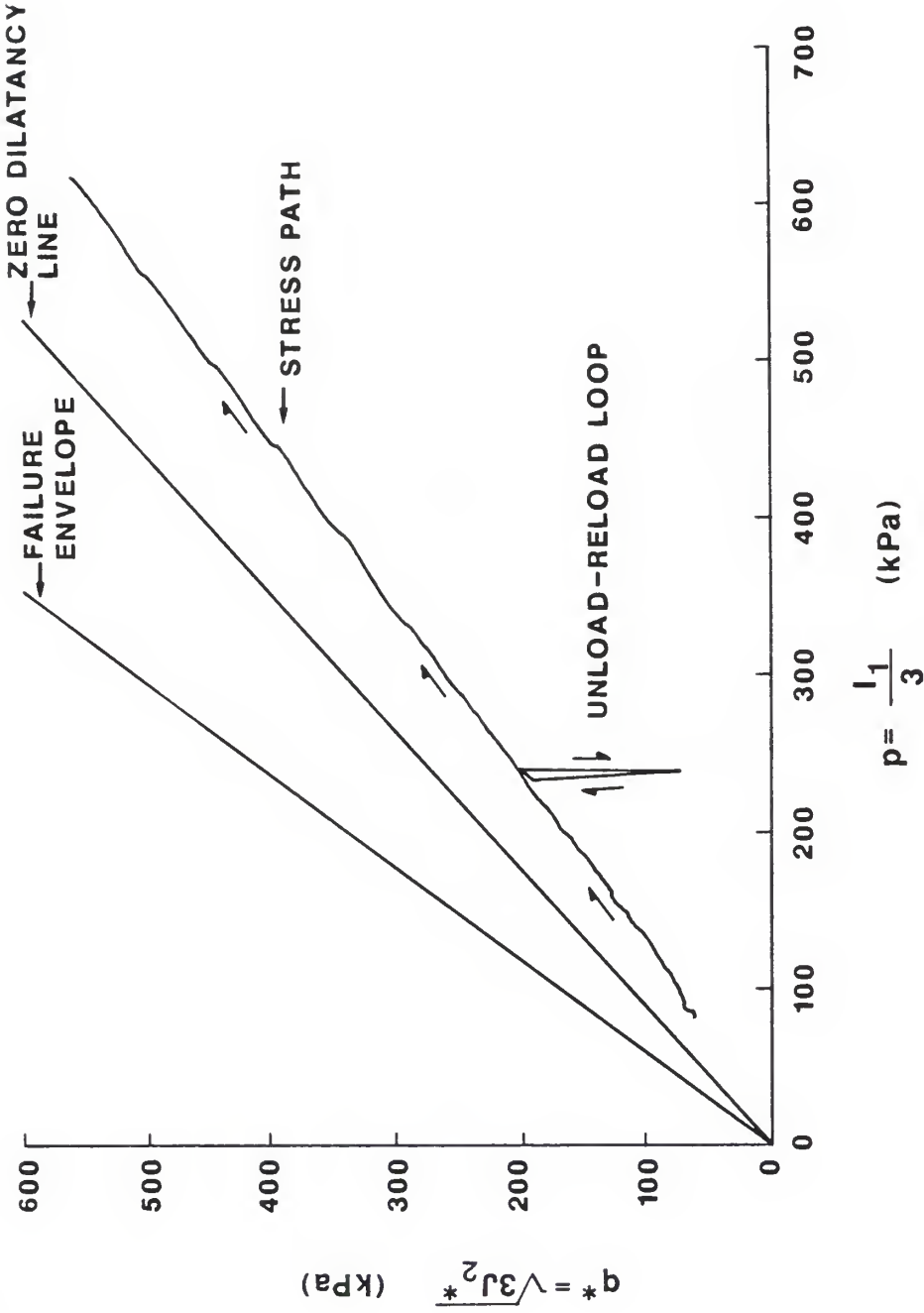


Figure 3.51 Meridional projection of stress path for element #1, pressuremeter test #2 (after Seereeram and Davidson, 1986)

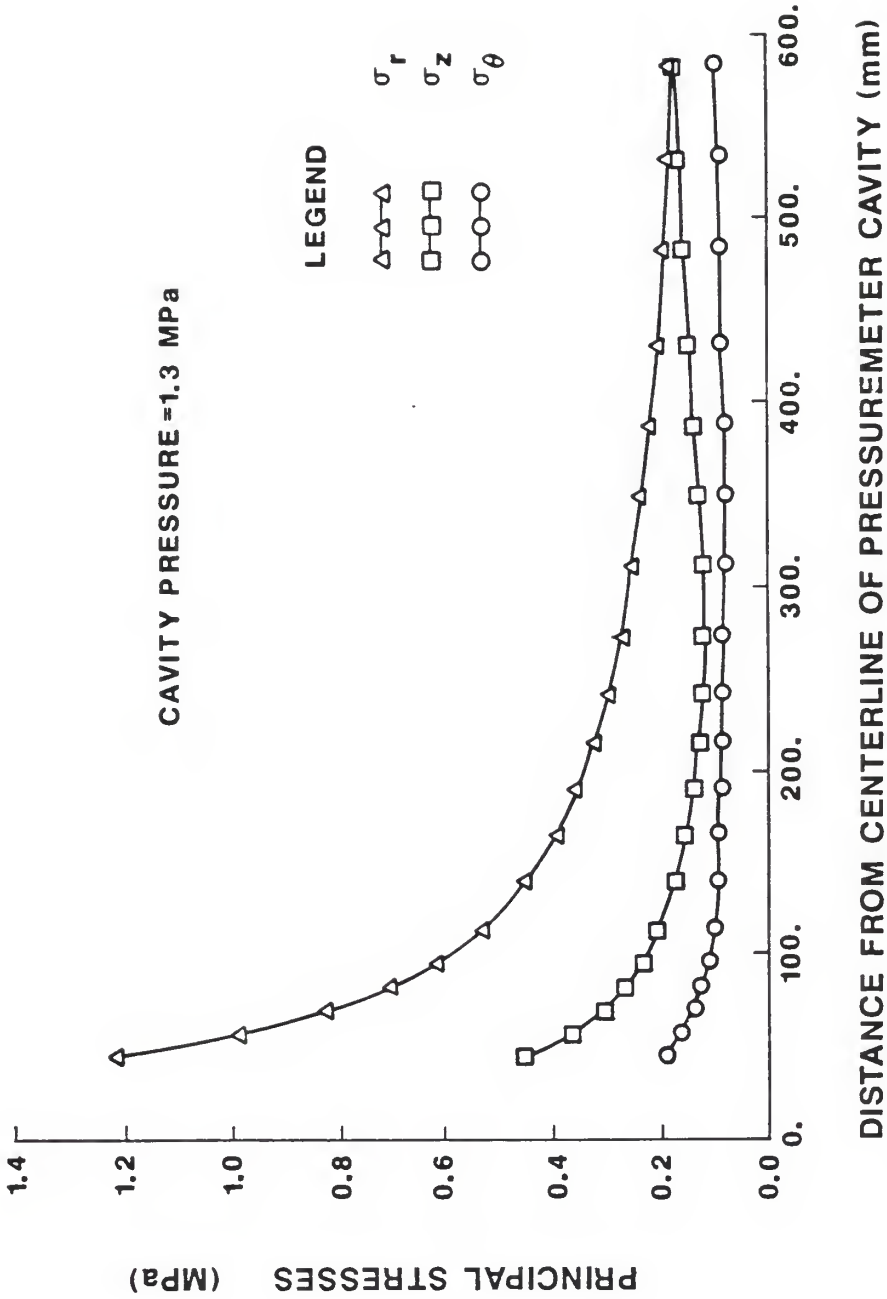


Figure 3.52 Principal stresses as a function of radial distance from axis of cavity at end of pressuremeter test #2 (after Seereeram and Davidson, 1986)

variety of experimental stress probes, that these surfaces have shapes similar to that of the limit surface.

Using the stress paths drawn in Figure 3.53, together with a Taylor-Quinney (1931) definition of "yield" (as depicted in Figure 2.8), Tatsuoka and Ishihara (1974b) have sketched the family of hardening control surfaces shown in Figure 3.54. For simplicity, it is assumed that these surfaces are smaller versions of the limit surface. So, for a straight line failure envelope, a hardening control surface F_p is defined by the maximum q/p ratio established by the loading history.

For the more general form of the failure surface (equation 3.4.9), the current mobilized stress ratio k_{mob} is

$$k_{mob} = (I_1/p_a)^m \frac{\sqrt{J_2^*}}{I_1} \quad (3.8.3.1)$$

As the stress point approaches the limit envelope, $k_{mob} \rightarrow k$. If unloading takes place (i.e., k_{mob} decreases), the maximum magnitude of k_{mob} is recorded and labelled the memorized stress ratio k_{mem} . This magnitude then specifies the size of the "boundary" or hardening control surface.

At any instant therefore, three stress ratios are known: i) a fixed magnitude k (which is the size of the stationary limit surface), ii) the current mobilized stress ratio k_{mob} , and iii) the memorized stress ratio k_{mem} (or the historical maximum of k_{mob}). If $k_{mob} = k_{mem}$, the virgin plastic modulus given by equation 3.4.7 is applicable, but if $k_{mob} < k_{mem}$ (a shear preloading), a stiffer modulus must be stipulated.

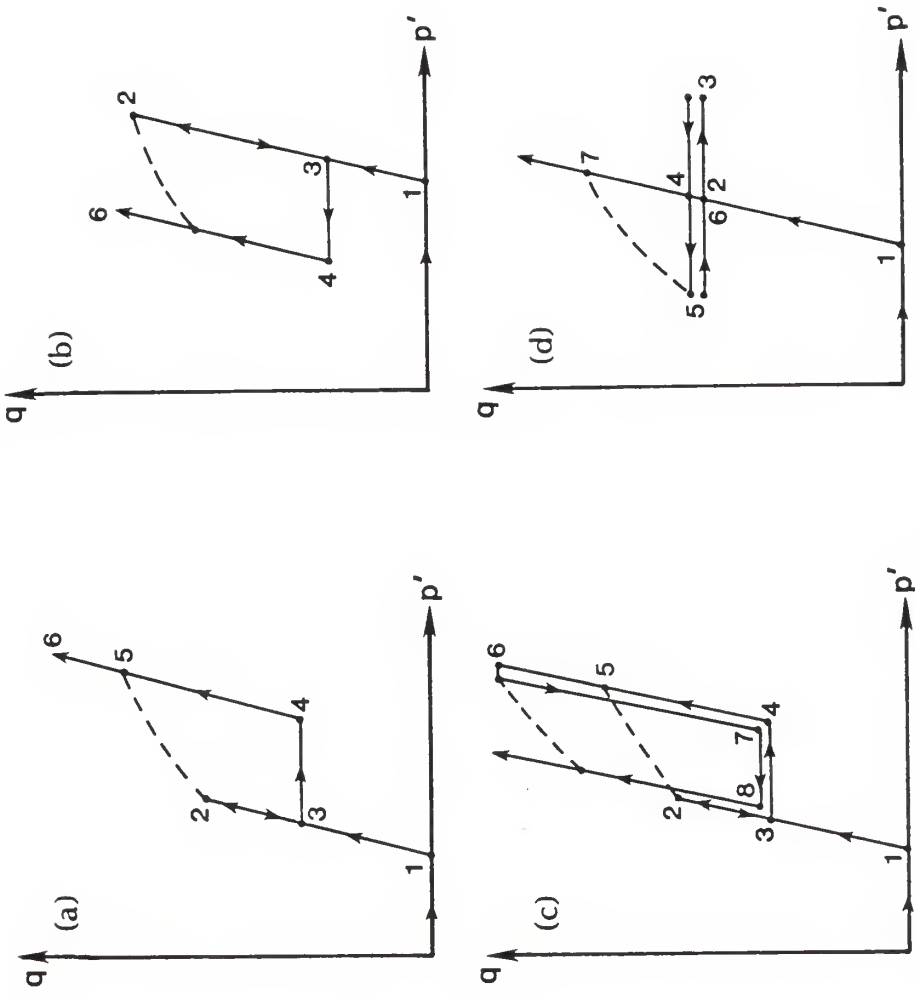


Figure 3.53 Experimental stress probes of Tatsuoka and Ishihara (1974b)

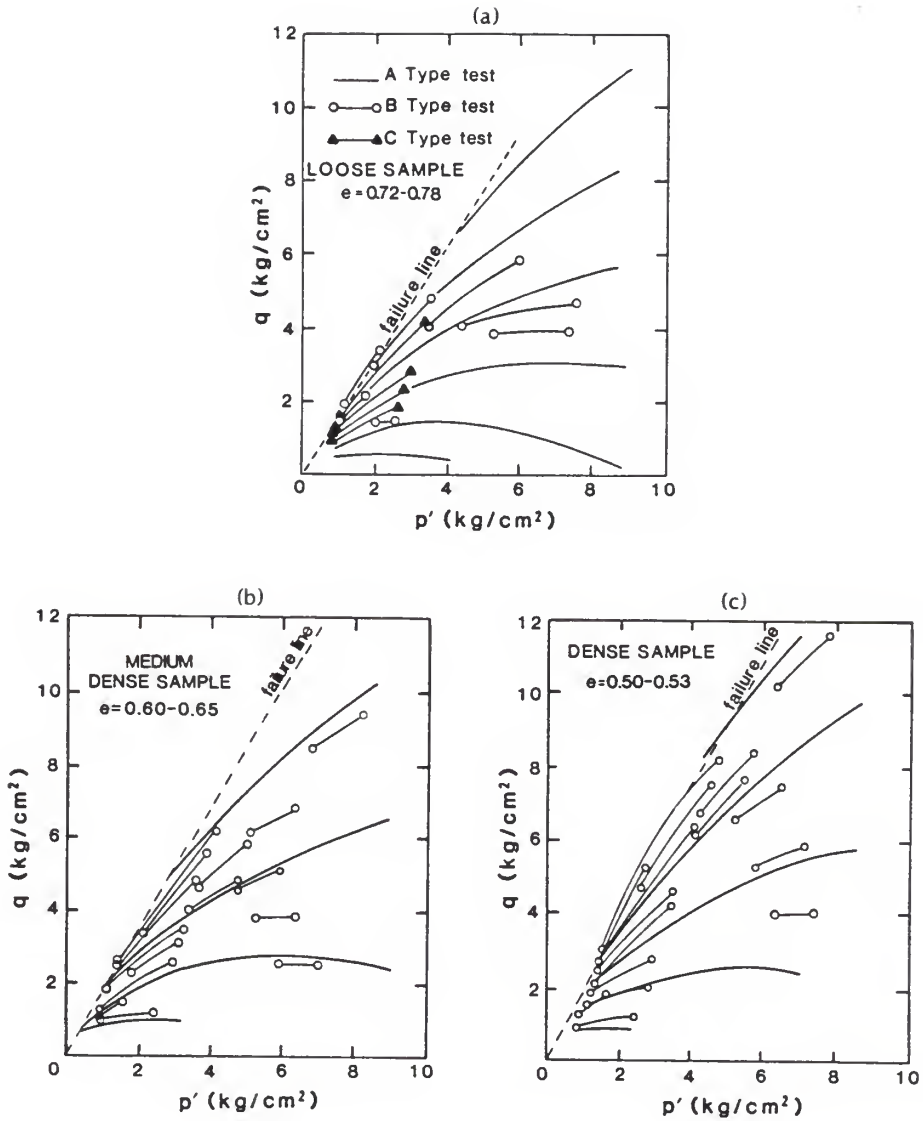


Figure 3.54 Shapes of the hardening control surfaces as evidenced by the study of Tatsuoka and Ishihara (1974b) on Fuji River sand

Equation 3.8.1.1 is again used to specify the reload modulus, and it is specialized here to

$$K_p = [(K_p)_0 - \bar{K}_p] \left(\frac{\delta}{\delta_0}\right)^{\gamma_1} + \bar{K}_p, \quad (3.8.3.2)$$

where γ_1 is a model constant. Observe that, as required, $K_p = \bar{K}_p$ when $\delta = 0$, and $K_p = (K_p)_0$ when $\delta = \delta_0$. In contrast to the previous bounding surface formulation, the origin of mapping is selected as the hydrostatic state on the octahedral plane containing the current stress point (Figure 3.55).

From equation 3.4.7, note that the virgin or prime plastic modulus \bar{K}_p at the conjugate point ($\bar{I}_1 = I_1, \sqrt{J_2}^*$) is simply

$$\bar{K}_p = \lambda I_1 [1 - (k_{\text{mem}}/k)]^n. \quad (3.8.3.3)$$

Also, recollect from equation 2.7.2.1 that the radius on the deviatoric plane is equal to $\sqrt{(2J_2)}$ so

$$\frac{\delta}{\delta_0} = (\sqrt{J_2}^* - \sqrt{J_2})/\sqrt{J_2} = [(k_{\text{mem}} - k_{\text{mob}})/k_{\text{mem}}]. \quad (3.8.3.4)$$

As in the first hardening option, the magnitude of the reload plastic modulus on the hydrostatic axis, $(K_p)_0$, is given by (cf. equation 3.8.1.7)

$$(K_p)_0 = \lambda I_0 [(I_0)_p/I_0]^{\gamma+1} = \lambda I_1 [(I_0)_p/I_1]^{\gamma+1}, \quad (3.8.3.5)$$

where $(I_0)_p$ is the point at which the largest yield surface intersects the hydrostatic axis (Figure 3.56). With \bar{K}_p , δ/δ_0 , and $(K_p)_0$ detailed in equations 3.8.3.3, 3.8.3.4, and 3.8.3.5 respectively, only the parameter γ_1 is needed to completely specify the reload modulus interpolation rule (equation 3.8.3.2).

But before completing the formulation, a shortcoming of equation 3.8.3.2 must be alluded to and amended. It occurs for shear paths

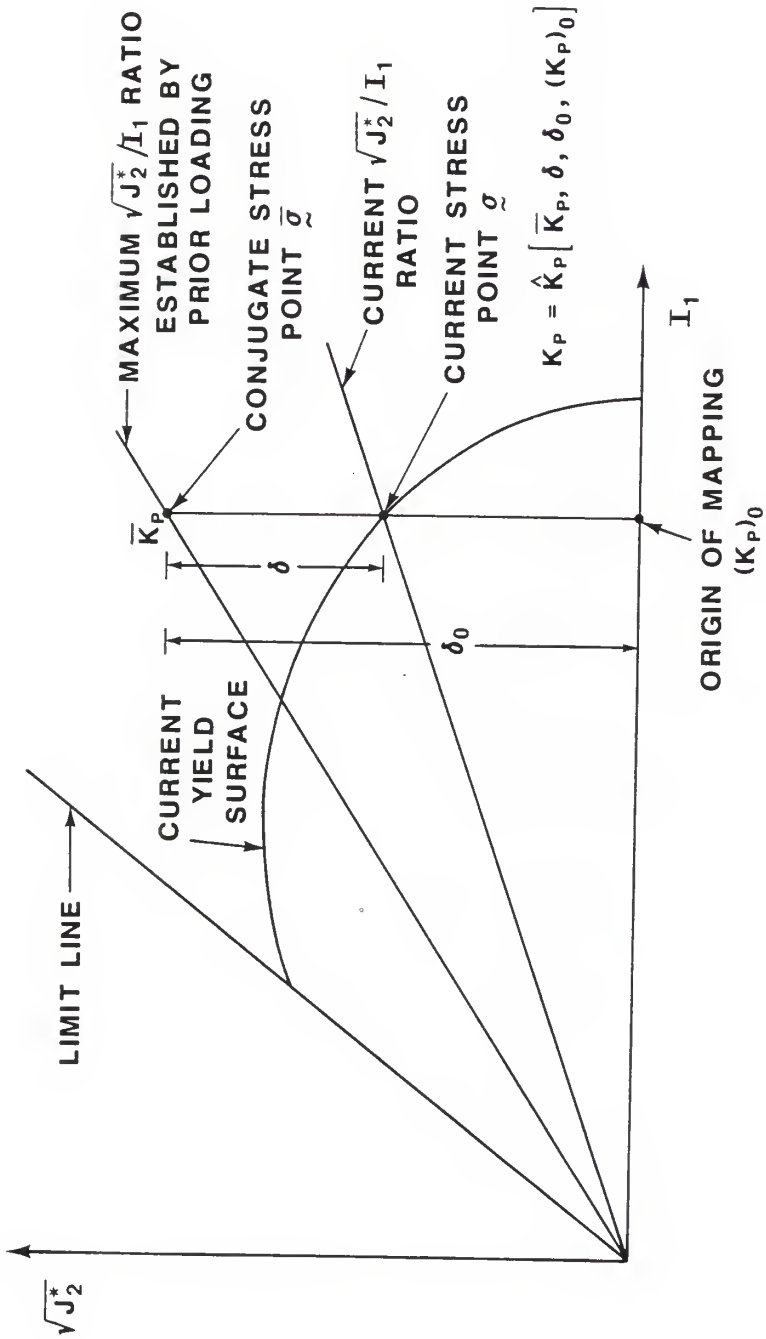


Figure 3.55 Illustration of proposed hardening control surface and interpolation rule for reload modulus

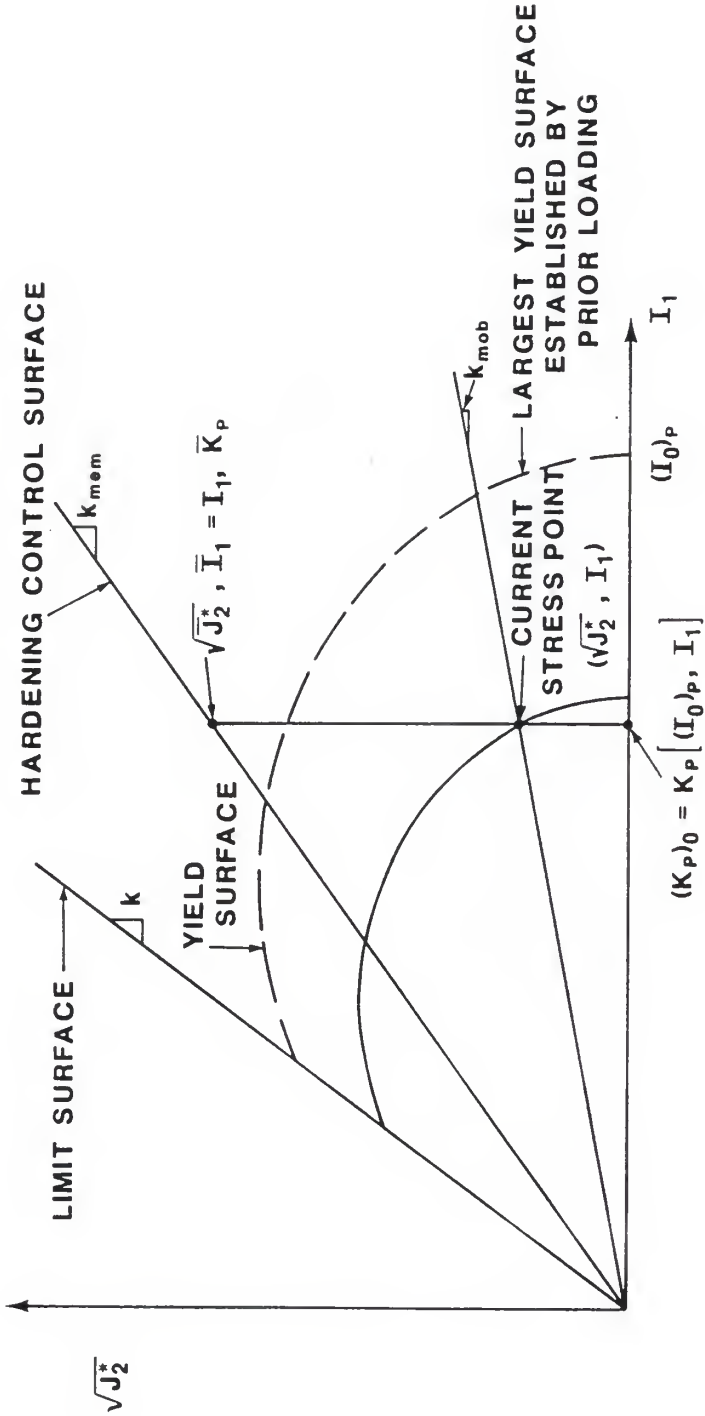


Figure 3.56 Illustration of the role of the largest yield surface (established by the prior loading) in determining the reload plastic modulus on the hydrostatic axis

following pure hydrostatic preconsolidation. Since in such a case k_{mem} is zero, no hardening is predicted for any subsequent shear path. The data of Hettler et al. (1984) in Figure 3.57 for a subsequent axial compression path contradicts this statement. Although any differences in the shear stress vs. axial strain and the dilative behavior are imperceptible, a conspicuous hardening effect shows up in the compaction volumetric strain. Consequently, a modification is sought to recognize isotropic or nearly isotropic preloading and to recover equation 3.8.3.5 as a special case for cyclic hydrostatic compression tests.

Since the preconsolidation process does not seem to have any effect on response in the dilation domain, it is not unreasonable to postulate that the effects of isotropic preloading should be ignored at some radial line at or below the zero dilation line. Such a modification can be effected by rewriting the plastic modulus formula (equation 3.4.7) as

$$K_p = \lambda I_1 (\beta')^{\gamma+1} \{1 - [f(\underline{\sigma})/k]\}^n, \quad (3.8.3.6)$$

where

$$\beta' = \beta \left[1 - \frac{\sqrt{J_2^*}}{X I_1 N} \right] + \frac{\sqrt{J_2^*}}{X I_1 N},$$

$X N$ = slope of the radial line beyond which "isotropic" preloading effects are ignored ($0 < X \leq 1$),

and β is the scalar radial mapping factor defined in equation 3.8.1.2.

In other words, the largest yield surface established by the prior loading acts somewhat like a cap to the "q/p" hardening control surface.

To test this hypothesis, the isotropically preloaded data of Figure 3.57 for Karlsruhe sand at 99% relative density was predicted using the relevant simple model parameters of Table 3.6 and the assumptions that
a) the entire elliptical portion of the yield surface acts as a cap to

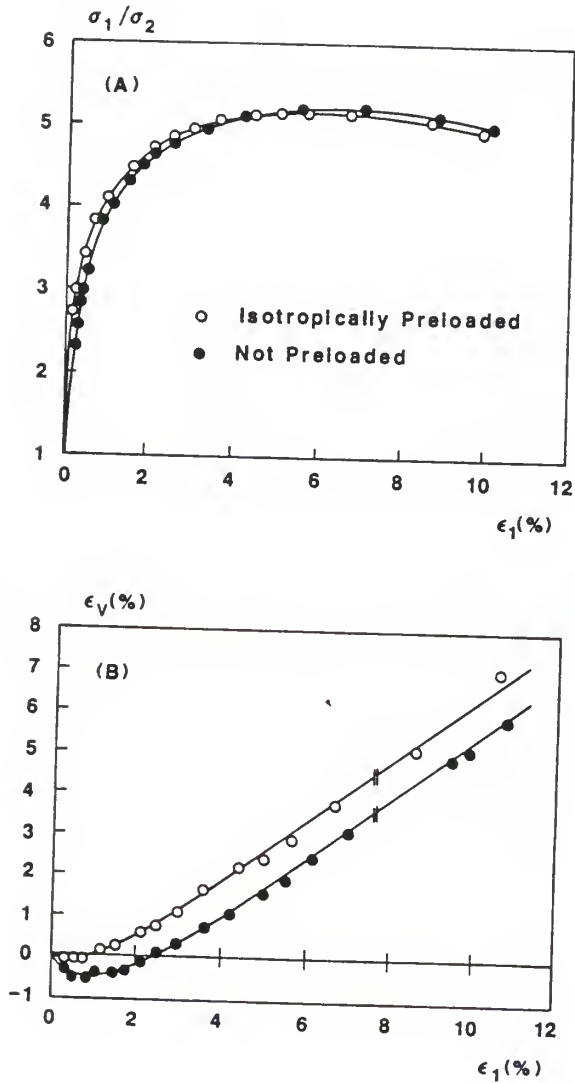


Figure 3.57 Influence of isotropic preloading on an axial compression test ($\sigma_3 = 200 \text{ kN/m}^2$) on Karlsruhe sand at 99% relative density (after Hettler et al., 1984)

the hardening control surface (i.e., $X = 1$), and b) $\gamma = 15$ (as for Reid-Bedford sand in Table 3.9). Since there was no shear preloading, the parameter γ_1 was not needed. Figure 3.58 shows the calculated and experimental results; the correspondence is excellent.

Figure 3.59 shows the axial strain accumulation in a constant amplitude stress-controlled cyclic axial compression test (Linton, 1986). The material tested was Reid-Bedford sand prepared at an initial relative density of 75%, and the external axial load was cycled between nominally fixed stress limits of 0 and 100 psi with an ambient pressure of 30 psi.

Granular base course and subbase course materials undergo this type of continued (or cyclic) hardening under repeated loads for as many as 10^4 cycles (Brown, 1974), beyond which point there is cyclic stability, or plastic shakedown, or sometimes a sudden degradation. Only a crude formulation for cyclic hardening is implemented here to demonstrate the versatility of the model to predict this ratchetting. The interested reader is referred to Eisenberg (1976) and Drucker and Palgen (1982) for examples of more general descriptions of cyclic hardening and cyclic softening, and to Mroz and Norris (1982) for an example of a cyclic degradation option for sand.

To simplify the theory, the response in cyclic hydrostatic compression is assumed to be immediately stable. That is, the parameter γ is assumed to be constant and the reload modulus on the hydrostatic axis, $(K_p)_0$, is unaffected by the number of load repetitions. This is not a bad assumption when one considers the relatively small plastic strains occurring in this non-critical region of stress space. With this assumption, cyclic hardening (or softening) effects are controlled

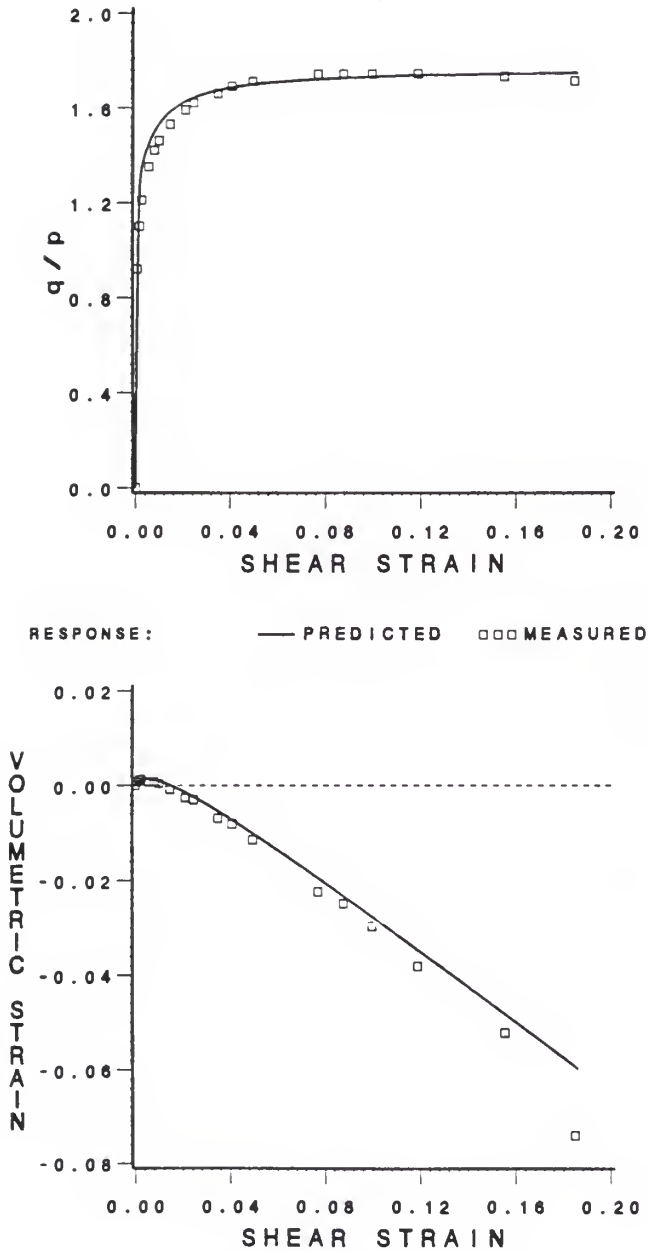


Figure 3.58 Predicted vs. measured results for hydrostatic preconsolidation followed by axial shear (measured data after Hettler et al., 1984; see Fig. 3.57)

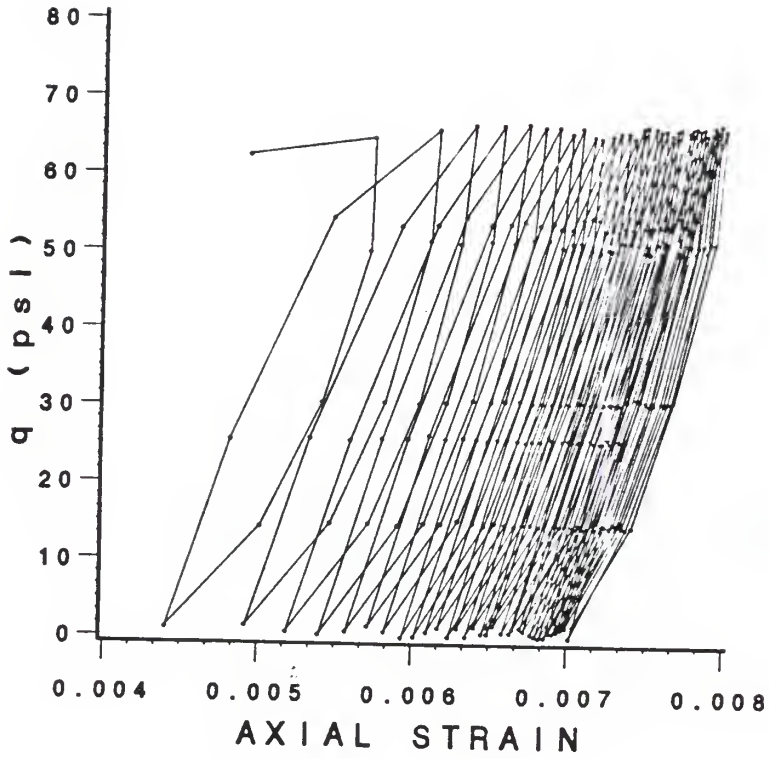


Figure 3.59 Shear stress vs. axial strain data for a cyclic axial compression test on Reid-Bedford sand at 75% relative density. Nominal stress amplitude $q = 70$ psi, and confining pressure $\sigma_3 = 30$ psi (after Linton, 1986)

solely by the exponent γ_1 of the reload modulus equation (eq. 3.8.3.2). Note that higher magnitudes of γ_1 produce a softer response.

Factors which affect the accumulation of permanent strain in cohesionless material have been reported to be the number of load repetitions, stress history, confining pressure, stress level, and density (Lentz and Baladi, 1980). All but the number of load repetitions and the stress history are implicit in the simple theory. Stress history effects have been included by the introduction of the hardening control surface, and now cyclic hardening is incorporated by replacing the parameter γ_1 with the empirical equation

$$\gamma_1 = \gamma_2 (N_{\text{REP}})^{\gamma_3}, \quad (3.8.3.7)$$

where N_{REP} is the number of load repetitions, γ_2 is the magnitude of γ_1 for the first reloading ($N_{\text{REP}}=1$), and γ_3 (a negative quantity) models the decrease in γ_2 , or the stiffening of the response with increasing numbers of load cycles. By assigning an appropriate magnitude of γ_1 for each cycle, $\log(\gamma_2)$ and γ_3 can be determined as the intercept and slope respectively of a straight line fit to a plot of $\log(\gamma_1)$ vs. $\log(N_{\text{REP}})$.

The permanent strain accumulation of Figure 3.59 was predicted using as appropriate a) the simple model plastic parameters and the reload modulus parameter γ of Table 3.9, b) the elastic constants of Table 3.4, and c) back-computed magnitudes for the cyclic hardening parameters γ_2 and γ_3 . To get a more precise prediction of the axial strain for the first (or virgin) loading, the strength parameter k was reduced slightly from .300 to .295. The parameters γ_2 and γ_3 were computed to be 5.23 and -0.11 respectively, and cyclic stability was

assumed after 25 cycles. Figure 3.60 shows how precisely the representation predicts this buildup of axial strain.

3.9 Limitations and Advantages

In conclusion, a number of limitations and advantages of the proposed theory are summarized.

At this early stage in the development of the model, its main limitations appear to be the following:

1. As shown in Figure 3.61, an unusual range of stress paths, moving from region A into region B, can penetrate the limit surface as elastic unloading or neutral loading paths.
2. The interpolation rule used to model the decrease in K_p as the stress point moves from the hydrostatic axis to the limit surface needs refinement. It is not capable of matching stress-strain curves which become soft at the lower stress ratios.
3. The proposed hardening options give up the ability to predict virgin response in extension following a prior loading in compression. This may be corrected by adding a degree of stress reversal variable similar to the ones used by Eisenberg (1976) and Ghaboussi and Momen (1982).

The model proposed here appears to be significantly more rational, more attractive, and more manageable than many of the present theories because

1. of the separate and independent status accorded the yield surface, the limit surface, and the hardening control surface;

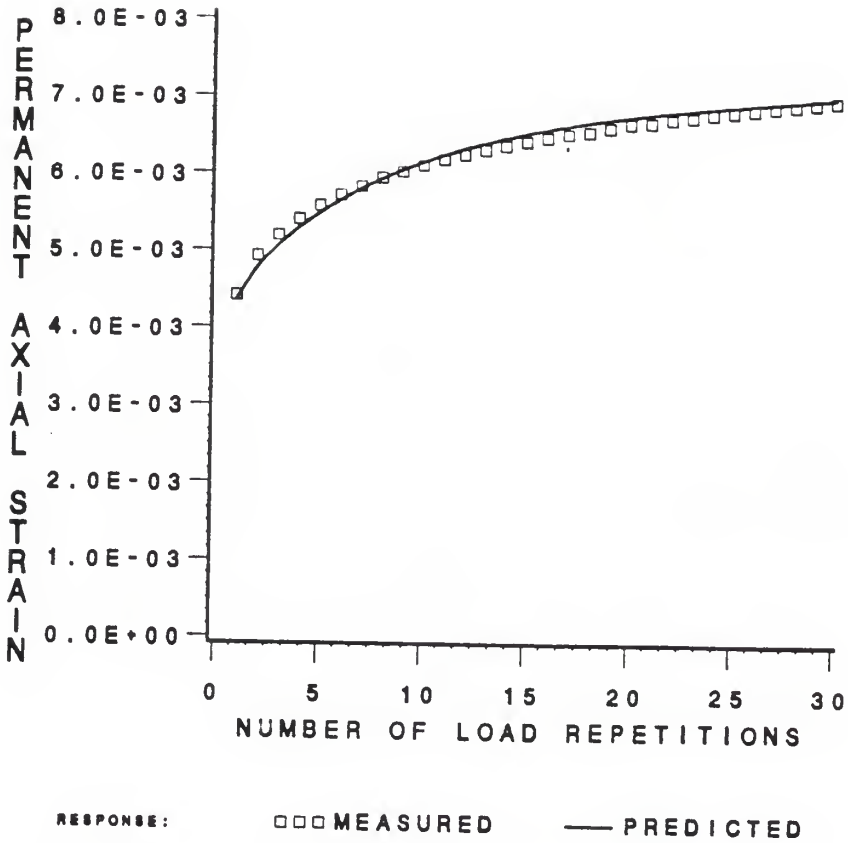


Figure 3.60 Prediction of the buildup of the axial strain data of Figure 3.59 using proposed cyclic hardening representation

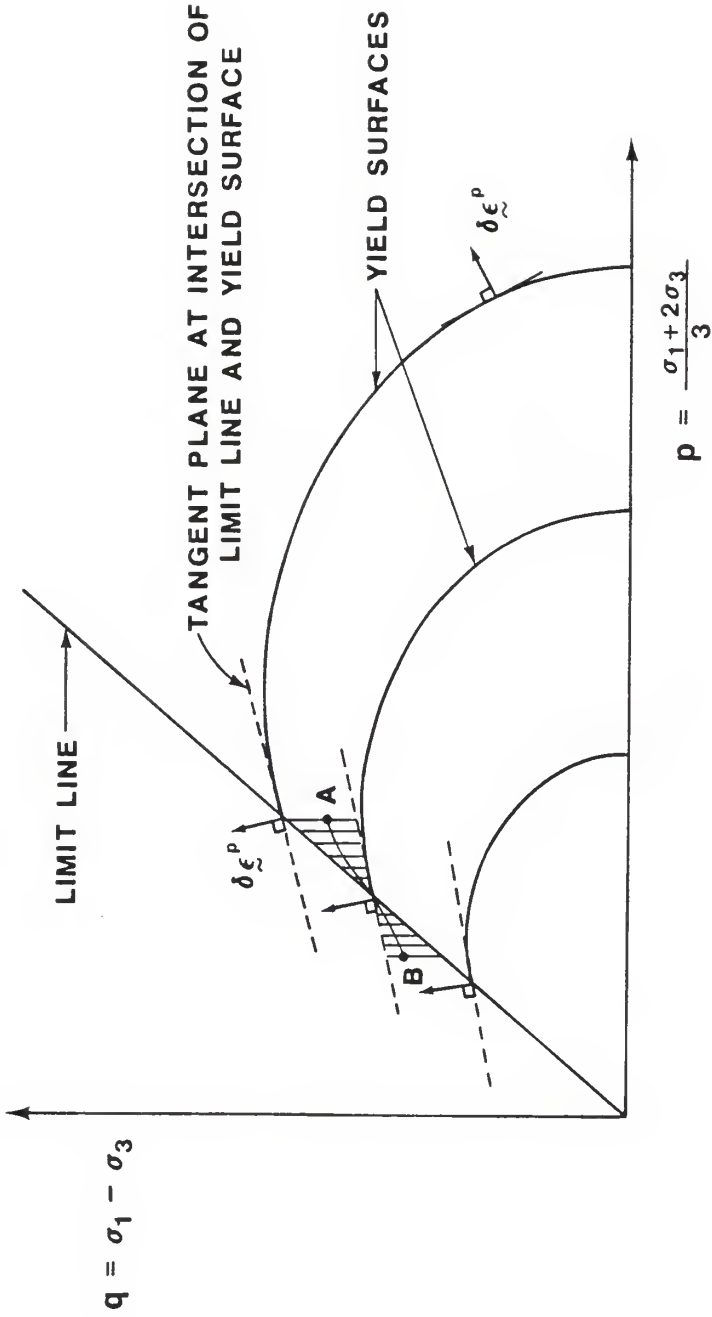


Figure 3.61 Any loading starting in the region A and moving to region B can go beyond the limit line as an elastic unloading or a neutral loading path

2. of the simplifications resulting from the automatic satisfaction of the consistency condition which therefore does not enter into the determination of the plastic modulus;
3. each parameter has a physical significance and each can be correlated to a stress-strain-strength concept in routine use by geotechnical engineers;
4. the experiments used for model calibration are the standard triaxial test and a hydrostatic compression test;
5. the initialization procedure is straightforward and can be carried out expeditiously;
6. varying degrees of sophistication can be achieved by adding model constants and by assuming numbers for, instead of rigorously calibrating, certain less-critical material parameters;
7. the model could predict reasonably accurately a wide variety of monotonic stress paths over a range of densities and sands of different genesis, and in its crudest form, it could also qualitatively simulate the more complicated type "A", type "B", and compression-extension stress paths of Tatsuoka & Ishihara (1974a, 1974b);
8. the model very precisely predicts the expansion of a cylindrical cavity, which, although not particularly complicated, is a boundary value problem of growing importance in soil mechanics;
9. satisfies the requirements of Drucker's postulate of stability in the small in the forward (or monotonic) sense, which contributes to computational stability;

10. an associative flow rule results in symmetric stiffness matrices in finite element calculations which are much more economical than the non-symmetric ones that emanate from non-associative flow rules;
11. it is computationally economical and easy to implement since there is no need to keep track of the evolution of any so-called plastic internal variables (such as plastic volumetric strain, plastic work, etc.) during the deformation;
12. by using some straightforward modifications (which are familiar to those acquainted with the bounding surface concept), the theory can be set up to model (cyclic) hardening aspects of sand behavior; and
13. the consolidation yield surface can be easily modified to model anisotropic plastic flow as a deviation from normality to the "isotropic" yield surface using the method suggested by Dafalias (1981).

CHAPTER 4
A STUDY OF THE PREVOST EFFECTIVE STRESS MODEL

4.1 Introduction

The stress-strain behavior of soil is strongly nonlinear, anisotropic, elastoplastic, hysteretic, and path dependent. Although inherently anisotropic materials can be modeled to a certain extent by nonlinear elastic and isotropically hardening elastic-plastic constitutive models, stress-induced anisotropy cannot be realistically accounted for in the framework of the simpler theories. Alternatively, more general models, which merge concepts from isotropic and kinematic plasticity, have evolved to simulate the response of soil for complicated three dimensional, and in particular, cyclic loading paths.

Prevost (1978) has utilized the field of work hardening moduli concept forwarded by Mroz (1967) to develop a series of elastic-plastic, anisotropic hardening models. Each of these was formulated to model a specific mode of soil response, ranging from the undrained behavior of saturated clays to the drained behavior of sands. In this study, only the drained behavior of cohesionless soils is considered so the pressure sensitive version (Prevost, 1978, 1980) is of primary interest.

4.2 Field of Work Hardening Moduli Concept

An understanding of the field of work hardening moduli concept is a fundamental prerequisite to this presentation. This concept is perhaps most simply illustrated by considering "rapid" (or undrained) tests on a saturated clay. The behavior of clay under these conditions resembles metal behavior in that the plastic volume change is negligible. As a consequence, the yield surface's projection on the octahedral plane is all that need concern us. Suppose a series of mean normal pressure tests, such as stress paths TC or TE of Figure 2.3, were carried out, each starting at the same hydrostatic stress state and moving radially outward in principal stress space (at varying Lode angles θ). For each test, the shear stress invariant q [$= \sqrt{(3 J_2)}$] versus the shear strain invariant $\bar{\epsilon}$ [$= \sqrt{\frac{3}{2} \underline{e}:\underline{e}}$] is recorded and plotted. Taking the steepest initial slope of all the q vs. $\bar{\epsilon}$ plots as twice the linear elastic shear modulus G ($= dq/2 d\bar{\epsilon}$), separate the elastic ($\bar{\epsilon}^e$) from the total ($\bar{\epsilon}$) to obtain the plastic strains ($\bar{\epsilon}^p$). Replot all stress-strain data as q vs. $\bar{\epsilon}^p$.

Along each of these linear shear paths, it is logical to expect that the plastic shear modulus K_p ($= dq/d\bar{\epsilon}^p$) will decrease with increasing distance from the starting point. Compute the slopes $dq/d\bar{\epsilon}^p$ at representative levels of stress (q), and connect the stress points of equal slopes (or plastic shear moduli) on all radial paths. This procedure results in a non-intersecting set of yield surfaces or iso-plastic modulus contours in stress space, each of which circumscribes the hydrostatic axis.

For simplicity, assume that these loci consist of a set of concentric circles or Mises yield surfaces [Fig. 4.1 (a)], the largest of which is a failure surface (with a plastic modulus of zero). Furthermore, assume that each yield surface undergoes pure kinematic hardening and remains unaltered until the stress point meets it. These a priori assumptions imply that the field of yield surfaces sketched from the aforementioned test data is also the initial field of yield surfaces that characterizes the material. If these yield surfaces were allowed to translate or change their size prior to contact by the stress point, the initialization procedure would not have been so straightforward.

With the location, size, and associated plastic modulus of each yield circle known, the working principles of such a representation can now be demonstrated. Say the stress point leaves the hydrostatic state and moves out on the deviatoric plane and engages the first yield surface (which encloses the purely elastic domain). The resident plastic modulus on this surface is employed in the flow rule (equation 2.7.3.12) to predict plastic strain increments. The normal vector at this point on the yield surface is also assumed to give the direction of plastic flow (i.e., an associative flow rule). As outward shearing continues, the active yield surface, with the stress point "pulling" it along, must translate towards its outer neighbor in such a manner that when both surfaces come into contact, they do not intersect. If they do happen to cross each other, a problem arises because the plastic modulus at the intersection points is not unique. The special translation rule

which prevents such an abnormality is known as the Mroz's hardening rule (Mroz, 1967), and it is stated in mathematical terms later in this chapter.

When the second surface is engaged by the stress point, its plastic modulus supplants that of surface #1 in the constitutive equation. This surface, which was stationary until contacted, now moves according to Mroz's hardening rule to the third surface in the field. The deactivated inner surface (#1) remains tangentially attached to the newly activated surface (#2) at the current stress point. This contact point is called a conjugate point. Since the rigid inner surface must satisfy the "nesting" or non-intersecting requirement, it is apparent that its translation is dictated solely by the movement of the active surface.

If shear loading continues and the second surface moves out to engage the third member of the family, the same transition process occurs, and surface #3, with surfaces #1 and #2 nested within it, now moves inside of surface #4.

If while on surface #3 (or any other surface for that matter), the stress path turns inward to the hydrostatic axis, the stress point disengages surface #3 and re-enters the region bounded by surface #1 or the elastic domain (Figure 4.1b). Accordingly, the plastic modulus is set to infinity. If unloading continues and the stress point moves toward the opposite end of circle #1, it reactivates this surface and its associated modulus on the way back, and reverse plastic strains are generated. Depending upon the arrangement of these surfaces prior to the unload, the stress point may encounter several other surfaces on an

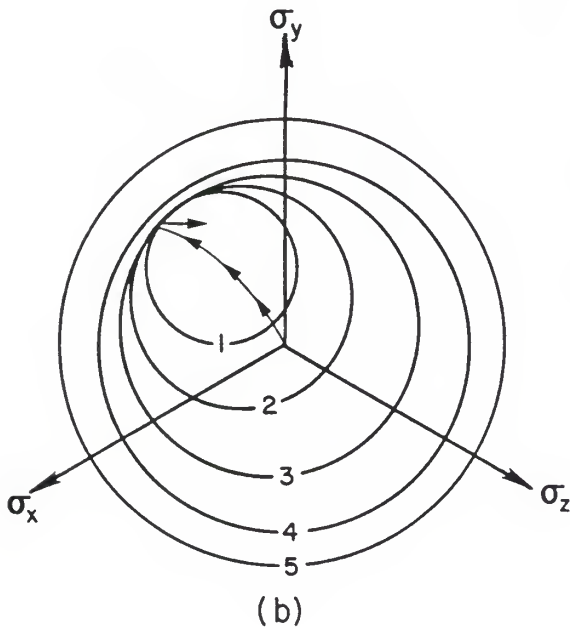
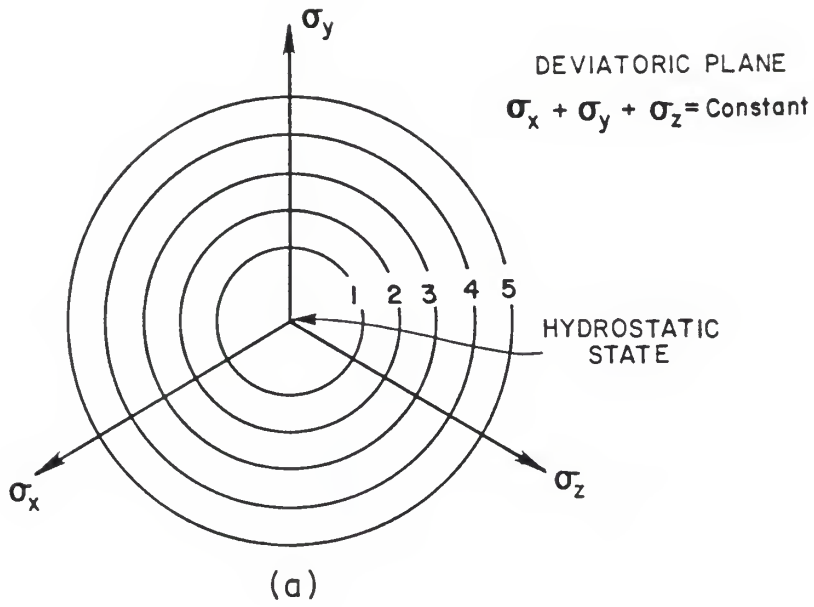


Figure 4.1 Initial (a) and subsequent (b) configurations of the deviatoric sections of the field of yield surfaces

unload or a redirected path. Memory of the loading, including induced anisotropy, is therefore reflected by the current configuration of the nest of yield surfaces.

In sketching the field of yield surfaces or plastic modulus contours, it may turn out that they are all not symmetrically placed with respect to the hydrostatic axis. Inherent anisotropy is manifest in such an initial off-centered arrangement.

Two simplifications of this multi-level memory structure have been introduced in soil mechanics. The first considers the existence of only yield surface #1 and an outermost or bounding surface, which may or may not be the limit surface. Mroz's translation rule still applies for this two surface configuration. Instead of the field of discrete hardening moduli, an interpolation rule prescribes the link between the plastic modulus (at the current state) and the distance from and the magnitude of K_p at the conjugate point on the boundary surface. Krieg (1975) and Dafalias and Popov (1975) independently elaborated this modified description of the field of work hardening moduli. Variations of this concept, with a vanishing elastic region, have led to yet another group of so-called bounding surface models in soil plasticity (Dafalias and Popov, 1977; Dafalias and Hermann, 1980; and Aboim and Wroth, 1982). In these later models, the degenerate nature of yield surface #1 "frees" the theoretician from the analytical rigor of Mroz's hardening rule, and allows the use of an experimentally verifiable mapping rule to locate a conjugate point on the boundary yield surface.

The second major modification to the discrete nesting surface idea is that the field of hardening moduli inside the bounding surface are given by an infinite number of nesting surfaces. In this

representation, the active plastic modulus is a function of the ratio of the radius of the instantaneous loading circle to the radius of the bounding surface. A loading surface is defined here as a subsequent surface into which an initial yield surface deforms and/or translates. If the radius of the loading surface continues to increase, then the plastic modulus is governed by the ratio of the radius of the loading surface to that of the bounding surface. If, on the other hand, the stress path reverses and is directed to the interior of the loading surface, the instantaneous location of the just disengaged loading surface is recorded and it is labelled a stress reversal surface. Prior to penetration of the stress reversal surface on an unloading or reloading path, the plastic modulus is controlled by the ratio of the size of the active loading surface to that of the stress reversal surface. Once the stress state exits the domain enclosed by the stress reversal surface, the interpolation rule reverts to its original form. Therefore, in essence, the memory of a loading event is only erased by another event of greater intensity. Pietruszczak and Mroz (1983) were the progenitors of this concept and they have applied it to model the behavior of clay and sand.

From these simple and rather appealing concepts has evolved a purportedly complete statement on elasto-plastic anisotropic hardening theory for soil: the Prevost Pressure Sensitive Isotropic/Kinematic Hardening Model (Prevost, 1978, 1980). The remainder of this chapter describes its essential features and looks at its performance in predicting a series of hollow cylinder tests on medium dense sand.

4.3 Model Characteristics

The pressure-sensitive version of the Prevost model is formulated in terms of directional stress components (i.e., the stress invariants are not used), and associative flow is assumed in the deviatoric subspace. The model does not explicitly involve plastic potentials, although their existence is implied because the computation of the volumetric component of the plastic strain relies on a special form of the modified flow rule (equation 2.7.7.3). Material frame indifference is satisfied in the formulation, but it is not certain whether energy is conserved under all conditions of loading and unloading (Sture et al., 1984). The development of the model is based on conventional flow or incremental plasticity theory, and hence most of the fundamental principles of Chapter 2 are but specialized here.

4.4 Yield Function

The model employs a yield function of the form

$$F^{(m)} = \frac{3}{2} [\underline{s} - \underline{\alpha}^{(m)}] : [\underline{s} - \underline{\alpha}^{(m)}] + C^2 [p - \beta^{(m)}]^2 - [k^{(m)}]^2 = 0, \quad (4.4.1)$$

where \underline{s} and p denote the deviatoric stress tensor and the mean stress respectively; $\underline{\alpha}^{(m)}$ represent the deviatoric components of the center of the yield surface "m", while $\beta^{(m)}$ is its center coordinate along the p axis; $k^{(m)}$ is its radius; and C is the axis ratio of the meridional section of the yield ellipse in q - p subspace. Deviatoric sections plot as translated circles. Prevost (1978, 1980) usually set the factor C^2 equal to $9/2$ so equation 4.4.1 frequently appears in the literature as

$$F^{(m)} = \frac{3}{2} [\underline{g} - \underline{\xi}^{(m)}] : [\underline{g} - \underline{\xi}^{(m)}] - [k^{(m)}]^2 = 0,$$

where $\xi^{(m)}$ are the components of the center coordinate of the yield surface m ,

$$\xi^{(m)} = \alpha^{(m)} + \beta^{(m)} \delta.$$

With this particular axis ratio, the yield surfaces plot as spheres of radius $\frac{\sqrt{2}}{3} k^{(m)}$ in stress space.

4.5 Flow Rule

The incremental plastic stress-strain relation is of the modified form stated in equations 2.7.7.3 and 2.7.7.4 of Chapter 2,

$$d\varepsilon_{kk}^p = \Lambda A_1 \frac{\partial F}{\partial \sigma_{kk}} \quad (4.5.1)$$

and

$$de_{ij}^p = \Lambda A_2 \frac{\partial F}{\partial s_{ij}}. \quad (4.5.2)$$

Prevost (1978) assumes normality in the deviatoric subspace, which means that the factor A_2 is unity, but he used the function A_1 to modify ∇F to bring it into agreement with the observed plastic volumetric strain.

To facilitate an easy comparison of the formulation reported here with Prevost's work, most of his nomenclature is retained: the tensors \underline{Q} and \underline{P} are the gradient tensors to the yield and plastic potential functions, replacing ∇F and ∇G respectively; and \underline{Q}' and \underline{P}' are the deviatoric components of \underline{Q} and \underline{P} respectively. If this alternate nomenclature is substituted into the general flow rule of Chapter 2 (equation 2.7.3.13), we find that

$$d\underline{\varepsilon}^p = \frac{1}{K_p} \frac{\underline{P}}{|\underline{P}|} \left\{ \frac{\underline{Q}}{|\underline{Q}|} : d\underline{\sigma} \right\},$$

which differs from the form

$$d\varepsilon^P = \frac{1}{K_p} \{Q:d\varepsilon\} \frac{1}{|Q|^2} P \quad (4.5.3)$$

used by Prevost (1978). All this means is that the magnitude of K_p in equation 4.5.3 differs from that in Chapters 2 and 3 by the factor $|P|/|Q|$; it is a trifling divergence from the general form of the flow rule. Observe, however, that the incremental stress-strain relationship (equation 2.7.8.8) must be altered to

$$d\varepsilon = \left[\underline{C}^e + \frac{(\underline{C}^e:P) (Q:\underline{C}^e)}{K_p \{Q:Q\} + (Q:\underline{C}^e:P)} \right] d\varepsilon$$

to accommodate this alternative statement of the flow rule.

The non-associativity function A_1 of equation 4.5.1 is assumed to be

$$A_1 = 1 + A_3 \frac{\sqrt{(Q':Q')}}{|\text{tr } Q|}, \quad \text{or}$$

$$\text{tr } P = \text{sign}(\text{tr } Q) A_3 \sqrt{(Q':Q')} + \text{tr } Q, \quad (4.5.4)$$

where A_3 is a constant affiliated with each surface. This choice models an increasing departure from associativity with increasing Q' , and when Q' is zero, the flow rule is associated, which ensures that pure plastic volumetric strains are predicted for an isotropic compression path if the center of the yield surface lies on the hydrostatic axis. Since the non-associativity of plastic flow is controlled by a single parameter, A_3 , the subscript on it is dropped in the sequel and it is referred to as simply the "A" parameter.

A pair of plastic modulus parameters $h^{(m)}$ and $B^{(m)}$ characterizes each surface. These parameters are used to calculate the generalized plastic modulus K_p for use in the incremental stress-strain relation.

As in the non-associativity function "A", the plastic modulus is assumed to vary only along the meridional section of a yield surface,

$$K_p = h^{(m)} + \frac{\text{tr } \underline{Q}}{\sqrt{(3\underline{Q}:\underline{Q})}} B^{(m)}, \quad (4.5.5)$$

where $h^{(m)}$ is the plastic shear modulus and $[h^{(m)} + B^{(m)}]$ and $[h^{(m)} - B^{(m)}]$ are the plastic bulk moduli associated with $F^{(m)}$ during loading and unloading in consolidation tests. The projections of the yield surfaces onto the deviatoric subspace thus define regions of constant plastic shear moduli.

4.6 Hardening Rule

The yield surfaces are assumed to follow an isotropic/kinematic hardening rule, the direction of translation being determined by Mroz's (1967) non-intersection requirement. There are three distinct computational steps to consider in this evolutionary rule: 1) isotropic and kinematic hardening of the outer (not yet reached) group of surfaces, 2) updating the location and size of the active surface, and 3) computation of the location of the inactive interior surfaces based on the status of the active surface (determined from step 2). The last step, which is also perhaps the easiest of the three, is described first.

First generalize the yield function to the form

$$F^{(m)} = \hat{F}^{(m)}[\underline{g} - \underline{\xi}^{(m)}] - [k^{(m)}]^n = 0, \quad n > 0 \quad (4.6.1)$$

where n is the degree of $\hat{F}^{(m)}$ in $[\underline{g} - \underline{\xi}^{(m)}]$. Further assume that all the yield surfaces are similar so $\hat{F} = \hat{F}^{(m)}$ for all m . The function \hat{F} is usually a homogenous function of order n of its arguments. What does

this mean? The yield function \hat{F} is said to be homogenous of order n if the following is satisfied:

$$\hat{F}[\Lambda (\underline{g} - \underline{\xi}^{(m)})] = \Lambda^n \hat{F}[\underline{g} - \underline{\xi}^{(m)}],$$

where Λ is a positive scalar.

When a surface m is moving toward surface $m+1$ in the field [Figure 4.2 (top)] the stress point on surface m , at M , moves to the corresponding conjugate point on surface $m+1$, at R , to avoid overlapping. Geometrically, it can be shown that the tensor linking the center coordinates of surface m , $\underline{\xi}^{(m)}$, to the stress point \underline{g} , at M , is directed in the same sense as the tensor connecting the center of surface $m+1$, $\underline{\xi}^{(m+1)}$, to the conjugate stress state at R , \underline{g}_R .

Mathematically, this statement means that

$$\underline{g} - \underline{\xi}^{(m)} = \Lambda [\underline{g}_R - \underline{\xi}^{(m+1)}], \quad (4.6.2)$$

where Λ is again a positive constant.

When surface m comes into contact with surface $m+1$, \underline{g}_R coincides with \underline{g} and equation 4.6.2 becomes

$$\underline{g} - \underline{\xi}^{(m+1)} = \Lambda [\underline{g} - \underline{\xi}^{(m)}]. \quad (4.6.3)$$

Combining this equation with equation 4.6.1 gives

$$\hat{F}[\underline{g} - \underline{\xi}^{(m+1)}] = \Lambda^n \hat{F}[\underline{g} - \underline{\xi}^{(m)}] = \Lambda^n [k^{(m)}]^n = [k^{(m+1)}]^n, \quad (4.6.4)$$

and therefore by merging equations 4.6.3 and 4.6.4, we see that

$$\frac{\underline{g} - \underline{\xi}^{(m+1)}}{k^{(m+1)}} = \frac{\underline{g} - \underline{\xi}^{(m)}}{k^{(m)}}. \quad (4.6.5)$$

This geometrical constraint goes into effect when surface $m+1$ is engaged and surface m becomes one of the interior inactive surfaces. Consequently, whenever the location and the size of the active surface

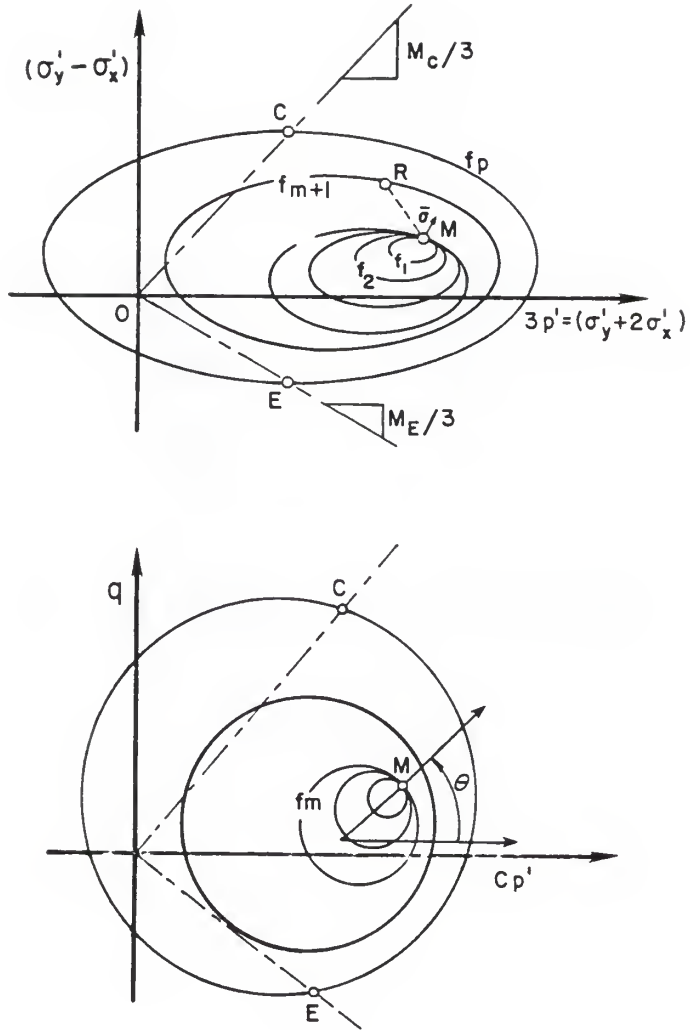


Figure 4.2 Field of nesting surfaces in p - q (top) and Cp - q subspaces (bottom) (after Prevost, 1980)

and the sizes of the interior surfaces are known, the location of all interior surfaces can be calculated forthwith; i.e.,

$$\frac{\sigma - \xi^{(m)}}{k^{(m)}} = \frac{\sigma - \xi^{(m-1)}}{k^{(m-1)}} = \frac{\sigma - \xi^{(m-2)}}{k^{(m-2)}} = \dots \text{etc.} \quad (4.6.6)$$

By combining equations 4.6.2 and 4.6.4, the expression for the translation direction μ , which joins the current stress state σ on surface $F^{(m)}$ to its conjugate point σ_R on the next larger surface $F^{(m+1)}$, can be derived:

$$\mu = \sigma_R - \sigma = \frac{k^{(m+1)}}{k^{(m)}} [\sigma - \xi^{(m)}] - [\sigma - \xi^{(m+1)}]. \quad (4.6.7)$$

All yield surfaces in the field are assumed to isotropically harden or soften with the total volumetric strain rate,

$$\frac{dk^{(m)}}{k^{(m)}} = \lambda d\epsilon_v, \quad (4.6.8)$$

where λ is a density hardening constant. Direct integration of this equation gives the instantaneous sizes of the yield surfaces,

$$k^{(m)} = k_0^{(m)} \exp(\lambda \epsilon_v), \quad (4.6.9)$$

where $k_0^{(m)}$ are the initial values of $k^{(m)}$ (at $\epsilon_v = 0$). Center coordinates of the yield surfaces exterior to the active surface $F^{(m)}$ are assumed to move radially with changes in the volume strain,

$$\begin{aligned} \xi^{(m+1)} &= \xi_0^{(m+1)} \exp(\lambda \epsilon_v), \\ \xi^{(m+2)} &= \xi_0^{(m+2)} \exp(\lambda \epsilon_v), \dots, \\ \xi^{(p)} &= \xi_0^{(p)} \exp(\lambda \epsilon_v), \end{aligned} \quad (4.6.10)$$

where $\xi_0^{(m+1)}, \dots, \xi_0^{(p)}$ are the initial center location of the surfaces $m+1$ to the consolidation (or outermost) surface p . As the material starts to dilate, the isotropic and kinematic rules compel the yield surfaces to shrink in size and move back toward the origin of stress

space. This, in effect, simulates a weakening or softening of the soil's structure with increasing porosity.

All but one aspect of the hardening rule has been stipulated: the computation of the magnitude of the incremental translation tensor $d\mu$ ($= d\mu_{ij}$) for the active yield surface m . Numerically, this is accomplished by first defining the translation direction μ (using equation 4.6.7) from the updated center location $\xi^{(m+1)}$ and the sizes $k^{(m)}$ and $k^{(m+1)}$ (equations 4.6.9 and 4.6.10 respectively). The consistency condition is now invoked to solve for the scalar $d\mu$.

If an arbitrary stress increment, $d\underline{g} = d\underline{s} + dp \underline{\delta}$, is applied, the active yield surface will translate and change its size such that

$$F(\underline{g} + d\underline{g}, k^{(m)} + dk^{(m)}, \xi^{(m)} + d\xi^{(m)}) = 0 \quad (4.6.11)$$

is satisfied at the end of the incremental loading. To make for a neater presentation, the implied superscript m , in reference to the active surface, is omitted hereafter. The attention to detail in this derivation may seem overzealous, but it is justified in that (to the writer's knowledge) it is presented here for the first time in published work.

For the yield ellipsoids used in Prevost's theory, equation 4.6.11 specializes to

$$F = \frac{3}{2} [(\underline{s} + d\underline{s}) - (\underline{\alpha} + d\underline{\alpha})] : [(\underline{s} + d\underline{s}) - (\underline{\alpha} + d\underline{\alpha})] + C^2 [(p + dp) - (\beta + d\beta)]^2 = [k + dk]^2. \quad (4.6.12)$$

A reorganization of this equation gives

$$F = \frac{3}{2} [(\underline{s} - \underline{\alpha}) + (d\underline{s} - d\underline{\alpha})] : [(\underline{s} - \underline{\alpha}) + (d\underline{s} - d\underline{\alpha})] + C^2 [(p - \beta) + (dp - d\beta)]^2 = [k + dk]^2 = k^2 + 2 k dk + dk^2,$$

which may then be expanded to

$$\begin{aligned} & \frac{3}{2} [(\underline{s} - \underline{\alpha}):(\underline{s} - \underline{\alpha})] + \frac{3}{2} [(d\underline{s} - d\underline{\alpha}):(\underline{d}s - d\underline{\alpha})] + \\ & 3 [(\underline{s} - \underline{\alpha}):(\underline{d}s - d\underline{\alpha})] + C^2 (p - \beta)^2 + C^2 (dp - d\beta)^2 + \\ & 2 C^2 (p - \beta)(dp - d\beta) = k^2 + 2 k dk + dk^2. \end{aligned} \quad (4.6.13)$$

Recall from equation 4.4.1 that

$$\frac{3}{2} (\underline{s} - \underline{\alpha}):(\underline{s} - \underline{\alpha}) + C^2 (p - \beta)^2 = k^2,$$

and this knowledge allows us to delete terms in equation 4.6.13 to obtain

$$\begin{aligned} & \frac{3}{2} [(d\underline{s} - d\underline{\alpha}):(\underline{d}s - d\underline{\alpha})] + 3 [(\underline{s} - \underline{\alpha}):(\underline{d}s - d\underline{\alpha})] + \\ & C^2 (dp - d\beta)^2 + 2 C^2 (p - \beta)(dp - d\beta) = 2 k dk + dk^2. \end{aligned} \quad (4.6.14)$$

The parenthetical terms of this equation are now expanded out to give

$$\begin{aligned} & \frac{3}{2} d\underline{s}:d\underline{s} + \frac{3}{2} d\underline{\alpha}:d\underline{\alpha} - 3 d\underline{s}:d\underline{\alpha} + 3 (\underline{s} - \underline{\alpha}):d\underline{s} - 3 (\underline{s} - \underline{\alpha}):d\underline{\alpha} + \\ & C^2 (dp)^2 + C^2 (d\beta)^2 - 2 C^2 dp d\beta + 2 C^2 (p - \beta) dp - \\ & 2 C^2 (p - \beta) d\beta - 2 k dk - dk^2 = 0. \end{aligned} \quad (4.6.15)$$

With the translation rate tensor written as

$$d\underline{\xi} = d\underline{\alpha} + d\beta \underline{\delta} = d\underline{\mu} \underline{\mu} = d\underline{\mu} (\text{dev } \underline{\mu} + \frac{\text{tr } \underline{\mu}}{3} \underline{\delta})$$

(where dev $\underline{\mu}$ are the deviatoric components of the tensor $\underline{\mu}$), $d\underline{\alpha}$ and $d\beta$ is replaced by $d\underline{\mu} \text{dev } \underline{\mu}$ and $d\underline{\mu} \frac{\text{tr } \underline{\mu}}{3}$ respectively in equation 4.6.15 to

get

$$\begin{aligned} & \frac{3}{2} d\underline{s}:d\underline{s} + \frac{3}{2} (d\underline{\mu} \text{dev } \underline{\mu}):(\underline{d}\mu \text{dev } \underline{\mu}) - 3 d\underline{s}:(d\underline{\mu} \text{dev } \underline{\mu}) + \\ & 3 (\underline{s} - \underline{\alpha}):d\underline{s} - 3 (\underline{s} - \underline{\alpha}):(\underline{d}\mu \text{dev } \underline{\mu}) + C^2 dp^2 + \\ & C^2 d\underline{\mu} \frac{\text{tr } \underline{\mu}}{3} d\underline{\mu} \frac{\text{tr } \underline{\mu}}{3} - 2 C^2 dp d\underline{\mu} \frac{\text{tr } \underline{\mu}}{3} + 2 C^2 (p - \beta) dp - \\ & 2 C^2 (p - \beta) d\underline{\mu} \frac{\text{tr } \underline{\mu}}{3} - 2 k dk - dk^2 = 0. \end{aligned} \quad (4.6.16)$$

Since the translation direction $\underline{\mu}$ is already specified (in equation 4.6.7), the objective is to solve for the (only) unknown $d\mu$ in equation 4.6.16. This equation is quadratic in $d\mu$, and must be treated accordingly. First collect the coefficients of $d\mu^2$, $d\mu$, and the constant terms and store them in descriptive variables A, B, and C' respectively,

$$A = \frac{3}{2} (\text{dev } \underline{\mu} : \text{dev } \underline{\mu}) + C^2 \frac{\text{tr } \underline{\mu}}{3} \frac{\text{tr } \underline{\mu}}{3}, \quad (4.6.17)$$

$$B = -3 \underline{ds} : (\text{dev } \underline{\mu}) - 3 (\underline{s} - \underline{\alpha}) : (\text{dev } \underline{\mu}) - 2 C^2 dp \frac{\text{tr } \underline{\mu}}{3} - 2 C^2 (p - \beta) \frac{\text{tr } \underline{\mu}}{3}, \quad (4.6.18)$$

and

$$C' = \frac{3}{2} \underline{ds} : \underline{ds} + 3 (\underline{s} - \underline{\alpha}) : \underline{ds} + C^2 dp^2 + 2 C^2 (p - \beta) dp - 2 k dk - dk^2. \quad (4.6.19)$$

With these collective variables, equation 4.6.16 is now rewritten more compactly as

$$A d\mu^2 + B d\mu + C' = 0,$$

from which the solution for the roots are

$$d\mu = \frac{-B \pm \sqrt{B^2 - 4 A C'}}{2 A}. \quad (4.6.20)$$

In numerical applications, such as the finite element computer code of Hughes and Prevost (1979), the coefficient B is usually replaced by an alternate variable $B' = -B/2$ such that

$$\begin{aligned} d\mu &= \frac{2B' \pm \sqrt{4B'^2 - 4 A C'}}{2 A}, \\ &= \frac{B' \pm \sqrt{B'^2 - A C'}}{A}, \end{aligned} \quad (4.6.21)$$

where A and C' are defined in equations 4.6.17 and 4.6.19, and

$$B' = \frac{-B}{2} = \frac{3}{2} \underline{ds} : (\text{dev } \underline{\mu}) + \frac{3}{2} (\underline{s} - \underline{\alpha}) : (\text{dev } \underline{\mu}) + C^2 dp \frac{\text{tr } \underline{\mu}}{3} + C^2 (p - \beta) \frac{\text{tr } \underline{\mu}}{3}.$$

Finally, the (plus or minus) root of equation 4.6.21 is selected on the basis that the scalar product $d\underline{\mu} : [\frac{3}{2} \underline{ds} + dp \underline{\delta}]$ be greater than zero.

4.7 Initialization of Model Parameters

The last and perhaps most singular feature of the Prevost model is its calibration procedure. As the author can attest to, this task can sometimes prove to be more challenging than any other aspect in the implementation of the model.

Quantification of material response is completely specified by the

- 1) initial positions and sizes of the yield surfaces $[\underline{\alpha}^{(m)}, \beta^{(m)}, \text{ and } k^{(m)}]$;
- 2) plastic moduli parameters associated with each surface $[h^{(m)} \text{ and } B^{(m)}]$;
- 3) non-associative flow parameter for each surface $[A^{(m)}]$;
- 4) density hardening parameter (λ); and
- 5) elastic bulk (K) and shear (G) moduli.

All parameters, except maybe for the elastic constants, are very important, and the model is not forgiving if accurate characterization is not initially achieved, as may be caused by non-smooth input data.

Three standard laboratory tests provide the input data for the initialization:

- 1) an axial compression stress path (CTC of Figure 2.3);
- 2) an axial extension path (RTE of Figure 2.3) which must start at the same hydrostatic stress state as the CTC; and
- 3) a one-dimensional (or K_0) consolidation test.

These paths are all restricted to the triaxial (or Rendulic) plane and the test specimen is assumed to be cross-anisotropic. The vertical (or y) axis is the axis of rotational symmetry (or the stiffer direction) and the horizontal (x-z) plane is isotropic. Many useful simplifications result from these stress path and anisotropy restrictions. Equation 4.4.1, the equation of the yield surface, simplifies to

$$F^{(m)} = [q - \alpha^{(m)}]^2 + C^2 [p - \beta^{(m)}]^2 - [k^{(m)}]^2 = 0, \quad (4.7.1)$$

where

$$q = \sigma_y - \sigma_x, \quad p = \frac{1}{3} (\sigma_y + 2 \sigma_x), \quad \text{and} \quad \alpha = 3 \alpha_y / 2 = -3 \alpha_x = -3 \alpha_z.$$

From both a mathematical and an intuitive standpoint, it is interesting to note that equation 4.7.1 represents a translated circle of radius k in Cp versus q stress space, with the center location at $[C\beta, \alpha]$. These circular plots are illustrated in Figure 4.2 (bottom), where the polar angle θ is also defined--this angle is not the same as the Lode angle θ . Observe from the lower picture in figure 4.2 that by geometry

$$q = \alpha + k \sin\theta, \quad (4.7.2)$$

and

$$p = \beta + \frac{k}{C} \cos\theta. \quad (4.7.3)$$

Substituting these transformed coordinates into the following "triaxial" elasto-plastic constitutive equations:

$$d\varepsilon_v = \frac{dp}{K} + \frac{1}{K_p} \text{tr}(\underline{P}) \frac{1}{|Q|^2} \{Q:dg\},$$

and

$$d\varepsilon_{yy} = \frac{1}{2G} ds_{yy} + \frac{1}{K_p} \frac{Q'}{|Q|^2} \{Q:dg\},$$

leads to

$$\frac{d\varepsilon_v}{dp} = \frac{1}{K} + \frac{1}{K_p} \{2C \cos\theta + \sqrt{6} A_m \cos\theta |\tan\theta|\} \frac{\{\sin\theta + C \gamma \cos\theta\}}{3 \gamma}, \quad (4.7.4)$$

and

$$\frac{d\bar{\varepsilon}}{dq} = \frac{1}{2G} + \frac{1}{K_p} \sin\theta \{\sin\theta + C \gamma \cos\theta\}, \quad (4.7.5)$$

where $\gamma = dp/dq$, $d\bar{\varepsilon} = d\varepsilon_y - d\varepsilon_x$, $d\varepsilon_v = 2 d\varepsilon_x + d\varepsilon_y$, and

$$K_p = h_m + B_m \cos\theta. \quad (4.7.6)$$

Model parameters are separated into two categories: group X parameters are the elastic and plastic moduli K , G , h_m and B_m , and group Y consists of the size/location parameters of the yield surface $\alpha^{(m)}$, $\beta^{(m)}$, and $k^{(m)}$. Group X parameters (or moduli) assume the pressure dependence,

$$X = X_1 \left(\frac{p}{p_1}\right)^n, \quad (4.7.7)$$

while the group Y parameters are hypothesized to vary with the volume strain as

$$Y = Y_1 \exp(\lambda \varepsilon_v), \quad (4.7.8)$$

where the subscript 1 refers to initial values, and λ and n are model constants. The dependency of the group Y parameters was alluded to previously in equations 4.6.9 and 4.6.10.

For most cohesionless soils, n is usually assumed equal to 0.5 (Lambe and Whitman, 1969), and the isotropic hardening parameter, λ , is determined from the slope of a log mean stress vs. volume strain plot using data obtained from a one-dimensional (or K_0) consolidation test,

$$\lambda = \frac{1}{p} dp + d\epsilon_v. \quad (4.7.9)$$

If we let θ_C and θ_E denote the magnitudes θ when the stress point reaches the yield surface $F^{(m)}$ in a CTC (or compression loading) and an RTE (or extension unloading) test respectively, equations 4.7.2 through 4.7.8 can then be combined to show that

$$\frac{1}{\tan \theta_C} \pm \frac{1}{\tan \theta_E} = \frac{1}{2 C} [3\gamma_C (X_C + Y_C) \pm 3\gamma_E (X_E + Y_E)], \quad (4.7.10)$$

and

$$\cos \theta_C - \cos \theta_E = R_{CE} (\sin \theta_C - \sin \theta_E), \quad (4.7.11)$$

where

$$R_{CE} = C \{ p_C - p_E \exp[\lambda(\epsilon_v^C - \epsilon_v^E)] \} + \{ q_C - q_E \exp[\lambda(\epsilon_v^C - \epsilon_v^E)] \},$$

$$\frac{1}{X_C} = (p_C/p_1)^n \frac{d\bar{\epsilon}}{dq} - \frac{1}{2 G_1},$$

$$\frac{1}{Y_C} = (p_C/p_1)^n \frac{d\epsilon_v}{dp} - \frac{1}{K_1},$$

with definitions similar to the last two equations applying to X_E and Y_E . The subscripts and superscripts C and E refer to CTC and RTE loading paths respectively. In equation 4.7.10, the plus sign (+) is used when $\tan \theta_C \tan \theta_E$ is less than zero, and the minus sign (-) otherwise.

With this repertoire of equations, the next step is to organize the data in a form suitable for direct computation of the model parameters,

and the procedure described in the following was developed with a "spreadsheet" computer program in mind.

Enter the quantities q , p , ϵ_v , $\bar{\epsilon}$ for the CTC and RTE test in columns of separate tables. Remember that the data must be obtained from a pair of tests which start at the same hydrostatic stress. From the digitized data, compute the slopes $dq/d\bar{\epsilon}$ and $dp/d\epsilon_v$ at each data point; the elastic bulk, K , and shear modulus, G , are assigned the larger of the initial values of the slopes $dp/d\epsilon_v$ and $dq/d\bar{\epsilon}$ respectively.

The following data must be known before the main computation can begin:

- 1) the isotropic hardening parameter λ ,
- 2) an estimate of the constant n ,
- 3) the initial values of the elastic parameters (K and G),
- 4) the slopes of the straight line CTC and RTE stress paths ($\gamma = dp/dq$), and
- 5) an assumed axis ratio C .

Begin by entering the table of CTC stress-strain data and select a representative slope $dq/d\bar{\epsilon}$ to be used in establishing the first yield surface. With this magnitude of $dq/d\bar{\epsilon}$, go into the extension test data and select the line of data with the same $dq/d\bar{\epsilon}$. If an exact match is not found, a simple linear interpolation scheme between lines can be devised. The data contained in these two lines are all that is needed to solve equations 4.7.10 and 4.7.11 simultaneously for θ_C and θ_E . In

carrying out this solution, recognize that equation 4.7.11 is more amenable in the form

$$\frac{1}{\tan\theta_C} + \frac{1}{\tan\theta_E} + [2 R_{CE} / (1 - R_{CE}^2)] \left[\frac{1}{\tan\theta_C \tan\theta_E} - 1 \right].$$

Once θ_C and θ_E have been determined for the selected magnitude of $dq/d\bar{\epsilon}$, the model parameters associated with $F^{(m)}$ are computed from a series of equations obtained by merging equations 4.7.2 to 4.7.5,

$$B_m = [X_C \sin\theta_C ZC - X_E \sin\theta_E ZE] + [\cos\theta_C - \cos\theta_E],$$

$$h_m = X_C \sin\theta_C ZC - B_m \cos\theta_C,$$

$$\sqrt{6} A_m = \frac{1}{|\tan\theta_C|} [3 \gamma_C (X_C/Y_C) - B_m \cos\theta_C],$$

$$k_1^{(m)} = [q_C \exp(-\lambda \epsilon_V^C) - q_E \exp(-\lambda \epsilon_V^E)] + [\sin\theta_C - \sin\theta_E],$$

$$\alpha_1^{(m)} = q_C \exp(-\lambda \epsilon_V^C) - k_1^{(m)} \sin\theta_C,$$

$$\beta_1^{(m)} = p_C \exp(-\lambda \epsilon_V^C) - \frac{k_1^{(m)}}{C} \cos\theta_C,$$

where

$$ZC = \sin\theta_C + C \gamma_C \cos\theta_C,$$

and

$$ZE = \sin\theta_E + C \gamma_E \cos\theta_E.$$

The procedure is repeated choosing another magnitude of $dq/d\bar{\epsilon}$ from the CTC data and calculating the parameters associated with the resulting surface. If it happens to be more convenient, we could just as well select $dq/d\bar{\epsilon}$ from the RTE test data and then proceed to find a corresponding data point in the CTC table.

Almost always, the computed configuration of yield surfaces turns out to be intersecting, and it usually takes a slight but subtle adjustment in one or more of the sizes and/or positions to rectify the arrangement. Moreover, it is evident that the degree of accuracy

achieved by such a representation depends directly on the number of $dq/d\bar{\epsilon}$ points or surfaces used to approximate the field of work-hardening moduli.

4.8 Verification

The model has been implemented in a computer code, initialized rigorously from and used to predict the same series of hollow cylindrical tests used for verification in Chapter 3 (Saada et al., 1983). All but the isotropic hardening parameter λ were determined from the axial compression and extension tests of Saada's data set. Results of an extensive series of one dimensional consolidation tests, performed at the U.S. Army Waterways Experiment Station (Al-Hussaini and Townsend, 1975), were used to estimate the parameter λ . No effort was spared in following the appropriate procedures for computing the model constants.

Although this feature is exactly what this type of model should thrive on, volumetric compression observed in the unloading extension test had to be wiped out to permit calculation of the parameters. This problem has also been reported by Mould et al. (1982). Table 4.1 is a summary of parameters used in this description.

Measured versus fitted response for the axial compression and extension paths are presented in Figures 4.3 and 4.5, while the configuration of the surfaces at the start and end of the simulation are depicted in Figures 4.4 and 4.6. Each of these loading paths recreates the measured response to a reasonable degree of accuracy. In order to minimize numerical discrepancies, 800 load steps were used for each simulation although the solutions were found to be stable with as few as 200 load steps.

Table 4.1 Prevost Model Parameters for Reid-Bedford Sand

Relative Density = 75%

G = 13500 psi, K = 17680 psi, n = 0.5, C = 3/√2, λ = 130,

Initial effective confining pressure = 30 psi,

Initial void ratio = 0.67,

Number of yield surfaces used to characterize field = 20

m	$\alpha^{(m)}$	$\beta^{(m)}$	$k^{(m)}$	$h^{(m)}$	$B^{(m)}$	$A^{(m)}$
2	6.408	31.27	6.951	25800	-4766	-.3538
3	8.813	30.94	12.002	22918	-7282	-.5238
4	12.345	31.45	18.028	12205	-4379	-.5792
5	12.867	32.02	21.778	8084	-2904	-.7157
6	15.796	32.43	27.317	5225	-2183	-.7133
7	19.500	34.19	34.345	2873	-1206	-.8528
8	20.001	34.60	36.257	2404	-998	-.8677
9	20.106	35.26	38.134	1963	-783	-.9433
10	23.111	37.66	44.265	1324	-468	-1.085
11	25.289	38.74	48.304	1075	-380	-1.118
12	27.572	40.47	53.206	878	-300	-1.179
13	29.333	41.71	56.713	736	-246	-1.230
14	33.178	44.29	63.402	562	-179	-1.317
15	35.950	46.11	68.734	465	-148	-1.364
16	39.355	48.64	75.509	388	-121	-1.434
17	46.289	54.03	89.040	293	-86	-1.510
18	51.052	59.62	101.946	236	-64	-1.6312
19	63.695	70.81	129.011	143	-37	-1.7759
20	65.566	77.95	144.322	95	-22	-1.8658

The true test of the generality of a constitutive model is its ability to predict and not to reproduce its initialization data. Except for the two calibration paths and the hydrostatic compression path, all hollow cylinder tests in the series have been predicted, and wherever possible, each is accompanied by plots of the initial and final configurations of field of yield surfaces (in $Cp'-q$ subspace). Only predictions of those stress paths on the triaxial plane--i.e., TC (or GC 0), RTC, and TE (or GT 90) of Figure 2.3--are presented in this chapter (Figures 4.7 to 4.12). The others have been appended (see Appendix G). No further study on this model was carried out beyond these hollow cylinder test predictions.

As can be seen on the stress-strain plots, comparisons of the calculated and measured results along the non-calibration paths are generally not encouraging. Most predictions are much stiffer than the measured response, but it is only fair to point out that the fitted curves (Figures 4.3 and 4.5) were also somewhat stiffer than the experimental data. Close examination of all plots reveals an unmistakable trend: as the trajectory of the stress path deviates further from either of the calibration paths, the predictions worsen. This statement can be verified by inspecting the not so bad prediction of the DCR 15 test (Figure F.1) and the disappointing GC 0 and RTC predictions (Figures 4.7 and 4.9).

The results raise many questions on the generality of the representation and its ability to give good qualitative answers. The writer believes that its drawbacks stem from a) the lack of an explicit incorporation of a path independent failure locus, and b) the inadequacy of a single parameter (A) to model deviation from associativity.

Despite these comments, the concepts underlying this model are extremely appealing, and with some critical modifications, this model may very well be able capture many aspects of real behavior for complicated stress paths.

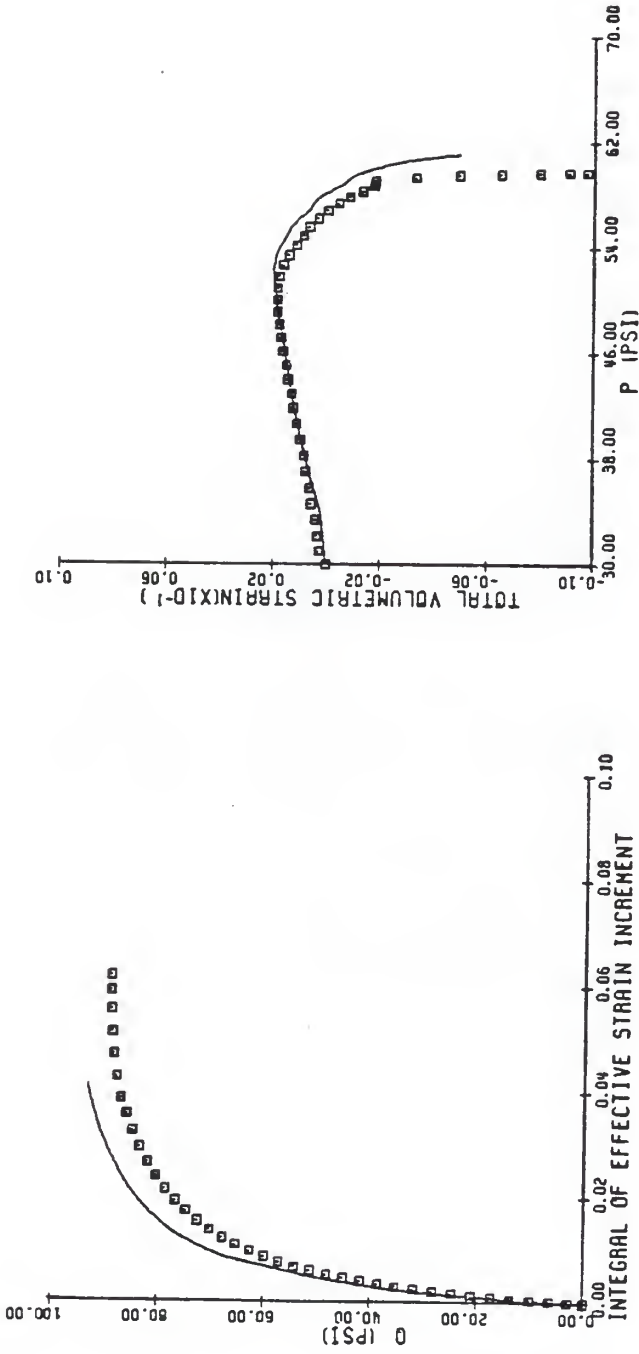


Figure 4.3 Measured vs. fitted stress-strain response for axial compression path using Prevost's model

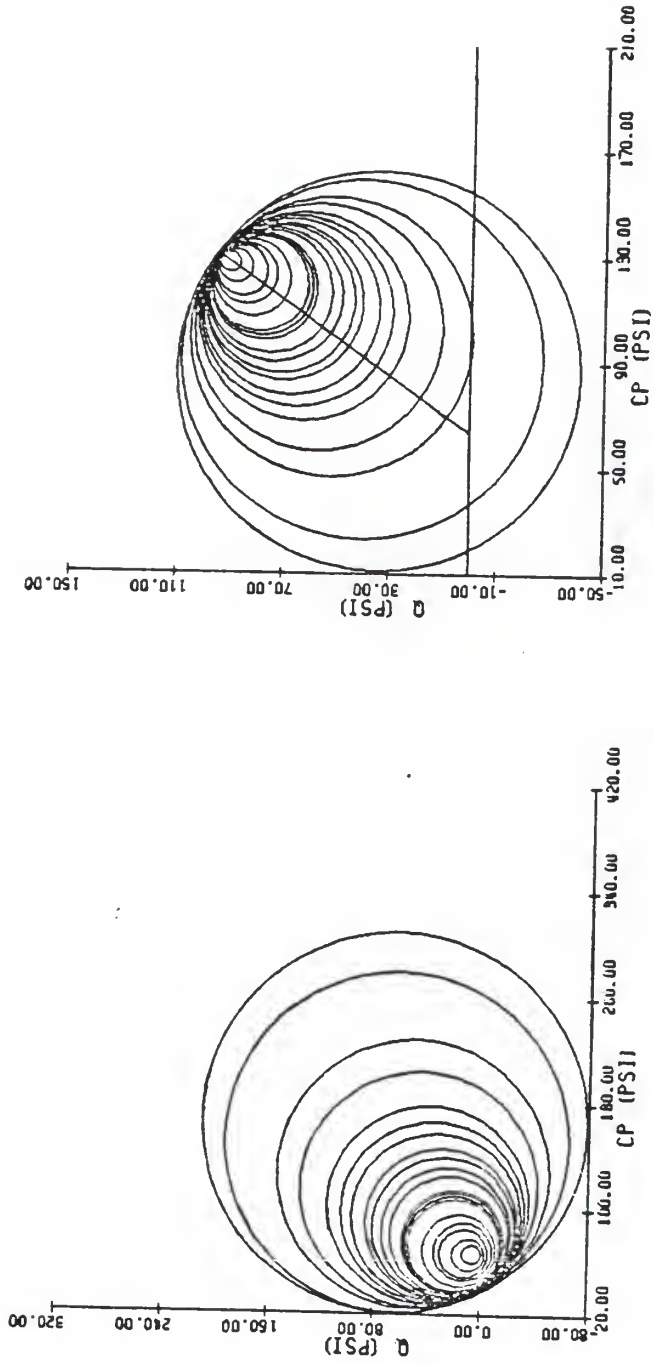


Figure 4.4 Initial and final configurations of yield surfaces for CTC path (see Fig. 2.3) simulation

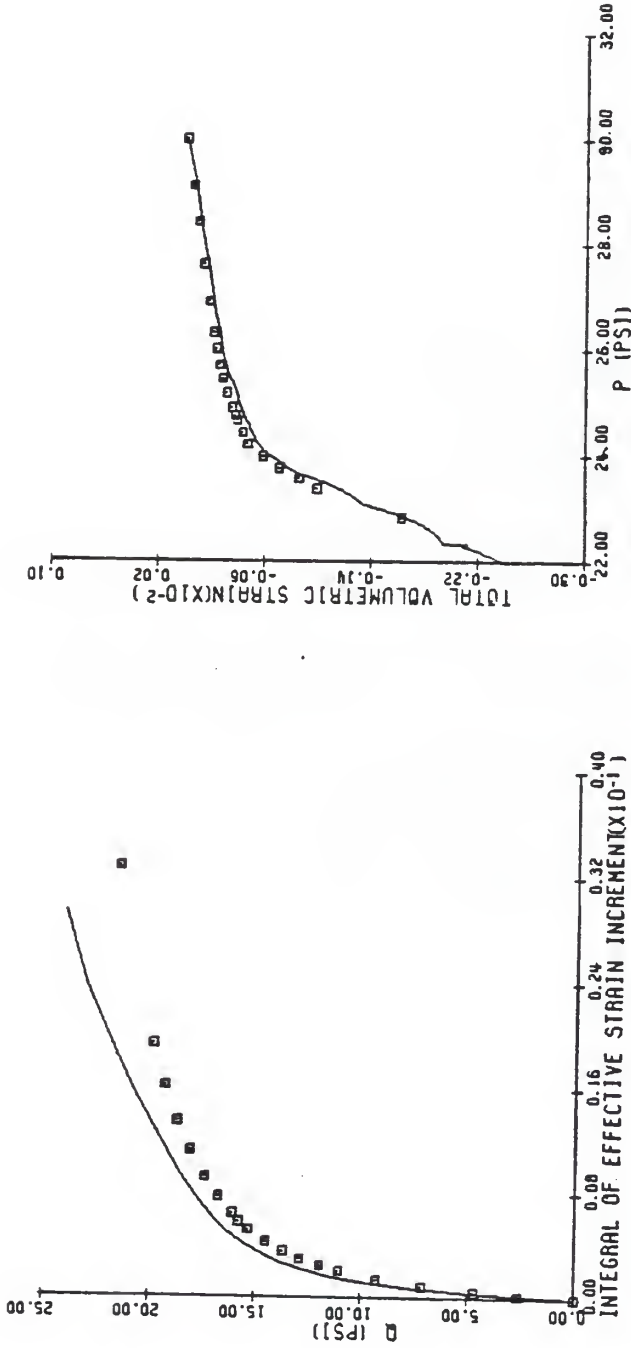


Figure 4.5 Measured vs. fitted stress-strain response for axial extension path using Prevost's model

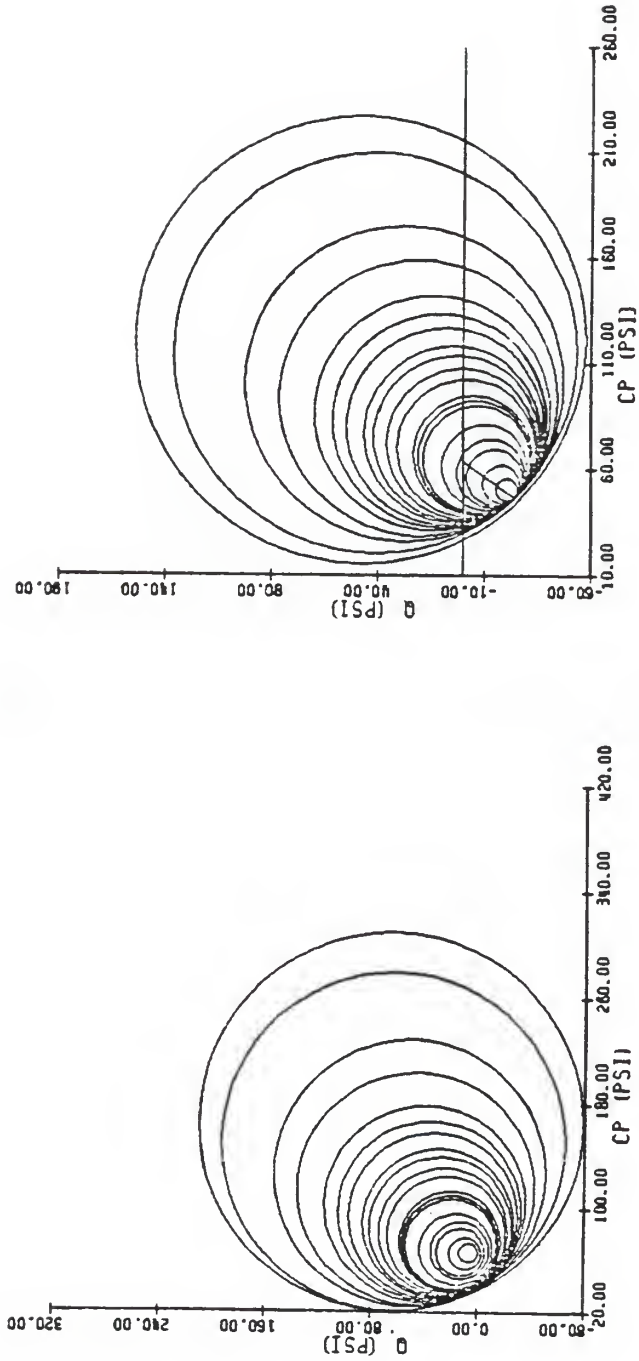


Figure 4.6 Initial and final configurations of yield surfaces for axial extension simulation

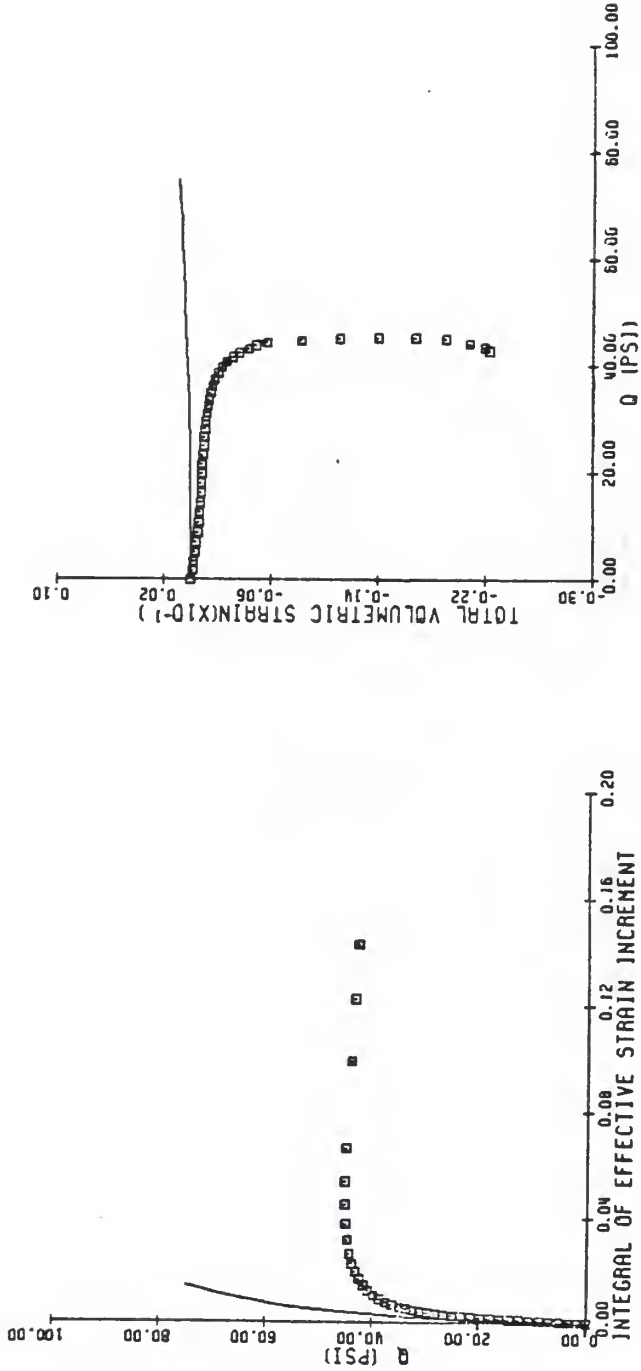


Figure 4.7 Measured vs. predicted stress-strain response for constant mean pressure compression (or TC of Fig. 2.3) path using Prevost's Model

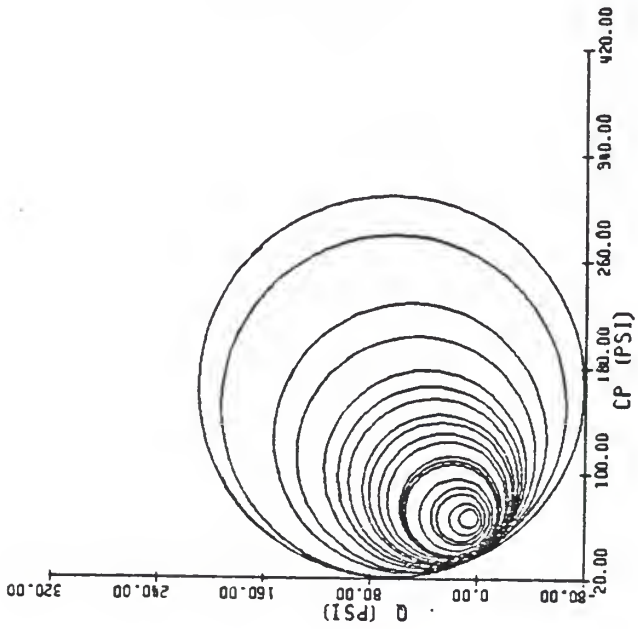
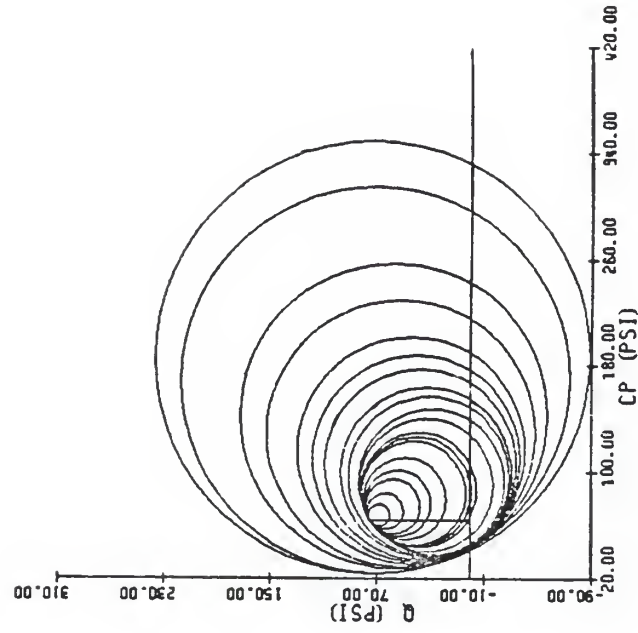


Figure 4.8 Initial and final configurations of yield surfaces for TC simulation

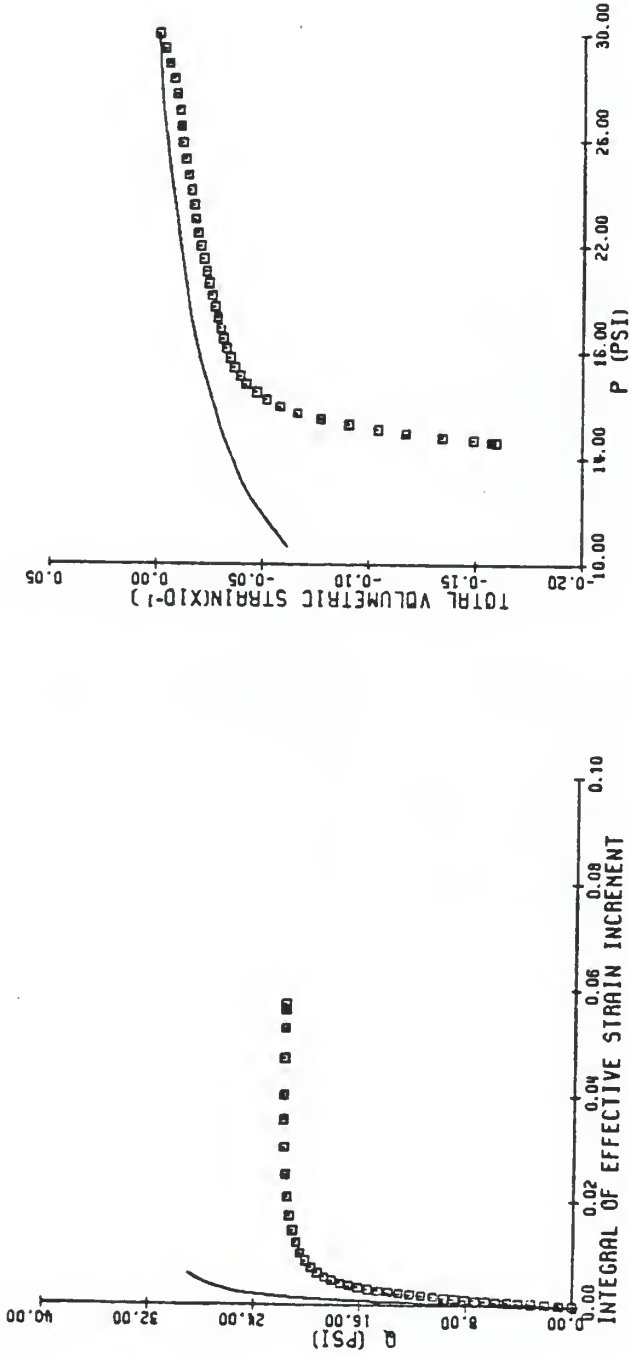


Figure 4.9 Measured vs. predicted stress-strain response for reduced triaxial compression (or RTC of Fig. 2.3) path using Prevost's model

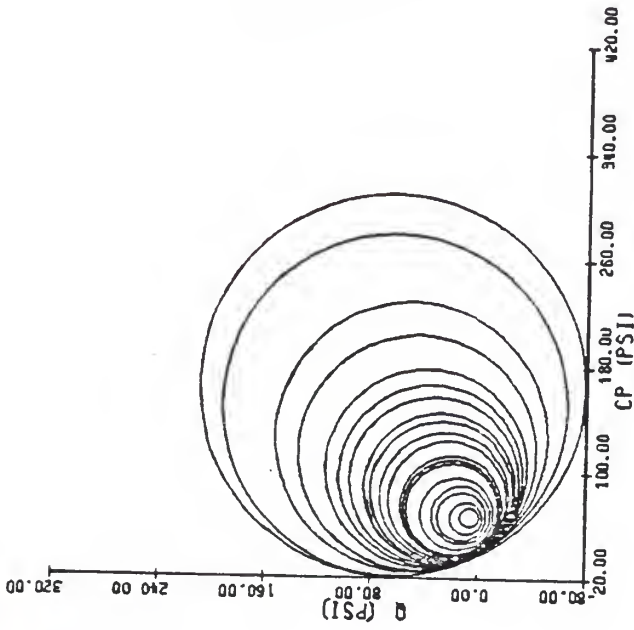
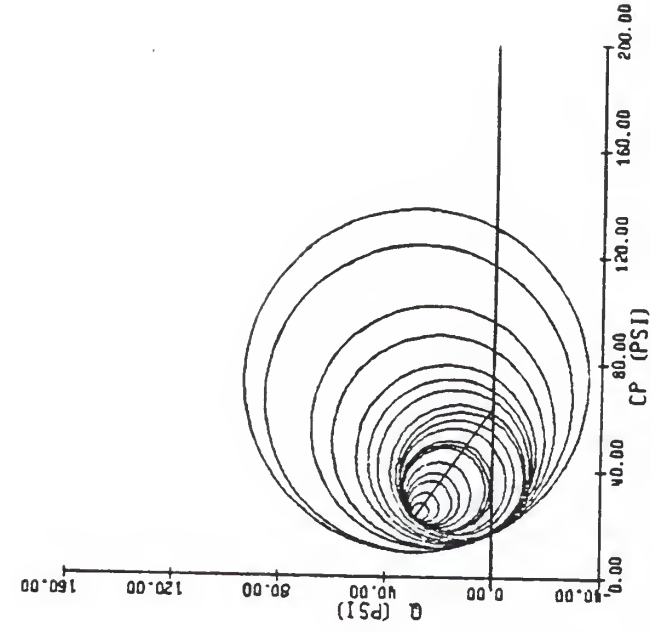


Figure 4.10 Initial and final configurations of yield surfaces for RTC simulation

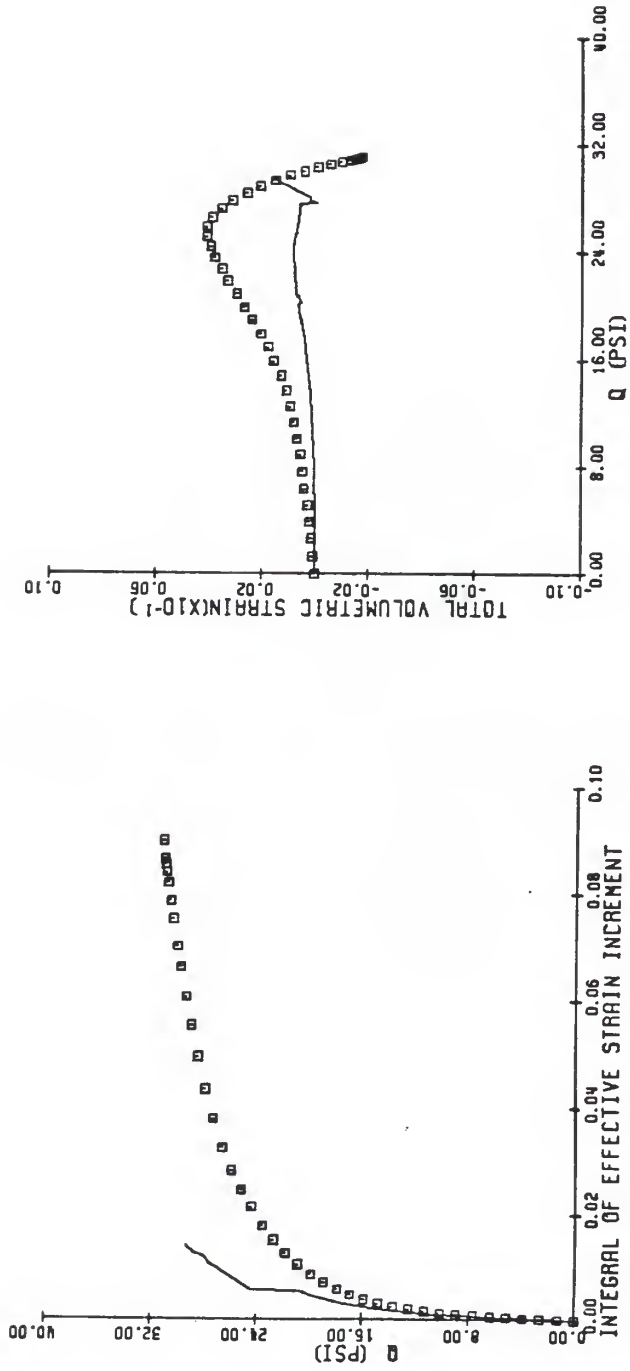


Figure 4.11 Measured vs. predicted stress-strain response for constant pressure extension (or TE of Fig. 2.3) path using Prevost's model

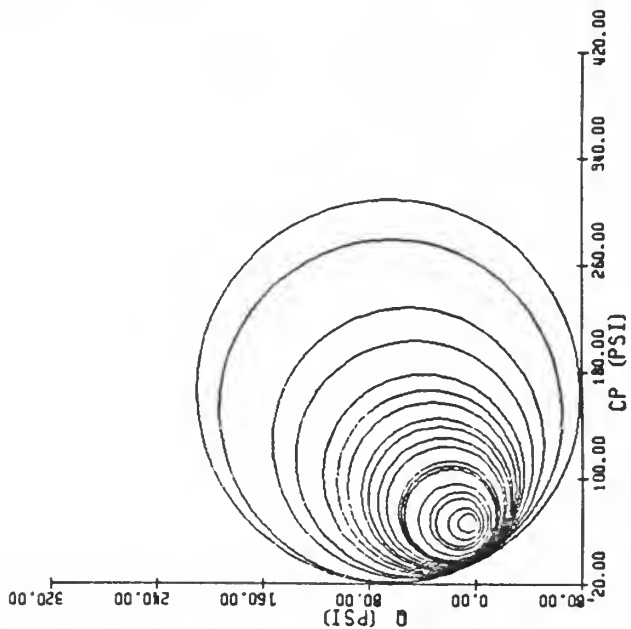
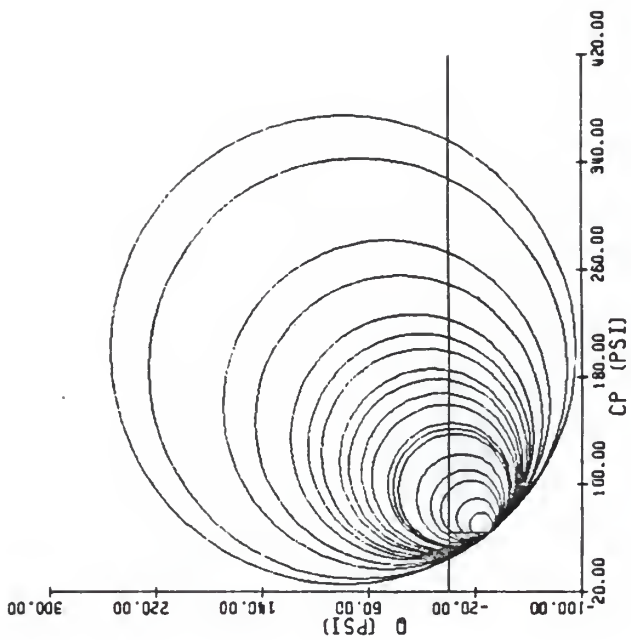


Figure 4.12 Initial and final configurations of yield surfaces for TF simulation.

CHAPTER 5
CONCLUSIONS AND RECOMMENDATIONS

Judging from its performance in predicting response for numerous stress paths, its intrinsic features, and its relative simplicity, the proposed constitutive model for granular material does seem to be an attractive new approach. With regard to its effectiveness in predicting stress paths, the following conclusions are drawn:

1. The representation predicted remarkably well a comprehensive series of axial compression paths over a wide range of densities and confinement pressures (data from Hettler et al., 1984). This attests to the rationality of the formulation in two respects: a) the density dependence of the material parameters, and b) the pressure sensitivity of the material response. The remaining data sets test the rationale for its extension to more general paths of loading.
2. Very realistic simulations were generated for a wide variety of linear monotonic stress paths emanating from a fixed point on the hydrostatic axis (data from Saada et al., 1983, and Linton, 1986). For this particular test series, inherent anisotropy and the experimental difficulties associated with extension loading on sand specimens are thought to be the causes for some

systematic deviation of the measured from the predicted response.

3. The pressuremeter simulations showed that the model performs sensibly along a stress path which is in general non-linear and non-proportional and which rotates on the octahedral plane (data from Davidson, 1983).
4. The stress paths of Tatsuoka and Ishihara (1974a, 1974b) demonstrated, primarily in a qualitative sense, the realistic aspects of the simple representation for the relatively complicated load-unload-reload loading programs shown in Figure 3.36. The simple model, with no hardening, appears to be particularly appropriate for reloading paths in which the direction of the shear stress is completely reversed (data from Tatsuoka and Ishihara, 1974a). Quantitatively, the calculated stress-strain curves are about twice as stiff as the measured data. The source of this problem is the one-parameter form of the interpolation rule used to model the decrease of the plastic modulus from its bulk modulus magnitude on the hydrostatic axis to zero at the limit line.
5. By using some straightforward hardening modifications, the flexibility of the formulation was illustrated by predicting a) the influence of isotropic preloading on a subsequent axial compression path (data from Hettler et al., 1984), and b) the accumulation of permanent strain (or cyclic hardening) in a cyclic uniaxial compression test (data from Linton, 1986).

From a practical viewpoint, the model is conceptually easy to understand and to implement, and it is also very economical from the computational standpoint. Its parsimony is a direct consequence of

1. the use of a stress dependent plastic modulus, which marks a break in the trend of placing the consistency condition central to the determination of the plastic modulus;
2. permitting the material to remain at yield during unloading;
3. hypothesizing that no change in state is a useful first approximation for sand;
4. using an infinitesimal strain definition of yield instead of the traditional offset or Taylor-Quinney (1931) definitions; and
5. according independent status to the yield surface, the limit surface, and the hardening control surface.

A number of factors dealing with the material constants also lend credibility to the proposal, and among these are

1. the ability to correlate each constitutive parameter to one of the "fundamental" geotechnical parameters;
2. the dependence of each parameter only on the initial porosity, as should be expected for sands; and
3. the straightforward initialization procedure which, because of the implicit linear mean pressure normalization, necessitates only input data from two standard experiments: an axial compression test and a hydrostatic compression test.

Despite the many positive comments, the seriousness of the model's limitations remain to be probed, and many avenues of research and

possible improvement are still to be explored. In the opinion of the writer, the main issues, presented in order of importance, are

1. How serious is the limitation of Figure 3.61 showing the range of stress increments which can penetrate the limit surface as elastic unloading or neutral loading paths? What class of practical problems (if any) will it affect? And if it does prove to be a major drawback, how can it be circumvented or corrected? With the theory in its present form, a check should be included in finite element applications to detect the possibility of stress points straying into the forbidden zone outside the limit surface.
2. How significant is the influence of anisotropy on plastic flow and strength of sands? If anisotropy has a significant influence on strength but only a marginal influence on the trajectory of the plastic strain increment vector, an anisotropic limit surface may be specified in conjunction with an isotropic yield surface. This possibility is mentioned because although the data of Saada et al. (1983) suggests that inherent anisotropy has a marked effect on strength, Habib and Luong's (1978) experiments showed virtually no influence of (inherent or stress-induced) anisotropy on the location of the zero dilation line--an integral element of the yield surface. However, if it is found that anisotropy also significantly affects the direction of flow, the isotropic yield surface must be replaced or modified. One possibility is to use the varying non-associative flow concept of Dafalias (1981) to model

anisotropic plastic flow as a deviation from normality to an isotropic yield surface.

3. What is the impact of the stability in the small assumption? Having rationalized the shape of the yield surface for predicting the trajectory of $d\bar{\epsilon}^P$ (i.e., the direction of the unit normal \underline{n}) and the field of plastic moduli (K_p), the primary concern here is with the quantity $\underline{n}:d\bar{g}$ of the flow rule,

$$d\bar{\epsilon}^P = \frac{1}{K_p} \underline{n} (\underline{n}:d\bar{g}),$$

for general paths of loading. For instance, the magnitudes of $\underline{n}:d\bar{g}$ for axial compression and extension paths differ at a given stress ratio (q/p) because of the pressure-sensitivity of the yield surface. Table 5.1 is a sampling of these quantities as gleaned from the simulations of Saada's (Saada et al., 1983) axial extension and compression tests. Note that for a non-frictional yield criterion, which has the same unit normal as the pressure sensitive yield surface at the zero dilation line, these magnitudes are identical and this dilemma does not arise. The difference in the magnitudes of $\underline{n}:d\bar{g}$ at the lower stress ratios may be a cause for concern because it affects the predictions of the compaction volumetric strains in extension, which as one may recall were very stiff compared to Saada's data. To check the possible influence of this aspect on the poor predictions of the extension compressive volumetric strains, the writer executed a simulation where the stress increment $d\bar{g}$ was assumed fully effective in producing plastic

Table 5.1 Typical Variation of the Magnitude of $\underline{n}:d\bar{g}$ Along Axial Extension and Compression Paths

Magnitude of axial stress increment = .225

Maximum stress ratio $\sqrt{J_2^*/I_1} = .300$

Mobilized Stress Ratio , $\sqrt{J_2^*/I_1}$	Extension $\underline{n}:d\bar{g}$	Compression $\underline{n}:d\bar{g}$
.02	.005	.214
.04	.115	.225
.06	.143	.220
.08	.155	.212
.10	.164	.206
.12	.170	.201
.14	.174	.196
.16	.176	.192
.18	.180	.189
.20	.182	.186
.218 (zero dilation line)	.184	(note equality) .184
.22	.185	.183
.24	.189	.175
.26	.193	.168
.28	.197	.160
.30 (failure)	.200	.153

deformation throughout the loading in the extension test (i.e., $\underline{n}:\underline{d}\underline{g} = |\underline{d}\underline{g}|$). Although this fully effective loading simulation predicted a peak compressive volumetric strain an order of magnitude greater than the true simulation ($.28 \times 10^{-3}$ vs. $.20 \times 10^{-4}$), it was itself an order of magnitude less than the recorded peak compressive volumetric strain of $.29 \times 10^{-2}$. For comparison, note that the observed peak overall volumetric compaction in the axial compression test, which is very close to the true prediction, was $.18 \times 10^{-2}$. Therefore, although this aspect may be a cause for concern, it could not be the sole cause of the poor prediction of the volumetric compression observed in Saada's axial extension test. Another option would be to probe the shape of the yield surface in extension stress space to see if its difference from compression stress space is as pronounced as the data suggests.

In a less general context, many other aspects of the model may be improved; for example

1. A more complicated interpolation rule may be selected for the field of plastic moduli to simulate stress-strain curves in which the plastic modulus decreases more rapidly below the zero dilation line.
2. Degradation effects as well as a stress path memory variable to monitor the degree of stress reversal may also be used to improve the hardening option. If one follows the approach used in this study, these variables will only influence the plastic modulus.

3. A phenomenological (second order) fabric tensor may also be included in the formulation to keep track of inherent and induced directional stiffness properties. The invariants of this tensor can also serve as a measure of the intensity of the anisotropy. One such approach, which can be applied directly to the simple model, has been presented by Dafalias (1981).

The following can be concluded regarding the study of the Prevost (1980) model described in Chapter 4:

1. Although this model has conceptual appeal and reproduces the input response along its calibration paths, the calculated results along non-calibration loading paths were very disappointing. The author believes that its main drawbacks stem from the lack of an explicit incorporation of the failure locus and the particular non-associativity assumption used to predict the direction of the plastic strain increment vector.
2. The initialization procedure is cumbersome and requires a great deal of effort. The computed yield surfaces invariably intersect, and the subsequent manual rearrangement procedure is extremely time-consuming. In addition to other tests, the parameter evaluation scheme requires data from an axial extension test, a test which, owing to experimental difficulties, is not yet routine in most commercial soil testing laboratories.
3. The model parameters depend on the initial stress state, and it is not clear if and how they can be normalized.

APPENDIX A
 DERIVATION OF ANALYTICAL REPRESENTATION OF
 THE DILATION PORTION OF THE YIELD SURFACE

Start by considering the following general second order equation (defined for convenience in an arbitrary rectangular Cartesian x-y coordinate system) to which the relevant constraints shall be subsequently applied:

$$F = a x^2 + b y^2 + c xy + d y + e x + f = 0. \quad (\text{A.1})$$

As a first step, equation A.1 can be divided by the coefficient of x^2 , "a", and then the constants can be renamed such that $b = b/a$, $c = c/a$, etc.; this algebraic operation results in

$$F = x^2 + b y^2 + c xy + d y + e x + f = 0. \quad (\text{A.2})$$

Inserting the stress invariant variables in place of x and y in equation A.2 yields

$$F = I_1^2 + b J_2^* + c I_1 \sqrt{J_2^*} + d \sqrt{J_2^*} + e I_1 + f = 0. \quad (\text{A.3})$$

Equation A.3 is now subjected to four consecutive constraints to ensure that the function is continuous with the ellipse and satisfies certain boundary stipulations.

Constraint #1: $F = 0$ at $I_1 = \sqrt{J_2^*} = 0$; this implies that the constant "f" is equal to zero, and as a result, equation A.3 reduces to

$$F = I_1^2 + b J_2^* + c I_1 \sqrt{J_2^*} + d \sqrt{J_2^*} + e I_1 = 0. \quad (\text{A.4})$$

Constraint #2: at $I_1 = \sqrt{J_2^*} = 0$, $d\sqrt{J_2^*}/dI_1 = S$, and this condition establishes that

$$\begin{aligned} d\sqrt{J_2^*}/dI_1 &= -\partial F/\partial I_1 + \partial F/\partial \sqrt{J_2^*} \\ &= -(2I_1 + c\sqrt{J_2^*} + e) + (2b\sqrt{J_2^*} + cI_1 + d) = S, \end{aligned}$$

from which we see

$$e = -Sd \quad . \quad (A.5)$$

Substitution of equation A.5 into equation A.4 gives

$$F = I_1^2 + bJ_2^* + cI_1\sqrt{J_2^*} + d\sqrt{J_2^*} - SdI_1 = 0. \quad (A.6)$$

Constraint #3: at $I_1 = (I_0/Q)$, $\sqrt{J_2^*} = N(I_0/Q)$. Substituting this information into equation A.6 shows that

$$d = (I_0/Q) [1 + bN^2 + cN] + [S - N]. \quad (A.7)$$

And now we can substitute A.7 into equation A.6 to obtain

$$F = I_1^2 + bJ_2^* + cI_1\sqrt{J_2^*} + (I_0/Q) \frac{[1 + bN^2 + cN]}{[S - N]} \{\sqrt{J_2^*} - SI_1\}. \quad (A.8)$$

Constraint #4: at the zero dilation point [$I_1 = I_0/Q$, $\sqrt{J_2^*} = N(I_0/Q)$],

$$d\sqrt{J_2^*}/dI_1 = -\partial F/\partial I_1 + \partial F/\partial \sqrt{J_2^*} = 0,$$

which implies that $\partial F/\partial I_1 = 0$. Using these requirements in equation A.8 results in

$$2I_1 + c\sqrt{J_2^*} - S(I_0/Q) \frac{[1 + bN^2 + cN]}{[S - N]} = 0,$$

from which we then see that

$$c = (S/N^2) - (2/N) - Sb. \quad (A.9)$$

Finally, the substitution of equation A.9 into equation A.8 gives the following expression for the yield surface characterizing the meridional section between the limit line and the zero dilation line:

$$\begin{aligned} F = I_1^2 + bJ_2^* + \frac{[S - 2 - Sb]}{N^2 N} I_1\sqrt{J_2^*} + \\ (I_0/Q) \frac{[1 - bN]}{N} \{\sqrt{J_2^*} - SI_1\} = 0. \end{aligned} \quad (A.10)$$

After exhausting all available constraints, inspection of equation A.10 reveals that we have eliminated all but one independent parameter (i.e., "b") from the original set (i.e., "a", "b", "c", "d", "e", & "f"). The slope S is usually fixed at a magnitude of 1.5.

Range of the parameter "b"

Following the standard procedure outlined by Beyer (1981, p. 250), the restrictions on the parameter b are investigated by looking at how its magnitude affects the nature of the graph of this quadratic in I_1 and $\sqrt{J_2}^*$. Table A.1 gives the details of the general procedure. For the particular function derived here, equation A.10,

$$\Delta = \frac{-1}{4} \left(\frac{I_0}{Q} \right)^2 \frac{(1 - bN)^2}{N} \frac{(S - 1)^2}{N},$$

$$J = b - \frac{1}{4} \left[\frac{S}{N^2} - \frac{2}{N} - Sb \right]^2,$$

$$I = 1 + b, \text{ and}$$

$$K = - (1 + S^2) \frac{1}{4} \left(\frac{I_0}{Q} \right)^2 \frac{(1 - bN)^2}{N}.$$

From these equations, we see that

$$b = \left(\frac{1}{N} - \frac{2}{S} \right)^2 \tag{A.11}$$

identifies a parabolic conic section. Magnitudes of b greater than that specified by equation A.11 give ellipses and those smaller than this magnitude give hyperbolas. Furthermore, to ensure that $\Delta \neq 0$, b must not be exactly equal to $\frac{1}{N^2}$. In fact, if $b = \frac{1}{N^2}$ the quadratic equation degenerates to case 9 of Table A.1 to give the equation of the zero dilation line $\sqrt{J_2}^*/I_1 = N$. As $b \rightarrow -\infty$, the equation of the yield surface, equation A.10, simplifies to

Table A.1 Formulas for Use in Inspecting the Nature of the Quadratic Function Describing the Dilation Portion of the Yield Surface

General quadratic in x and y : $ax^2 + 2hxy + by^2 + 2gx + 2fy + c = 0$

Definitions: $\Delta = a(bc - f^2) - h(hc - gf) + g(hf - bg)$

$$J = ab - h^2$$

$$I = a + b$$

$$K = ac - g^2 + bc - f^2$$

CASE	Δ	J	Δ/I	K	CONIC
1	$\neq 0$	> 0	< 0		real ellipse
2	$\neq 0$	> 0	> 0		imaginary ellipse
3	$\neq 0$	< 0			hyperbola
4	$\neq 0$	0			parabola
5	0	< 0			real intersecting lines
6	0	> 0			conjugate complex intersecting lines
7	0	0		< 0	real distinct parallel lines
8	0	0		> 0	conjugate complex parallel lines
9	0	0		0	coincident lines

$$F = J_2^* - S I_1 \sqrt{J_2^*} - (I_0/Q) N \{ \sqrt{J_2^*} - S I_1 \} = 0,$$

or alternatively,

$$F = (\sqrt{J_2^*} - S I_1) \left(\sqrt{J_2^*} - N \frac{I_0}{Q} \right) = 0,$$

which shows that it represents two straight line portions: the horizontal line $\sqrt{J_2^*} = N (I_0/Q)$ intersecting the line $\sqrt{J_2^*}/I_1 = S$.

Therefore, from these two extreme cases, we see that the parameter b must lie in the range

$$-\infty < b < \frac{1}{N^2}. \quad (\text{A.12})$$

APPENDIX B
COMPUTATION OF THE GRADIENT TENSOR TO THE YIELD SURFACE

The gradient to the yield surface is

$$\frac{\partial F}{\partial \underline{\sigma}} = \frac{\partial F}{\partial I_1} \frac{dI_1}{d\underline{\sigma}} + \frac{\partial F}{\partial \sqrt{J_2}} \frac{d\sqrt{J_2}}{d\underline{\sigma}} + \frac{\partial F}{\partial \theta} \frac{d\theta}{d\underline{\sigma}}, \quad (\text{B.1})$$

where (cf. equation 2.2.2.33)

$$\sin 3\theta = \frac{[3\sqrt{3} (J_3/\sqrt{J_2}^3)]}{2}. \quad (\text{B.2})$$

From equation B.2 we find that

$$\frac{d\theta}{d\underline{\sigma}} = \frac{\sqrt{3}}{2 \cos 3\theta} \left\{ \frac{\partial J_3}{\partial \underline{\sigma}} \frac{1}{[\sqrt{J_2}]^3} - \frac{3 J_3}{[\sqrt{J_2}]^4} \frac{\partial \sqrt{J_2}}{\partial \underline{\sigma}} \right\}. \quad (\text{B.3})$$

Substitution of equation B.3 into equation B.1 yields (in indicial notation)

$$\begin{aligned} \frac{\partial F}{\partial \sigma_{ij}} = \nabla F = & \frac{\partial F}{\partial I_1} \frac{\partial I_1}{\partial \sigma_{ij}} + \left\{ \frac{\partial F}{\partial \sqrt{J_2}} - \frac{\sqrt{3}}{2 \cos 3\theta} \frac{3 J_3}{[\sqrt{J_2}]^4} \frac{\partial F}{\partial \theta} \right\} \frac{\partial \sqrt{J_2}}{\partial \sigma_{ij}} + \\ & \left\{ \frac{\sqrt{3}}{2 \cos 3\theta} \frac{1}{[\sqrt{J_2}]^3} \frac{\partial F}{\partial \theta} \right\} \frac{\partial J_3}{\partial \sigma_{ij}} \end{aligned} \quad (\text{B.4})$$

where

$$\frac{dI_1}{d\sigma_{ij}} = \delta_{ij}, \quad (\text{B.5})$$

$$\frac{d\sqrt{J_2}}{d\sigma_{ij}} = \frac{1}{2\sqrt{J_2}} s_{ij}, \quad (\text{B.6})$$

$$\frac{dJ_3}{d\sigma_{ij}} = \{a'_{ij}\}^T + \frac{1}{3} J_2 \delta_{ij}, \quad (\text{B.7})$$

and

$$\{a'_3\}^T = \{(s_{22}s_{33} - s_{23}^2), (s_{11}s_{33} - s_{13}^2), (s_{11}s_{22} - s_{12}^2), \\ (s_{23}s_{13} - s_{33}s_{12}), (s_{13}s_{12} - s_{11}s_{23}), (s_{12}s_{23} - s_{22}s_{13})\}.$$

In order to find the gradient tensor, we need therefore only to compute the partial derivatives $\frac{\partial F}{\partial I_1}$, $\frac{\partial F}{\partial J_2}$, and $\frac{\partial F}{\partial \theta}$ of equations 3.3.3.1

and 3.3.4.1. We find from equation 3.3.3.1,

$$\frac{\partial F}{\partial I_1} = 2(I_1 - \frac{I_0}{Q}), \quad (B.8)$$

$$\frac{\partial F}{\partial J_2} = 2 \frac{\{(Q-1)/N\}^2 \sqrt{J_2}}{[g(\theta)]^2}, \quad (B.9)$$

and

$$\frac{\partial F}{\partial g(\theta)} = -2 \frac{\{(Q-1)/N\}^2 J_2}{[g(\theta)]^3}. \quad (B.10)$$

Also, from equation 3.3.1.8, recognize that

$$\frac{dg(\theta)}{d\theta} = \frac{6R(1-R)\cos 3\theta}{\{[1+R] - [1-R]\sin 3\theta\}^2} \quad (B.11)$$

which is to be used in the following:

$$\frac{\partial F}{\partial \theta} = \frac{\partial F}{\partial g(\theta)} \frac{dg(\theta)}{d\theta}.$$

And for the more complicated choice of $g(\theta)$ (equation 3.3.1.6),

$$\frac{dg(\theta)}{d\theta} = \frac{v \frac{du}{d\theta} - u \frac{dv}{d\theta}}{v^2}, \quad (B.12)$$

where

$$u = A(1-R^2) + (2R-1)\sqrt{[(2+B)(1-R^2) + 5R^2 - 4R]},$$

$$v = (1-2R)^2 + 2(1-R^2) + B(1-R^2),$$

$$\frac{du}{d\theta} = (1-R^2) \frac{dA}{d\theta} + \frac{1}{2} \frac{(2R-1)(1-R^2)}{\sqrt{[(2+B)(1-R^2) + 5R^2 - 4R]}} \frac{dB}{d\theta},$$

$$\frac{dv}{d\theta} = (1-R^2) \frac{dB}{d\theta},$$

$$A = \sqrt{3} \cos \theta - \sin \theta,$$

$$B = \cos 2\theta - \sqrt{3} \sin 2\theta,$$

$$\frac{dA}{d\theta} = -\sqrt{3} \sin \theta - \cos \theta,$$

and

$$\frac{dB}{d\theta} = -2 \sin 2\theta - 2\sqrt{3} \cos 2\theta.$$

Similarly, from equation 3.3.4.1, we find that

$$\frac{\partial F}{\partial I_1} = 2 I_1 + \left[\frac{S}{N^2} - \frac{2}{N} - Sb \right] \sqrt{J_2} \frac{1}{[g(\theta)]} - (I_0/Q) \left[\frac{1}{N} - bN \right] S, \quad (B.13)$$

$$\begin{aligned} \frac{\partial F}{\partial \sqrt{J_2}} = 2 \frac{b}{[g(\theta)]^2} \sqrt{J_2} + \left[\frac{S}{N^2} - \frac{2}{N} - Sb \right] I_1 \frac{1}{[g(\theta)]} + \\ (I_0/Q) \left[\frac{1}{N} - bN \right] \frac{1}{[g(\theta)]}, \end{aligned} \quad (B.14)$$

and

$$\begin{aligned} \frac{\partial F}{\partial g(\theta)} = -\frac{2b}{[g(\theta)]^3} J_2 - \left[\frac{S}{N^2} - \frac{2}{N} - Sb \right] I_1 \sqrt{J_2} \frac{1}{[g(\theta)]^2} - \\ (I_0/Q) \left[\frac{1}{N} - bN \right] \frac{1}{[g(\theta)]^2} \sqrt{J_2}. \end{aligned} \quad (B.15)$$

APPENDIX C
EQUATIONS FOR UPDATING THE SIZE OF THE YIELD SURFACE

When the stress state resides on the consolidation portion of the surface (i.e., when $\frac{\sqrt{J_2^*}}{I_1} \leq N$),

$$I_0 = \max \left\{ \frac{-B_1 \pm \sqrt{(B_1^2 - 4 A_1 C_1)}}{2 A_1} \right\} \quad \text{if } Q > 2 \quad (C.1)$$

$$= -C_1/B_1 \quad \text{if } Q = 2 \quad (C.2)$$

$$= \min \left\{ \frac{-B_1 \pm \sqrt{(B_1^2 - 4 A_1 C_1)}}{2 A_1} \right\} \quad \text{if } Q < 2 \quad (C.3)$$

where

$$A_1 = \frac{2}{Q} - 1,$$

$$B_1 = -2 I_1/Q,$$

and

$$C_1 = I_1^2 + \frac{(Q - 1)^2}{N^2} J_2^*.$$

For the dilation portion of the yield surface, when $\frac{\sqrt{J_2^*}}{I_1} > N$, we

have

$$I_0 = -\frac{D_1}{E_1}, \quad (C.4)$$

where

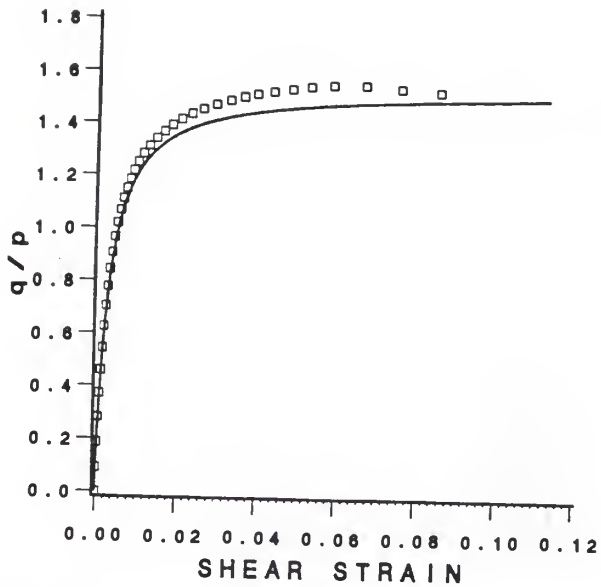
$$D_1 = I_1^2 + b J_2^* + \left[\frac{S}{N^2} - \frac{2}{N} - Sb \right] I_1 \sqrt{J_2^*},$$

and

$$E_1 = \frac{1}{Q} \left(\frac{1}{N} - bN \right) (\sqrt{J_2^*} - SI_1).$$

APPENDIX D

PREDICTION OF HOLLOW CYLINDER TESTS USING PROPOSED MODEL



RESPONSE: — PREDICTED □□ MEASURED

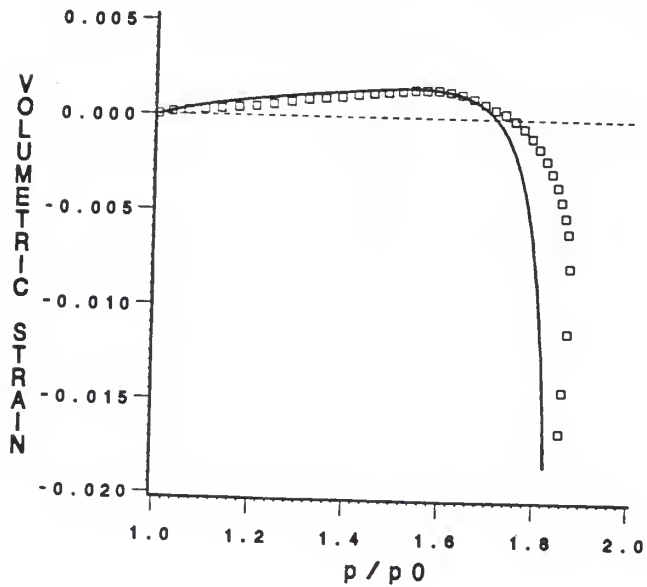


Figure D.1 Measured vs. predicted stress-strain response for DCR 15 stress path using proposed model

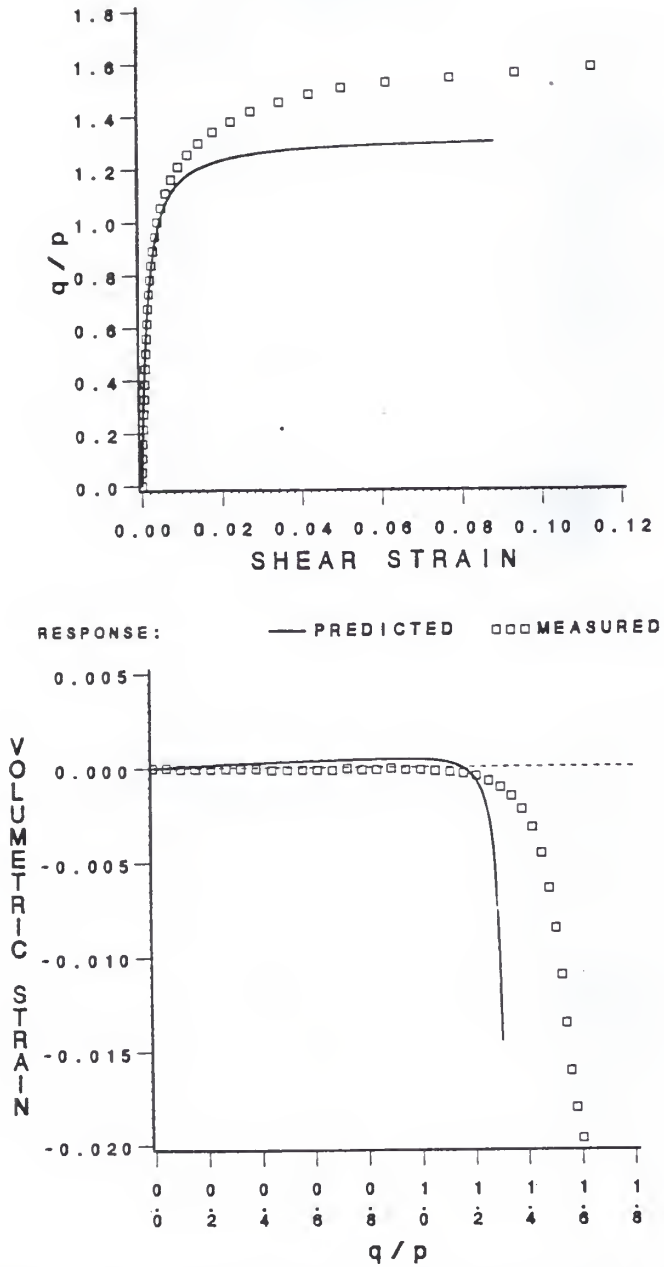


Figure D.2 Measured vs. predicted stress-strain response for DCR 32 stress path using proposed model

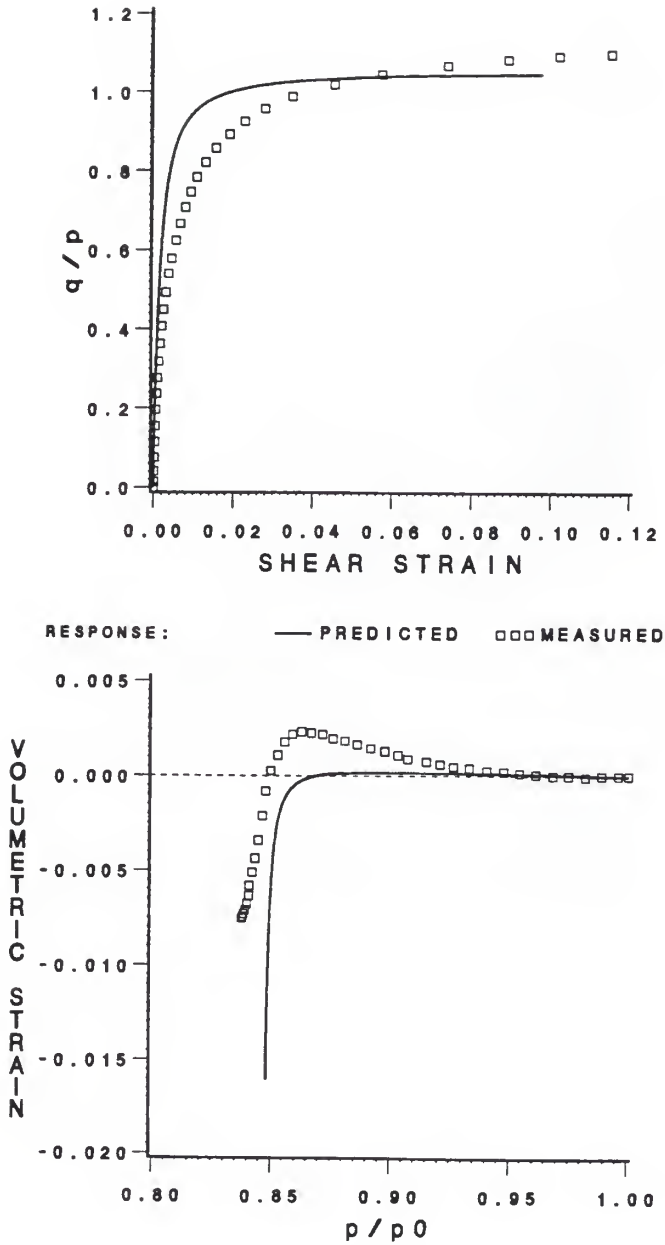


Figure D.3 Measured vs. predicted stress-strain response for DTR 58 stress path using proposed model

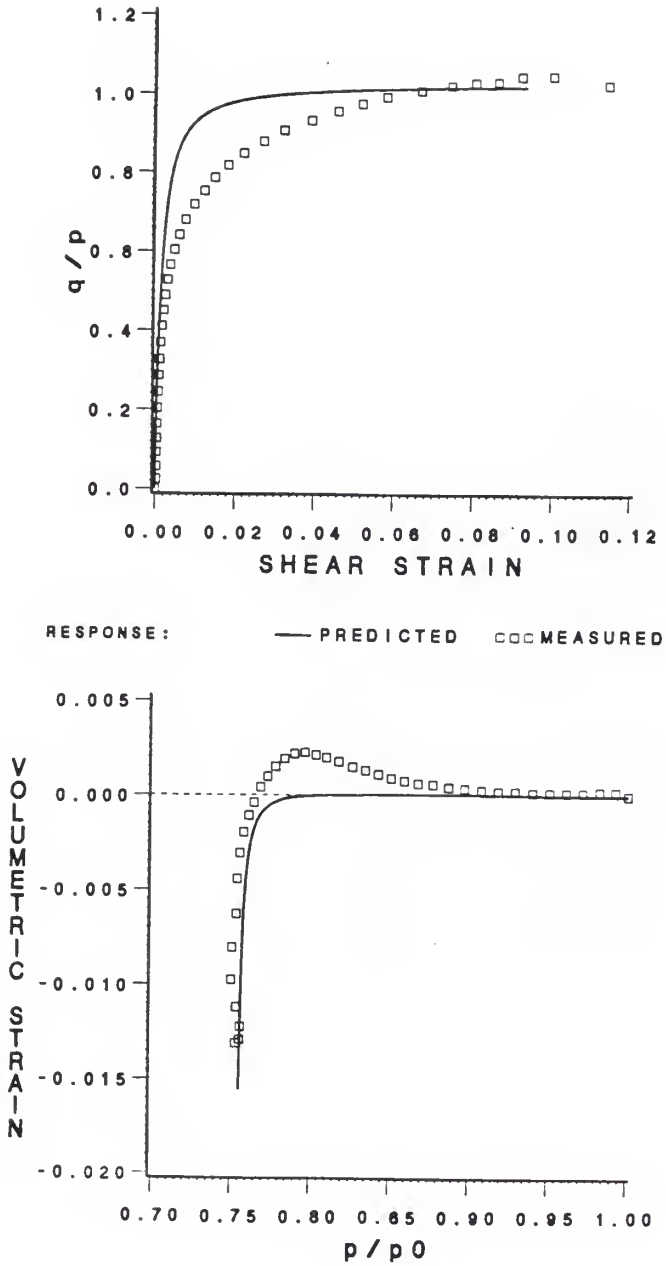


Figure D.4 Measured vs. predicted stress-strain response for DTR 75 stress path using proposed model

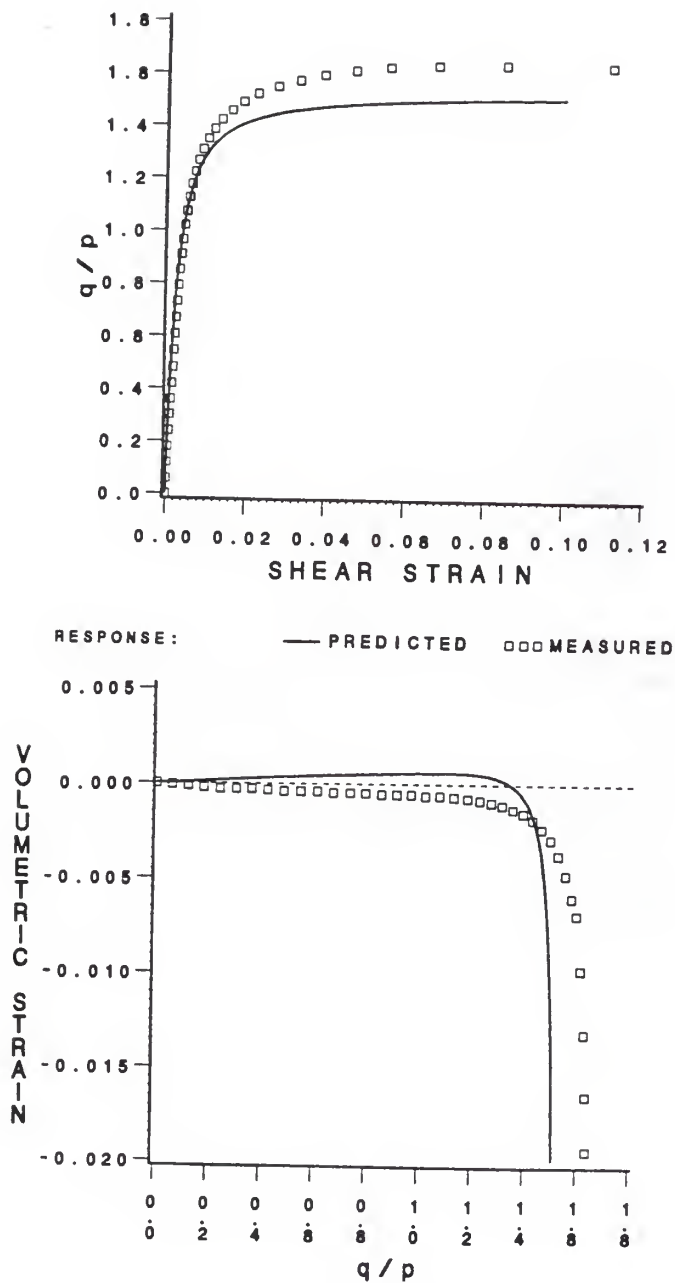


Figure D.5 Measured vs. predicted stress-strain response for GCR 15 stress path using proposed model

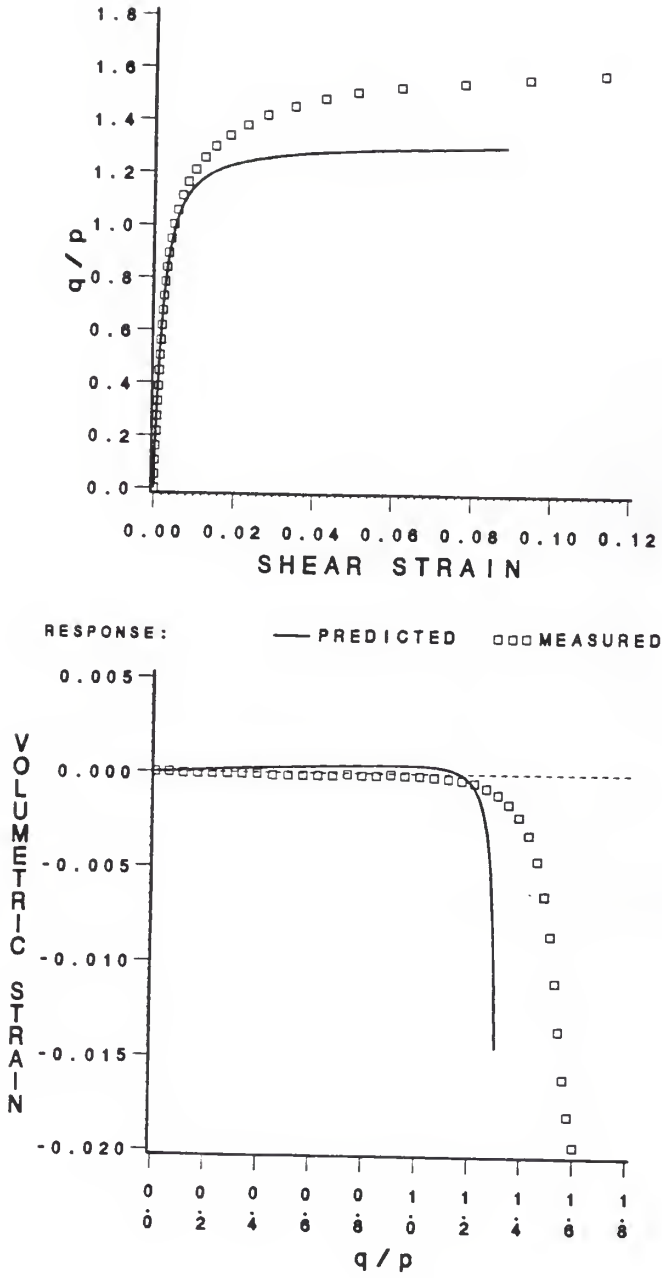


Figure D.6 Measured vs. predicted stress-strain response for GCR 32 stress path using proposed model

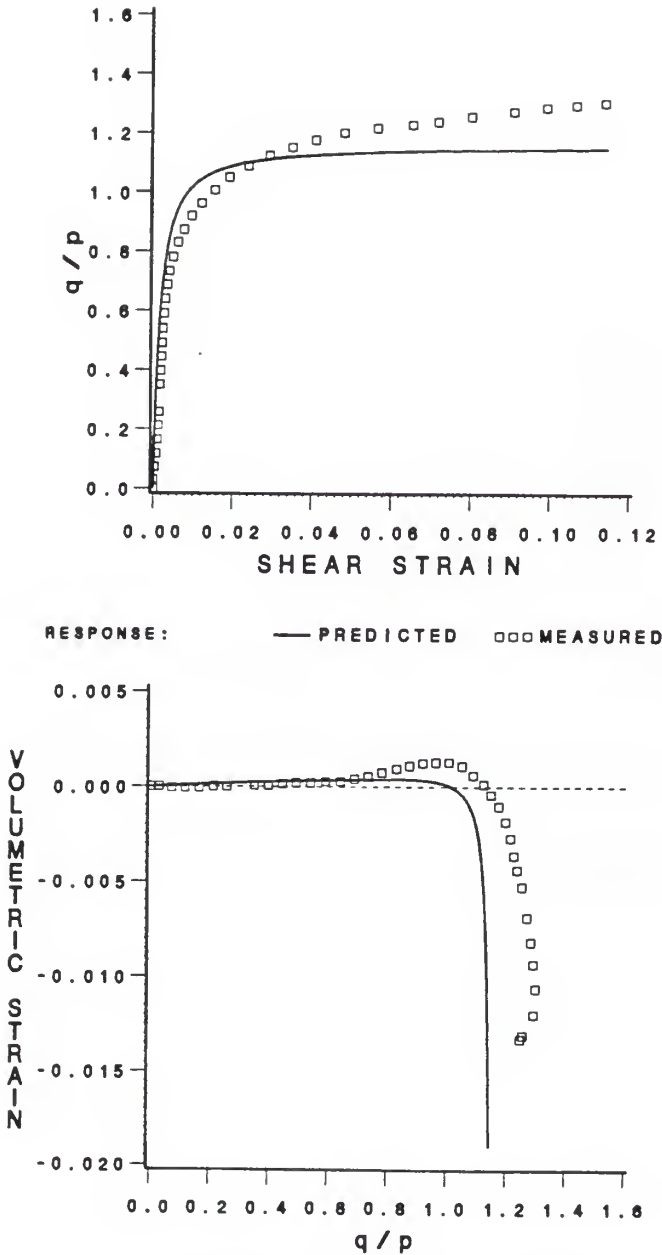


Figure D.7 Measured vs. predicted stress-strain response for R 45 (or pure torsion) stress path using proposed model

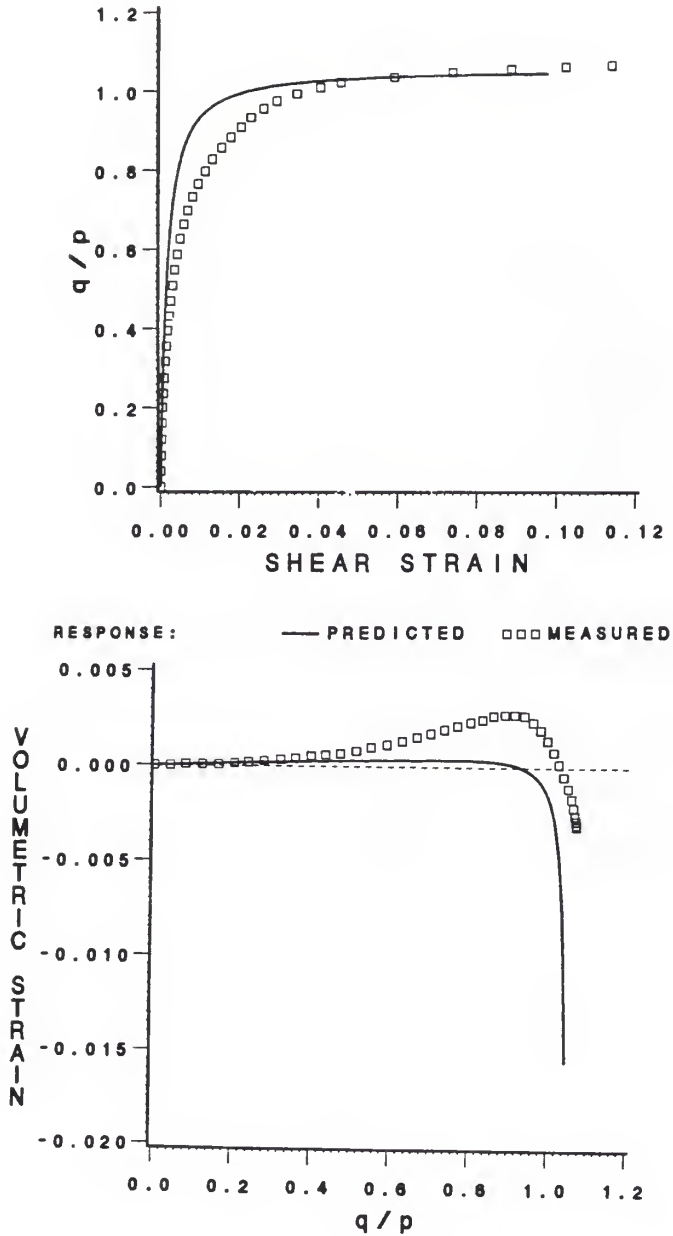


Figure D.8 Measured vs. predicted stress-strain response for GTR 58 stress path using proposed model

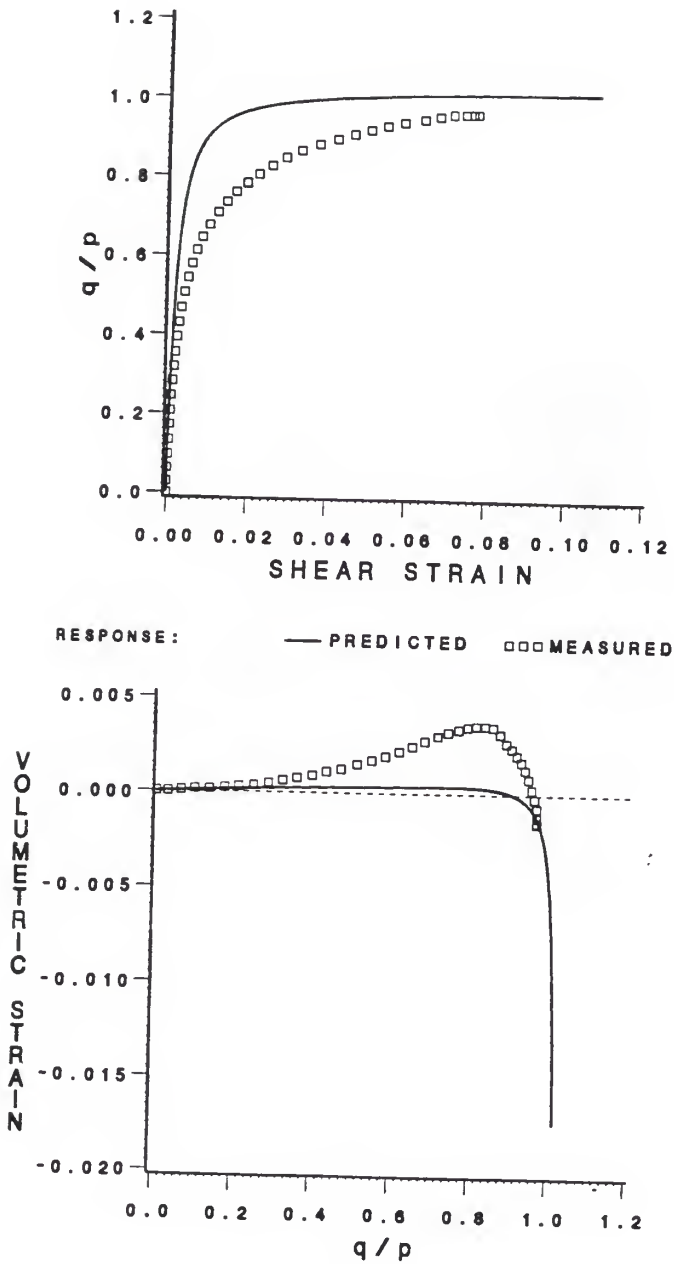


Figure D.9 Measured vs. predicted stress-strain response for GTR 75 stress path using proposed model

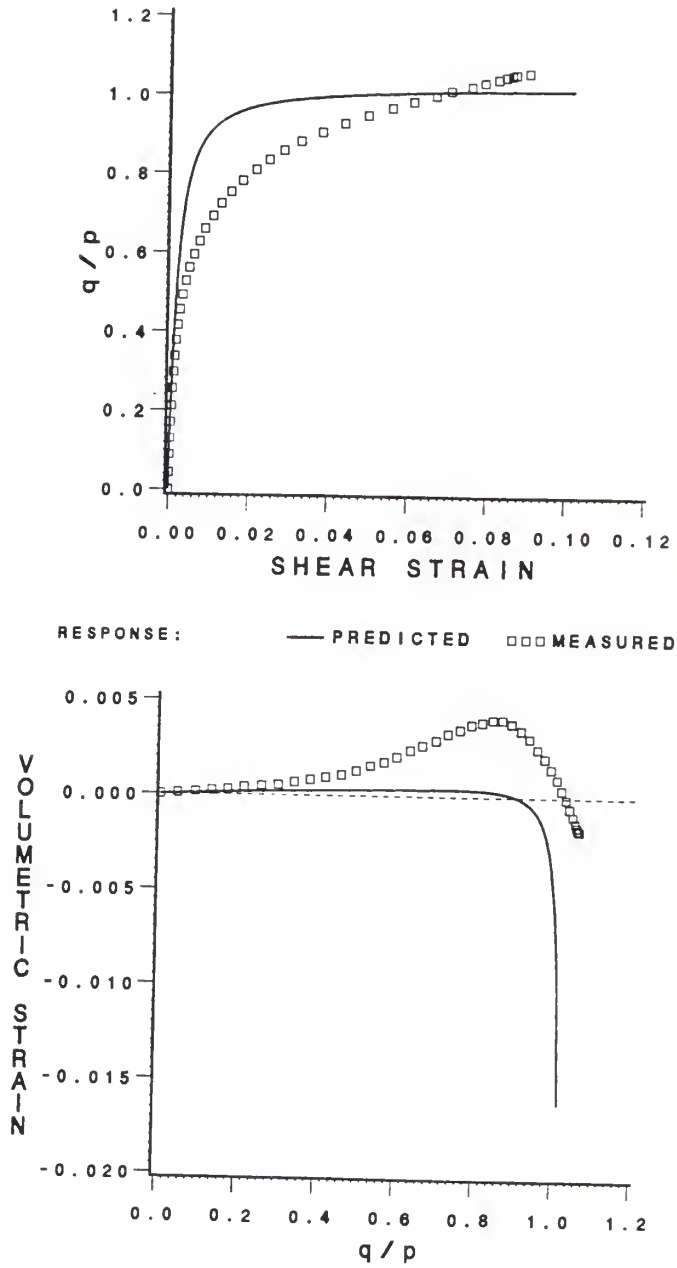


Figure D.10 Measured vs. predicted stress-strain response for GT 90 stress path using proposed model

APPENDIX E

PREDICTION OF HETTLER'S DATA USING PROPOSED MODEL

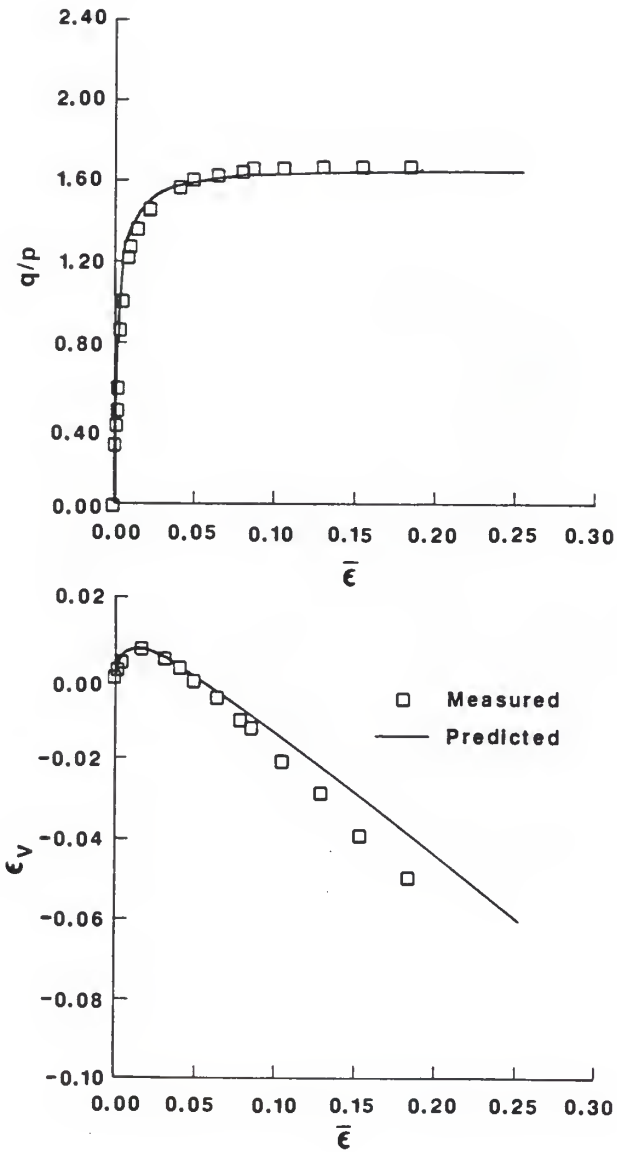


Figure E.1 Measured and predicted response for axial compression test ($\sigma_3 = 400 \text{ kN/m}^2$) on Karlsruhe sand at 92.3% relative density (measured data after Hettler et al., 1984)

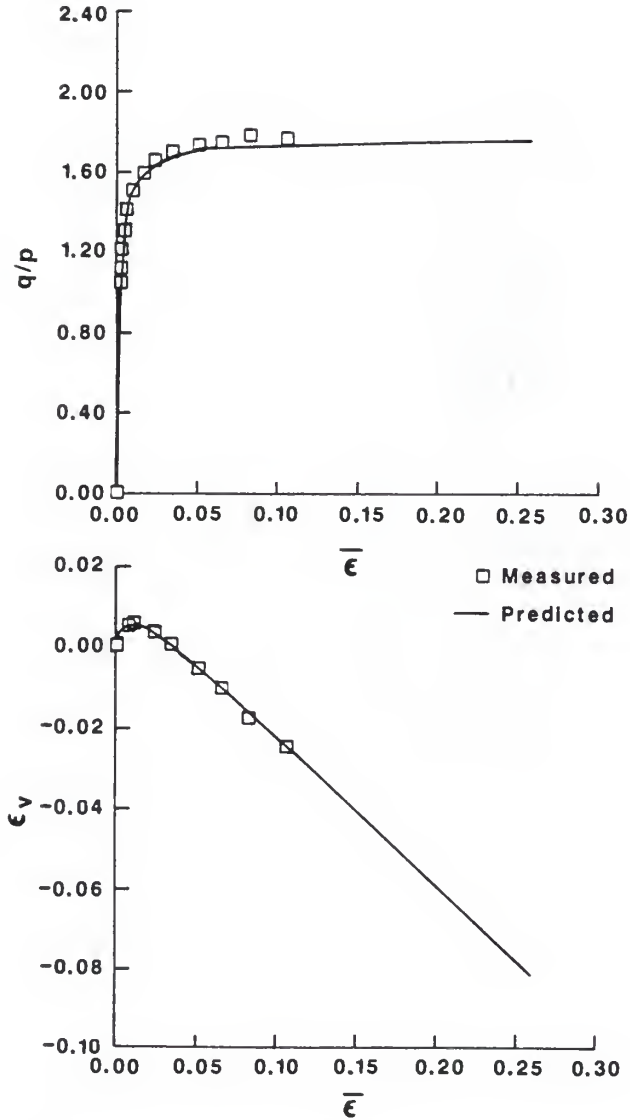


Figure E.2 Measured and predicted response for axial compression test ($\sigma_3 = 80 \text{ kN/m}^2$) on Karlsruhe sand at 99.0% relative density (measured data after Hettler et al., 1984)

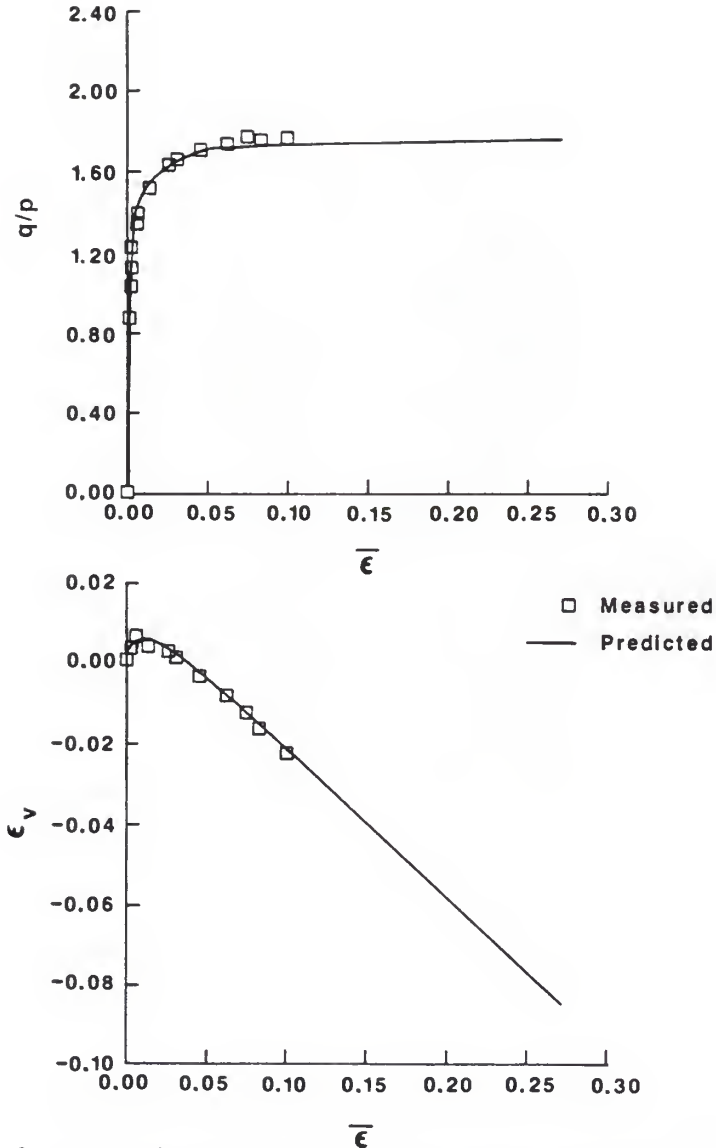


Figure E.3 Measured and predicted response for axial compression test ($\sigma_3 = 200 \text{ kN/m}^2$) on Karlsruhe sand at 99.0% relative density (measured data after Hettler et al., 1984)

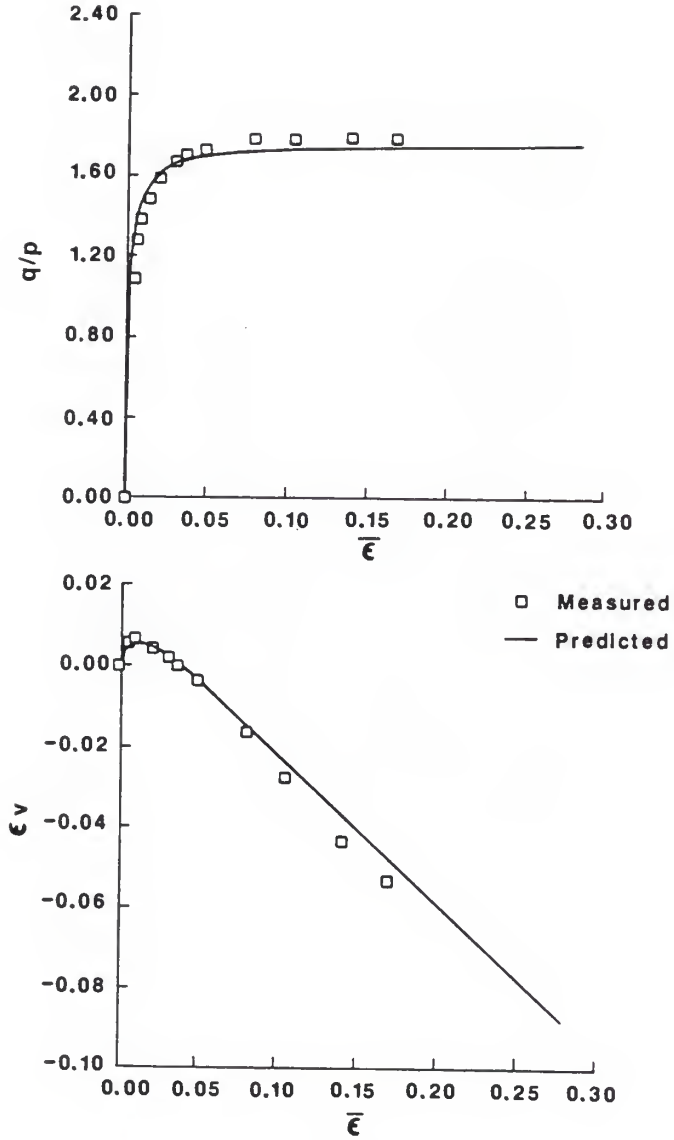


Figure E.4 Measured and predicted response for axial compression test ($\sigma_3 = 300 \text{ kN/m}^2$) on Karlsruhe sand at 99.0% relative density (measured data after Hettler et al., 1984)

APPENDIX F
COMPUTATION OF THE BOUNDING SURFACE SCALAR MAPPING PARAMETER β

When the stress state resides on the consolidation surface (i.e., when $\frac{\sqrt{J_2^*}}{I_1} \leq N$),

$$\beta = \frac{-B_2 \pm \sqrt{(B_2^2 - 4 A_2 C_2)}}{2A_2}, \quad 1 \leq \beta \leq \infty$$

where

$$A_2 = I_1^2 + \frac{\{(Q-1)/N\}^2 J_2}{[g(\theta)]^2},$$

$$B_2 = -2 (I_0/Q) I_1,$$

and

$$C_2 = I_0^2 \{(2/Q)-1\}.$$

For the dilation surface, when $\frac{\sqrt{J_2^*}}{I_1} > N$, we have

$$\beta = \frac{D_2}{E_2},$$

where

$$D_2 = - (I_0/Q) \left[\frac{1}{N} - bN \right] \left\{ \frac{1}{[g(\theta)]} \sqrt{J_2} - S I_1 \right\},$$

and

$$E_2 = I_1^2 + \frac{b}{[g(\theta)]^2} J_2 + \left[\frac{S}{N^2} - \frac{2}{N} - S b \right] I_1 \sqrt{J_2} \frac{1}{[g(\theta)]}.$$

APPENDIX G

PREDICTION OF HOLLOW CYLINDER TESTS USING PREVOST'S MODEL

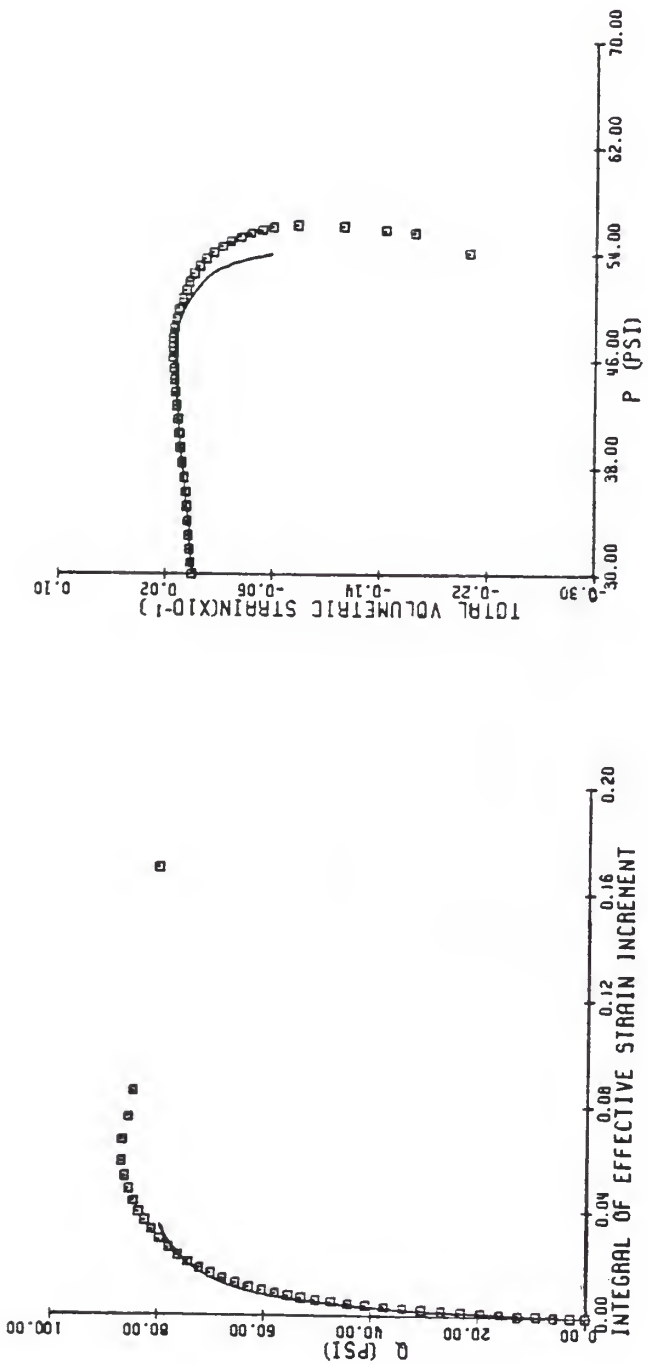


Figure G.1 Measured vs. predicted stress-strain response for DCR 15 stress path using Prevost's model

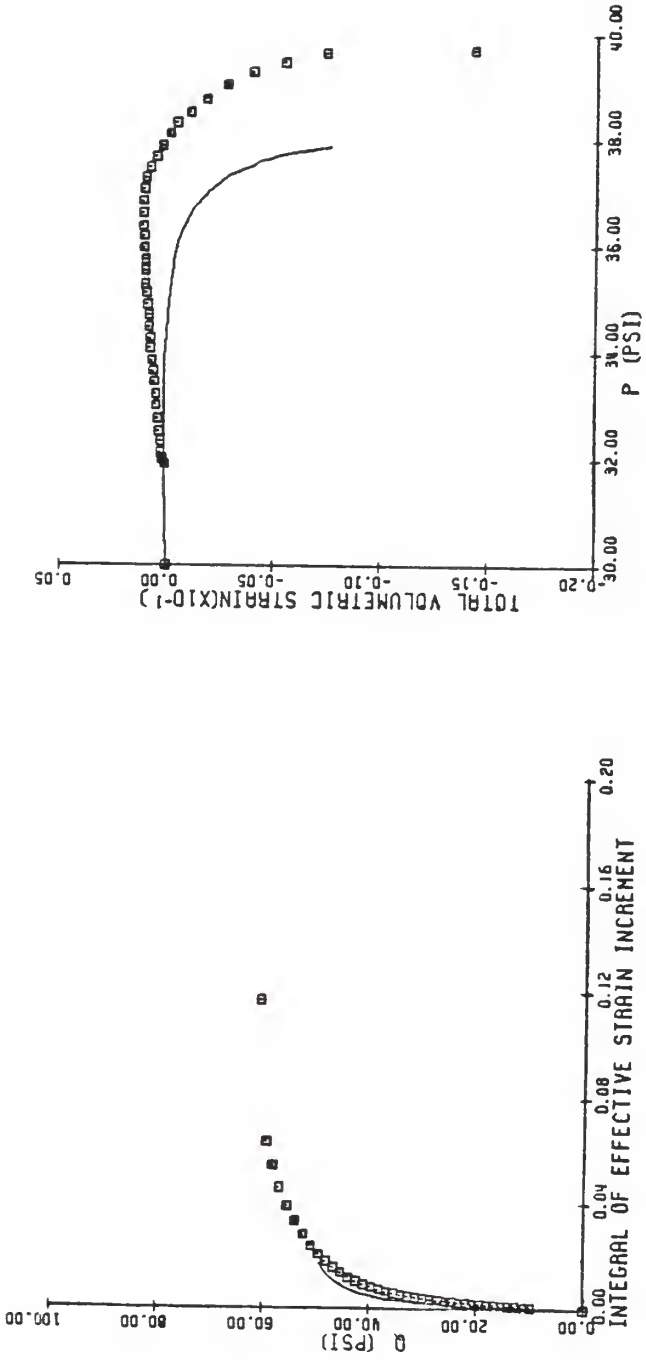


Figure G.2 Measured vs. predicted stress-strain response for DCR 32 stress path using Prevost's model

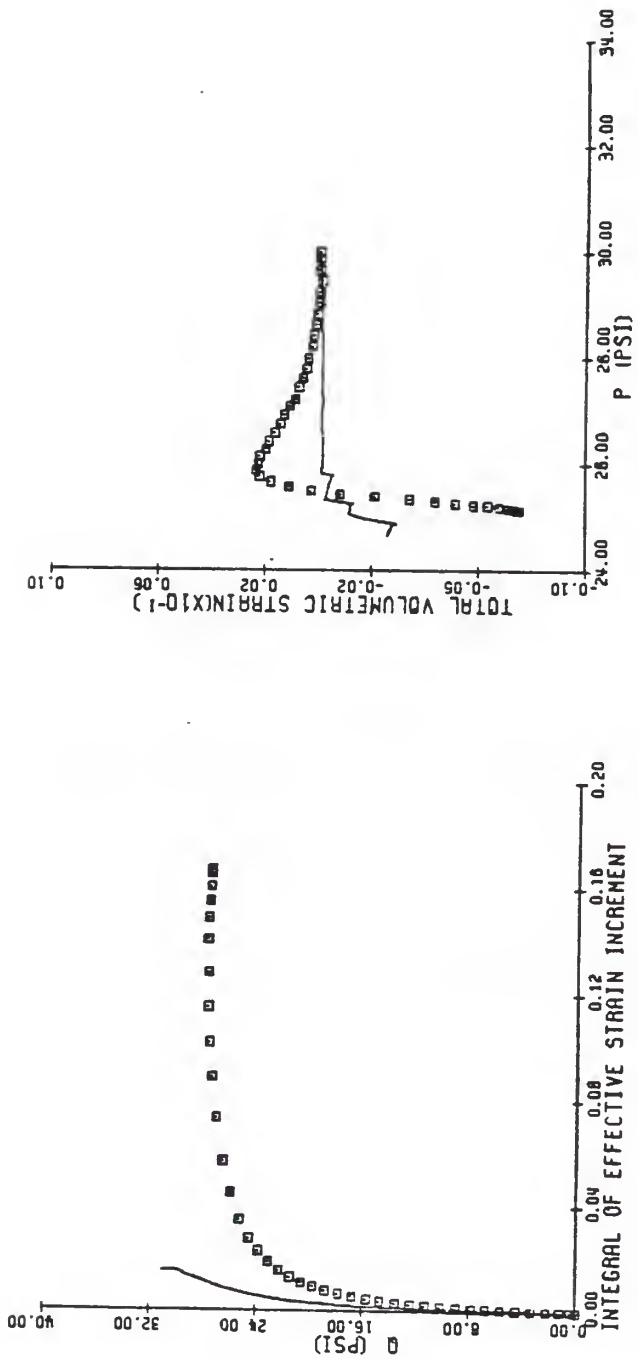


Figure G.3 Measured vs. predicted stress-strain response for DTR 58 stress path using Prevost's model

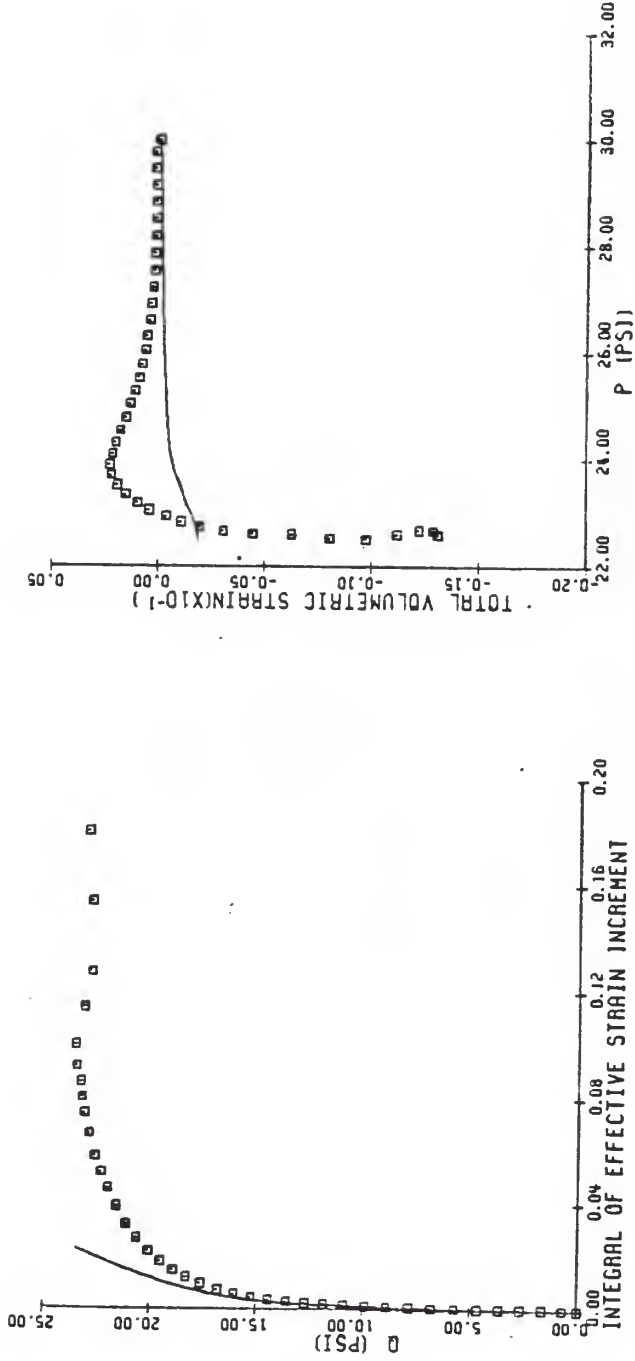


Figure G.4 Measured vs. predicted stress-strain response for DTR 75 stress path using Prevost's model

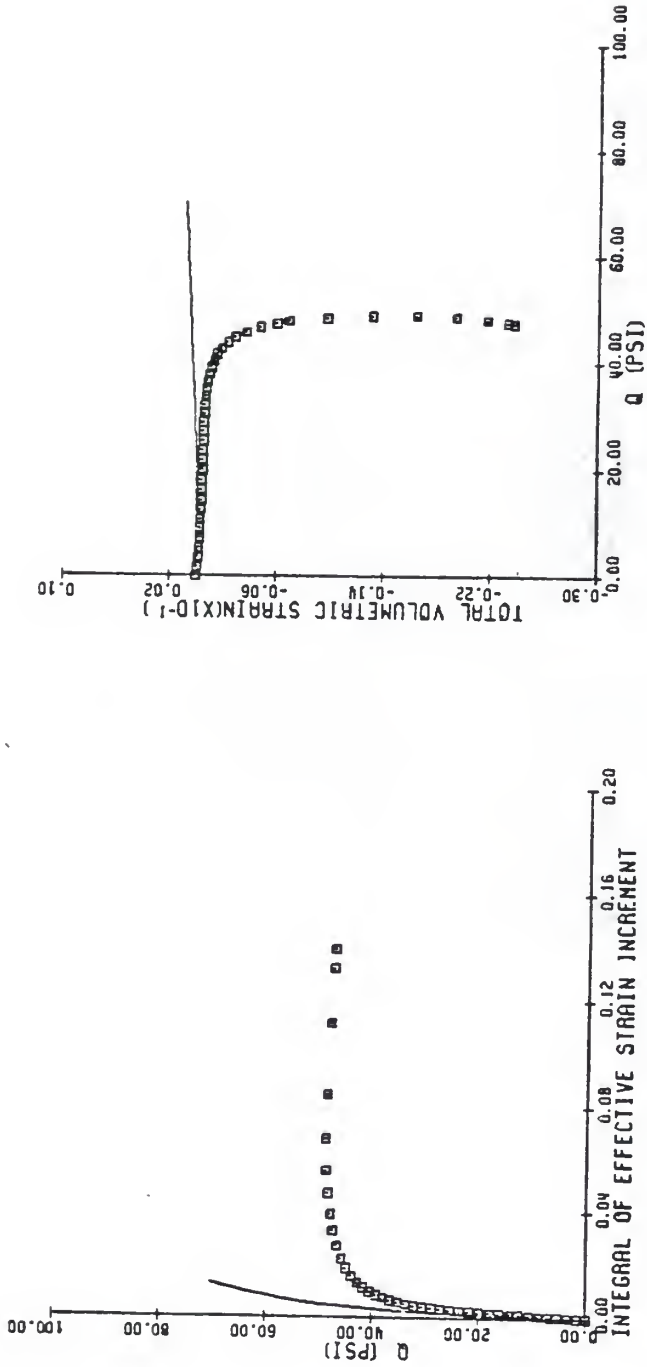


Figure G.5 Measured vs. predicted stress-strain response for GCR 15 stress path using Prevost's model

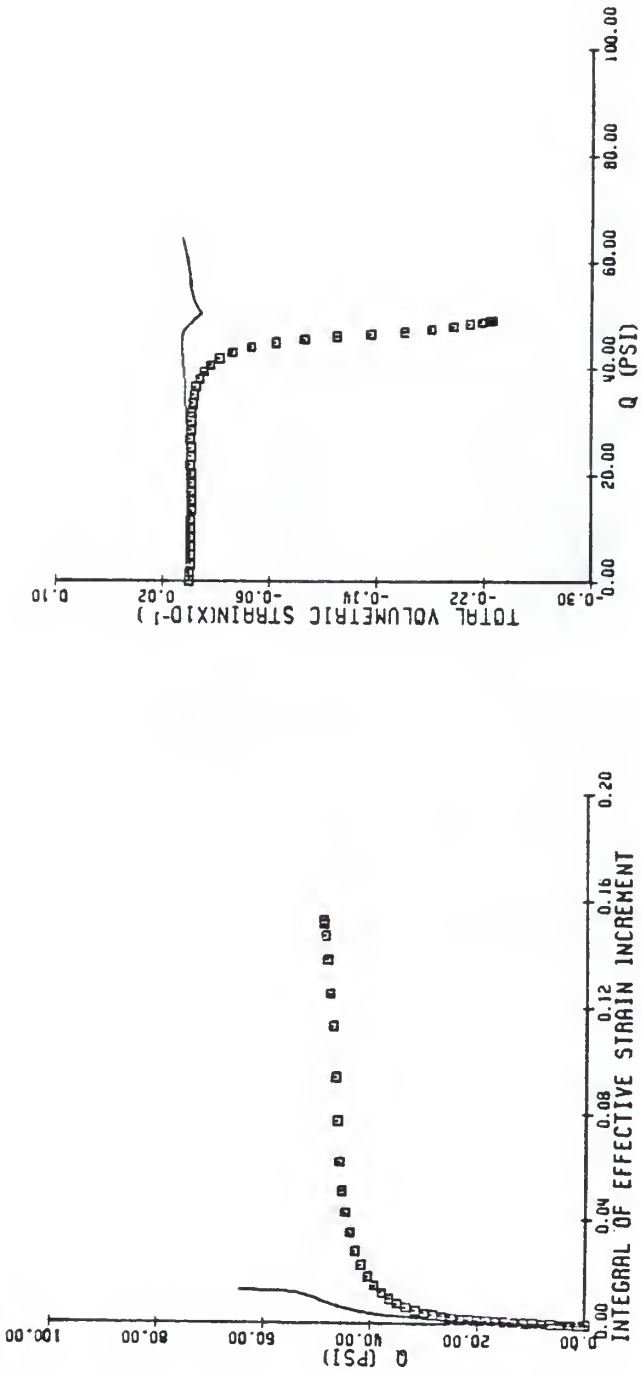


Figure G.6 Measured vs. predicted stress-strain response for GCR 32 stress path using Prevost's model

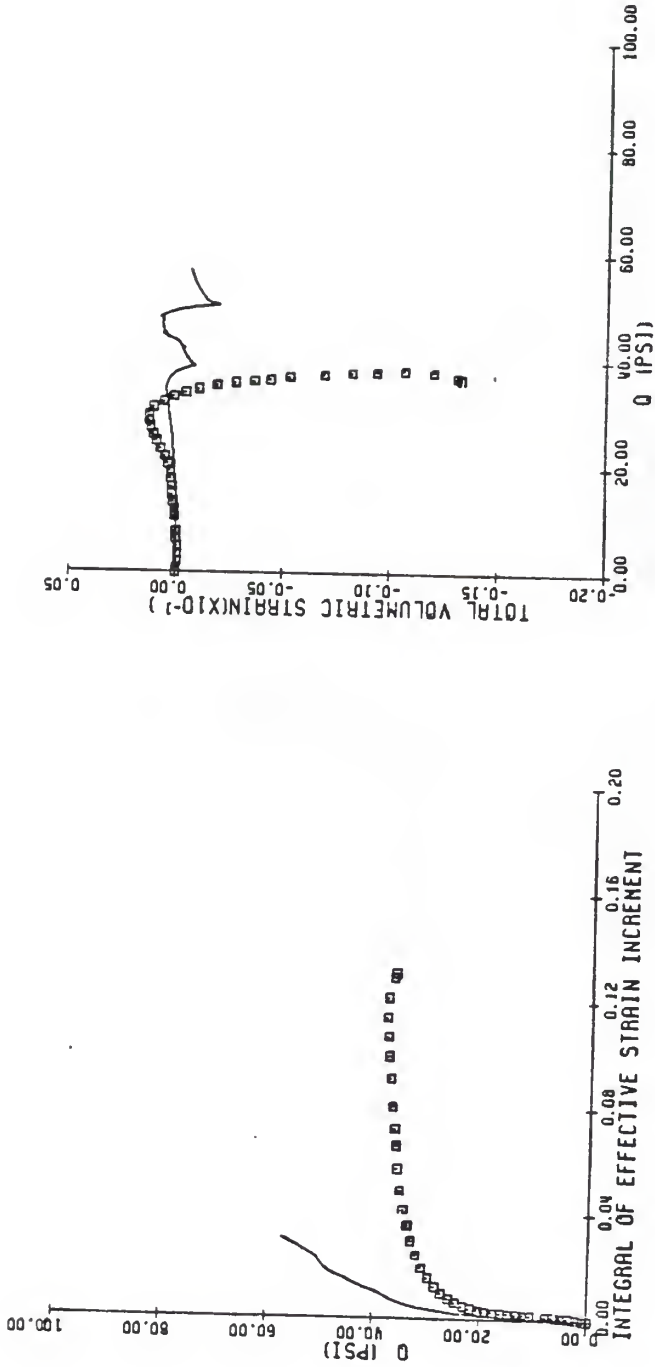


Figure G.7 Measured vs. predicted stress-strain response for R 45 stress path using Prevost's model

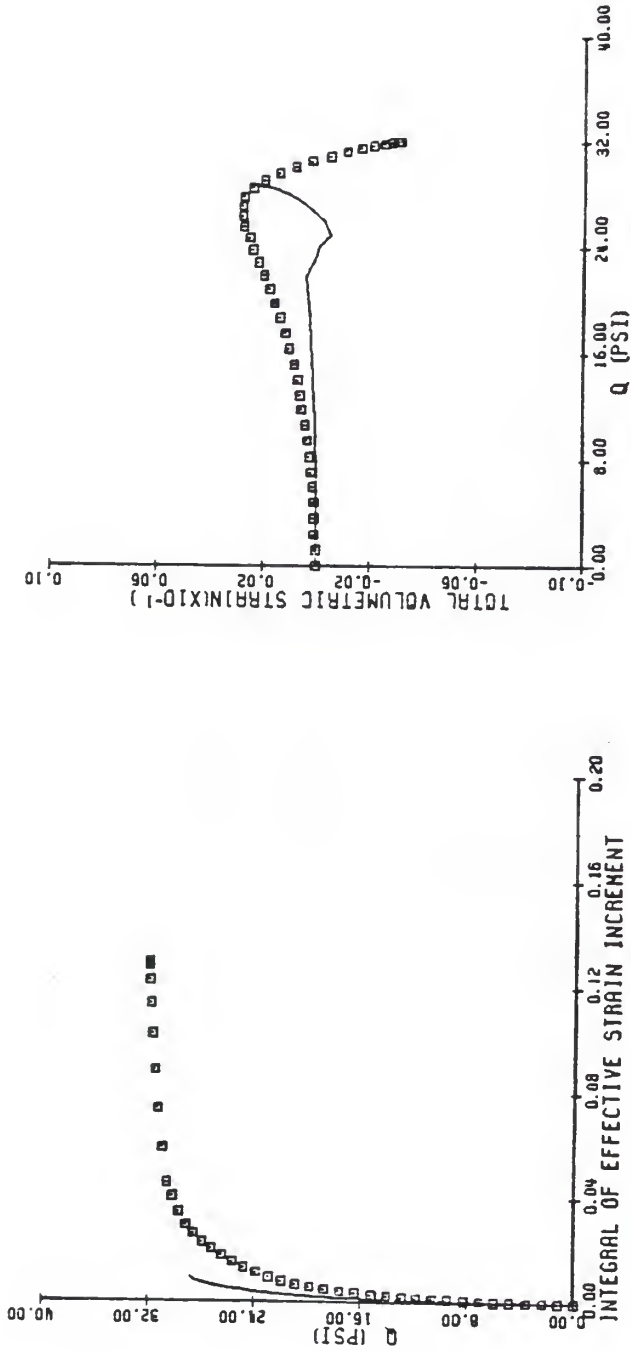


Figure 6.8 Measured vs. predicted stress-strain response for GTR 58 stress path using Prevost's model

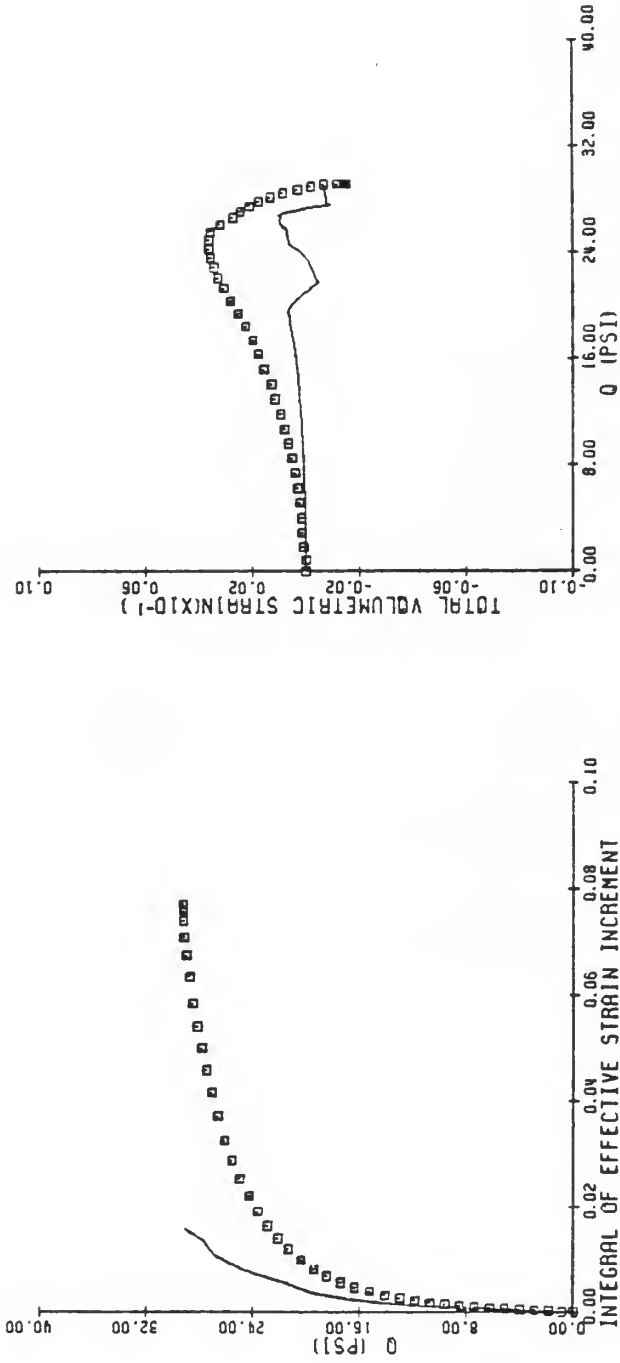


Figure G.9 Measured vs. predicted stress-strain response for CFR 75 stress path using Prevost's model

LIST OF REFERENCES

- Aboim, C.A., and W.H. Roth. "Bounding-Surface Plasticity Theory Applied to Cyclic Loading of Sand." In International Symposium on Numerical Methods in Geomechanics (held in Zurich, Switzerland, 13-17 September, 1982), edited by R. Dungar, G.N. Pande, and J.A. Studer. Rotterdam: A.A. Balkema, 1982.
- Akivis, M.A., and V.V. Goldberg. An Introduction to Linear Algebra and Tensors. Translated and edited by R.A. Silverman. New York: Dover Publications Inc., 1972.
- Al-Hussaini, M.M., and F.C. Townsend. Investigation of K_0 Testing in Cohesionless Soils. Technical Report S-75-16. Vicksburg, Mississippi: Soils and Pavements Laboratory, U.S. Army Engineers Waterways Experiment Station, 1975.
- Anandarajah, A., Y.F. Dafalias, and L.R. Herrmann. "A Bounding Surface Plasticity Model for Anisotropic Clays." In Proceedings of the ASCE Fifth Engineering Mechanics Division Speciality Conference (held in Laramie, Wyoming, 1-3 August, 1984), edited by A.P. Boreisi and K.P. Chong. New York: American Society of Civil Engineers (ASCE), 1984.
- Baltov, A., and A. Sawczuk. "A Rule of Anisotropic Hardening." Acta Mechanica, Vol. 1, No. 2 (1965): 81-92.
- Bauschinger, J. "Ueber die Veraenderungen der Elasticitaetsgrenze von Eisen und Stahl." Dingler's Polytechnisches Journal, Vol. 266 (1887): 216-220.
- Beyer, W.H., Editor. CRC Standard Mathematical Tables. 26th Edition. Boca Raton, Florida: CRC Press, Inc., 1981.
- Bishop, A.W. "The Strength of Soils as Engineering Materials." Geotechnique, Vol. 16, No. 2 (1966): 91-128.
- Bishop, A.W., and D.J. Henkel. The Measurement of Soil Properties in the Triaxial Test. London: William Arnold, 1975.
- Bridgman, P.W. "Flow and Fracture." Transactions of the American Institute of Mining, Metallurgical, and Petroleum Engineers (AIME), Iron and Steel Division, Vol. 162 (1945): 569-583.

- Brown, S.F. "Repeated Load Testing of a Granular Material." Journal of the Geotechnical Engineering Division, ASCE, Vol. 100, No. GT7 (1974): 825-841.
- Cambou, B. "Orientational Distributions of Contact Forces as Memory Parameters in a Granular Material." In IUTAM Conference on Deformation and Failure of Granular Materials (held in Delft, Netherlands, 31 Aug.-3 Sept., 1982), edited by P.A. Vermeer and H.J. Luger. Rotterdam: A.A. Balkema, 1982.
- Casagrande, A. "The Determination of the Preconsolidation Load and Its Practical Significance." In Proceedings First International Conference on Soil Mechanics and Foundation Engineering, Vol. 3 (June 22-26, 1936) Cambridge, Massachusetts: Graduate School of Engineering, Harvard University, 1936.
- Casagrande, A., and N. Carillo. "Shear Failure of Anisotropic Materials." Journal of the Boston Society of Civil Engineers, Vol. 31 (1944): 74-87.
- Cherian, T.V., P. Pietrokowsky, and J.E. Dorn. "Some Observations on the Recovery of Cold Worked Aluminum." Transactions of the American Institute of Mining, Metallurgical, and Petroleum Engineers (AIME), Iron and Steel Division, Vol. 185 (1949): 948-956.
- Clough, R.W., and R.J. Woodward, III. "Analysis of Embankment Stresses and Deformations." Journal of Soil Mechanics and Foundation Engineering, ASCE, Vol. 93, No. SM4 (1967): 529-549.
- Coulomb, C.A. "Essai sur une application des règles de maximis et minimis à quelques problèmes de statique, relatifs à l'architecture." Memoires de mathematique et de physique, présentés à l'Académie Royale des Sciences, par divers savans, & lus dans ses assemblées, Vol. 7 (1773): 343-382.
- Cowin, S.C. "Microstructural Continuum Models for Granular Materials." In Proceedings of the U.S.-Japan Seminar on Continuum Mechanical and Statistical Approaches in the Mechanics of Granular Materials (held in Sendai, Japan, June 5-9, 1978), edited by S.C. Cowin and M. Satake. Gakujutsu Bunken Fukyukai, Tokyo: The Kajima Foundation, 1978.
- Cowin, S.C., and M. Satake, Editors. Proceedings of the U.S.-Japan Seminar on Continuum Mechanical and Statistical Approaches in the Mechanics of Granular Materials (held in Sendai, Japan, June 5-9, 1978). Gakujutsu Bunken Fukyukai, Tokyo: The Kajima Foundation, 1978.
- Dafalias, Y.F. "Initial and Induced Anisotropy of Cohesive Soils by means of a Varying Non-Associated Flow Rule." In Proceedings of the International Symposium on the Behavior of Anisotropic Plastic Solids, C.N.R.S. No. 319, Villard-de-Lans, France: N.P., 1981.

- Dafalias, Y.F. "Modelling Cyclic Plasticity: Simplicity Versus Sophistication." In Mechanics of Engineering Materials, edited by C.S. Desai and R.H. Gallagher. New York: John Wiley & Sons Ltd., 1984.
- Dafalias, Y.F., and L.R. Herrmann. "A Bounding Surface Soil Plasticity Model." In Proceedings of the International Symposium on Soils Under Cyclic and Transient Loading (held in Swansea, Wales, 7-11 January, 1980), edited by G.N. Pande and O.C. Zienkiewicz. Rotterdam: A.A. Balkema, 1980.
- Dafalias, Y.F., and E.P. Popov. "A Model of Nonlinearly Hardening Materials for Complex Loadings." Acta Mechanica, Vol. 21 (1975): 173-192.
- Dafalias, Y.F., and E.P. Popov. "Cyclic Loading for Materials With a Vanishing Elastic Region." Nuclear Engineering and Design, Vol. 41 (1977): 293-302.
- Davidson, J.L. "Self-Boring Pressuremeter Testing in Sand in the University of Florida Calibration Chamber." Final Report, EIES Project No. 245*W516, Gainesville, Florida: Department of Civil Engineering, University of Florida, 1983.
- Davis, R.O., and G. Mullenger. "A Rate-Type Constitutive Model for Granular Media with a Critical State." International Journal for Numerical and Analytical Methods in Geomechanics, Vol. 12 (1978): 255-282.
- Desai, C.S. "A General Basis for Yield, Failure and Potential Functions in Plasticity." International Journal for Numerical and Analytical Methods in Geomechanics, Vol. 4 (1980): 361-375.
- Desai, C.S., and R.H. Gallagher, Editors. International Conference on Constitutive Laws for Engineering Materials (Theory and Applications) (held in Tucson, Arizona, January 10-14, 1983), published in book form as Mechanics of Engineering Materials. New York: John Wiley & Sons, 1984.
- Desai, C.S., and H.J. Siriwardane. "A Concept of Correction Functions to Account for Nonassociative Characteristic of Geologic Media." International Journal for Numerical and Analytical Methods in Geomechanics, Vol. 4 (1980): 377-387.
- Desai, C.S., and H.J. Siriwardane. Constitutive Laws For Engineering Materials With Emphasis On Geologic Materials. Englewood Cliffs, New Jersey: Prentice-Hall Inc., 1984.
- DiMaggio, F.L., and I.S. Sandler. "Material Models for Granular Soils." Journal of the Engineering Mechanics Division, ASCE, Vol. 97, No. EM3 (1971): 936-950.

- Drucker, D.C. "Some Implications of Work-Hardening and Ideal Plasticity." Quarterly of Applied Mechanics, Vol. 7 (1950a): 411-418.
- Drucker, D.C. "Stress-Strain Relations in the Plastic Range: A Survey of Theory and Experiment." Office of Naval Research (ONR) Technical Report, Contract N7-onr-358. Providence, Rhode Island: Graduate Division of Applied Mathematics, Brown University, 1950b.
- Drucker, D.C. "A More Fundamental Approach to Stress-Strain Relations." In Proceedings of the 1st U.S. National Congress for Applied Mechanics. New York: American Society of Mechanical Engineers, 1951.
- Drucker, D.C. "Coulomb Friction, Plasticity, and Limit Loads." Journal of Applied Mechanics, Vol. 21 (1954): 71-74.
- Drucker, D.C. "On Uniqueness in the Theory of Plasticity." Quarterly of Applied Mathematics, Vol. 14, No. 1 (1956): 35-42.
- Drucker, D.C. "Plasticity." In First Symposium on Naval Structural Mechanics, Report C11-41. Providence, Rhode Island: Division of Applied Mathematics, Brown University, 1958.
- Drucker, D.C. "Concept of Path Independence and Material Stability for Soils." In Proceedings of the IUTAM Symposium on Rheology and Mechanics of Soils (held in Grenoble, France), edited by J. Kravtchenko and P.M. Sirieys. Berlin: Springer, 1966.
- Drucker, D.C., R.E. Gibson, and D.J. Henkel. "Soil Mechanics and Work-Hardening Theories of Plasticity." ASCE Transactions, Vol. 22, No. 2864 (1957): 338-346.
- Drucker, D.C., and L. Palgen. "On Stress-Strain Relations Suitable for Cyclic and Other Loading." Journal of Applied Mechanics, Vol. 48 (1981): 479-485.
- Drucker, D.C., and W. Prager. "Soil Mechanics and Plastic Analysis or Limit Design." Quarterly of Applied Mathematics, Vol. 10, No. 157 (1952): 157-165.
- Drucker, D.C., and D. Seereeram. "Remaining at Yield During Unloading and Other Unconventional Elastic-plastic Response." submitted for publication, 1986.
- Duncan, J.M., and C.Y. Chang. "Non-linear Analysis of Stress and Strain in Soils." Journal of Soil Mechanics and Foundation Engineering, ASCE, Vol. 96, No. SM5 (1970): 1629-1653.
- Eisenberg, M.A. "A Generalization of Plastic Flow Theory With Application to Cyclic Hardening and Softening Phenomena." Journal of Engineering Materials and Technology, ASME, Vol. 98 (1976): 221-228.

- Eringen, A.C. Nonlinear Theory of Continuous Media. New York: McGraw-Hill, Inc., 1962.
- Gerrard, G.M. "Background to Mathematical Modelling in Geomechanics: The Role of Fabric and Stress History." In Finite Elements in Geomechanics, edited by G. Gudehus. London: John Wiley & Sons Ltd., 1977.
- Ghaboussi, J., and H. Momen. "Modelling and Analysis of Cyclic Behaviour of Sands." In Soil Mechanics: Transient and Cyclic Loads, edited by G.N. Pande and O.C. Zienkiewicz. Chichester, England: John Wiley & Sons Ltd., 1982.
- Girijavallabhan, C.V., and L.C. Reese. "Finite Element Method Applied to Some Problems in Soil Mechanics." Journal of Soil Mechanics and Foundation Engineering, ASCE, Vol. 94, No. SM2 (1968): 473-496.
- Goldscheider, M. "True Triaxial Tests on Dense Sand." In Results of the International Workshop on Constitutive Relations for Soils (held in Grenoble, France, 6-8 September, 1982), edited by G. Gudehus, F. Darve, and I. Vardoulakis. Rotterdam: A.A. Balkema, 1984.
- Goodman, M.A., and S.C. Cowin. "A Continuum Theory for Granular Materials." Archive for Rational Mechanics and Analysis, Vol. 44 (1972): 321-339.
- Gudehus, G. "Gedanken zur Statistischen Boden Mechanik." Bauingenieur, Vol. 43 (1968): 320-326.
- Gudehus, G. "Elastoplastische Stoffgleichungen für trockener Sand." Ingenieur Archiv., Vol. 42 (1973): 151-169.
- Gudehus, G., and F. Darve, Editors. International Workshop on the Constitutive Behavior of Soils (Grenoble, 6th - 8th September, 1982). Rotterdam: A.A. Balkema, 1984.
- Habib, P., and M.P. Luong. "Sols Pulverulents sous Chargement Cyclique." In Materiaux et Structures sous Chargement Cyclique, Palaiseau, France: Association Amicale des Ingenieurs Anciens Elèves de l'École Nationale des Ponts et Chaussées, 1978.
- Hartmann, J.P., and J.H. Schmertmann. "FEM Study of Elastic Phase of Pressuremeter Test." In Proceedings of the ASCE Specialty Conference on Insitu Testing, Vol. 1. New York: American Society of Civil Engineers (ASCE), 1975.
- Hay, G.E. Vector and Tensor Analysis. New York: Dover Publications, Inc., 1953.
- Hettler, A., I. Vardoulakis, and G. Gudehus. "Stress-Strain Behavior of Sand in Triaxial Tests." In Results of the International Workshop on Constitutive Relations for Soils (held in Grenoble, France, 6-8 September, 1982), edited by G. Gudehus, F. Darve, and I. Vardoulakis. Rotterdam: A.A. Balkema, 1984.

- Hill, R. The Mathematical Theory of Plasticity. Ely House, London: Oxford University Press, 1950.
- Horne, M.R. "The Behavior of an Assembly of Rotund, Rigid, Cohesionless Particles (I & II)." Proceedings of the Royal Society of London, Vol. 286 (1964): 62-97.
- Hughes, J.M.O., Wroth, C.P., and Windle, D. "Pressuremeter Tests in Sands." Geotechnique, Vol. 27, No. 4 (1977): 455-477.
- Hughes, T.J.R., and J.H. Prevost. "DIRT II: A Nonlinear Quasi-Static Finite Element Analysis Program." Pasadena, California: California Institute of Technology, 1979
- Ishihara, K., F. Tatsuoka, and S. Yasuda. "Undrained Deformation and Liquefaction of Sand Under Cyclic Stresses." Soils and Foundations, Vol. 15, No. 1 (1975): 29-44.
- Ivey, H.J. "Plastic Stress-Strain Relations and Yield Surfaces for Aluminum Alloys." Journal of Mechanical Engineering Sciences, Vol. 3 (1961): 15-31.
- Iwan, W.D. "On a Class of Models for the Yielding Behavior of Continuous and Composite Systems." Journal of Applied Mechanics, Vol. 89 (1967): 612-617.
- Jain, S.K. Fundamental Aspects of the Normality Rule. Blacksburg, Virginia: Engineering Publications, 1980.
- Jamal, A.K. "Triaxial Extension Tests on Hollow Cylinder Sand Specimens." Canadian Geotechnical Journal, Vol. 8, No. 1 (1971): 119-133.
- Janbu, N. "Soil Compressibility as Determined by Oedometer and Triaxial Tests." In European Conference on Soil Mechanics and Foundation Engineering, Vol. 1. Wiesbaden, Germany: N.P., 1963.
- Jaunzemis, W. Continuum Mechanics. New York: Macmillan Publishing Co., Inc., 1967.
- Kirkpatrick, W.M. "Discussion on Soil Properties and their Measurement." In Proceedings 5th International Conference on Soil Mechanics, Vol. 3 (17-22 July, 1961). Paris: Dunod, 1962.
- Ko, H.Y., and S. Sture. "State of the Art: Data Reduction and Application for Analytical Modeling." In Proceedings of the Symposium on Laboratory Shear Strength of Soil (held in Chicago, Illinois, 25 June, 1980), edited by R.N. Yong and F.C. Townsend. Philadelphia: American Society for Testing and Materials, 1980.
- Krieg, R.D. "A Practical Two-Surface Plasticity Theory." Journal of Applied Mechanics, Vol. 42 (1975): 641-646.

- Kulhawy, F.H., J.M. Duncan, and H.B. Seed. Finite Element Analysis of Stresses and Movement in Embankments During Construction. Report 569-8, Vicksburg, Mississippi: U.S. Army Engineers Waterways Experiment Station, 1969.
- Lade, P.V. "Cubical Triaxial Tests on Cohesionless Soil." Journal of the Soil Mechanics and Foundations Division, ASCE, Vol. 99, No. SM10 (1973): 793-812.
- Lade, P.V. "Elasto-plastic Stress-Strain Theory for Cohesionless Soil with Curved Yield Surfaces." International Journal of Solids and Structures, Vol. 13 (1977): 1019-1035.
- Lade, P.V. "Localization Effects in Triaxial Tests on Sand." In IUTAM Conference on Deformation and Failure of Granular Materials (held in Delft, Netherlands, 31 Aug.-3 Sept., 1982), edited by P.A. Vermeer and H.J. Luger. Rotterdam: A.A. Balkema, 1982.
- Lade, P.V., and J.M. Duncan. "Elasto-plastic Stress-Strain Theory for Cohesionless Soil." Journal of the Geotechnical Engineering Division, ASCE, Vol. 101, No. GT10 (1975): 1037-1053.
- Lade, P.V., and M. Oner. "Elasto-Plastic Stress-Strain Model, Parameter Evaluation, and Predictions for Dense Sand." In Results of the International Workshop on Constitutive Relations for Soils (held in Grenoble, France, 6-8 September, 1982), edited by G. Gudehus, F. Darve, and I. Vardoulakis. Rotterdam: A.A. Balkema, 1984.
- Laier, J.E., Schmertmann, J.H., and J.H. Schaub. "Effect of Finite Pressuremeter Length in Dry Sand." In Proceedings of the ASCE Specialty Conference on Insitu Testing, Vol. 1. New York: American Society of Civil Engineers (ASCE), 1975.
- Lambe, T.W., and R.V. Whitman. Soil Mechanics. New York: John Wiley & Sons, 1969.
- Lanier, J., and P. Stutz. "Supplementary True Triaxial Tests in Grenoble." In Results of the International Workshop on Constitutive Relations for Soils (held in Grenoble, France, 6-8 September, 1982), edited by G. Gudehus, F. Darve, and I. Vardoulakis. Rotterdam: A.A. Balkema, 1984.
- Lentz, R.W., and G.Y. Baladi. "Simplified Procedure to Characterize Permanent Strain in Sand Subject to Cyclic Loading." In Proceedings of the International Symposium on Soils Under Cyclic and Transient Loading (held in Swansea, Wales, 7-11 January, 1980), edited by G.N. Pande and O.C. Zienkiewicz. Rotterdam: A.A. Balkema, 1980.
- Linton, P.F. "A Study of a Sand in the Standard Triaxial Chamber Equipped With a Computerized Data Acquisition System." Master's Thesis, Department of Civil Engineering, University of Florida, Gainesville, Florida, May, 1986.

- Lode, W. "Versuche ueber den Einfluss der mittleren Hauptspannung auf das Fliessen der Metalle Eisen, Kupfer, und Nickel." Zeitschrift fur Physik, Vol. 36 (1926): 913-939.
- Loret, B. "On the Choice of Elastic Parameters for Sand." International Journal for Numerical and Analytical Methods in Geomechanics, Vol. 9 (1985): 285-292.
- Lublinter, J. "A Simple Theory of Plasticity." International Journal of Solids and Structures. Vol. 10 (1974): 313-319.
- Luong, M.P. "Stress-Strain Aspects of Cohesionless Soils Under Cyclic and Transient Loading." In Proceedings of the International Symposium on Soils Under Cyclic and Transient Loading (held in Swansea, Wales, 7-11 January, 1980), edited by G.N. Pande and O.C. Zienkiewicz. Rotterdam: A.A. Balkema, 1980.
- Malvern, L.E. Introduction to the Mechanics of a Continuous Medium. Englewood Cliffs, New Jersey: Prentice Hall Inc., 1969 .
- Matsuoka, H., and T. Nakai. "Stress-Deformation and Strength Characteristics of Soil Under Three Different Principal Stresses." Proceedings of the Japanese Society of Civil Engineers, Vol. 232 (1974): 59-70.
- Melan, E. "Zur Plastizitaet des raeumlichen Kontinuums." Ingenieur Archiv., Vol. 9 (1938): 116-126.
- Mises, R. von. "Mechanik der plastischen Formaenderung von Kristallen." Zeitschrift fur Angewandte Mathematik und Mechanik, Vol. 8 (1928): 161-185.
- Mould, J.C., S. Sture, and H.Y. Ko. "Modeling of Elastic-Plastic Anisotropic Hardening and Rotating Principal Stress Directions in Sand." In IUTAM Conference on Deformation and Failure of Granular Materials (held in Delft, Netherlands, 31 Aug.-3 Sept., 1982), edited by P.A. Vermeer and H.J. Luger. Rotterdam: A.A. Balkema, 1982.
- Mroz, Z. "On the Description of Anisotropic Work Hardening." Journal of Mechanics and Physics of Solids, Vol. 15 (1967): 163-175.
- Mroz, Z. "On Isotropic Hardening Constitutive Models in Soil Mechanics." In Results of the International Workshop on Constitutive Relations for Soils (held in Grenoble, France, 6-8 September, 1982), edited by G. Gudehus, F. Darve, and I. Vardoulakis. Rotterdam: A.A. Balkema, 1984.
- Mroz, Z., and V.A. Norris. "Elastoplastic and Viscoplastic Constitutive Models for Soils with Application to Cyclic Loading." In Soil Mechanics - Transient and Cyclic Loads, edited by G.N. Pande and O.C. Zienkiewicz. New York: John Wiley & Sons, 1982.

- Naghdi, P.M. "Stress-Strain Relations in Plasticity and Thermoplasticity." In Plasticity, Proceedings of the 2nd Symposium on Naval Structural Mechanics, edited by E.H. Lee and P.S. Symonds. Oxford: Pergamon Press, 1960.
- Naghdi, P.M., F. Essenburg, and W. Koff. "An Experimental Study of Initial and Subsequent Yield Surfaces in Plasticity." Journal of Applied Mechanics, Vol. 25 (1958): 201-209.
- Nayak, G.C., and O.C. Zienkiewicz. "Convenient Form of Stress Invariants for Plasticity." Journal of the Structural Division, ASCE, Vol. 98, NO. ST4 (1972): 949-954.
- Nemat-Nasser, S. "On Dynamic and Static Behaviour of Granular Materials." In Soil Mechanics - Transient and Cyclic Loads, edited by G.N. Pande and O.C. Zienkiewicz. New York: John Wiley & Sons, 1982.
- Nemat-Nasser, S., and M.M. Mehrabadi. "Micromechanically Based Rate Constitutive Descriptions for Granular Materials." In Mechanics of Engineering Materials, edited by C.S. Desai and R.H. Gallagher. New York: John Wiley & Sons, 1984.
- Nova, R., and D.M. Wood. "A Constitutive Model for Sand in Triaxial Compression." International Journal for Numerical and Analytical Methods in Geomechanics, Vol. 3 (1979): 255-278.
- Oda, M. "The Mechanism of Fabric Change During Compressional Deformation of Sand." Soils and Foundations, Vol. 12, No. 2 (1972): 1-18.
- Oda, M. "Fabric Tensor for Discontinuous Geological Materials." Soils and Foundations, Vol. 22, No. 4 (1982): 96-108.
- Oda, M., J. Konishi, and S. Nemat-Nasser. "Some Experimentally Based Fundamental Results on the Mechanical Behaviour of Granular Materials." Geotechnique, Vol. 30, No. 4 (1980): 479-495.
- Odqvist, F.K.G. "Die Verfestigung von flusseisenaehnlichen Koerpern." Zeitschrift fur Angewandte Mathematik und Mechanik, Vol 13 (1933): 360-363.
- Pande, G.N., and O.C. Zienkiewicz, Editors. Proceedings of the International Symposium on Soils Under Cyclic and Transient Loading (held in Swansea, Wales, 7-11 January, 1980). Rotterdam: A.A. Balkema, 1980.
- Parkin, A.K., C.M. Gerrard, and D.R. Willoughby. "Discussion on Deformation of Sand in Hydrostatic Compression." Journal of Soil Mechanics and Foundation Engineering, ASCE, Vol. 94, No. SM1 (1968): 336-340.
- Phillips, A., and G.J. Weng. "An Analytical Study of an Experimentally Verified Hardening Law." Journal of Applied Mechanics, Vol. 42 (1975): 375-378.

- Pietruszczak, St., and Z. Mroz. "On Hardening Anisotropy of K₀ Consolidated Clays." International Journal for Numerical and Analytical Methods in Geomechanics, Vol. 7 (1983): 19-38.
- Podgorski, J. "General Failure Criterion for Isotropic Media." Journal of Engineering Mechanics, ASCE, Vol. 111, No. 2 (1985): 188-201.
- Poorooshasb, H.B., I. Holubec, and A.N. Sherbourne. "Yielding and Flow of Sand in Triaxial Compression: Part I." Canadian Geotechnical Journal, Vol. 3, No. 4 (1966): 179-190.
- Poorooshasb, H.B., I. Holubec, and A.N. Sherbourne. "Yielding and Flow of Sand in Triaxial Compression: Parts II and III." Canadian Geotechnical Journal, Vol. 4, No. 4 (1967): 376-397.
- Poorooshasb, H.B., R.N. Yong, and B. Lelievre. "Anisotropic Hardening Yield Loci for Sand." In IUTAM Conference on Deformation and Failure of Granular Materials (held in Delft, Netherlands, 31 Aug.-3 Sept., 1982), edited by P.A. Vermeer and H.J. Luger. Rotterdam: A.A. Balkema, 1982.
- Prager, W. "Recent Developments in the Mathematical Theory of Plasticity." Journal of Applied Physics, Vol. 20, No. 3 (1949): 235-241.
- Prager, W. "The Theory of Plasticity: A Survey of Recent Achievements." In Proceedings of the Institution of Mechanical Engineers (James Clayton Lecture), Vol. 169, No. 21 (1955): 41-57.
- Prevost, J.H. "Plasticity Theory for Soil Stress-Strain Behavior." Journal of the Engineering Mechanics Division, ASCE, Vol. 104, No. EM5 (1978): 1177-1194.
- Prevost, J.H. "Nonlinear Anisotropic Stress-Strain-Strength Behavior of Soils." In Proceedings of the Symposium on Laboratory Shear Strength of Soil (held in Chicago, Illinois, 25 June, 1980), edited by R.N. Yong and F.C. Townsend. Philadelphia: American Society for Testing and Materials, 1980.
- Romano, M. "A Continuum Theory for Granular Media with a Critical State." Archive for Rational Mechanics and Analysis, Vol. 26 (1974): 1011-1028.
- Roscoe, K.H., and J.B. Burland. "On the Generalized Stress-Strain Behaviour of 'Wet' Clay." In Engineering Plasticity, edited by J. Heyman and F.A. Leckie. Bentley House, London: Cambridge University Press, 1968.
- Rowe, P.W. "The Stress-Dilatancy Relation for Static Equilibrium of an Assembly of Particles in Contact." Proceedings of the Royal Society of London, Vol. 269 (1962): 500-527.

- Saada, A.S., G. Bianchi, and P. Puccini. "The Mechanical Properties of Anisotropic Granular Soils." In International Symposium No. 351 of the National Center for Scientific Research. Grenoble, France: N.P., 1983.
- Saada, A.S., and F.C. Townsend. "State of the Art: Laboratory Strength Testing of Soils." In Proceedings of the Symposium on Laboratory Shear Strength of Soil (held in Chicago, Illinois, 25 June, 1980), edited by R.N. Yong and F.C. Townsend. Philadelphia: American Society for Testing and Materials, 1980.
- Saleeb, A.F., and W.F. Chen. "Nonlinear Hyperelastic (Green) Constitutive Models for Soils: Theory and Calibration." In Proceedings of the Workshop on Limit Equilibrium, Plasticity and Generalized Stress-Strain in Geotechnical Engineering (held in Montreal, Canada, 28-30 May, 1980), edited by R.N. Yong and H.Y. Ko. New York: American Society of Civil Engineers (ASCE), 1980.
- Sandler, I.S., F.L. DiMaggio, and G.Y. Baladi. "Generalized Cap Model for Geologic Materials." Journal of the Geotechnical Engineering Division, ASCE, Vol. 102, No. GT7 (1976): 683-699.
- Satake, M. "Constitution of Mechanics of Granular Materials through the Graph Theory." In Proceedings of the U.S.-Japan Seminar on Continuum Mechanical and Statistical Approaches in the Mechanics of Granular Materials (held in Sendai, Japan, June 5-9, 1978), edited by S.C. Cowin and M. Satake. Gakujutsu Bunken Fukyukai, Tokyo: The Kajima Foundation, 1978.
- Schmidt, R. "Ueber den Zusammenhang von Spannungen und Formaenderungen im Verfestigungsarbeit." Ingenieur Archiv., Vol. 3 (1932): 215-235.
- Schofield, A., and C.P. Wroth. Critical State Soil Mechanics. London: McGraw-Hill, 1968.
- Scott, R.F. "Plasticity and Constitutive Relations in Soil Mechanics." 19th Terzaghi Lecture, Journal of the Geotechnical Engineering Division, ASCE, Vol. 111, No. 5 (1985): 563-605.
- Seereeram, D., and J.L. Davidson. "Prediction of Pressuremeter Tests in Sand Using a New Elasto-plastic Model." submitted for publication, 1986.
- Seereeram, D., M.C. McVay, and P.F. Linton. "Generalized Phenomenological Cyclic Stress-Strain-Strength Characterization of Anisotropic Granular Media." Annual Report, Grant No. AFOSR-84-0108, Gainesville, Florida: Department Of Civil Engineering, Division of Soil Mechanics, University of Florida 1985.
- Shield, R.T. "On Coulomb's Law of Failure in Soils." Journal of Mechanics and Physics of Solids, Vol. 4 (1955): 10-10.

- Sture, S., J.C. Mould, and H.Y. Ko. "Elastic-Plastic Anisotropic Hardening Constitutive Model and Prediction of Behavior for Dry Quartz Sand." In Results of the International Workshop on Constitutive Relations for Soils (held in Grenoble, France, 6-8 September, 1982), edited by G. Gudehus, F. Darve, and I. Vardoulakis. Rotterdam: A.A. Balkema, 1984.
- Synge, J.L., and A. Schild. Tensor Calculus. Toronto: University of Toronto Press, 1949.
- Tatsuoka, F. "A Fundamental Study on the Deformation of a Sand by Triaxial Tests." Doctoral Dissertation (translated from Japanese by D.M. Wood), Department of Civil Engineering, University of Tokyo, Bunkyo-ku, Tokyo 113, Japan, 1972.
- Tatsuoka, F., and K. Ishihara. "Drained Deformation of Sand Under Cyclic Stresses Reversing Directions." Soils and Foundations, Vol. 14, No. 3 (1974a): 51-65.
- Tatsuoka, F., and K. Ishihara. "Yielding of Sand in Triaxial Compression." Soils and Foundations, Vol. 14, No. 2 (1974b): 63-76.
- Taylor, G.I., and H. Quinney. "The Plastic Distortion of Metals." Philosophical Transactions of the Royal Society, Vol. 230 (1931): 323-362.
- Tresca, H. "Mémoire sur l'écoulement des corps solides soumis à de fortes pressions." Comptes Rendus hebdomadaires des seances de l'Academie des Sciences, Vol. 59 (1864): 754-760.
- Truesdell, C. "Hypoelasticity". Archive for Rational Mechanics and Analysis, Vol. 4 (1955): 83-133.
- Vermeer, P.A., and H.J. Luger, Editors. IUTAM Conference on Deformation and Failure of Granular Materials (held in Delft, Netherlands, 31 Aug.-3 Sept., 1982). Rotterdam: A.A. Balkema, 1982.
- Wiedemann, G. "Ueber die Torsion, die Biegung und den Magnetismus." Verhandlungen der naturforschenden Gessellschaft in Basel, Vol. 2 (1860): 168-247.
- Willam, K.J., and E.P. Warnke. "Constitutive Model for the Triaxial Behavior of Concrete." In Proceedings of the International Association of Bridge and Structural Engineers' Seminar on Concrete Structures Subjected to Triaxial Stresses. Bergamo, Italy: N.P., 1974.
- Wrede, R.C. Introduction to Vector and Tensor Analysis. New York: Dover Publications, Inc., 1972.
- Wu, T.H., A.K. Loh, and L.E. Malvern. "Study of the Failure Envelope of Soils." Proceedings of the American Society of Civil Engineers, Vol. 89, No. SM1 (1963): 145-181.

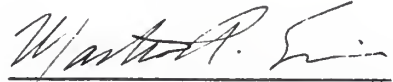
- Wylie, C.R., and L.C. Barrett. Advanced Engineering Mathematics. New York: McGraw-Hill Book Co., 1982.
- Yong, R.N., and H.Y. Ko. "Soil Constitutive Relationships and Modelling of Soil Behavior." In Workshop on Limit Equilibrium, Plasticity and Generalized Stress-Strain in Geotechnical Engineering (held in Montreal, Canada, 28-30 May, 1980), edited by R.N. Yong and H.Y. Ko. New York: American Society of Civil Engineers (ASCE), 1980a.
- Yong, R.N., and H.Y. Ko, Editors. Workshop on Limit Equilibrium, Plasticity and Generalized Stress-Strain in Geotechnical Engineering (held in Montreal, Canada, 28-30 May, 1980). New York: American Society of Civil Engineers (ASCE), 1980b.
- Ziegler, H. "A Modification of Prager's Hardening Rule." Quarterly of Applied Mathematics, Vol. 17, No. 1 (1959): 55-65.
- Zienkiewicz, O.C., and Z. Mroz. "Generalized Plasticity Formulation and Applications to Geomechanics." In Mechanics of Engineering Materials, edited by C.S. Desai and R.H. Gallagher. New York: John Wiley & Sons, 1984.

BIOGRAPHICAL SKETCH

Devo Seereeram was born on July 4th, 1957, in Chaguanas, Trinidad, where he attended Montrose Vedic School until the age of 12. His secondary education continued at Presentation College over the next five years, culminating in a first place high school ranking in the University of Cambridge's General Certificate of Education at the "Ordinary Level". Two years later he achieved a similar ranking at the "Advanced Level".

After high school, Devo spent two years working in his father's highway construction company before deciding to further his education at the University of Florida. He graduated in Spring 1982 with a B.S.C.E. degree (High Honors) and proceeded immediately into the U.F. Master of Engineering program. In Fall 1983, he completed the master's program with a specialization in geotechnical engineering and decided to continue uninterruptedly toward a doctoral degree. He expects to earn his doctorate in Spring 1986. Upon completion of the Ph.D program, Devo intends to seek an academic position or a job in industry either in the United States or in his home country.

I certify that I have read this study and that in my opinion it conforms to acceptable standards of scholarly presentation and is fully adequate, in scope and quality, as a dissertation for the degree of Doctor of Philosophy.



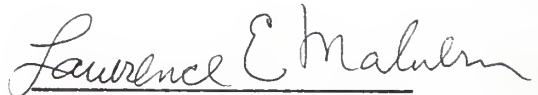
Martin A. Eisenberg
Professor of Engineering
Sciences

I certify that I have read this study and that in my opinion it conforms to acceptable standards of scholarly presentation and is fully adequate, in scope and quality, as a dissertation for the degree of Doctor of Philosophy.



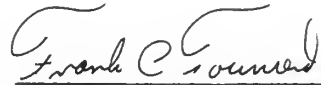
William G. Goldhurst
Professor of English

I certify that I have read this study and that in my opinion it conforms to acceptable standards of scholarly presentation and is fully adequate, in scope and quality, as a dissertation for the degree of Doctor of Philosophy.



Lawrence E. Malvern
Professor of Engineering
Sciences

I certify that I have read this study and that in my opinion it conforms to acceptable standards of scholarly presentation and is fully adequate, in scope and quality, as a dissertation for the degree of Doctor of Philosophy.



Frank C. Townsend, Chairman
Professor of Civil Engineering

I certify that I have read this study and that in my opinion it conforms to acceptable standards of scholarly presentation and is fully adequate, in scope and quality, as a dissertation for the degree of Doctor of Philosophy.



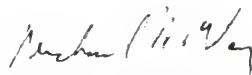
Daniel C. Drucker
Graduate Research Professor of
Engineering Sciences

I certify that I have read this study and that in my opinion it conforms to acceptable standards of scholarly presentation and is fully adequate, in scope and quality, as a dissertation for the degree of Doctor of Philosophy.



John L. Davidson
Associate Professor of Civil
Engineering

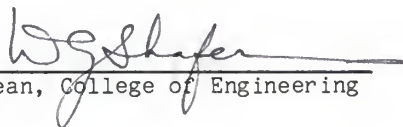
I certify that I have read this study and that in my opinion it conforms to acceptable standards of scholarly presentation and is fully adequate, in scope and quality, as a dissertation for the degree of Doctor of Philosophy.



Michael C. McVay
Assistant Professor of Civil
Engineering

This dissertation was submitted to the Graduate Faculty of the College of Engineering and to the Graduate School and was accepted as partial fulfillment of the requirements for the degree of Doctor of Philosophy.

May 1986



Dean, College of Engineering

Dean, Graduate School

UNIVERSITY OF FLORIDA



3 1262 08554 4467